Development of Instrumentation for Low Energy Beams

Thesis submitted in accordance with the requirements of

the University of Liverpool for the degree of Doctor in Philosophy

by

Janusz Harasimowicz

February 2013

b

Abstract

Ion and antiproton beams at keV energies are very attractive for a number of fundamental studies. The diagnostic of these beams, however, is a challenge because most detectors are either not sensitive enough or too disturbing.

In this work, a set of optimised detectors has been developed to suit the particular beam diagnostic needs of the novel Ultra-low-energy Storage Ring (USR) at the future Facility for Low-energy Antiproton and Ion Research (FLAIR), accommodating as few as 10^7 particles at energies down to 20 keV.

The instrumentation includes beam profile monitors based on scintillating screens and secondary electron emission, ultra-sensitive Faraday cups for absolute intensity measurements, and capacitive pick-ups for on-line beam position monitoring.

This thesis presents results from theoretical studies and modelling, the design of prototypes of all monitors, and results from measurements with beam. All detectors are characterised in detail, their individual limitations are described and options for further improvements are indicated.

Whilst initially developed for the USR, the instrumentation described in this thesis is also well suited for use in other low-intensity, low-energy accelerators, storage rings, and beam lines.

0. ABSTRACT

Contents

Acronyms

AA Antiproton Accumulator
AC Antiproton Collector
AD Antiproton Decelerator
ADC analogue-to-digital converter
AEGIS Antihydrogen Experiment: Gravity, Interferometry, Spectroscopy
ALPHA Antihydrogen Laser PHysics Apparatus
ASACUSA Atomic Spectroscopy And Collisions Using Slow Antiprotons
ATRAP Antihydrogen TRAP

BCT beam current transformer

CAD computer-aided design
CCC cryogenic current comparator
CCD charge-coupled device
CERN Conseil Européen pour la Recherche Nucléaire
CR Collector Ring
CSDA continuous slowing-down approximation
CSR Cryogenic Storage Ring
CVD chemical vapour deposition

DESIREE Double ElectroStatic Ion Ring ExpEriment
DFT discrete Fourier transform
DLA delay line anode

ELENA Extra-Low-ENergy Antiproton ring
ELISA ELectrostatic Ion Storage ring, Aarhus
EXCYT EXotics at the CYclotron and Tandem

FAIR Facility for Antiproton and Ion Research

Acronyms

Fermilab Fermi National Accelerator Laboratory
FLAIR Facility for Low-Energy Antiproton and Ion Research
FLSR Frankfurt Low-energy Storage Ring
FRIBS in-Flight Radioactive Ion BeamS
FWHM full width at half maximum

GANIL Grand Accélérateur National d'Ions Lourds
GEM gas electron multiplier
GSI Gesellschaft für Schwerionenforschung
GUI graphical user interface

HITRAP Heavy Ion TRAP
HPD hybrid photo diode
HV high voltage

ICT integrating current transformer
INFN-LNS Istituto Nazionale di Fisica Nucleare - Laboratori Nazionali del Sud
IPM ionization profile monitor
ISOLDE ISOtope separator on-Line DEtector

KEK Kō Enerugī Kasōki Kenkyū Kikō

LEAR Low-Energy Antiproton Ring
LEIR Low-Energy Ion Ring
LHC Large Hadron Collider
LSR Low-energy Storage Ring

MCP microchannel plate
MPI-K Max-Planck-Institut für Kernphysik
MSL Manne Siegbahn Laboratory
MWPC multi-wire proportional chamber

NESR New Experimental Storage Ring

PPIC parallel-plate ionization chamber
PS Proton Synchrotron
PTFE polytetrafluoroethylene
PU pick-up

QE quantum efficiency

RESR Recuperated Experimental Storage Ring
REX-ISOLDE Radioactive beam EXperiment at ISOLDE
RF radio-frequency
RFQD radio-frequency quadrupole decelerator
RGM residual gas monitor
RMS root mean square
ROI region of interest

SEM secondary emission monitor
SFOP scintillating fibre optic plate
SNR signal-to-noise ratio
SPIRAL Système de Production d'Ions Radioactifs en Ligne
SPS Super Proton Synchrotron
SQUID superconducting quantum interference device

TMU Tokyo Metropolitan University
TSR Test Storage Ring

UHV ultra-high vacuum
USR Ultra-low-energy Storage Ring

Acknowledgements

I would like to express my appreciation and gratitude to my supervisor, Prof. Dr. Carsten P. Welsch, who has fully supported and secured not only my scientific work but also work-life balance.

I would like to acknowledge the generous support of the European Commission under Contract No. PITN-GA-2008-215080, Helmholtz Association of National Research Centers (HGF) and GSI Helmholz Center for Heavy Ion Research (GSI) under Contract No. VH-NG-328, and STFC Cockcroft Institute Core Grant No. ST/G008248/1.

I am very grateful to our colleagues from the National Institute of Nuclear Physics INFN-LNS in Catania, particularly Paolo Finocchiaro, Luigi Cosentino, Alfio Pappalardo and Antonino Amato as well as INFN accelerator and ion source staff, for their endless support over the years and possibility to run so many beam experiments at their facility. The reader of this thesis will easily notice the amount of work that has been done together with and thanks to this fantastic group of people.

I would like to thank the AEGIS team at CERN, particularly Michael Doser, Angela Gligorova and Germano Bonomi, for their support and help. I hope to return the favour to Germano one day for the spare time he devoted to perform Geant4 simulations for the here-described Faraday cup studies.

I appreciate the invaluable help of Anders Källberg and Andras Paál of the Manne Siegbahn Laboratory who shared their broad knowledge and experience in low-energy beam diagnostics and electronics. Special thanks go to Andras who designed and manufactured the customised low-noise amplifiers for the here-described capacitive pick-up.

There are many other people who have supported and helped me over the years and I appreciate their good will and patience to answer my numerous questions. I would like to express my deep gratitude to Felix Laux, Manfred Grieser, Thomas Sieber, Kai-Uwe Kühnel, Peter Forck, Piotr Kowina, Andreas Peters, Masaki Hori, Fredrik John Carl Wenander, Helge Knudsen, Michele Siggel-King, Andrzej Wolski, Ian Shinton, Petteri Pusa, Scott Hamilton, Ian Burrows and many, many others. Special thanks

go to Juan Luis Fernando-Hernandez for running Fluka simulations for the secondary emission monitor studies.

Thanks to all members of the QUASAR group at the Cockcroft Institute, Max Planck Institute and CERN, and to all DITANET trainees for sharing the journey through my PhD studies. Everyone has contributed to the joy of this time, but the most influential will remain Massimiliano Putignano who always asked the right questions.

Finally, I would like to thank my family, my parents, Bożena and Ryszard, my parents in law, Hanna and Krzysztof, and my beloved wife, Anna. I am very grateful for your endless support and taking care of everyday life problems so that I could focus on my research work. To you all, thanks for always being there for me.

Chapter 1

Introduction

1.1 Background

The antiproton ($\bar{p}$), the antiparticle of the proton, has been a central point of interest and an invaluable tool for many research studies. It was predicted by Paul Dirac at the beginning of the 1930s [1] and observed experimentally in 1955 [2, 3]. Unfortunately, early experiments had to deal with antiprotons in the form of secondary beams with low intensity and broad energy, contaminated by negatively charged pions. It was only decades later that dedicated machines were built at the European Organization for Nuclear Research (CERN) in Geneva and Fermi National Accelerator Laboratory (Fermilab) in Batavia, Illinois to deliver $\bar{p}$ beams with high intensity, purity and energy resolution. This started a new era for antimatter research. In 1983, proton-antiproton collision studies confirmed the existence of new particles, the W and Z bosons [4,5]. In 1995, the first in-beam production of fast antihydrogen atoms was reported [6]. In 2002, cold antihydrogen was obtained [7,8] which was an important step towards magnetically trapped neutral antimatter. Eight years later, in 2010, antihydrogen was stored for the first time [9], paving the way to precision spectroscopy and gravitational tests with antiatoms. Technological developments can now open up new possibilities to employ antiprotons to fundamental and applied research [10–13]. Of special interest are studies of matter-antimatter symmetry [14], ionization of atoms and molecules by antiparticle impact [15], antiprotonic atoms spectroscopy [16], antimatter gravity [17, 18], or even applications of antiprotons to cancer treatment [19] and space propulsion [20].

1.2 Antiproton Machines

The following subsections are intended to present the road from early high-energy accelerators to future ultra-low-energy storage rings designed to study physics with antimatter. The main focus is placed on the pursuit of delivering high quality beams at the lowest energies, hence some machines are not covered, such as high- or medium-energy rings at the future Facility for Antiproton and Ion Research (FAIR) [10] or Fermilab [21].

1.2.1 Production of Antiprotons

A collision of protons with a fixed target at a sufficiently high energy creates new particles, including antiprotons. The latter can be produced above the 5.6 GeV kinetic energy threshold in the reaction with a stationary proton [22]:

$$\mathrm{p} + \mathrm{p} \rightarrow \mathrm{p} + \mathrm{p} + \mathrm{p} + \bar{\mathrm{p}}. \tag{1.1}$$

Created antiprotons have a broad energy spectrum, travel in random directions and are accompanied by other particles, such as pions, muons and electrons. In order to obtain a clean, well-focused beam of high intensity required for experiments, antiprotons need to be guided at a selected energy by magnetic fields and stacked in a storage ring for deceleration and cooling.

Beam cooling means that the transversal emittance, a measure of the area occupied by particles of a beam in phase space, proportional to the transversal momentum and the diameter of the beam, is decreased, i.e. the density of particles in phase space is increased. Cooling is necessary because deceleration only reduces the longitudinal momentum of the beam while it increases the transversal momentum due to adiabatic beam expansion (beam blow-up) [23].

1.2.2 Antiproton Accumulator (AA) and CERN $\mathrm{p\bar{p}}$ Collider

At the beginning of the 1980s, an Antiproton Accumulator (AA) [24, 25] was ready to provide high quality $\bar{\mathrm{p}}$ beams at CERN. A 25 GeV proton beam from the Proton Synchrotron (PS) [26] was used on a fixed iridium target to produce antiprotons at about 2.8 GeV, creating approximately one antiproton per 10^6 incident protons. The role of the AA was to stack and cool the 2.8 GeV antiparticles and the machine was able to store a few times 10^{11} antiprotons per day. The technique used for beam cooling was based on detection of deviation of individual charged particles in the beam

from the ideal orbits and correcting their positions by means of a magnetic or electric "kicker" device; it is known as stochastic cooling. In 1986, a second ring, the Antiproton Collector (AC) [24, 25, 27], was built around the existing AA in order to improve the antiproton production rate by a factor of 10. The cooled antiparticles were reinjected into the PS, accelerated to 25 GeV and injected into the Super Proton Synchrotron (SPS) converted into a proton-antiproton collider [28]. Counter-rotating in the same beam tube, both the antiproton and proton beams were accelerated to 270 GeV, or 315 GeV after the upgrade, and brought into collision. In 1990, the SPS $p\bar{p}$ collider experimental program was brought to an end.

1.2.3 Low Energy Antiproton Ring (LEAR)

Inspired by the discoveries and new concepts in the accelerator field, physicists realized that cooling and deceleration of antiprotons could provide beams of intensity and purity for low energy physics not known before. For this reason, a Low-Energy Antiproton Ring (LEAR) [29] was brought to life shortly after the AA had been operating.

Antiprotons accumulated in the AA were extracted, decelerated in the PS and then injected into LEAR for further deceleration or acceleration [29]. LEAR provided high quality $\bar{p}$ beams with energies between 5.3 MeV and 1.3 GeV. A beam with an initial intensity of as much as $5 \cdot 10^{10}$ antiprotons was kept circulating for many hours or even days for in-ring experiments with a gas jet target. In addition, LEAR offered both slowly extracted beams and single or several bunches extracted by a fast kicker for trap experiments. Stochastic cooling was used from the beginning, but also an electron cooler was incorporated into LEAR at a later stage. Electron cooling is based on merging an ion beam with a beam of cold electrons having the same average velocity in the longitudinal direction; the ions undergo Coulomb scattering in the electron "gas" and their momentum spread is reduced.

In 1996, the AA, AC and LEAR were closed down in order to free resources for the Large Hadron Collider (LHC). LEAR was converted into the Low-Energy Ion Ring (LEIR), a high quality source of ion beams. However, there were strong requests from the user community to continue the experiments with low-energy antiprotons. The solution was to use the AC alone as an antiproton cooler and decelerator ring.

1.2.4 Antiproton Decelerator (AD)

A project to convert the AC into an Antiproton Decelerator (AD) was approved in 1997 and the new facility has become operational in 2000 [30–32].

Similarly to the AA, the AD requires the PS as a source of high energy protons for $\bar{p}$ creation. The 25 GeV beam consisting of about $1.3 \cdot 10^{13}$ protons is sent onto a water cooled iridium target. Approximately $4 \cdot 10^7$ antiprotons with an energy of 2.8 GeV are then captured and injected into the AD. The beam is decelerated to 5.3 MeV in steps with pauses for stochastic and electron cooling.

Although the low-energy antiproton source has been saved and the machines involved have been reduced from five to two, the users have had to accept some limitations. Compared to LEAR, the AD has offered a 10-times smaller antiproton flux and no slow extraction has been made available. A single bunch of about $3 \cdot 10^7$ antiprotons is delivered approximately every 100 seconds, but particles can be stacked in trap experiments from successive pulses. However, the lowest energy of 5.3 MeV is too high for trapping and additional solutions have had to be found to reduce it to less than a few tens of keV suitable for experiments with traps.

Two experiments, ALPHA [33] and ATRAP [34], use a set of thin metal degraders to slow the AD beam to a few keV kinetic energy. This results in a poor efficiency due to adiabatic expansion of beam emittance as well as scattering in the degraders and annihilation. As a consequence, less than 0.5% of the AD beam can be trapped [35,36]. A similar technique based on foil degraders is planned to be used also at the AEGIS experiment [37].

The ASACUSA collaboration [38] use a radio-frequency quadrupole decelerator (RFQD) [39] to slow antiprotons down to approximately 50 – 120 keV, thus a thinner plastic foil can be used to reduce the energy further to less than 10 keV. An radio-frequency (RF) quadrupole is a linear accelerator used at low energies that accelerates, bunches and focuses a continuous beam of charged particles, but if used as a decelerator, all its functions are "reversed". Due to absence of cooling, beam deceleration is accompanied by adiabatic expansion which causes significant reduction in trapping efficiency. About 70% of the beam is lost after passing through the RFQD, but also the transverse beam size reaches about 160 mm, and only a short beam transport of a few metres is possible [35, 36]. Further complications come from the fact that tuning of the transfer line from the AD to RFQD is difficult and time consuming. Eventually, about 3 – 5% of the AD antiprotons can be captured at ASACUSA.

1.2.5 Extra Low Energy Antiproton Ring (ELENA)

The need for a solution which could provide high quality $\bar{p}$ beams at keV energies existed already in the LEAR era. The first proposal for such a machine, called Extra-Low-

ENergy Antiproton ring (ELENA), was made in 1982, but the most recent low-energy upgrade to the AD was accepted only recently [40, 41].

The idea of using a smaller ring to further decelerate the AD antiproton beam to an energy where the trapping efficiency could be greatly enhanced was revived in 2003 with an initial study of a new ELENA ring. The design slowly evolved with various feasibility and cost studies, to be finally approved as a CERN project in June 2011. The ring commissioning is scheduled for 2015 with the installation and setting-up of the electrostatic beam lines a year later [41, 42].

ELENA is a compact storage ring, only 30.4 m in circumference, which is expected to slow the AD antiprotons to 100 keV, cool them via integrated electron cooling, and deliver to various experiments via electrostatic beam lines. The total number of extracted antiprotons is estimated to be approximately $2 \cdot 10^7$. An improvement of up to 2 orders of magnitude can be expected as compared to the energy degraders.

The energy of 100 keV has been chosen to meet the requirements for beam quality that can be degraded at lower energies when extracted through foils separating the ultra-high vacuum (UHV) environment of trap experiments from the beam lines at a higher pressure. Additionally, it has been proposed to divide the beam into four equal bunches and deliver it to four different experiments quasi-simultaneously [36, 41–43].

The low-energy AD upgrade at CERN is a near-future solution that will provide users with higher deceleration efficiency and an increased number of trapped antiprotons. However, features such as slow extraction of quasi-DC beams over a broad energy range, ultra-short bunches of only a few nanoseconds duration for in-ring studies or fast extraction at only tens of keV for efficient loading into traps can be provided only in a long-term perspective. For this reason, a dedicated antiproton facility offering a wide range of antiproton beam parameters has been sought after for many years.

1.2.6 Facility for Low Energy Antiproton and Ion Research (FLAIR)

A future Facility for Low-Energy Antiproton and Ion Research (FLAIR), part of FAIR, was designed to be a next-generation low-energy antiproton complex providing both fast and slow extracted cooled beams at two orders of magnitude lower energy and two orders of magnitude higher intensity than the existing AD [44, 45].

The FAIR facility is currently being built at the GSI Helmholtz Centre for Heavy Ion Research in Darmstadt [46], see Fig. 1.1. For the production of antiprotons, it is planned to employ the SIS100 synchrotron to accelerate intense proton beams with about $2 \cdot 10^{13}$ particles per spill to an energy of 29 GeV. After a nickel target and a magnetic

separator, about 10^8 antiprotons per cycle at 3 GeV will be collected in the Collector Ring (CR). Stochastically cooled particles will then be transferred to a Recuperated Experimental Storage Ring (RESR) where a large stack of up to 10^{11} cooled antiprotons can be accumulated. Next, a New Experimental Storage Ring (NESR) can be used to decelerate antiprotons to a minimum energy of 30 MeV [10, 47].

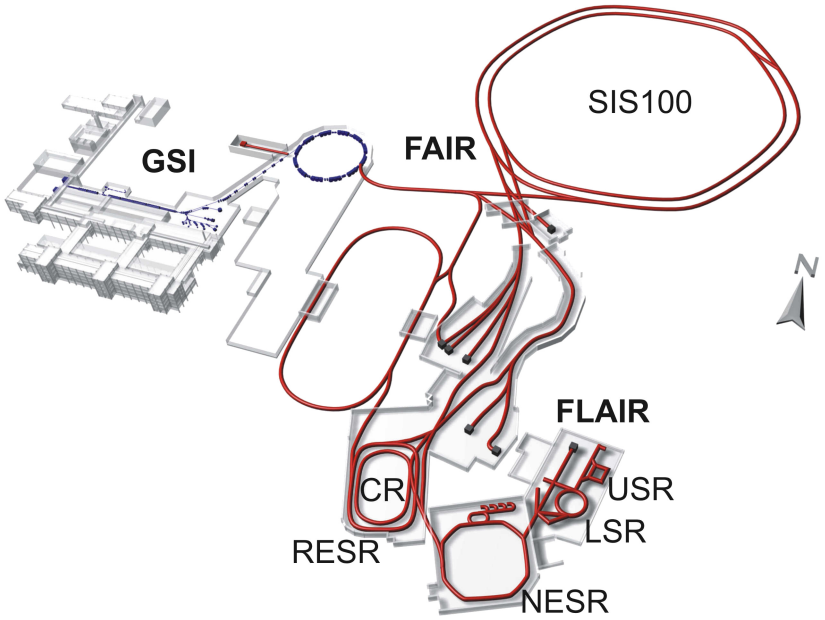

Figure 1.1: Overview of the FAIR facility. On the left, the existing GSI facility is shown (blue), and on the right, the newly planned complex (red). Only accelerators relevant for FLAIR are labelled, see text for details.

Within FLAIR, 30 MeV antiprotons delivered from NESR will be decelerated in two steps. First, the beam will be cooled and slowed down to an energy of 300 keV in a conventional magnetic ring, the Low-energy Storage Ring (LSR) [48], based on the modified CRYRING machine [49, 50]. Next, it will be transferred into an electrostatic Ultra-low-energy Storage Ring (USR) and decelerated further to 20 keV or even less [51]. The latter ring is of central interest for the here-presented work.

1.2.7 Ultra Low Energy Storage Ring (USR)

The USR will provide world-wide unique conditions for both in-ring studies with cooled stored antiprotons as well as for experiments requiring extracted slow beams. The ring will be able to accept 300 keV particles and decelerate them to 20 keV or possibly to

even lower energies. A wide range of beam configurations will be available, ranging from very short pulses in the nanosecond regime to a coasting beam. The ring also features a combined fast and slow extraction scheme that can provide external experiments with cooled beams of various time structures. Due to space charge limitations, approximately $2 \cdot 10^7$ single-charged 20 keV particles can be stored [48], but the effective antiproton rates, i.e. number of particles times revolution frequency, for in-ring experiments can reach even 10^{12} $\bar{\text{p}}$/s. With a slow extraction scheme, as few as $5 \cdot 10^5$ – 10^6 $\bar{\text{p}}$/s, corresponding to beam currents of approximately 100 fA, are expected. With fast extraction, all antiprotons will be ejected into traps within a time shorter than the revolution period. The ring circumference is 42.6 m, hence the revolution time of stored particles is 5.6 µs at 300 keV and 22 µs at 20 keV. Table 1.1 summarizes the most important USR beam parameters. Although antiprotons are of the main interest at the USR, other particles, such as protons or H^- ions, will be used for the initial commissioning of the machine.

Table 1.1: General parameters of the antiproton ($\bar{\text{p}}$) beams in the USR.

Beam energy	300 keV → 20 keV
Relativistic $\beta = v/c$	0.025 → 0.006
Revolution time	5.6 μs → 22 μs
Revolution frequency	178 kHz → 46 kHz
Number of particles	$\leq 2{\cdot}10^7$ $\bar{\text{p}}$ @ 20 keV
Effective in-ring $\bar{\text{p}}$ rates	10^{10} $\bar{\text{p}}$/s – 10^{12} $\bar{\text{p}}$/s
Average rates of extracted $\bar{\text{p}}$'s	$5{\cdot}10^5$ $\bar{\text{p}}$/s – 10^6 $\bar{\text{p}}$/s
Bunch length	1 ns – DC beam
Beam diameter	few mm – several cm

The layout of the USR, shown in Fig. 1.2, is based on a four fold symmetry split-achromat geometry. Each achromatic 90° ring quarter comprises five electrostatic quadrupoles, two 8° and two 37° electrostatic cylinder deflectors. Four 4 m long straight sections accommodate different RF systems for a short bunch operation mode, an electron cooler, a decelerating drift tube, elements for fast and slow extraction, beam diagnostics and a so-called reaction microscope [51]. The USR will be operated at room temperature and at a vacuum pressure of 10^{-11} mbar.

By applying different settings to the quadrupole electrodes, the machine can be operated in various regimes [51]. A "round beam mode" will be used for injection and during electron cooling. The "achromatic mode" combines a small beam size in the middle of the experimental straight section with a reasonably large beam size in

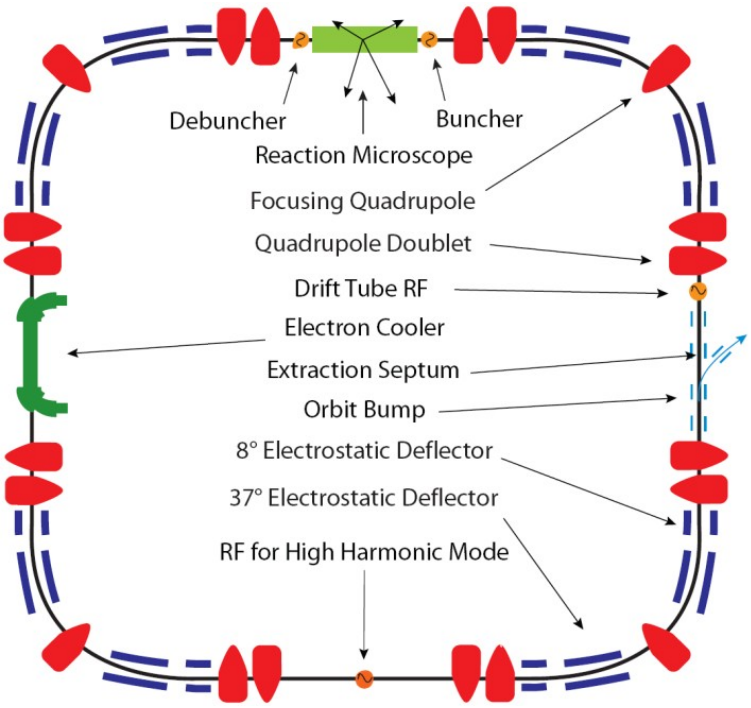

Figure 1.2: Layout of the USR.

the electron cooler section. It will be applied for in-ring experiments to maximize the number of antiprotons in a small interaction region. Finally, the USR lattice can also be set up for a "slow extraction mode". Depending on the quadrupole settings, applied cooling and location in the ring, the transversal beam size will vary from few millimetres to several centimetres.

1.3 Project Goals

A set of beam instrumentation will be required for the initial commissioning phase as well as a later operation of the USR. Optimisation of various diagnostic methods is necessary as most of the standard high-energy solutions no longer work. The challenges include very low energies down to 20 keV, ultra-low intensities down to a hundred fA and both, particles and antiparticles that need to be monitored.

The aims of the project were to study available diagnostic techniques and their applicability to the USR, to optimise, design and experimentally test detectors for beam profile, position and intensity monitoring, and to choose a set of solutions for low-energy, low-intensity beams at the future FLAIR facility.

Chapter 2

Low-Energy Beam Diagnostics

In this chapter, the state of the art beam instrumentation for low-energy, low-intensity beams is reviewed. The main focus is placed on the boundary conditions of the USR and techniques for measuring beam profile, position and intensity.

2.1 Introduction

A particle accelerator can only be as good as its instrumentation which provides information on particle beam behaviour and properties. These include intensity, transverse profiles, position in the beam tube, bunch length, time structure, energy and energy spread, emittance, beam losses, number of transverse oscillations per turn, known as tune, and its dependence on momentum, known as chromaticity [52–56]. A range of beam monitors are required for various stages of accelerator performance optimisation and its later operation. Although non-perturbative devices are preferred, also destructive solutions are used for transfer lines and first turn diagnostics.

The boundary conditions of the USR put challenging demands on its beam instrumentation. First, low-energy particles can be easily disturbed and any intercepting solution will result in emittance blow-up and, eventually, beam loss. For instance, 300 keV protons traversing an aluminium layer as thin as 500 nm undergo multiple scattering and lose more than 40 keV of their kinetic energy, whereas 20 keV protons are already fully stopped in the same layer [57]. Second, the limited number of particles in the USR result in very low intensities to be measured. Approximately 10^7 protons or antiprotons circulating in the ring correspond to a few hundreds of nanoamperes, well below the detection limits of standard beam current transformers used in high-energy accelerators [53,54]. The same amount of particles passing only once through a transfer

line generates average currents in the femtoampere range. These are difficult to measure even outside an accelerator environment. Third, although antiprotons are of the main interest at the USR, also protons or H^- ions will be used for the initial commissioning of the machine. However, stopped antiparticles generate completely different signals than the corresponding particles. The energy released in annihilation of keV antiprotons is a few orders of magnitude higher than the energy deposited by keV protons [58]. Among various types of secondary particles, high energy pions and strongly ionizing ions are created and constitute an important contribution to the response of a detector.

In order to develop adequate diagnostics for the USR, instrumentation used at other low-energy ion and antiproton facilities was reviewed and analysed. Among electrostatic ion storage rings, only three are currently in operation. The first was ELISA at the Institute for Storage Ring Facilities in Aarhus which enables experiments with stored ions at an energy up to 22 keV per nucleon [59–62]. Two others are at the High Energy Accelerator Research Organization KEK in Tsukuba [63, 64] and at the Tokyo Metropolitan University (TMU) [65–67], both working at an energy up to 30 keV. Several other electrostatic rings have been under development and construction, including the DESIREE at the Manne Siegbahn Laboratory (MSL) in Stockholm operating in a merged beam configuration [68, 69], Frankfurt Low-energy Storage Ring (FLSR) at the University of Frankfurt working at an energy up to 50 keV [70, 71], and a Cryogenic Storage Ring (CSR) at the Max Planck Institute for Nuclear Physics (MPI-K) in Heidelberg offering energies between 20 and 300 keV [72, 73]. Of special interest were also magnetic antiproton rings, mainly the AD [74], CRYRING/LSR [48] and ELENA [75], together with their transfer lines and experimental areas [76]. Other facilities at which low-energy and/or low-intensity beams have to be monitored include REX-ISOLDE at CERN [77–79], HITRAP at GSI [80, 81], EXCYT and FRIBS at the National Institute of Nuclear Physics INFN-LNS in Catania [82, 83], as well as SPIRAL1 and SPIRAL2 at GANIL in Caen [84–86].

In the following sections, techniques for monitoring various beam parameters are discussed and related to the low-energy, low-intensity beams at the USR.

2.2 Beam Profile Measurements

2.2.1 Beam Scrapers

Beam scrapers are destructive devices that can be used to measure beam profiles and reduce physical aperture [55]. Two pairs of blades, one in the horizontal and one in the

vertical plane, can be moved inside the vacuum chamber by stepper motors in order to intercept the beam. The profile is reconstructed from beam intensity or beam loss measurements for various positions of the scrapers.

At the AD, 1 mm thick tungsten blades have been used to obtain a precise measurement of the beam centre and shape, and to tailor it to a desired size or intensity [74]. They have been valuable during tests with intense proton beams, for example to verify the effectiveness of stochastic and electron cooling. In the case of antiprotons, downstream scintillators detect particles produced in the annihilation process between antiparticles and the scraper blade.

Although scrapers were introduced in the design of many low-energy storage rings listed previously [60, 63, 67, 69], their practical implementation and usability to beam profile monitoring have not been reported in detail. This can be explained by the fact that the technique is slow and time consuming, thus not very practical [87].

2.2.2 Gaseous Ionization Detectors

Gaseous detectors generate an electronic signal out of the ionization produced by the passage of a charged particle through a gas volume [88–92]. A potential difference is applied between electrodes of the detector and an electrostatic field is created in the gas where ionization takes place. This way, created ions are collected onto a position sensitive detector, such as a grid of electrodes, and the beam profile can be reconstructed.

Ionization Chambers and Proportional Counters

Gaseous detectors can vary in the design and methods to form the total number of electron-ion pairs and several solutions have been used with antiproton beams at CERN. These include parallel-plate ionization chambers (PPICs) [93], multi-wire proportional chambers (MWPCs) [89] and gas electron multipliers (GEMs) [94]. However, the monitors contain a gas volume separated from the outside atmosphere by 20-50 μm thick Kapton films. In addition, they need to be separated from vacuum, usually with a 20 μm thick stainless steel window. The total amount of matter traversed by a beam makes these detectors unsuitable for keV antiprotons which would be stopped even before reaching the active area of a profile monitor.

Residual Gas Monitor

A solution introducing no vacuum windows is a residual gas monitor (RGM), also known as an ionization profile monitor (IPM), which is free of problems related to

the disturbing foils. An example of such a monitor is shown in Fig. 2.1. The idea is to detect the ionized products from collisions of the beam particles with the residual gas atoms or molecules present in the vacuum tube [53]. An external electric field of the order of 1 kV/cm is applied by electrodes installed in vacuum outside the beam path. To obtain a uniform accelerating gradient, guide strips are usually added on the sides, hence the distribution of the residual ions can be registered by a spatial detector. Two monitors are required to observe the beam profile projection onto a vertical and horizontal plane.

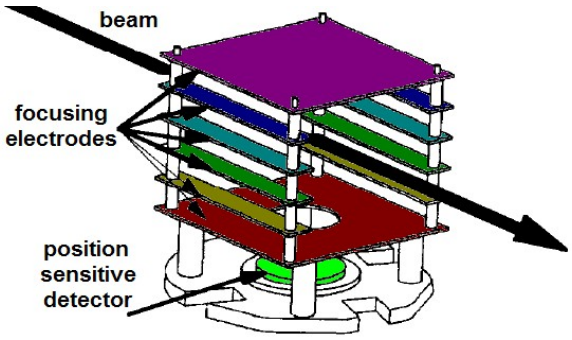

Figure 2.1: Sketch of a residual gas monitor. Picture taken from [95].

An RGM is used at CRYRING/LSR [48] and the AD [96]. As reported for the latter, the electron-ion pair production was low due to the high vacuum in the ring, approximately 10^{-11} mbar, and the small number of circulating particles. In order to obtain meaningful signals, a N_2 gas injection system has been installed for each detector to create a local pressure bump of about 10^{-9} mbar and enhance the production rate [97]. However, the overall vacuum level can be affected if the gas expands in all directions and spreads around the whole ring. Additional differential pumping is required in such a case which needs to meet the design constraints of the respective accelerator. For instance, the solution has been discarded at the CSR where a cryogenic environment and vacuum as low as 10^{-14} mbar are foreseen [73]. Instead, a supersonic gas jet-based monitor is planned to be used.

Supersonic Gas Jet Screen

A way around the problem of a residual gas pressure is to use a highly directional supersonic neutral gas jet target [98]. The principle of the device is illustrated in Fig. 2.2. Appropriate collimators shape the gas jet geometry in the form of a thin curtain angled at 45° with respect to the incoming beam. The beam ionizes the gas and

resulting ions are collected through an electric field onto a position sensitive detector. Two compensation electric fields are added upstream and downstream the monitor to correct for the kick undergone by the primary beam under the influence of the extraction field. The highly directional jet is dumped onto a pumping section placed on the opposite side, thus the technique is suitable for UHV.

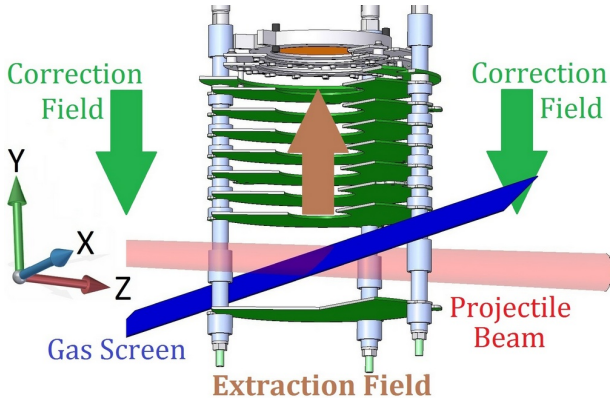

Figure 2.2: Supersonic gas jet-based beam profile monitor setup. The projectile beam (red) crosses the gas jet screen (blue) and an electric field extracts the ionization products towards the detector. Picture taken from [99].

As a minimally interceptive profile monitor, the supersonic gas jet screen has been under development for the USR within the frame of another project [99]. The monitor can be operated with residual gas pressures as low as 10^{-11} mbar without affecting the vacuum level and features sub-mm spatial resolution. Furthermore, it can be used with the USR beam without any supersonic jet, in residual gas operation mode, with a spatial resolution of less than 100 µm, if the residual gas pressure exceeds 10^{-8} mbar. Finally, the design enables an upgrade of the monitor to an experimental station for momentum spectroscopy of molecular collisions. Its disadvantages, however, are the complexity and cost which make it impractical for beam profile measurements at many locations. For this reason, simpler and more compact diagnostic techniques are also required at the USR.

2.2.3 Scintillating Screens

The most direct and simplest way to observe a beam profile is to use scintillators [53]. When a particle traverses a scintillating material, its energy loss is transformed into light which can be registered by a camera. With a luminescent screen placed at 45° with respect to the beam, the beam image can be observed through a viewport as shown

in Fig. 2.3. The measurement is destructive for low-energy beams, but the monitor can be retracted from the beam path by means of an actuator.

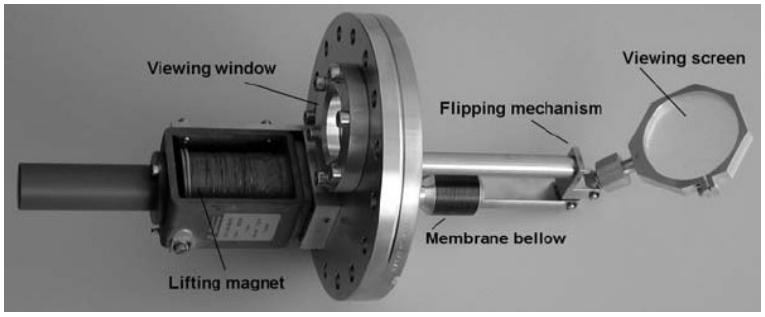

Figure 2.3: Scintillating screen-based beam profile monitor. Image taken from [54].

At KEK, injected beam currents from tens to hundreds nanoamperes can be observed destructively with screens made of aluminium oxide (Al_2O_3) doped with oxide chromium [63]. Similar viewers were reported also for ELISA [59], the TMU ring [65] and CRYRING [100].

To find an appropriate scintillating material for the CSR diagnostics, tests with 20 keV beams of deuteron and argon ions at 1 nA – 1 μA were performed [101]. A number of scintillators were investigated: beryllium oxide (BeO), Chromox-6 aluminium oxide doped with chromium oxide (Al_2O_3:Cr_2O_3), ruby (Al_2O_3:Cr), zirconium oxide (ZrO_2), quartz (SiO_2), boron nitride (BN) and yttrium aluminium garnet (YAG). The BeO and the YAG showed the best performance, followed by the Chromox-6. Beam profiles were observed with the Ar beam down to 80 nA and with the D beam down to 1 nA at spot sizes of 10 mm × 20 mm. However, after several hours of irradiation with deuteron ions and after only a few minutes of irradiation with argon ions at 10^{-7} mbar vacuum pressure, a drastic irreversible decrease of luminosity was measured for all materials.

In contrast, other studies show more promising results for scintillators. Preliminary tests with a caesium iodide doped with thallium (CsI:Tl) crystal plate were performed at INFN-LNS with ions in an energy range of 40 – 170 keV [102]. It was demonstrated that light ion beams (H, O, F, Ni, Ag) with intensities going down to the order of < 100 fA, i.e. about $5 \cdot 10^5$ particles per second, can be observed. In a transfer line at LEAR, a CsI screen with an intensifier setup was used to measure a proton beam profile at intensities even as low as $2.5 \cdot 10^4$ particles per second [103]; this, however, was with MeV-energy-scale beams. More quantitative investigation into detection limits of

CsI and its suitability for beam diagnostics in the keV range is needed.

Antiprotons have also been observed by means of scintillators. Caesium iodide screens have been used at the RFQD installed for the ASACUSA collaboration at CERN. Initially, the decelerator was tested with protons at Aarhus and 1 mm thick CsI scintillators were employed [104]. Some of them were with holes of various diameters which enabled a beam of nominal divergence to pass unperturbed. When the beam was tuned, the signal from the beam profile tails was minimized. Afterwards, the RFQD was installed at CERN and a similar commissioning was performed with antiprotons. The CsI screens, with and without holes, provided information on the beam, but the images were too bright due to annihilation of antiprotons. Eventually, the detectors were replaced with less sensitive plastic scintillators, 0.5 mm thick BC408 [105].

At LEAR, antiproton beams were observed with inorganic scintillators, such as NE902 or silver doped zinc sulphide (ZnS:Ag, PS11), used with position sensitive photomultipliers [106]. Particles were stopped in the screens to produce high-luminosity scintillation through the products of their annihilation. However, on application of scintillators to antiproton beam imaging, it is difficult to accurately determine beam size and intensity due to multiple interactions inside a screen and image blurring [76].

2.2.4 Secondary Emission Monitors

Instead of scintillation light, secondary electrons released by a primary beam traversing a medium can be detected. Instrumentation built for this purpose is often referred to as secondary emission monitors (SEMs). When a beam impinges on a surface of a foil or a wire, eV range electrons are emitted. This charge depletion is proportional to the local density of the beam and can be used to measure a density profile [56]. Alternatively, secondaries can be collected on a spatial detector in a way preserving their initial distribution. In both cases, information on the beam profile can be obtained.

Microchannel Plate

A microchannel plate (MCP) is a specially fabricated type of an electron multiplier which consists of many thousands of closely packed glass tubes, clustered together and sliced in a thin plate [53,107]. Its schematic drawing and operation principle are shown in Fig. 2.4. Each tube, or channel, acts as an independent electron multiplier and is typically 15 – 50 μm in diameter. A particle beam striking the MCP surface releases a number of secondary electrons. These are accelerated by a potential difference applied across the thickness of the MCP and give rise to creation of further electrons within

each channel. A gain of the order of 10^4 for a single plate can be obtained, but further amplification is possible by combining several plates. After leaving the MCP, multiplied signal carriers can be registered by a position sensitive detector, such as a phosphor screen with a camera or a wire delay line anode (DLA).

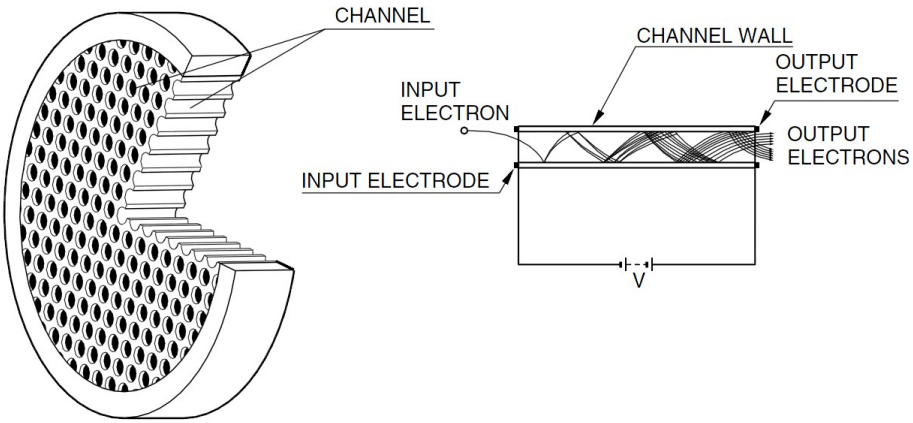

Figure 2.4: A schematic drawing of an MCP (left) and electron multiplication process in a single channel (right). Picture taken from [108].

MCPs have been widely used at electrostatic ion storage rings [59,64,66,69,71]. The monitors are usually installed at the end of straight sections to register neutralised ions leaving the ring. The solution provides a direct real-time observation of the projection of the circulating ion beam in a non-invasive way, but is not suitable for protons, i.e. charged particles that cannot be easily neutralised. Alternatively, an MCP can be placed directly in the ring as a destructive monitor.

At the ALPHA experiment at CERN, a microchannel plate with a phosphor screen is introduced in the beam path to image bursts of approximately 10^5 antiprotons for only over 10 ms every about 100 s [109,110]. Larger amounts saturate the detector due to secondary particles produced in annihilation at its surface. They excite additional cascades, enhancing the MCP gain and therefore limit its application to low-intensity $\bar{\text{p}}$ beams. Moreover, MeV-scale heavy ions produced at the surface introduce spurious signal, thus the beam image appears blurred with additional hot spots and tracks as shown in Fig. 2.5.

At the ASACUSA experiment, a long-term activation of an MCP bombarded with antiprotons was investigated [112]. The microchannel plate equipped with a DLA was irradiated by approximately 10^7 antiparticles over a period of 8 hours. The initial background rate of the detector had increased by a factor of 3 and plastic scintillators

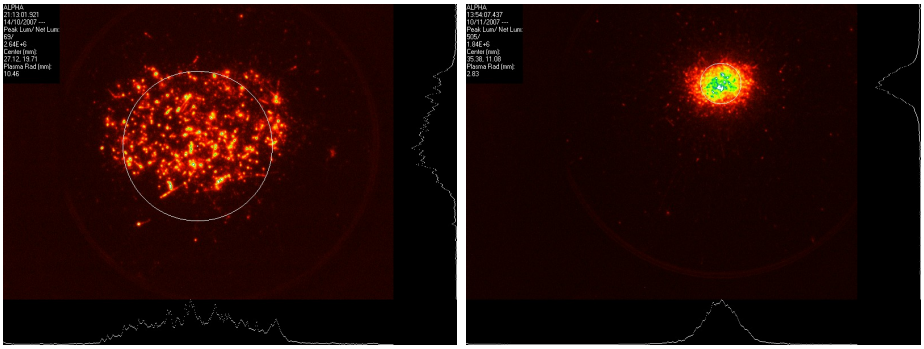

Figure 2.5: Images of an antiproton beam impinging on an MCP at the ALPHA experiment: before (left, 10.5 mm beam diameter) and after compression (right, 2.8 mm beam diameter) [111].

were used for coincidence measurements to reject the noise.

Secondary Emission Foil

A metal foil or a plate introduced at 45° with respect to the beam can be a source of secondary electrons due to particle beam bombardment. By applying an external electric field, low-energy secondaries can be guided towards a spatial detector and the beam image is registered. An example of a foil-based SEM is shown in Fig. 2.6. The advantage of the method is that it minimizes the thickness of components traversed by the particle beam as compared to the MCP. Furthermore, the geometry protects the detection system from a direct beam hit, which is important for a microchannel plate which can be damaged if exposed to high instantaneous currents.

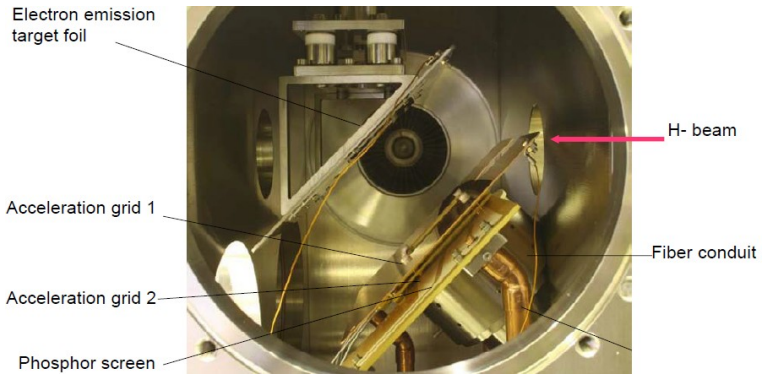

Figure 2.6: Carbon foil-based SEM, see [113] for details. Picture taken from [114].

The most common technique to guide secondary electrons is to apply a negative

high voltage of several kV to an emissive metal foil and place a grounded mesh parallel to it at a distance of a few millimetres [95,115–118]. The primary beam passes through the mesh, impinges on the metal surface and liberates secondary electrons. These are pulled away by a high potential gradient towards an imaging system placed a few centimetres away. Alternative solutions with accelerating electrodes distributed along the way to the spatial detector [113, 119] or introducing additional magnetic field [86] have been prepared as well. Due to image broadening caused by a drift of secondary electrons, a spatial resolution of about 2 mm is usually obtained [113, 115, 118].

Secondary Emission Grid

A SEM grid or a harp is another approach to secondary emission monitoring [54, 120, 121]. Instead of collecting emitted electrons onto a distant spatial detector, an electric signal due to extracted charge is measured from individual wires intercepting the beam. A weak external electric field, about 10 V/mm, improves the extraction of secondary electrons. The charge depletion is measured in the form of a signal current via individual pre-amplifiers connected to each wire and used to reconstruct the beam profile. The method is less sensitive than a similar technique used in a multi-wire proportional chamber [54, 121] where additional gain is obtained due to enclosed gas ionisation. However, it is superior for low-energy beams because it intercepts only a small fraction of a beam and most particles can pass through unaffected.

A SEM grid, shown in Fig. 2.7, was developed for the ASACUSA beam line and used to measure antiproton beams of energies between 25 keV and 5.3 MeV [122]. The device can monitor profiles of beam pulses containing about 10^6 – 10^7 antiprotons with spatial resolution of 2 mm [76], but is unable to measure low intensities, i.e. below approximately 10^4 particles [113]. Only about 2% of the beam is stopped in the SEM grids which makes it a perfect match for beam diagnostics in low-energy transfer lines. However, it is destructive in storage rings and more than 98% of circulating particles would be lost after only 200 turns.

Wire Scanner

Instead of a grid of wires with a finite pitch and individual electronics, a single wire can be scanned through the beam to obtain higher spatial resolution [54, 120]. A fast wire can be used even on a circulating beam and speeds of 20 m/s have been be achieved [55]. The signal can be obtained either by measuring a current in the wire or by detecting high-energy secondary particles. The latter would not be created by keV protons, but

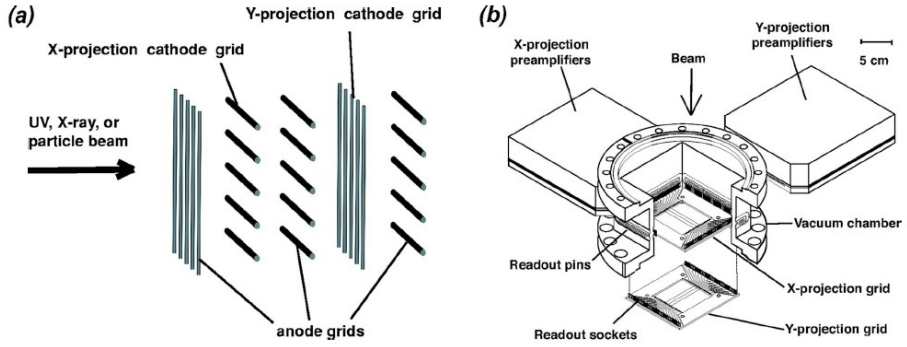

Figure 2.7: SEM grid monitor used at ASACUSA: a) configuration of the two position-sensitive cathode and three anode grids, b) schematic design. Picture taken from [122].

annihilating antiprotons produce 100-MeV-scale pions which can be registered outside the vacuum tube by means of a scintillator.

Several difficulties with scanners should be considered. A moving wire samples profile points at different times, and longitudinal intensity modulation of the beam is mixed with transverse variations, especially during the rise time of a beam pulse [54]. Also, exact synchronization of a complex electromechanical system with a pulse arrival time is not trivial. Finally, the signal-to-noise ratio of a fast scanner cannot be enhanced by integration of the acquired signal as opposed to a profile grid system. For instance, sensitivity of scanners used at ISOLDE is limited to tens of picoamperes even with scanning speeds below 200 mm/s and a narrow bandwidth amplifier [78].

2.2.5 Semiconductor Detectors

Semiconductor detectors are solid-state devices that use a semiconductor, such as silicon or germanium, to detect charged particles [90]. Similarly to gaseous detectors, the electronic signal is generated out of the ionization produced by the passage of a particle through an active volume of the detector, a semiconducting material in this case. An externally applied electric field collects the separated charges onto electrodes which can be segmented into strips or pixels [123]. Such segmentation enables spatial measurements of the ionization. Semiconductors are widely used in high-energy physics, but they have found application also in beam diagnostics [124].

A significant difference in the interaction of protons and antiprotons with matter makes a choice of one semiconductor detector design for both types of keV-range particles extremely difficult. Low-energy protons generate very weak signals and can

be stopped in a dead layer of a monitor, whereas antiprotons produce a number of secondary particles with a wide energy range. Annihilation products would saturate electronics of a semiconductor detector optimised for low-intensity proton beams, and other solutions, such as signal integration, would have to be found [125, 126]. Another complication is related to radiation damage which can be caused by a high flux of antiparticles. Antiprotons fragmentate the surface they hit on, yielding energetic recoils, which can lead to a significant dose. Above approximately 10^{14} neutrons/cm^2 equivalent [125], a reduced charge collection efficiency can be observed due to detector deterioration. For this reason, it would be more appropriate to introduce a light atomic number foil, which activates less, in front of the semiconductor and register only pions which make orders of magnitude less damage than antiprotons [125]. Although a semiconductor detector has been tested directly in the beam of 126 MeV antiprotons [127], no experiments with low-energy antiprotons have been performed in a foil-based configuration for profile monitoring. However, this technique was not pursued further within the frame of this thesis.

2.3 Beam Position Measurements

The beam centre position can be measured in a non-destructive way by monitors that couple to the electromagnetic field generated by bunches of charged particles [121, 128]. The devices are known as pick-ups (PUs), because of the way they detect the beam, and are used in nearly any accelerator. In low-energy hadron machines, beam position monitors with capacitive coupling to the beam's electric field are usually employed, hence they are referred to as capacitive (or electrostatic) PUs. They consist of four metal electrodes surrounding the beam. As the particle bunches pass through, electric charges are induced on the electrodes, with a higher signal amplitude on the side which is closer to the beam. The difference signal Δ of opposite electrodes normalized to the sum signal Σ yields the beam's centre-of-mass for two transverse planes. Various shapes can be used, but a high signal amplitude and linearity can be achieved for large area electrodes with a diagonal cut, as shown in Fig. 2.8. Depending on the signal-to-noise ratio and bandwidth, different time scales of measurements are possible, ranging from bunch-by-bunch observation to averaged closed-orbit determination.

At ELISA and the KEK and TMU rings, four horizontal and four vertical capacitive PUs are used [60, 63, 67]. The difference signals Δ reflect the bunched beam positions, whereas the sum signals Σ provide relative information on the beam intensity. As

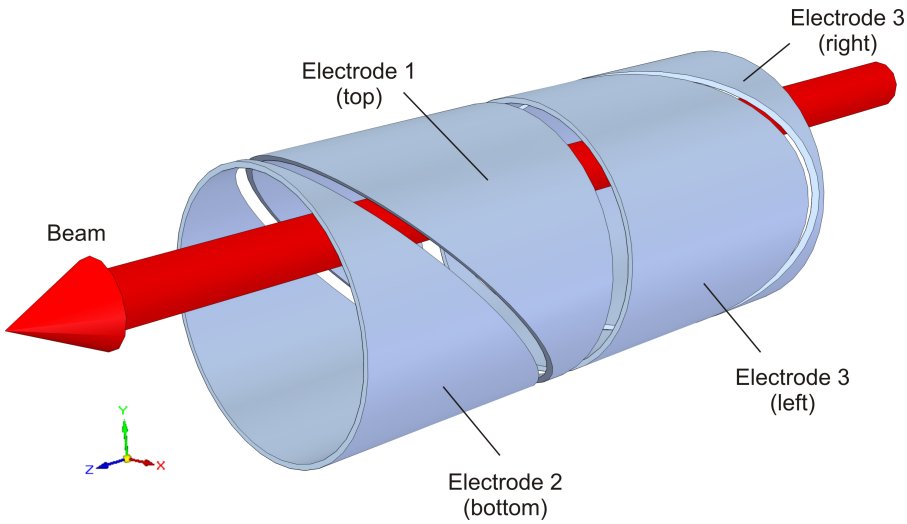

Figure 2.8: Simplified model of a capacitive pick-up with a diagonal cut measuring the beam position in both planes.

reported for the TMU ring [66], the electrodes are in a shape of four crosswise plates bent around the beam, thus the pick-up response does not change linearly with the beam position. The detection limit of the PU signal is equivalent to 3.2 nA for a 20 keV argon beam, but the uncertainty of the beam position is less than 1 mm for 100 nA. The result is improved by averaging repeated signals.

The closed-orbit measurement system for the CERN AD employs 59 electrostatic PUs [129]. Each PU consists of one annular electrode that provides the intensity signal Σ and two diagonally-cut cylindrical electrodes from which the difference signal Δ is derived. Purpose-built low-noise amplifiers with an equivalent input noise of 0.6 nV/$\sqrt{\text{Hz}}$ and 1 kHz narrowband filters enable the beam positions to be measured to $\pm$0.5 mm with about $5 \cdot 10^6$ stored particles resulting in beam currents of 0.1 – 0.2 nA. In addition, two different gains have to be used to cover a large dynamic range for intensities between $2 \cdot 10^{10}$ and $5 \cdot 10^6$. An orbit measurement takes from 0.2 to 12 s depending on the beam intensity and the precision required. A similar system, but with the Σ value obtained as a sum of the signals from the opposite electrodes, is currently under development for ELENA where 10 PUs are foreseen [43, 130].

At the CSR, six horizontal and six vertical diagonally-cut cylindrical pick-ups will be installed [73, 131]. They are planned to be built as part of a resonant amplification circuit. The system was tested with the Test Storage Ring (TSR) PUs at MPI-K with a 60 nA $^{12}C^{6+}$ ion beam at 73.3 MeV. The closed orbit measurement was performed in

about 160 ms, but the observed beam position was shifted by 1.3 mm compared with a non-resonant measurement which is believed to be a cross-talk between the pick-up and the RF system. At the CSR, it is expected to obtain a precision of 0.5 mm for a 10 nA ion beam at 300 keV [132].

2.4 Beam Intensity Measurements

2.4.1 Beam Current Transformers

Beam current can be determined in a non-destructive way by monitoring its magnetic field with a beam current transformer (BCT) [53, 133]. A schematic drawing of the monitor is shown in Fig. 2.9. The beam passes through a highly permeable torus as the "primary winding". An insulated wire is wound around the torus and serves as the "secondary winding". A signal is generated in the "secondary winding" by a time varying magnetic flux due to the beam current.

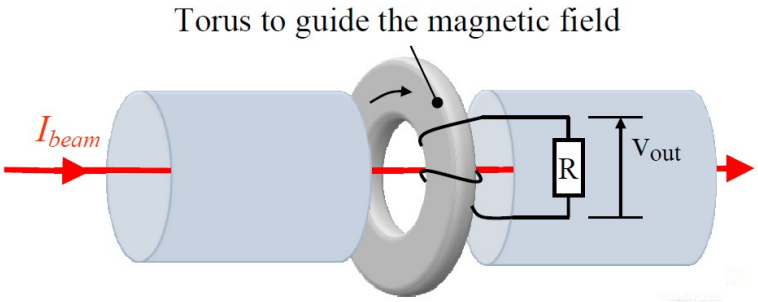

Figure 2.9: Sketch of a beam current transformer. Image taken from [53].

At the CERN AD, high and low beam intensities are observed by different systems [74]. A DC beam transformer provides direct measurement of the beam current with a resolution of 1.5 µA. This value is adequate to measure protons used in the commisioning mode with a typical beam of $5 \cdot 10^9$ particles, but is insufficient for the operational antiproton beams of approximately $5 \cdot 10^7$ particles. At such low beam intensities, a wideband ultra-low-noise ferrite-loaded AC beam transformer is employed as a longitudinal pick-up [134,135]. The device is made resonant to reduce the noise and "broad-banded" by an active feedback. For bunched beams, the intensity is obtained by measuring the amplitude of the fundamental and second RF Fourier components. On the magnetic plateaus the beam is debunched for stochastic or electron cooling and longitudinal beam properties, including intensity, momentum spread and mean momentum, are measured by Fourier transform-based spectral analysis of Schottky

signals [56]. Calibration against a BCT at high beam currents is needed, but the reproducibility in the intensity measurement by Schottky scans at the AD corresponds to 10^4 antiprotons [55].

At CRYRING, two types of BCTs have been used [48]. Initially, a commercial Parametric Current Transformer from Bergoz [136] was employed which is a DC device with sensitivity of 10 mV/μA and nominal resolution of 0.5 μA for 0.1 s integration time. Its accuracy in the 500 nA current range is not better than ±10% even with averaging over many ring cycles [137]. For low beam currents, there is also an AC beam monitor, an integrating current transformer (ICT) from Bergoz. This device, equipped with a purpose-built low-noise wideband amplifier, has a current noise of approximately 1 nA RMS at 20 Hz bandwidth limited by its 50 Ω shunt resistor, thermal noise, and the RF background [138].

A special type of a BCT is a cryogenic current comparator (CCC) [139]. The sensor consists of a high permeability toroid acting as a flux concentrator, a superconducting magnetic shield, a pick-up coil and a high-precision superconducting quantum interference device (SQUID) [140]. The azimuthal magnetic field of the beam generates screening currents on the surface of the cylindrical magnetic shield. The magnetic field of these screening currents is detected by a single-turn pick-up coil around the ferromagnetic core. The pick-up signal is measured by means of a high-precision DC SQUID. To effectively suppress disturbing non-azimuthal components of external magnetic fields, a superconducting shield with sophisticated geometry is required. The complexity of the monitor and its operation in a noisy accelerator environment makes the sensitivity of various prototypes built so far vary between tens to hundreds pA/$\sqrt{\text{Hz}}$ [141]. The CCC technology is still in development.

2.4.2 Capacitive Pick-ups

Non-destructive beam position monitors are capable of measuring low-current beams as described in Section 2.3. In principle, they can provide only relative information on the number of stored particles, but techniques to extend their applicability to low beam intensities exist [56, 138, 142].

At CRYRING, the current of a bunched beam is measured with the ICT at the same time as the sum signal Σ from an electrostatic pick-up [48, 138]. The PU voltage signal is calibrated against the ICT at higher values and absolute currents down to 100 pA can be measured.

2.4.3 Faraday Cups

A Faraday cup is a beam collector isolated from the vacuum chamber and connected to a current meter [54]. It stops all beam particles and the resulting signal is measured to obtain information on the beam intensity. The accuracy of the method depends on the noise level present in the system and the charge collection efficiency. A schematic drawing of a Faraday cup is shown in Fig. 2.10.

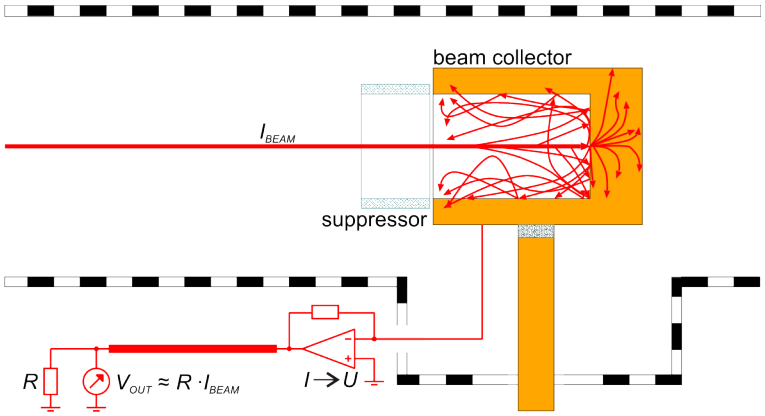

Figure 2.10: Sketch of a Faraday cup system. Image taken from [143].

In spectrometers, Faraday cups usually enable current measurements in the picoampere range, but their detection limits can be lowered to about 1 fA with state-of-the-art electronics [144]. However, in the noisy environment of an accelerator, with long cables and actuation, these destructive monitors have not shown such performance. Also, long integration times, of the order of seconds, are required. At low-energy beam transport lines at GANIL [85] and INFN-LNS [145], the intensity range of Faraday cups extends down to a few picoamperes. At REX-ISOLDE, currents down to 0.5 pA have been observed with commercial electrometers and multiplexers, and down to 0.2 pA with purpose-built amplifiers [78].

Low-energy beams can be easily stopped in a metal plate, but backscattered and secondary particles can carry the charge away. For protons or ions, it is resolved with additional suppression by means of an electric field, but becomes problematic for antiprotons. Charged pions at hundreds of MeV created in annihilation can leave the monitor and falsify the current value, making only relative measurements possible.

2.4.4 Particle Counters

Should the detection limits of a Faraday cup be insufficient, particle counters can be employed for ultra-low current measurements [53, 54]. These include scintillators equipped with photomultiplier tubes [54, 146], secondary emission monitors with electron multipliers [147–150] and semiconductor detectors [151]. Gaseous detectors, such as ionization chambers, are unsuitable due to the presence of thick vacuum windows as described in Section 2.2.2. In general, in-beam particle counters are not applicable to measurements with antiprotons, because of the high flux of secondary particles released in annihilation. Additionally, absolute calibration is necessary because of collection efficiency and a number of other parameters which cannot be controlled or known in a precise manner.

2.4.5 Annihilation Monitors

It is possible to take advantage of the interaction of antiprotons with matter and perform measurements which cannot be applied to proton or ion beams. Most of such monitoring techniques have been developed for experiments with $\bar{\mathrm{p}}$ beams at CERN.

External Detectors

Beam intensity can be evaluated by means of external detectors registering annihilation products of stopped antiprotons. Such monitors include plastic scintillators connected to either proximity focused hybrid photo diodes (HPDs) [152] or photomultipliers [153], Cherenkov counters [154] and silicon microstrip detectors with CsI crystals [153, 155]. For detecting high instantaneous rates, such as 10^{14} pions per second during the AD $\bar{\mathrm{p}}$ pulse [153], the HPD-based detectors are used. They do not count single particles but operate in current mode, measuring the total charge deposited by annihilation products. Eventually, the external detectors need to be calibrated against an absolute beam current monitor.

Nuclear Activation Measurement

The number of antiprotons can be obtained by directing the $\bar{\mathrm{p}}$ beam onto a thick aluminium plate and measuring the induced activation [93, 152, 153]. Due to irradiation of aluminium, antiprotonic aluminium atoms are produced which are destroyed in picoseconds as the antiprotons annihilate on the nuclei. This results in the production of radioactive sodium $^{24}\mathrm{Na}^{*}$ which in turn decays by γ emission with characteristic

energies of 1.37 MeV and 2.75 MeV. The half-life of $^{24}Na^*$ is known, thus the beam intensity can be derived from the foil activation [152]. The estimated values agreed to within 10 – 30% of the beam intensities derived using the DC curent transformer and Schottky pick-up at the AD [93, 152, 153]. The method is less accurate than the Schottky analysis and requires long irradiation times as well as access to the activated sample, i.e. breaking the vacuum and working with an open radiation source.

2.5 Summary

A wide range of instruments and techniques for beam profile, position and intensity measurements were discussed. Most of them cannot be applied to the USR in their current form, due to either limited sensitivity or high responsiveness to annihilation products. Further investigation and optimisation is needed to provide solutions suitable for low-energy, low-intensity beams of antiprotons and protons at the USR.

For profile measurements, several techniques can be applied. A minimally interceptive ionization profile monitor has been under development [99], but its complexity and cost make it impractical for beam measurements at many ring positions. For this reason, simpler and more compact solutions are also needed. Previous attempts to produce on-line beam images with scintillators in the keV energy and femtoampere range were unsuccessful [102]. However, detection limits of caesium iodide are not well documented and should be explored further. Similarly, an MCP-based monitor has not been optimised nor used for light charge particles in the keV energy range. Further studies are needed to investigate into the applicability of in-beam scintillating screens and foil-based SEMs to the USR diagnostics for antiprotons and protons beams.

For position monitoring, non-destructive pick-ups are the device of choice, but their sensitivity and applicability to low-velocity beams requires careful considerations and design optimisation. No device exists that could be used directly with the USR beams.

For intensity measurements, a non-interceptive current transformer would be an ideal tool, but limited sensitivity necessitates development of other solutions suitable also for beam transfer lines. A Faraday cup can be used for the initial commissioning with protons and a reference for pick-ups calibration, but femtoampere beam currents pose a challenge to the existing designs. Careful study of detection limits should shed light on applicability of the monitor to low-intensity beams.

The following chapters present a set of diagnostic tools which have been investigated, optimised, built and experimentally tested for the USR within the frame of this thesis.

They include scintillating screens, capacitive pick-ups, Faraday cups and secondary emission monitors. The final chapter summarises the current status of the work and presents future development perspectives.

Chapter 3

Scintillating Screens

In this chapter, the application of scintillators to low-energy, low-intensity beam profile measurements is discussed. The first section gives the rationale for the performed studies. Next, a theoretical basis of scintillation mechanisms is given. The main focus is on the choice of a scintillating material for proton and antiproton beam diagnostics and the competing challenges between these two. The following section presents the experimental resolution and detection limits studies of several scintillators tested with keV protons. Although no antiproton beams were available for comparable experiments, the theoretical and experimental findings give sufficient base for conclusions on a possible application of scintillators to beam diagnostics at the USR. These are summarised in the final section of the chapter.

3.1 Motivation

In terms of simplicity, cheapness and effectiveness, scintillators are among the best suited instruments for beam profile monitoring. Although they are not as sensitive as detectors equipped with amplification devices, such as microchannel plates, see Chapter 6, their ultimate detection limits have not been investigated in great detail. A further challenge comes from the fact that the USR requires beam diagnostics for both, antiprotons and protons, and the choice of a suitable scintillating material becomes even more complicated. It is important to decide whether scintillators can be applied to low-energy antiproton beam diagnostics and if a single solution for both types of particles exist. The lack of comprehensive data for scintillators used in the low-intensity, low-energy regime was the main motivation for the here-presented studies.

3.2 Theoretical Background

3.2.1 Scintillation Mechanisms

Scintillators are luminescent materials in which the excitation energy of electronic states of the atoms is converted to light, usually in the visible, ultra-violet or infra-red range. Depending on the time scale of the light emission, luminescence can be divided into two categories: fluorescence and phosphorescence. The first is a prompt emission of light from a substance, whereas the latter takes place some time after the excitation. The definitions are not rigorous, but the time scale for the phosphorescence can be tens of milliseconds or more. Good scintillators are materials that respond to radiation in the fluorescence regime. Quite often, however, they show both, fast and slow, decay components.

The choice of a particular scintillator depends on the application and is often a compromise between various factors. The most widely used are inorganic scintillators which have the highest light yield and linearity but are relatively slow in their response time. They also contain a large fraction of atoms with a high atomic number Z and therefore are sensitive to X- and γ-rays. Organic scintillators are generally faster but produce lower light output. Their low Z value makes them better suited for β spectroscopy and fast neutron detection. Examples of various scintillator types and their characteristics can be found in [90, 91, 156–158].

Organic Scintillators

The scintillation mechanism in organic materials is due to transitions made by free valence electrons excited by incoming particles. These electrons occupy the molecular orbitals and are not associated with any particular atom. Because the excitation and emission spectra for a given molecular species are the same independent of their physical state, a variety of organic scintillators are available, including crystals, liquid solutions or plastics.

The light output L of organic materials is proportional to the energy E deposited by the ionizing particle. However, L is limited by the existence of de-excitation paths that do not lead to the emission of light but to other quenching processes, such as lattice vibrations or heat dissipation. A semi-empirical formula for the light output taking these into consideration was proposed by Birks [159]:

$$\frac{dL}{dx} = \frac{S \cdot \frac{dE}{dx}}{1 + k \cdot B \cdot \frac{dE}{dx}}, \tag{3.1}$$

where S is the absolute scintillation efficiency, k is the quenching parameter, and B is an empirical constant. Although the equation can give reasonable results, deviations from experimental data had to be explained by "higher order" expressions with additional empirically fitted parameters [156, 160]. Furthermore, dependence of dL/dx on the specific particle type in addition to dE/dx is observed.

Inorganic Scintillators

The scintillation mechanism in inorganic materials is due to the electronic band structure in crystals. Electrons in the valence band are bound at lattice sites, whereas electrons in the conduction band can move freely within the crystal. Both energy bands are separated by the forbidden band gap. An incoming particle can excite an electron into the conduction band and leave a positive hole in the valence band. Alternatively, an electron-hole pair is created and migrates together in the crystal. If impurity atoms, called activators, are added to the lattice, additional electronic levels in the forbidden gap are created. Because the ionization energy of the impurity centre is less than that of a typical lattice atom, the hole drifts to its location and ionizes it. Consequently, electrons in the conduction band can fall into the ionized activator site. A properly chosen impurity atom has its own set of excited energy states and electrons can make a quick transition to the ground state, emitting visible photons. It is also possible that electron gets trapped in a metastable state. Due to a thermal excitation, it can receive additional energy to move to a state from which it can de-excite and create delayed emission, known as afterglow.

Similar to organic scintillators, the light output L of inorganic materials is proportional to the energy E deposited by the ionizing particle. However, quenching and various de-excitation mechanisms lead to deviation from linearity at energies of few keV [90, 156].

3.2.2 Considerations for Protons

A scintillator usable for the USR should enable reliable beam profile monitoring during the commissioning stage with protons or ions. Although beam image quality will depend also on the distortions introduced by the monitoring system, such as profile widening due to scattering in the scintillating screen, the main challenge is to obtain signal-to-noise ratio (SNR) > 1. The signal strength registered by a camera is directly linked to the light yield and thus is proportional to the beam intensity and kinetic energy. At the USR, these are only $5 \cdot 10^5$ – 10^6 particles per second, i.e. about 100 fA, and between 20

keV and 300 keV. Additional image averaging can be applied, but only over the beam delivery time which is of the order of some tens of seconds in the slow extraction mode. For this reason, a critical feature of a scintillating material for the USR is its response, or scintillation efficiency, when exposed to weak beams of single-charged particles in the keV energy range.

Previous studies seem to indicate that limited sensitivity makes scintillators not suitable for low-energy, low-intensity beam diagnostics [101, 161]. As mentioned previously in Chapter 2, none of the screens, including aluminium oxide (Al_2O_3), beryllium oxide (BeO) and yttrium aluminium garnet (YAG), tested by the MPI-K group was suitable for beam currents below 1 nA [101]. Similar results were reported by the GSI group for P43 (Gd_2O_2S) and P46 (YAG) scintillators [161].

In contrast, other studies indicate that high scintillation efficiency can be expected for some inorganic scintillators, especially caesium iodide (CsI) [102–104, 162, 163]. In most cases, however, the main research focus has been put on either high-energy or highly-charged ion beams.

The lack of comprehensive data for scintillators used for proton beam diagnostics in the low-intensity, low-energy regime was the main motivation to investigate detection limits of scintillating screens, CsI in particular. Although a wide range of scintillating materials or even doping agents could have been tested in terms of sensitivity, decay time or energy resolution, the choice of scintillators used in this study was based on the experience and available resources kindly provided by the group of Paolo Finocchiaro at INFN-LNS in Catania. The materials and methods used as well as the results of the measurements are described in Sections 3.3 and 3.4.

3.2.3 Considerations for Antiprotons

Antiprotons impose additional challenges to the application of scintillators to beam profile monitoring. The antiparticles can either annihilate in-flight if they come close to a nucleus or can be stopped in matter with many small energy transfers to electrons. If the antiprotons are slowed down to less than a keV, they are captured by an atom by means of their negative charge, entering an atomic orbital. Such exotic atoms created in the process are not stable, because antiprotons cascade down by the emission of Auger electrons and X-rays. In the end, annihilation with a proton or neutron takes place and 1.88 GeV is released. In most cases, various combinations of pions (π^+, π^-, π^0), about five on average, emerge at 100-MeV-scale energies. Among the three pions, π^0 has a short lifetime and decays into γ-rays. In a few percent of the annihilations,

kaons and hypernuclei are produced. Due to momentum conservation, nuclear recoils of a few tens of MeV, depending on the target material, are also observed. A fraction of annihilations induce the production of an unstable nucleus with the lifetime reaching seconds or minutes. The nuclear breakup results in fragments, mostly in the sub-MeV range, emitted in all directions and ionizing surrounding atoms. Also some pions interacting with the nucleus cause intra-nuclear cascade. The overall picture gets extremely complicated: fast pions are absorbed or scattered; Δ-baryons or additional pions are produced; protons, neutrons, deuterons, tritons, α-particles or other light nuclei are knocked out; and finally, the hot nucleus evaporates neutrons and protons. The interaction of antiprotons with matter is still a subject of intensive theoretical, numerical and experimental studies. [11, 19, 58, 164–166].

Due to the nature of the processes following the annihilation, the response of a scintillator to keV antiprotons is much different than to protons at the corresponding energy and intensity. For proton impact, the light output is proportional to the kinetic energy which is of the order of 100 keV in this case. In contrast, the energy deposition for antiproton annihilation is about 2 GeV. If the annihilation takes place on a heavy nucleus, such as caesium, nuclear fission fragments and slow neutrons created in the process can transfer even more energy to the scintillator. It means that for antiproton impact, the energy released in a scintillating material is several orders of magnitude higher and can easily saturate the detector. Furthermore, the variety and range of annihilation products can result in an increase of the observed beam size as well as in additional hot spots and tracks. It was also reported that a sensitive scintillator will strongly respond even if the antiprotons do not strike it directly [105]. Annihilation events at the walls of a beam line generate MeV γ-rays and pions which can reach the scintillator even through the stainless steel walls and light it up.

It is concluded that no single scintillating material can be found for both, proton and antiproton beams. This is because of the difference in the energy deposition mechanisms and, consequently, the different light yield produced. Scintillators sensitive enough for protons will be too sensitive for antiprotons at the corresponding energy and intensity.

3.3 Experimental Setup

3.3.1 Beam Line

In order to produce low-energy proton beams, the 450 kV injector of the Tandem accelerator at the INFN-LNS was employed [167]. Fig. 3.1 shows the beam line setup

used for tests with various scintillators.

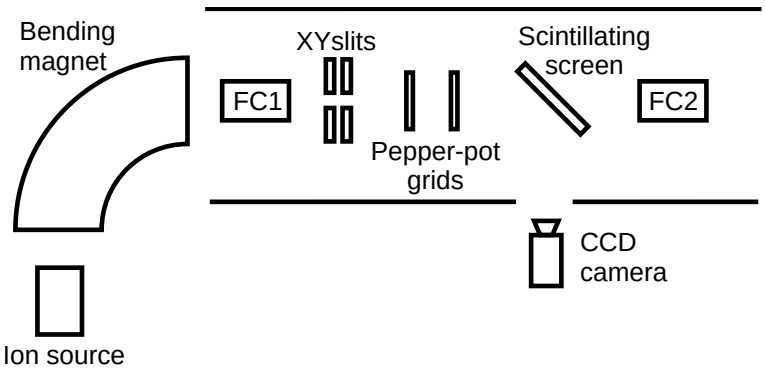

Figure 3.1: Experimental setup for scintillators tests at INFN-LNS.

Downstream the ion source and 90° analysing magnet, a conventional electrostatic Faraday cup (FC1), normally used for ion source mass analysis, was installed. After the cup, a pair of X and Y variable slits was used as collimators, followed by two removable "pepper-pot" grids for intensity reduction. The size of a single hole in such a grid was of the order of 0.2 mm with approximately half a millimetre spacing. Following the beam attenuators, a scintillating screen was placed for the tests. Finally, the second Faraday cup (FC2) was located behind the screen. All measurements were made under 10^{-6} mbar vacuum.

The injector was operated with settings much different from the conditions it had been designed for. Its nominal energy is 450 keV and beam currents are in the microampere range [167]. It was possible to lower the energy to 200 keV, later also to 50 keV, and to keep the beam intensity at the pA level. Below approximately 50 keV and a few pA, no stable operation of the injector was possible and no beam could be delivered to the experiment. The "pepper-pot" attenuators had to be used to study the response of the screens in the sub-pA region.

3.3.2 Test Setup

The scintillating screens under tests were installed on a support used for other experiments at INFN-LNS, as shown in Fig. 3.2, and moved to their positions by means of a motor controlled actuator. They were placed at 45° with respect to the beam axis, so that the beam image could be observed by a charge-coupled device (CCD) camera located outside a vacuum window. The system arrangement is presented in Fig. 3.1.

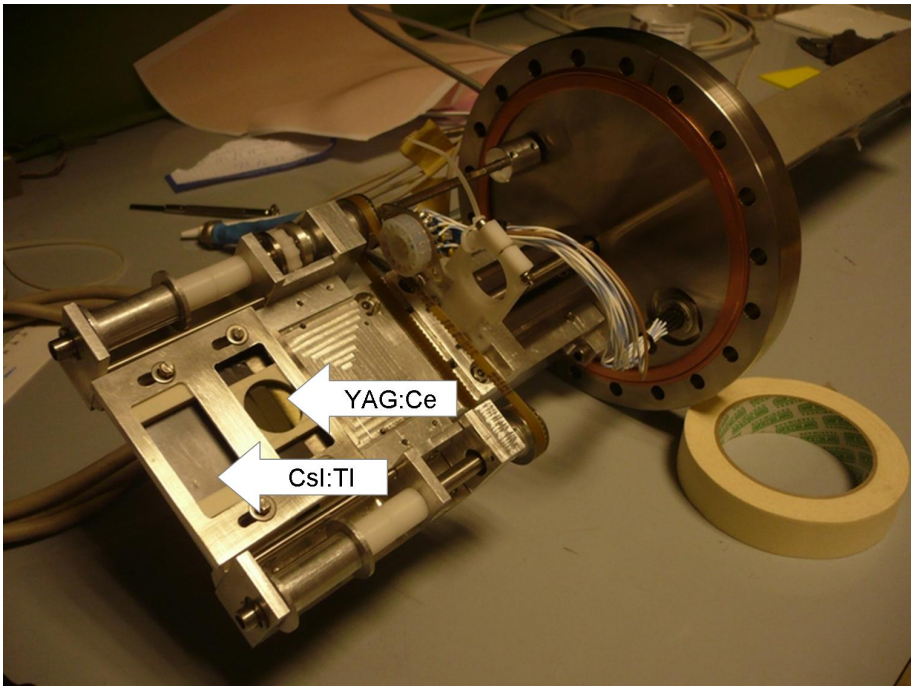

Figure 3.2: Support frame used for the scintillating screens.

3.3.3 Scintillating Screens

Three different scintillating screens were proposed for tests by the INFN-LNS team based on their experience and available resources as potentially the most sensitive solutions: caesium iodide doped with thallium (CsI:Tl), a terbium-doped glass scintillating fibre optic plate (SFOP) and an yttrium aluminium garnet ($Y_3Al_5O_{12}$) crystal doped with cerium (YAG:Ce).

The size of the CsI:Tl screen, manufactured by Hilger Crystals [168] and shown in Fig. 3.3a, was $50 \times 50 \times 1$ mm^3. Its nominal scintillation yield is 60 000 photons/MeV when exposed to X/γ radiation. The two main light decay time constants are 0.73 µs and 3.2 µs. The maximum emission is around 550 nm.

The SFOP, manufactured by Collimated Holes [169] and shown in Fig. 3.3b, was made from a bundle of terbium-doped glass scintillating fibres. Each fibre in the bundle was 10 µm in diameter, while the overall plate size was $25 \times 25 \times 2$ mm^3. Its nominal scintillation yield is 10 000 photons/MeV when exposed to X/γ radiation. Its maximum emission is around 550 nm. A bundle of glass fibres has different optical properties than a bulk scintillator of the same material and outer dimensions. Because the light is confined to the individual fibre in which it was emitted, the loss of spatial resolution

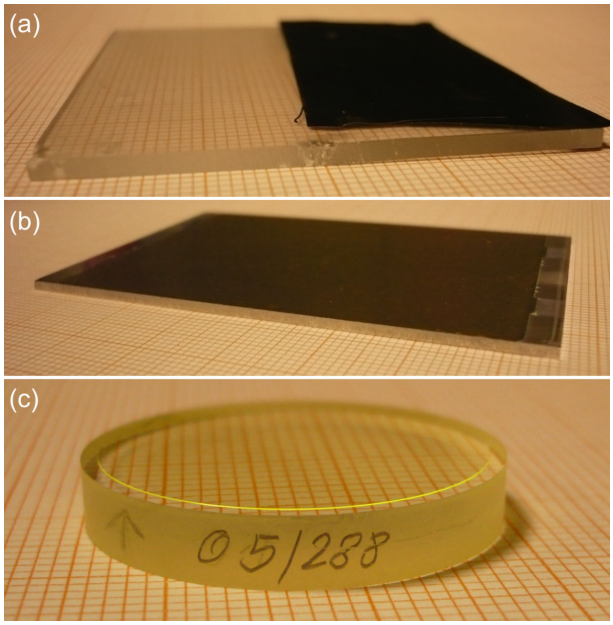

Figure 3.3: The screens under tests: (a) CsI:Tl, (b) SFOP, and (c) YAG:Ce.

caused by the light spread in a bulk scintillator is avoided.

The YAG:Ce crystal, manufactured by Crytur [170] and shown in Fig. 3.3c, was round with a diameter of 23 mm and a thickness of 0.05 mm. It was deposited onto a 4 mm thick glass base with 25 mm diameter. Its nominal scintillation yield is 9 000 photons/MeV when exposed to X/γ radiation. Its maximum emission is around 550 nm. Unfortunately, due to mechanical misalignment and limited beam time the collection of representative and systematic data for this screen was not possible. Therefore only general comments can be made on its response to low-energy beams.

3.3.4 Image Recording

The beam images were recorded with a high performance 14-bit CHROMA CX3 still camera produced by DTA [171], featuring a 1534×1024 pixel KAF1600 CCD, manufactured by Kodak [172]. The device was connected to a frame grabber board which enabled live display capture. The images were binned at 3×3 with an effective number of 512×341 pixels. In order to minimize thermal noise, the CCD was cooled to 5°C throughout all measurements. Systematic noise, due to intrinsic non-uniformity of the CCD response and its readout, was reduced by taking an image under the same conditions, but with the shutter closed and subtracting it from a real image. This dark

image subtraction was done automatically by the camera software.

3.4 Results with Protons

3.4.1 Beam Profiles

Recorded images of scintillation light emitted by the screens under different irradiation condition were analyzed off-line, yet real-time observation was also possible. For image handling, the public-domain image processing program ImageJ was used [173]. Sample images of the 200 keV proton beam taken with the CsI:Tl screen are shown in Fig. 3.4. With the "pepper-pot" grids fully retracted, a beam of elliptical cross-section was observed as shown in Fig. 3.4a. The attenuators introduced later resulted in a multi-peak structure of the beam presented in Fig. 3.4b-d. Acquisition time was 1 s for images 3.4a-c and 20 s for image 3.4d. Different contrast/brightness window settings were applied.

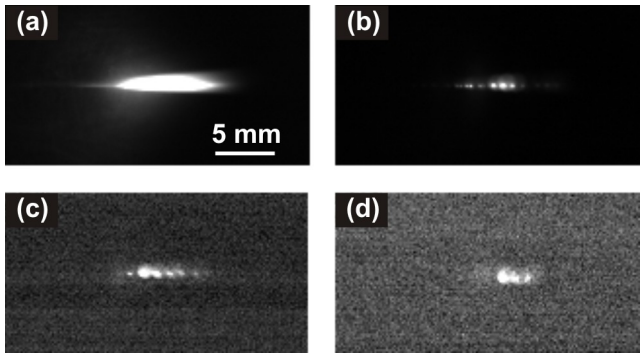

Figure 3.4: Beam images taken with the CsI:Tl screen for 200 keV protons and (a) no "pepper-pot" grids, (b) first grid only, (c) second grid only, and (d) both grids.

In order to translate the number of pixels to millimetres, an image of a reference grid placed at the screen surface was taken, see Fig. 3.5. The reference grid was illuminated by a light source placed outside the vacuum window and the image was registered by the CCD camera in the same geometry as for the beam measurements. This provided a calibration factor of 6.1 $\pm$ 0.1 pixels/mm.

Each beam image was analysed according to the same procedure. A dark image had been automatically subtracted before any off-line analysis was started. Afterwards, a region of interest (ROI) was selected in a repeatable manner and the intensity values of the two-dimensional (2D) picture were projected onto the x axis. From a projected ROI, the background noise was subtracted. Initially, this had been done simply by fitting a

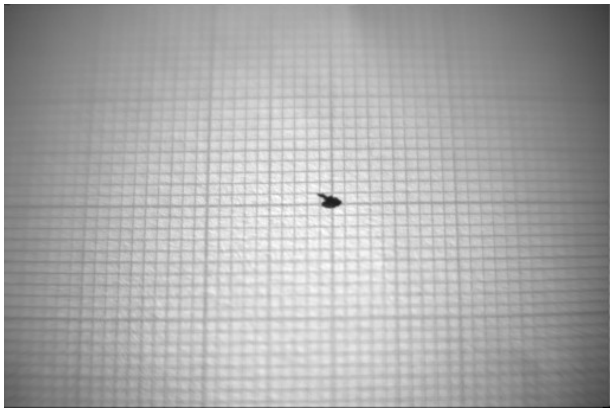

Figure 3.5: An image of a reference millimetre paper placed on the surface of the scintillator.

baseline to the projected data, but light reflections present in the images had not been corrected for in this case. The procedure was improved when two separate regions of the same area were considered: one covering the beam image and the other outside the main beam area. The latter served as a background image which was subtracted from the main ROI. A sample result of this procedure is shown in Fig. 3.6. It can be seen that the final procedure reduced the scattered light present in the initial image. For example, a small bump visible on the right hand side in Fig. 3.6a was due to a light leak through an opening in the system supporting the screen. The noise was removed with other scattered light and a clear image of a symmetric distribution of the incident particles was obtained. Since the acquisition time varied for various configurations, from 1 s without attenuation to 20 s with both grids placed in the beam path for a 200 keV beam and from 5 s to 60 s respectively for a 50 keV beam, all images were normalized with respect to time. Normalization was done also in terms of the CCD gain. An example of the resulting distribution is presented in Fig. 3.6b. By integrating the area under the normalized graphs, the number of acquired photoelectrons for each image was obtained with uncertainties below 0.02% for the most intense beams and below 4% for fully attenuated beams.

3.4.2 Resolution

The "pepper-pot" grids, included in the experiment to decrease the beam current, made it possible to assess the resolution of the system. Protons hitting the attenuator were removed from the beam, thus the total number of particles reaching the scintillating

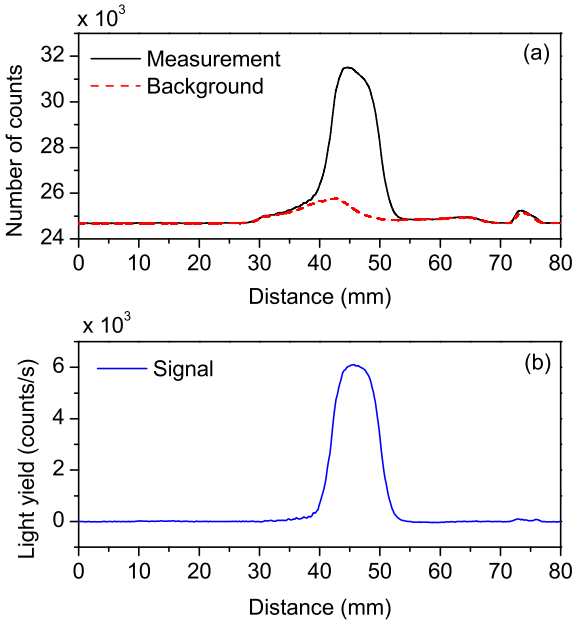

Figure 3.6: The background subtraction procedure: (a) projection of the ROI including the beam image (solid line) and the background (dotted line); (b) the resulting graph after normalization. See text for details.

screen was reduced. This led to a multi-peak distribution of the particles. Figure 3.7 shows images obtained with the CsI:Tl screen and the SFOP. Each bin shown in the histograms has a width of a single pixel, which is 0.16 mm. Narrow peaks are clearly visible and their full width at half maximum (FWHM) varies between 0.3 mm and 0.8 mm.

Although the result of 0.3 mm is encouraging, it is not the resolution limit. First, the plots in Fig. 3.7 show projections of two dimensional pictures onto the x axis which result in an averaging of y values and may cause a widening of the narrow peaks. Second, the grid hole size of about 0.2 mm together with the divergence of the beam as well as the granularity of the digital system, for which 1 pixel corresponds to 0.16 mm, limited the performance. It can be improved by changing the geometry of the setup and the binning chosen for the high resolution camera.

An example of a more complex intensity modulation is presented in Fig. 3.8 and 3.9. The first graph shows a histogram obtained with the procedure used for producing the previous plots. The other figure contains two images of the 2D intensity distribution before the projection onto the x axis. In Fig. 3.9a, the granularity of the digitized image can be observed, whereas the smooth shapes in Fig. 3.9b are a result of a sim-

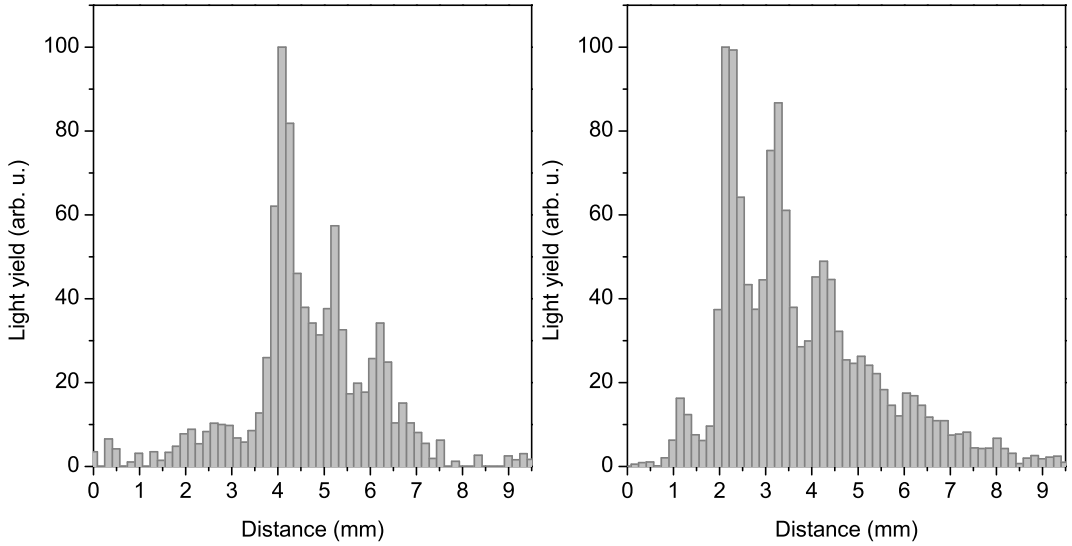

Figure 3.7: Image projection onto the x axis for proton impact at 200 keV with two "pepper-pot" grids for CsI:Tl (left) and the SFOP (right); the images do not reflect the same beam profile.

ple nearest neighbour smoothing technique applied with the Interactive 3D Surface plugin for ImageJ. The images are shown from a perspective, but the lines of peaks are parallel to each other and to the x axis. Nevertheless, it is clear that projection and averaging affect the resolution, whereas 2D images exhibit a finer structure of the beam. Therefore, one should not rely only on projected images when analyzing the beam profile.

3.4.3 Beam Current

Diagnostics of the discussed beams was a challenge not only in terms of the profile measurements, but also, and perhaps mainly, in terms of measuring the impinging beam current. Intensities in the fA range are extremely difficult to measure already in the simplest setups due to theoretical and practical noise limitations [174]. The situation is far more complicated in a real accelerator where many noise sources, such as vacuum-to-air feedthroughs, long cables or vibrating vacuum pumps, cannot be eliminated. On top of that, the ion source used in the presented experiments had been designed for delivering neither ultra-low energies nor ultra-low currents. Thus beam stability below the standard operation values was not guaranteed.

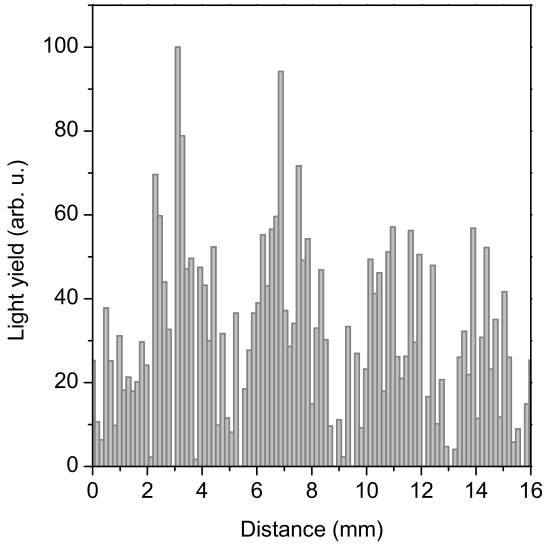

Figure 3.8: Image projection onto the x axis for the CsI:Tl screen and two grids for proton impact at 50 keV.

Faraday Cups FC1 and FC2

To monitor the beam current, it was planned to use the electrostatic Faraday cups FC1 and FC2, but their usability in the sub-pA region was quickly put into question. There was no guarantee that the Faraday cups collect all the particles of the wide beam delivered with the non-standard operation of the injector. Furthermore, the number of particles impinging on the screen surface placed at a different location was not necessarily the same. Finally, the detection limits of the current monitors were reached when both the "pepper-pot" grids were placed in the beam path. In the latter configuration, no useful signal was measured by FC2. As a result, it was decided not to rely on the Faraday cups readings.

Attenuation Factors

In principle, the amount of particles transmitted through the "pepper-pot" grids could be calculated for the known holes size and spacing, but such calculations were of very limited use. The main problem comes from the fact that the spatial distribution of particles is not uniform after passing through the first grid, and is further modulated by the second grid. The effect, a geometrical correlation or a spatial resonance, strongly depends on the positioning of the grids with respect to each other and to the beam. Consequently, the final attenuation is not a simple composition of two known attenua-

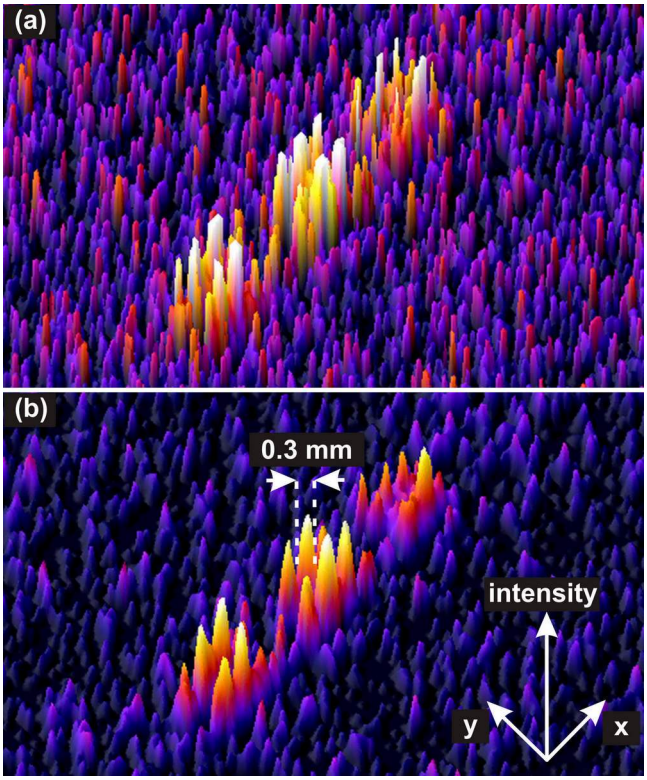

Figure 3.9: Perspective view on a beam image before the projection onto one axis without averaging (a) and with a smoothing filter applied (b).

tion factors and the method cannot be used for reliable beam intensity calculations.

The spatial resonance can be seen in Fig. 3.9. Three bigger intensity bumps created by the first grid are modulated further by the second grid. As a result, each bump consists of smaller peaks.

Absolute Calibration of Scintillation Light

In order to estimate the beam current, a method of absolute calibration of the scintillation light yield was applied [175, 176]. An ^{241}Am source, which is an α emitter, was used as a reference. It was placed behind the CsI:Tl screen on a mechanical holder with a collimator and thin Al or C foils used as energy degraders. The collimator, made of black PVC, was a 6 mm thick hollow cylinder with 7.5 mm diameter aperture, whereas the thickness of the foils was chosen to obtain various energies of particles reaching the scintillator. The resulting scintillation light was registered by the same equipment used for the profile measurements with the proton beam and "pepper-pot" grids.

The ^{241}Am source emits α particles with kinetic energies of 5.433 MeV and 5.486 MeV which have the branching ratios of 0.13 and 0.87, respectively. It corresponds to the weighted average energy of 5.480 MeV. In order to prevent any dispersion of the radioactive source to the environment, its surface was coated with a 3.8 μm thick layer of Ag [175].

In order to measure the number of α particles impinging on the scintillator, the CsI:Tl screen was replaced by a silicon detector. The energy spectrum of the α particles was acquired and the source count rate was measured; it was 249.08 ± 0.02 counts per second.

The thin aluminium and carbon foils were used to vary the energy reaching the scintillator and to obtain the response of the system to 2–3 MeV particles. For example, a 0.32 μm thick carbon foil resulted in 3.35 MeV average energy of α particles. The energy degradation was verified experimentally with the silicon detector and agreed within 1% with the simulations performed with a simple Monte Carlo code, SRIM [177].

The image registration, background subtraction and determination of the number of acquired photoelectrons were performed in the same manner as described in Section 3.4.1. To reduce the statistical fluctuations, the integration time for the images was 600 s. Each image was acquired several times to verify the reproducibility. The average amount of photoelectrons for various foil configurations was calculated.

The number of photons registered by the CCD camera is different from the number of scintillation photons generated in the CsI:Tl screen. However, the latter can be estimated following a careful consideration of all the factors affecting the transport of light from the scintillator to the photosensor.

The light is isotropically emitted from the 10 μm layer of CsI:Tl that corresponds to the range of 2–3 MeV α particles. A fraction of these photons is transmitted through the scintillator and can be calculated according to a transmission coefficient function of the refractive index n [175]:

$$t = \frac{2 \cdot n}{n^2 + 1}. \tag{3.2}$$

The light undergoes refraction while crossing the interface between the scintillator and vacuum, and widens its emission angle from the screen. The widening effect is taken into account when calculating the solid angle of the front lens of the CCD camera. An effective lens semiaperture was computed as [175]:

$$a' = D \cdot \tan\left\{\arcsin\left[\frac{1}{n} \cdot \sin\left(\arctan(\frac{a}{D})\right)\right]\right\}, \tag{3.3}$$

where D is the distance between the centre of the lens and the screen, and a is the geometrical semiaperture of the lens.

Not all of the photons falling within the effective solid angle of the lens reach the CCD: the transmission factor of the objective lens, as provided by the manufacturer, accounts for this effect caused by the back reflections and/or absorption by the optical elements inside it.

Finally, only a fraction of all the photons impinging on the CCD are detected. It is considered in the scaling factor known as quantum efficiency (QE). Because the QE is a function of the wavelength, a numerical convolution between the emission spectrum of CsI:Tl and the QE of the sensor was calculated as shown in Fig. 3.10 [176]. By integrating the resulting function with respect to the wavelength, an effective value of QE $= 0.29 \pm 1.9\%$ was obtained.

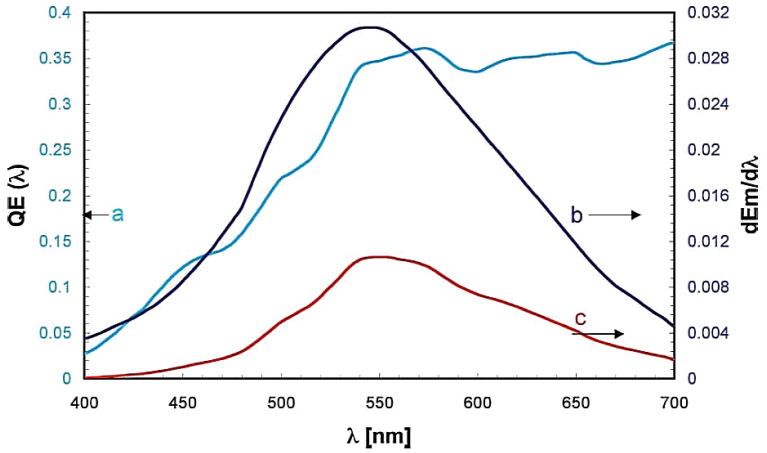

Figure 3.10: Quantum efficiency (QE) of the CCD sensor (a, left scale), emission spectrum of CsI:Tl (b, right scale) and the convolution of the two curves (c, right scale) as a function of the wavelength [176].

With all the scaling factors, it was possible to extrapolate the number of the acquired photoelectrons to the total number of photons produced in the scintillator. Dividing it by the number of α particles impinging on the surface of the CsI:Tl screen within the acquisition time, the average number of photons emitted per projectile was obtained. Finally, the number of photons per MeV was calculated for the known energies of the α particles and resulted in approximately $(3 \cdot 10^4 \pm 10\%)$ photons/MeV [175, 176].

The results for 2–3 MeV α particles were extrapolated to 200 keV and 50 keV protons. The light yield ratio between protons and α particles is about 1.5–2 at a few MeV with a higher value for the lower energies [178–180]. The ratio varies slowly at

a few MeV, but can be significantly different at keV energies. It is reflected in the change in the stopping power around 1 MeV for α particles as shown in Fig. 3.11. The light yield as a function of energy for protons and α particles was measured in [181]. It can be concluded that the extrapolation to protons at the same energy as α particles should lead to a smaller error if done at 2–3 MeV and not at 200 keV for which the p/α light yield ratio is more sensitive to small energy variations. The approximately linear change of the light yield with decreasing proton energy [181] can justify the linear scaling of the response from the MeV range to 200 keV and 50 keV. With the obtained number of particles per second, the beam current can be estimated. Its values obtained for the CsI:Tl screen were used as a reference for the SFOP since both plates were irradiated under the same beam conditions.

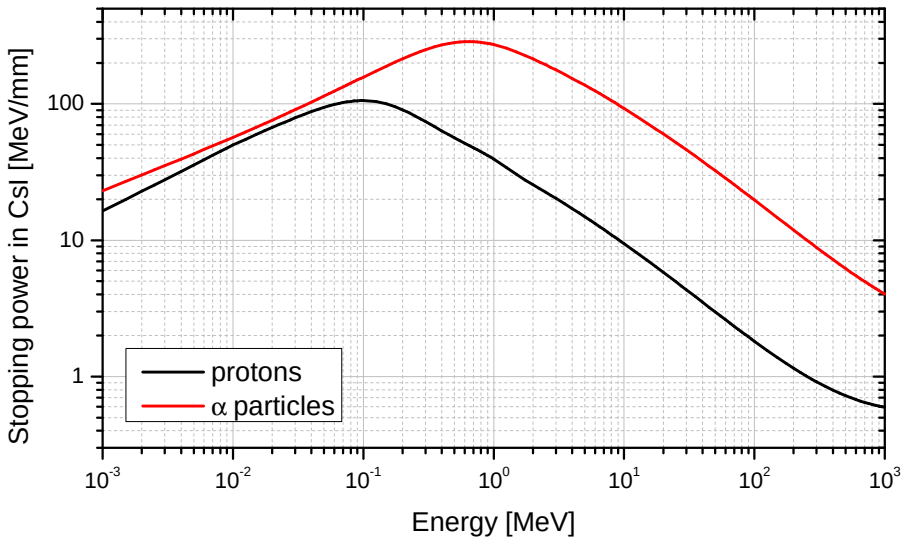

Figure 3.11: Total stopping power for protons and α particles in caesium iodide [57].

The calibration procedure is not very accurate and a systematic indetermination needs to be assumed, not larger than one order of magnitude though. As a result, every following consideration about the absolute beam current is bound to the effective value of the light yield and can thus scale up/down accordingly. Nevertheless, the technique gives reasonable predictions as compared to the approximate Faraday cup measurements and was the only solution for sub-pA estimations.

3.4.4 Detection limits

The main goal was to study the detection limits of the scintillating screens used in the experiment. The on-line monitoring gave a possibility to judge the results in a very rough, qualitative manner already during the measurements. However, with the known number of acquired photoelectrons and the corresponding beam currents, it was possible to investigate the sensitivity in terms of the absolute values.

As can be seen in Fig. 3.12, the CsI:Tl plate produced a higher light yield as compared to the SFOP and beam images were obtained even at intensities below 1 fA. It should be emphasised again, however, that the beam current was estimated, thus the results may shift to lower or higher currents within the uncertainty of one order of magnitude.

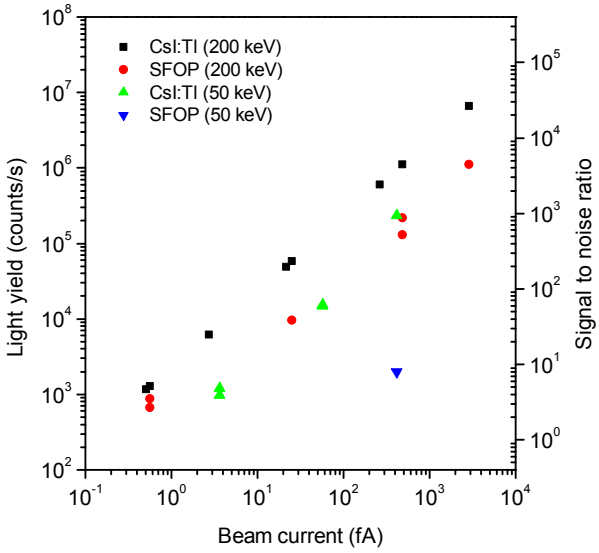

Figure 3.12: Calibrated light output and signal-to-noise ratio as a function of beam current for CsI:Tl and SFOP, irradiated with 200 keV and 50 keV proton beams. Light yield output uncertainties are smaller than the data points, whereas uncertainty of one order of magnitude is assumed for current values calibration.

The results were strongly dependent on the incident beam energy. For 50 keV, it was impossible to produce reasonable images in the same current range as for 200 keV. The limiting factor was the noise which could have been lowered by longer irradiation times. Because the beam slow extraction time in the USR is of the order of some tens of seconds, the acquisition time was limited to a maximum of 60 s. The right hand side y axis of the plot shown in Fig. 3.12 presents the signal-to-noise ratio. The light emitted

from CsI:Tl at 50 keV was lost in the noise with both "pepper-pot" grids placed in the beam path, while for the SFOP there was already not enough signal with one of the grids used. This dramatic change in sensitivity was due to a lower energy transfer to the scintillator which, in turn, produced less light. At 50 keV, the decrease in light output for CsI:Tl was around a factor of 4, which is in agreement with the assumption that the light yield scales with energy. The response of the SFOP was affected much stronger and it was possible to collect only data point at this beam energy; the signal was burried in noise for lower intensities and further studies are needed to quantify screen response at higher currents.

One important difference between the screens can be noticed: although the CsI:Tl plate emits almost 10 times more light than the SFOP in the pA region, this difference is reduced to a factor of less than 2 for the ultra-low currents. No saturation in the higher current region was observed. A possible explanation could be the following. The acquisition time was of the order of a second for the beams without attenuation, whereas it reached 20 s for the attenuated beams. The SFOP, made of terbium glass, has an afterglow constant of some seconds [182]. This is probably due to traps with a long lifetime that can cause a long delayed light emission. In the case of intense beams, these traps, but not the luminescence centres, would be fully populated and a predominance of the primary light with the 3 ms decay time is observed. When the beam intensity is sufficiently low, the light released by the traps would become comparable to the primary light. This would become an additional contribution to the observed light and could explain why an enhanced yield of the SFOP was observed. CsI:Tl also has afterglow, but this is confined within milliseconds [183].

As mentioned previously, it was not possible to collect representative data for the YAG:Ce plate, thus it cannot be compared with the other scintillators in a systematic manner. However, results obtained by other groups indicate it should be less than both CsI:Tl and the SFOP. [90, 161].

3.5 Perspectives

It was shown that the CsI:Tl screen and SFOP are suitable for the monitoring of keV beams in the femtoampere regime. They can be used as simple, yet sensitive, robust and inexpensive detectors for beam profile observation and are preferred over more expensive, complex and delicate devices.

Both the scintillating materials investigated at INFN-LNS can be used during the

initial commissioning of the USR with protons or H^- ions. For this reason, a design of the beam profile monitor based on a bulk scintillator was developed as shown in Fig. 3.13. It consists of an adjustable screen holder mounted on an actuator which can be moved in and out of the beam line. The scintillator is installed in a vacuum vessel at 45° to the beam axis and is observed by means of a CCD camera placed outside the vacuum window, similarly to the setup at INFN-LNS.

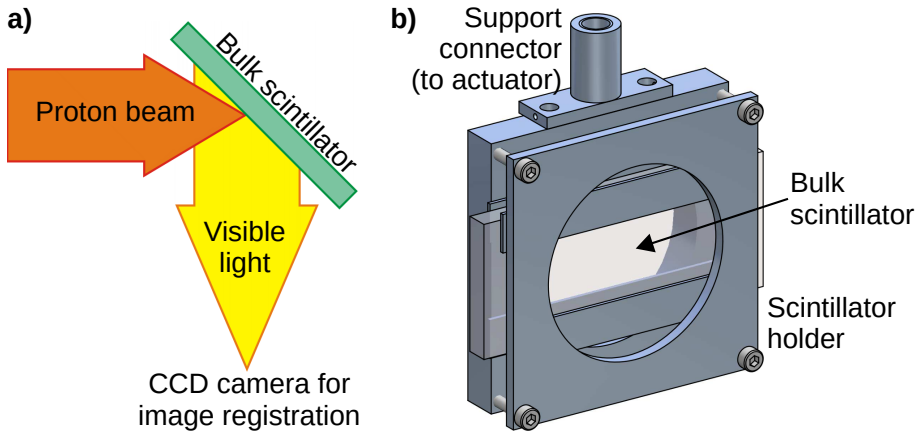

Figure 3.13: Scintillator holder as proposed for the USR.

Antiprotons add further challenges and complicate the already difficult task of the ultra-low energy, ultra-low intensity beam diagnostics: stopped in a scintillator, they annihilate and produce a variety of secondary particles. The annihilation products, mainly weakly ionizing, high energy pions and recoiling, strongly ionizing MeV-scale nuclear fragments, transfer enormous energy to the detector. As opposed to protons, the light yield due to the kinetic energy of antiprotons is only a small fraction of the light output due to the energy released after annihilation. As a result, two adverse effects can be observed: saturation, caused by the amount of the energy deposited locally, and ghost structures in the image due to secondary particles travelling through the scintillator and exciting electrons further away from the primary interaction point.

A profile monitor for antiproton beams should be optimized with the annihilation-related processes carefully taken into account. A scintillator suitable for ultra-low intensity proton beams, such as CsI:Tl, is expected to be too sensitive to highly ionizing annihilation products. Nevertheless, observations of $\bar{p}$ beams are still possible also with the simple scintillator-based monitor using, for example, plastic or quartz glass [105]. Instead of a bulk scintillator, a perforated screen can be employed to observe halo particles. It could be used for the machine parameters tuning to make sure that most

of the beam passes through the small aperture in the monitor. Alternatively, two pairs of screens for vertical and horizontal planes could be mounted on actuators with stepper motors and act as beam scrapers for fine beam tuning and observation.

Alternative techniques, not based on scintillators, are discussed in the further parts of this thesis, mainly in Chapters 6 and 7.

3.6 Summary

The application of scintillating screens to low-energy, low-intensity beam diagnostics was discussed. Various scintillation mechanisms were presented and the challenges imposed by keV protons and antiprotons were shown. It is concluded that no single solution can be found for both types of particles. In order to find a scintillating material suitable for proton beam diagnostics, measurements with several screen materials were performed at INFN-LNS.

It was shown that CsI:Tl and the SFOP are sensitive enough for proton beam profile monitoring in the ultra-low energy, ultra-low intensity regime. With 200 keV beams, it is possible to measure currents even in the sub-fA range corresponding to about $5 \cdot 10^3$ particles per second. For 50 keV beams, the sensitivity of CsI:Tl drops down by a factor of about 4. Only one data point was collected for the SFOP at this energy and no general conclusion on screen sensitivity change can be drawn. It was not possible to collect representative data for the YAG:Ce screen and it cannot be compared with the other scintillators in a systematic manner. However, it is not as sensitive as CsI:Tl or SFOP and is not planned to be used at the USR.

An absolute light yield calibration technique was applied to estimate the beam current of the impinging proton beam. The method is less accurate than direct measurements, but these were not possible due to the detection limits of the Faraday cups installed in the beam line. A systematic indetermination not larger than one order of magnitude is assumed, yet femtoampere currents can be observed.

A resolution of at least 0.3 mm was shown. It can be improved by optimising the geometry of the setup as well as the granularity of the digital read-out. In addition, it should be kept in mind that two dimensional intensity maps can reveal complex structures present in images produced with “pepper-pot” grids.

A sensitive scintillator will be very important during the commissioning stage of the USR with proton or H^- beams. CsI:Tl was shown to be best suited for the initial beam profile monitoring at this storage ring. A design of the monitor based on the scintillator

under investigation has been developed and can be used at the USR. However, a bulk scintillating screen introduced in the beam path is not suitable for the accurate imaging of low-energy antiproton beams.

Chapter 4

Capacitive Pick-Up

In this chapter, a capacitive pick-up for low-intensity, low-energy beam position measurements is presented. The challenges imposed by the USR for the non-destructive position monitoring are described and the theoretical basis of the signal detection are given. The formalism used to describe the response of the monitor to ultra-relativistic beams is introduced and extended to incorporate the effect of low beam velocities. Next, the design considerations are presented with the estimates of signals and noise expected at the USR. Additionally, position determination uncertainties due to noise, mechanical inaccuracies and signal digitisation are analysed. This is followed by the description of the mechanical design of the pick-up prototype with its signal processing hardware and software. The performance of the monitoring system is experimentally tested with a current-carrying-wire setup. To complete the study, the response of the pick-up to particle beams at various velocities is modelled with a finite integration technique-based software. The simulations are compared with the theoretical predictions and stretched-wire measurements. Finally, the results of the work and future perspectives are discussed.

4.1 Motivation

As discussed in Section 2.3, a capacitive pick-up is the device of choice for beam position measurements in most particle accelerators due to their non-destructive nature. The monitor can deliver information on the transverse position of the beam centre or even on the time structure of individual bunches without affecting the beam. Furthermore, the charge induced on a metal electrode at relativistic velocities is a direct image of the bunches and the description of the monitor response becomes very simple [121].

The USR puts challenging demands on the beam pick-ups which should be capable of measuring beam position at both low intensities and low velocities. The number of antiprotons in the USR is expected to result in signals that are close to the noise level of state-of-the-art electronics [129, 131]. A low-noise signal processing system with a reduced bandwidth is therefore required. Moreover, the velocities of the decelerated particles in the USR complicate the already difficult task of beam position determination. The low energies correspond to only a fraction of the speed of light and the induced charged distribution is not a direct image of the beam any more. It becomes dependent on the bunch length, repetition frequency and transverse displacement. All these parameters need to be carefully addressed to provide a diagnostics system capable of monitoring the low-intensity, low-energy antiproton beams at the USR.

4.2 Theory of Capacitive Pick-Ups

4.2.1 General Formalism

A charged particle beam passing through a hollow metal cylinder generates an image current which can be fed into an amplifier for further processing. This situation is shown schematically in Fig. 4.1.

The effect of the beam on the electrode can be described by two current sources, one for the beam entering the pick-up, $I(t)$, and one for the beam leaving it, $I'(t)$. It is assumed that the image current induced on the metal tube is equal to the beam current. Additionally, it can be expected that no beam losses occur during the time $\Delta t = l/v$ required by the particles travelling at velocity v to exit the electrode of length l. Consequently, current I' at time t is equal to current I which entered the pick-up at $t - \Delta t$:

$$I'(t) = I(t - \Delta t). \tag{4.1}$$

The overall capacitance C of the pick-up is given by the area of the electrode and its distance to the beam tube as well as the connections between the electrode and the amplifier input. This amplifier has an input resistance R.

The pick-up can be seen as an electrical circuit node to which Kirchhoff's current law can be applied. The sum of the currents flowing into the node should be equal to the sum of the currents flowing out of this node:

$$I(t) = I(t - \Delta t) + I_R(t) + I_C(t). \tag{4.2}$$

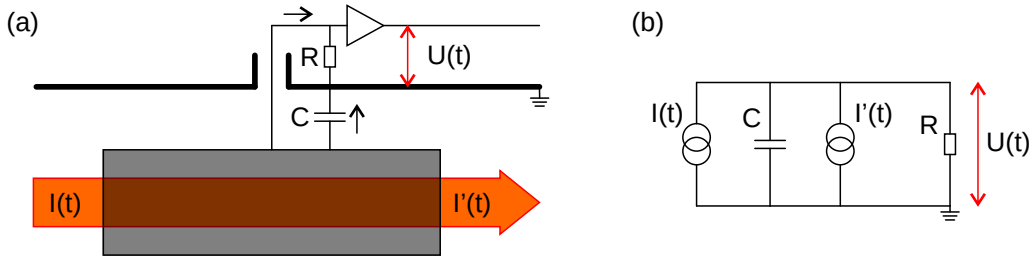

Figure 4.1: A schematic diagram of: (a) a capacitive pick-up electrode represented by a hollow cylinder, and (b) its equivalent electrical circuit.

For small Δt, the term $I(t-\Delta t)$ can be approximated by a Taylor series:

$$I(t-\Delta t) = I(t) - \dot{I}(t)\cdot\Delta t + \ddot{I}(t)\cdot\frac{\Delta t^2}{2} + ... \tag{4.3}$$

Considering only the linear term of the series 4.3, equation 4.2 can be rewritten, with $\Delta t = l/v$, as:

$$\frac{l}{v}\cdot\dot{I}(t) = I_R(t) + I_C(t). \tag{4.4}$$

For $I_R(t) = U(t)/R$ and $I_C(t) = C\cdot\dot{U}(t)$, equation 4.4 becomes:

$$\frac{l}{v}\cdot\dot{I}(t) = \frac{U(t)}{R} + C\cdot\dot{U}(t). \tag{4.5}$$

Equation 4.5 can be simplified if a high input impedance amplifier is used. In this case, most of the current flows through the capacitance C and term $1/R$ is negligible. After integration, the equation can be reduced to:

$$U(t) = \frac{l}{C\cdot v}\cdot I(t). \tag{4.6}$$

A constant of integration can be omitted as a voltage offset. In principle, a pick-up can be seen as a high-pass RC filter with a cut-off frequency $f_{cut} = (2\cdot\pi\cdot R\cdot C)^{-1}$. For $R \gg (2\cdot\pi\cdot f\cdot C)^{-1}$, the pick-up signal is a direct image of the bunch shape. However, due to the high-pass characteristics caused by the finite value of R, a DC component of the signal is disregarded and a baseline shift is observed. The unipolar beam current is transformed to an AC voltage with the baseline at zero [121].

4.2.2 Principle of Position Measurement

The main application of capacitive pick-ups is the non-destructive measurement of beam position. By surrounding the beam with electrodes, the signals generated on each of

them can be compared and a displacement of the beam centre from the reference trajectory can be detected. In a first approximation, the beam position can be determined from the difference of the opposite electrodes signals, two in the horizontal and two in vertical direction. However, the response of the pick-ups may not change linearly with the beam offset and other signal processing procedures are often applied [121,184,185].

The most common approach is the so-called "difference-over-sum" calculation. In this case, the information on the beam displacement in each direction, x and y, is reconstructed from the difference of the signals from the opposite electrodes, ΔU, normalised to the sum of the signals, ΣU. Consequently, the position of the centre-of-mass of the beam with respect to the centre of the vacuum tube can be calculated from:

$$x = k_x(x, y) \cdot \frac{\Delta U_x}{\Sigma U_x}, \tag{4.7}$$

$$y = k_y(x, y) \cdot \frac{\Delta U_y}{\Sigma U_y}, \tag{4.8}$$

where k is a scaling factor with an index x or y for corresponding axes. Very often, also the inverse of k, called position sensitivity $S \equiv 1/k$, is used to characterise the pick-up response [121].

In hadron storage rings, a diagonally cut capacitive pick-up is a commonly used beam position monitor. A typical device of this type, shown schematically in Fig. 2.8, consists of two pairs of long metal electrodes. Each pair responds to the beam position only in one direction and two pairs, rotated by 90° with respect to each other, are required to enable both, horizontal and vertical measurements. The shape of the monitor is of particular interest, because the signal amplitude becomes proportional to the fraction of the beam covered by the electrodes as projected on a given plane. In turn, the response of the pick-up changes linearly with the beam position. Additionally, bunches in hadron machines are typically much longer than the electrodes and a high input impedance is used, thus equation 4.6 can be applied. Furthermore, the configuration results in a high sensitivity compared to other pick-up types [121].

4.2.3 Response of a Diagonally Cut Pick-Up

The linear response and symmetry of the diagonally cut pick-up lead to the simplest form of scaling factors k_x and k_y. Both parameters are equal and do not depend on the position in x and y:

$$k_x(x, y) = k_y(x, y) \equiv k = \text{const.} \tag{4.9}$$

To calculate k, a simple model can be used that is schematically shown in Fig. 4.2. The diagonally cut pick-up consists of two electrodes, has radius r and total length l. A beam passes through the detector at position x and generates signals proportional to the path projected on the electrodes, l_1 and l_2, respectively. With the gap between the electrodes small compared to the pick-up length, it can be written that $l \approx l_1 + l_2$. Also a full symmetry of the circuit is assumed with capacitances C and input impedances R identical for both channels. Additionally, coupling capacitance C_c between the adjacent electrodes is considered. Length s is omitted in order to simplify the following discussion, but a generalised formula incorporating the parameter is provided afterwards.

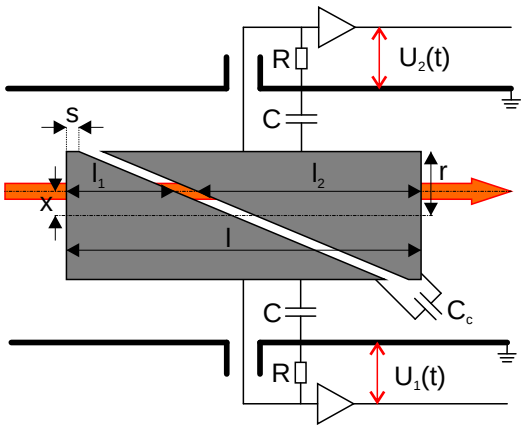

Figure 4.2: A schematic diagram of a capacitive pick-up with diagonally cut electrodes as part of an electrical circuit.

Following the reasoning which led to equation 4.6, one can write for each of the electrodes:

$$\frac{l_1}{v} \cdot \dot{I} = \frac{U_1}{R} + C \cdot \dot{U_1} + C_c \cdot (\dot{U_1} - \dot{U_2}), \tag{4.10}$$

$$\frac{l_2}{v} \cdot \dot{I} = \frac{U_2}{R} + C \cdot \dot{U_2} + C_c \cdot (\dot{U_2} - \dot{U_1}). \tag{4.11}$$

As before, a high input impedance of the amplifiers is assumed and the terms with $1/R$ can be neglected. The difference of equations 4.10 and 4.11 is then:

$$\frac{l_1 - l_2}{v} \cdot \dot{I} = (C + 2 \cdot C_c) \cdot \Delta\dot{U}, \tag{4.12}$$

where $\Delta U = U_1 - U_2$. From the intercept theorem [186], one can conclude:

$$\frac{l_1}{x + r} = \frac{l}{2 \cdot r} \quad \Rightarrow \quad l_1 = \frac{x + r}{2 \cdot r} \cdot l. \tag{4.13}$$

With $l_2 = l - l_1$, it can be written that:

$$l_1 - l_2 = \frac{x}{r} \cdot l, \tag{4.14}$$

and equation 4.11 becomes:

$$\frac{x}{r} \cdot \frac{l}{v} \cdot \dot{I} = (C + 2 \cdot C_c) \cdot \Delta\dot{U}. \tag{4.15}$$

Similarly, the sum of equations 4.10 and 4.11 is:

$$\frac{l}{v} \cdot \dot{I} = C \cdot \Sigma\dot{U}, \tag{4.16}$$

where $\Sigma U = U_1 + U_2$. Both the equations, 4.15 and 4.16, can be integrated and their ratio calculated, which leads to the formula for x in terms of the difference-over-sum:

$$x = r \cdot \frac{C + 2 \cdot C_c}{C} \cdot \frac{\Delta U}{\Sigma U}. \tag{4.17}$$

Equation 4.17 gives the expression for the scaling factor:

$$k = r \cdot \left(1 + 2 \cdot \frac{C_c}{C}\right). \tag{4.18}$$

A more general expression incorporating length s shown in Fig. 4.2 is slightly modified [131]:

$$k = \frac{r}{1 - 2 \cdot s/l} \cdot \left(1 + 2 \cdot \frac{C_c}{C}\right). \tag{4.19}$$

The scaling factor is proportional to the radius of the pick-up and depends on the coupling capacitance. The smallest value of k corresponds to the highest sensitivity and, as a result, a small beam displacement generates a large difference signal. The parasitic coupling between the adjacent electrodes increases k and limits the sensitivity of the pick-up. The lowest coupling capacitance is therefore desired.

4.2.4 Low-Velocity Beams

All the above considerations are based on the assumption that the charge distribution induced on the pick-up electrodes is a direct image of a moving bunch. This is true only for ultra-relativistic particles [187, 188]. At velocities close to the speed of light, the electric field lines are perpendicular to the bunch direction of motion due to the Lorentz contraction of the longitudinal components. Consequently, the bunches induce a wall image current which has the same time structure as the beam. However, at low beam velocities, the longitudinal component of the electric field does not vanish

and the image charge distribution is broader than the bunch length. Furthermore, it depends also on the beam distance to the metallic wall and a non-linear response of the pick-up is expected. The following section extends the simple formalism introduced at the beginning of the chapter and investigates the influence of low velocities on the USR pick-ups sensitivity and linearity.

A repetitive beam current $I_b(t)$ can be represented by a Fourier series expansion:

$$I_b(t) = \bar{I}_b \cdot \left[1 + 2 \cdot \sum_{n=1}^{\infty} A_n \cdot \cos(2 \cdot \pi \cdot n \cdot f_{RF} \cdot t + \phi_n)\right], \tag{4.20}$$

where $\bar{I}_b$ is the average beam current, A_n is a bunch-shape-dependent form factor, n is the harmonic number, f_{RF} is the bunching frequency, and ϕ_n is the phase of the n^{th} harmonic [188]. For a $\cos^2$-like charge distribution, the form factor is:

$$A_n = \frac{\sin\left[(\alpha_n - 2) \cdot \pi/2\right]}{(\alpha_n - 2) \cdot \pi} + \frac{\sin\left(\alpha_n \cdot \pi/2\right)}{\alpha_n \cdot \pi/2} + \frac{\sin\left[(\alpha_n + 2) \cdot \pi/2\right]}{(\alpha_n + 2) \cdot \pi}, \tag{4.21}$$

with $\alpha_n = n \cdot \pi \cdot t_{bunch} \cdot f_{RF}$ and a full width at the base of bunch t_{bunch} [189].

A beam centred in a conducting cylindrical beam tube, or a pick-up, of radius r induces a uniformly-distributed beam current density on the inner wall of the metallic enclosure. For modulated beams, the magnetic field associated with the DC part of equation 4.20 appears outside the beam tube and the wall currents include only the AC components. In a relativistic case, the situation can be simplified to a two-dimensional (2D) problem in the plane of the cross-section of the beam tube. The instantaneous Fourier harmonic amplitudes of the image currents, integrated over 2π, are the same as those for the beam itself. For a beam tube with infinite conductivity, the wall current density is the beam current divided by the beam tube circumference [189]:

$$i_w = \frac{-I_b(t)}{2 \cdot \pi \cdot r}. \tag{4.22}$$

If the beam is displaced in horizontal plane by x from the centre of the beam tube of radius r, the expression for the wall image current density at r and azimuthal position ϕ can be written as [188, 189]:

$$i_w(r, \phi, t) = \frac{-I_b(t)}{2 \cdot \pi \cdot r} \cdot \left[1 + 2 \cdot \sum_{m=1}^{\infty} \left(\frac{x}{r}\right)^m \cdot \cos(m \cdot \phi)\right]. \tag{4.23}$$

The beam tube can be cut in a vertical plane into two symmetric halves and form a cylindrical pick-up consisting of two metal electrodes, denoted L and R for "left" and

"right". Assuming that they are grounded, have angular width of π and that the beam displacement x is towards the right electrode, the resulting currents flowing in parallel to the beam on the inner surface of the electrodes are [189]:

$$I_{w,R}(t) = \frac{-I_b(t)}{2} \cdot \left[1 + \frac{4}{\pi} \cdot \sum_{m=1}^{\infty} \frac{1}{m} \cdot \left(\frac{x}{r}\right)^m \cdot \sin\left(\frac{1}{2} \cdot \pi \cdot m\right)\right], \tag{4.24}$$

$$I_{w,L}(t) = \frac{-I_b(t)}{2} \cdot \left[1 + \frac{4}{\pi} \cdot \sum_{m=1}^{\infty} \frac{1}{m} \cdot \left(\frac{x}{r}\right)^m \cdot \sin\left(\frac{3}{2} \cdot \pi \cdot m\right)\right]. \tag{4.25}$$

It is assumed that the beam position is determined by the pick-up response to a certain n^{th} frequency or, in other words, that a narrowband signal processing is employed. In this case, a single Fourier frequency component of the beam current can be used to derive the azimuthal distribution of the beam tube image currents. The root mean square (RMS) amplitude of the beam current at a single frequency $f = n \cdot f_{RF}$ is [188]:

$$I_b(f) = \sqrt{2} \cdot \bar{I}_b \cdot A_n, \tag{4.26}$$

whereas the RMS wall image currents are [188]:

$$I_{w,R}(f) = \frac{A_n \cdot \bar{I}_b}{\sqrt{2}} \cdot \left[1 + \frac{4}{\pi} \cdot \sum_{m=1}^{\infty} \frac{1}{m} \cdot \left(\frac{x}{r}\right)^m \cdot \sin\left(\frac{1}{2} \cdot \pi \cdot m\right)\right], \tag{4.27}$$

$$I_{w,L}(f) = \frac{A_n \cdot \bar{I}_b}{\sqrt{2}} \cdot \left[1 + \frac{4}{\pi} \cdot \sum_{m=1}^{\infty} \frac{1}{m} \cdot \left(\frac{x}{r}\right)^m \cdot \sin\left(\frac{3}{2} \cdot \pi \cdot m\right)\right]. \tag{4.28}$$

The above considerations are valid for a 2D approximation which can be applied only to fields generated by ultra-relativistic bunches. In order to investigate the effects of low beam velocities, the problem needs to be solved in three dimensions [188]. The respective equations become more complicated [187, 188]:

$$I_{w,R}(f,\beta) = \frac{A_n \cdot \bar{I}_b}{\sqrt{2}} \cdot \left[\frac{I_0(g_n \cdot x)}{I_0(g_n \cdot r)} + \frac{4}{\pi} \cdot \sum_{m=1}^{\infty} \frac{1}{m} \cdot \frac{I_m(g_n \cdot x)}{I_m(g_n \cdot r)} \cdot \sin\left(\frac{1}{2} \cdot \pi \cdot m\right)\right], \tag{4.29}$$

$$I_{w,L}(f,\beta) = \frac{A_n \cdot \bar{I}_b}{\sqrt{2}} \cdot \left[\frac{I_0(g_n \cdot x)}{I_0(g_n \cdot r)} + \frac{4}{\pi} \cdot \sum_{m=1}^{\infty} \frac{1}{m} \cdot \frac{I_m(g_n \cdot x)}{I_m(g_n \cdot r)} \cdot \sin\left(\frac{3}{2} \cdot \pi \cdot m\right)\right], \tag{4.30}$$

where I_m represents the modified Bessel function of order m [190], and:

$$g_n = \frac{2 \cdot \pi \cdot n \cdot f_{RF}}{\beta \cdot \gamma \cdot c}, \tag{4.31}$$

with relativistic $\beta = v/c$ and Lorentz factor $\gamma = 1/\sqrt{1-\beta^2}$.

4.3 Design Considerations

4.3.1 Pick-Up Signals Estimation

Equation 4.6 can be used to estimate the pick-up voltage signals. The average beam current $\bar{I}$ circulating in a storage ring is the product of total charge Q carried by the particles and their revolution frequency f_0. For protons/antiprotons, Q is the number of particles N times the elementary charge e, whereas f_0 depends on beam velocity v and machine circumference L. The voltage generated at one half of a metal cylinder is then:

$$\hat{U} = \frac{1}{2} \cdot \frac{l}{C \cdot v} \cdot \bar{I} = \frac{1}{2} \cdot \frac{l}{L} \cdot \frac{N \cdot e}{C}. \tag{4.32}$$

Pick-Up Signals in the USR

Equation 4.32 can be applied to estimate the signals expected in the USR. For a 20 keV antiproton beam, the revolution frequency is 46 kHz, the velocity is only 0.6% of the speed of light and the space charge limit is about $2 \cdot 10^7$ particles. These correspond to an average beam current of approximately 100 nA. For a 300 keV beam, $\beta = 0.025$ and $f_0 = 178$ kHz, the average beam current is almost one order of magnitude higher if the same total number of particles is considered. According to equation 4.32, the resulting amplitudes of the voltage signals are comparable at both energies. However, the space charge limit at 300 keV is higher and more partciles, approximately 10 times more, can be expected [191].

Several further assumptions have been made to estimate the pick-up signals at the USR. The expected length and radius of the pick-up are $l = 100$ mm and $r = 50$ mm, respectively, whereas $C = 100$ pF, which is a typical capacitance value for a monitor of such dimensions [121, 131]. Additionally, the scaling factor $k = 100$ mm is assumed. Note should be taken that the final performance of the system will depend on the overall design of the pick-up and its processing system. The parameters reflect the lower limit of the expected signals and sensitivity.

Under these assumptions, the expected voltage for each electrode is approximately 37 µV at both beam energies. Consequently, the sum signal $\Sigma\hat{U}$ is about 75 µV. According to equation 4.17, the difference signal $\Delta\hat{U}$ between two adjacent electrodes for a small beam displacement x can be approximated by:

$$\Delta\hat{U} = \frac{x}{k} \cdot \Sigma\hat{U}. \tag{4.33}$$

With $k = 100$ mm, the expected difference signal is about 75 nV at $x = 0.1$ mm and 0.75 µV at $x = 1$ mm.

The dynamic range of the detection system needs to cover both, the lowest difference signal and the sum peak voltage to be monitored. Also the overall noise should be lower than the expected minimum voltage.

Time Structure and Frequency Analysis

A more detailed analysis of the signals varying with time was also performed. The temporal structure of the bunches in a storage ring is defined by the RF buncher. Its frequency, f_{RF}, cannot be random but has to be an integer multiple of the revolution frequency f_0 of the particles in the ring:

$$f_{RF} = h \cdot f_0, \tag{4.34}$$

where h is the harmonic number corresponding to the number of bunches. For a standard operation of the USR with $h = 10$, one can expect $2 \cdot 10^6$ particles per bunch.

Each bunch occupies only a fraction of the RF period $1/f_{RF}$ and its length, l_{bunch}, depends on various factors, such as the average beam current $\bar{I}$, RF voltage U_{RF} and beam cooling. If the amplitude of the RF voltage is small, e.g. < 100 V, the temporal longitudinal bunch shape follows a $\cos^2$-like distribution [131]. However, if electron cooling is applied, the bunches become compressed and their length can be approximated, at the space charge limit condition, with the following formula [192]:

$$l_{bunch} = 2 \cdot L \cdot \sqrt[3]{\frac{3 \cdot (1 + 2 \cdot \ln(D/d)) \cdot \bar{I}}{2^4 \cdot \pi^2 \cdot c^4 \cdot \epsilon_0 \cdot \gamma^2 \cdot h^2 \cdot \beta^4 \cdot U_{RF}}}, \tag{4.35}$$

where L is the storage ring circumference, D and d are the diameters of the beam tube and the beam, respectively, c is the speed of light in vacuum, ϵ_0 is the vacuum permittivity and γ it the relativistic Lorentz factor. The bunch described by equation 4.35 is assumed to be parabolic in shape, but also a $\cos^2$-like distribution can be fitted [193].

Two possible charge distributions are considered for the following studies: $\cos^2$ for a weakly bunched, uncooled beam, and compressed $\cos^2$-like bunches for an electron cooled beam. In the latter configuration, the particles are contained in a smaller space and the bunch length is only 20% of the RF period. Idealised pick-up signals for both distributions, together with the corresponding frequency spectra, are shown in Fig. 4.3

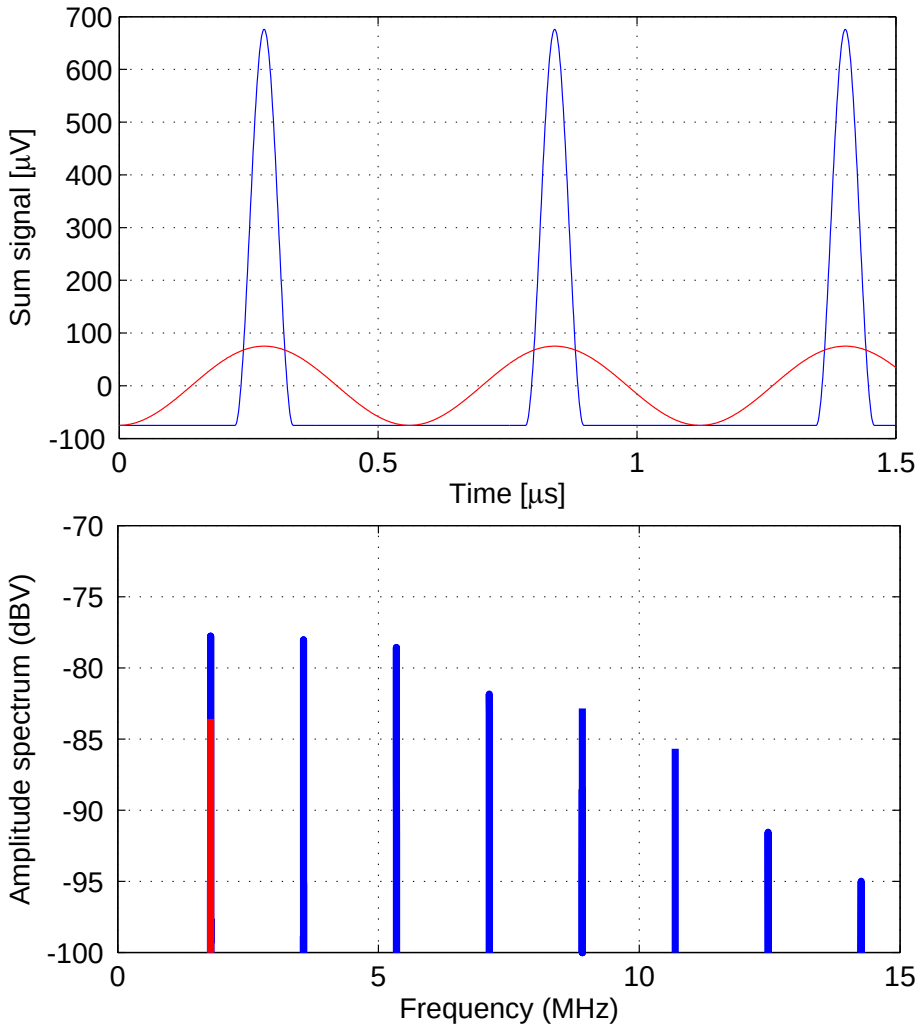

Figure 4.3: Estimated pick-up signals (top) and the corresponding frequency spectra (bottom) for an uncooled charge distribution (red) and electron cooled bunches (red) at 300 keV and $f_{RF} = 1.78$ MHz.

for 300 keV particles at $f_{RF} = 1.78$ MHz. At 20 keV, the corresponding time scale is longer due to the lower velocity of particles.

For the uncooled beam, the peak-to-peak values of the sum and difference signals are 150 μV and 1.5 μV/mm, respectively. The corresponding values for the compressed bunches are 750 μV and 7.5 μV/mm. The maximum signal amplitude U_{max} which needs to be measured for the positive part of the signal is therefore approximately 700 μV, whereas the smallest amplitude $U_{min} = \hat{U}$ is about 0.75 μV/mm.

4.3.2 Corrections for Low-Velocity Beams

The beam velocities at the USR are much smaller than the speed of light, thus the deviation from the ultra-relativistic distribution of the signals needs to be estimated. The image wall currents for a pick-up radius $r = 50$ mm are calculated according to equations 4.29 and 4.30. It is assumed that the beam position is determined by the pick-up response to a single frequency at $n = 1$ which is the bunching frequency f_{RF}. Also a $\cos^2$-like current modulation is considered, thus the bunch length is simply the inverse of f_{RF}.

In Fig. 4.4, the difference-over-sum $\Delta I_w/\Sigma I_w$ is plotted as a function of beam position for $\beta = 0.025$ (300 keV) and for a relativistic beam, i.e. $\beta = 1$. For the latter, the response of the pick-up does not depend on the bunching frequency, whereas such a dependence is clear for low-β beams. The frequencies shown in the figure are integer multiples of the USR revolution frequency at harmonic numbers $h = 10$ (1.78 MHz), 100 (17.8 MHz), 200 (35.6 MHz), 300 (53.4 MHz) and 400 (71.2 MHz). The corresponding bunch lengths are shown in brackets. The calculations made for a 20 keV beam would be indistinguishable from 300 keV results if plotted together in Fig. 4.5.

With the known response of the pick-up to low-velocity beams at various frequencies, the error due to the relativistic treatment of the signals can be calculated. Figure 4.5 shows the discrepancy between the beam position determined from the difference-over-sum calculation at various bunching frequencies and the actual beam position. Only integer multiples of the revolution frequency are allowed in the storage ring and some of them are indicated in the figure. At 20 keV, the non-linear effect becomes stronger at lower frequencies, but is similar for both USR energies if the same harmonic numbers are compared. It can be concluded that the deceleration process should have only a minimal effect on the performance of the pick-ups. Any beam shift indicated by the position monitors after decreasing the energy to 20 keV at a fixed harmonic number is expected to be caused by a real beam displacement.

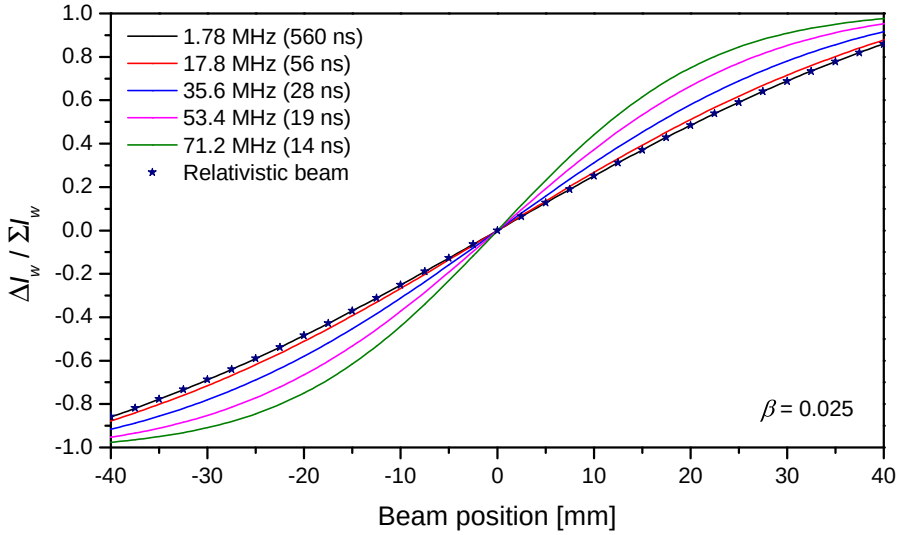

Figure 4.4: Pick-up response as a function of bunching frequency at $\beta = 0.025$ (300 keV) for a pick-up radius of 50 mm. Results for a relativistic beam, i.e. $\beta = 1$, do not change with frequency and are represented by star symbols.

At the chosen harmonic number $h = 10$, the low-β correction to the pick-up response at a single frequency is negligible. The discrepancy between the beam position expected from the relativistic model and the position calculated for the low-velocity beams is smaller than 0.02 mm. This can be explained by the fact that the chosen bunching frequencies correspond to bunch lengths of a few metres. The longitudinal component of the electric field for such bunches is significant only at their beginning and their end. With increasing frequency, the bunch length decreases and the edge effects start to dominate in the pick-up signal generation. Therefore, low-β correction becomes significant only for high frequencies and short bunches.

4.3.3 Noise Estimation

For a pick-up equipped with a high input impedance amplifier, the noise is determined mainly by the amplifier voltage noise density e_{amp} [129]. However, the contribution of thermal noise density e_{th} and amplifier current noise density i_{amp} is also considered. The total noise can be calculated as:

$$U_{noise} = \sqrt{\left(e_{th}^2 + |Z|^2 \cdot i_{amp}^2 + e_{amp}^2\right) \cdot \Delta f}, \tag{4.36}$$

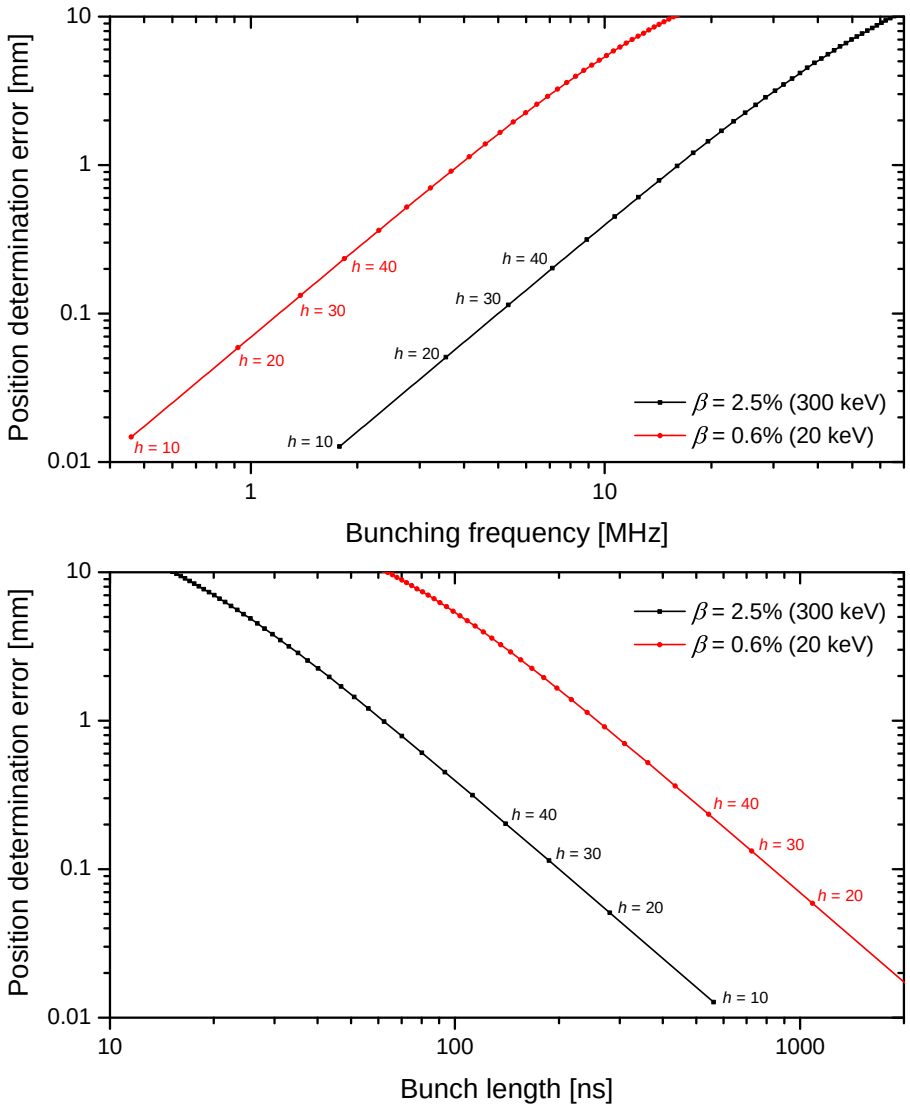

Figure 4.5: Beam position determination error as a function of bunching frequency (top) and bunch length (bottom) at $\beta = 0.025$ (300 keV) and $\beta = 0.006$ (20 keV) for a pick-up of 50 mm radius and a single frequency response.

where Δf is the bandwidth of the system and Z is the impedance of the equivalent RC circuit of the pick-up:

$$Z = \left(R^{-1} + i \cdot \omega \cdot C\right)^{-1}. \tag{4.37}$$

The thermal noise density is given by:

$$e_{th} = \sqrt{4 \cdot k_B \cdot T \cdot \mathrm{Re}(Z)}, \tag{4.38}$$

where T and k_B are the temperature and Boltzman constant, respectively.

Depending on the bandwidth chosen, several modes of beam position monitoring are possible. With a high bandwidth, the structure of individual bunches can be observed. In this case, Δf should be approximately 10 times the RF frequency. A slightly lower bandwidth, i.e. comparable to f_{RF}, is required for the observation of the bunch-by-bunch position variation. If the position of a reference bunch on each turn is important, the bandwidth can be reduced further. In such a turn-by-turn mode, Δf is comparable to the revolution frequency. Finally, the lowest bandwidth is required for the closed orbit measurements when only slow beam variations are observed. In this case, the average behaviour over thousands of turns is monitored and a high resolution can be achieved [121].

In order to monitor the structure of individual bunches, a high-bandwidth system is required. The 10% – 90% rise time t_{rise} of the simulated electron cooled bunches is approximately 30 ns and the signal bandwidth can be approximated as $0.35/t_{rise}$ [194]. The Nyquist-Shannon theorem states that the bandwidth used to sample the signal should be at least two times higher than that [194]. It is therefore concluded that $\Delta f > 20$ MHz should be used to properly characterise the structure of the bunches. Assuming only a thermal noise density contribution of 0.1 nV/$\sqrt{\mathrm{Hz}}$, the noise at 20 MHz bandwidth is about 0.5 µV. A SNR greater than 1, where the signal is $\Delta\hat{U}$, is achieved only for $x > 0.6$ mm. However, the noise in the real setup can be 10 times higher [129], thus much worse performance is expected. Nevertheless, the signal from a single electrode is high enough to provide sufficient information on the longitudinal beam profile even at noise 80 times higher. Consequently, the change of the bunch shape due to electron cooling can be followed.

To achieve SNR ≥ 1 at $x = 0.1$ mm, the total noise needs to be smaller than 75 nV. Such a constraint can be satisfied with a low-noise-density system and a narrowband signal processing.

4.3.4 Effect of Noise on the Beam Position Determination

Assuming that the total voltage noise U_{noise} is the main source of position uncertainty and that it is equal for both electrodes, uncertainty σ_x of position x can be calculated as:

$$\sigma_x = \sqrt{\left(\frac{\partial x}{\partial U_1} \cdot U_{noise}\right)^2 + \left(\frac{\partial x}{\partial U_2} \cdot U_{noise}\right)^2}. \tag{4.39}$$

Applied to equation 4.17, where $\Delta U = U_1 - U_2$ and $\Sigma U = U_1 + U_2$, equation 4.39 leads to:

$$\sigma_x = 2 \cdot k \cdot U_{noise} \cdot \frac{\sqrt{U_1^2 + U_2^2}}{(U_1 + U_2)^2}. \tag{4.40}$$

The above expression can be simplified if the beam is positioned in the pick-up centre. In this case, $U_1 = U_2 = \hat{U}$ and the position uncertainty is:

$$\sigma_x(x = 0) = \frac{k}{\sqrt{2}} \cdot \frac{U_{noise}}{\hat{U}}. \tag{4.41}$$

With equations 4.41 and 4.32, it is possible to estimate the minimum number of stored particles required for a given on-axis position uncertainty. The signal estimated in Section 4.3.1 together with the total noise density of 1 nV/$\sqrt{\text{Hz}}$ [129] are assumed. Under such conditions, the minimum number of particles in the USR can be derived as a function of bandwidth. Fig. 4.6 demonstrates it for various expected position uncertainties. The greyed out region corresponds to the intensities unavailable at the USR due to the space charge limit of $2 \cdot 10^7$ particles at 20 keV. With $\sigma_x = 0.05$ mm, the maximum bandwidth that can be used at 1 nV/$\sqrt{\text{Hz}}$ noise density is less than 700 Hz. It corresponds to approximately 25 nV noise.

4.3.5 Mechanical Tolerances and Misalignment

It is important to know the influence of the machining precision on the beam position monitor performance. The pick-up can be manufactured with the tolerances ρ for the diameter and λ for the length. One can investigate a scenario that two adjacent electrodes are produced with the dimensions $l_{left} = l$, $d_{left} = d$ and $l_{right} = l - \lambda$, $d_{right} = d + \rho$, respectively. Following the reasoning from Section 4.2.3, the beam position for the given differences in length and diameter is given as [54]:

$$x' = k \cdot \frac{\Delta U}{\Sigma U} \cdot \frac{2 + \frac{\lambda}{l} \cdot \left(\left(\frac{\Delta U}{\Sigma U}\right)^{-1} - 1\right)}{2 + \frac{\lambda}{l} \cdot \left(\frac{\Delta U}{\Sigma U} - 2\right) + \frac{\rho}{d} \cdot \left(\frac{\Delta U}{\Sigma U} - 2\right)}. \tag{4.42}$$

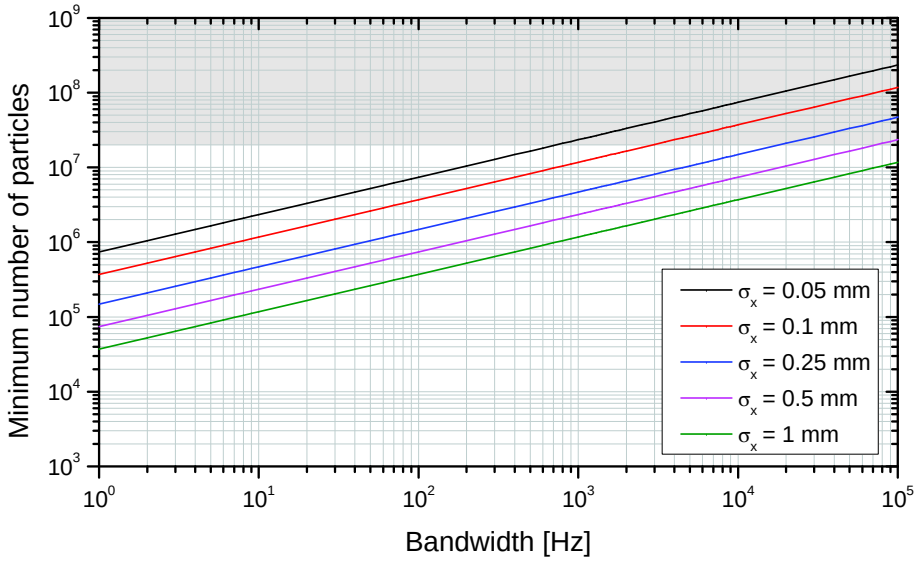

Figure 4.6: The minimum number of stored particles required for different position uncertainties as a function of bandwidth of an analogue signal processing system. See text for details.

The influence of machining accuracy on the pick-up response for the geometry discussed previously, i.e. $l = 100$ mm and $d = 100$ mm, is considered. Assuming reasonable tolerances $\lambda = \rho = 0.1$ mm, the position alteration compared to the perfectly manufactured electrodes, $x' - x$, is 0.025 mm at $x = 0.1$ mm. Although the expected difference is a non-linear function of beam displacement, as shown in Fig. 4.7, the discrepancies are acceptable for small values of x.

A similar calculation can be performed for a rotation of the pick-up by a small angle α around the centre of the monitor. In this case, the expression for the beam position becomes [54]:

$$x' = k \cdot \frac{\Delta U}{\Sigma U} \cdot \frac{1 + \frac{l}{d} \cdot \alpha}{1 - \frac{l}{d} \cdot \alpha}. \tag{4.43}$$

Assuming a pick-up tilt of 1°, the difference in the position measurement compared to the perfectly aligned monitor is 3.5 µm at $x = 0.1$ mm, but increases linearly with the beam displacement to 0.35 mm at $x = 10$ mm. The effect is even stronger for $\alpha = 2°$, where $x' - x = 7.2$ µm and 0.72 mm for $x = 0.1$ mm and 10 mm, respectively. The misalignment caused by rotation does not result in significant discrepancies at small beam displacements, but can be problematic at large values of x as shown in Fig. 4.8

A possible pick-up shift in x and y with respect to the beam axis introduces misalignment errors δ_x and δ_y. They can be measured and incorporated in equations 4.7

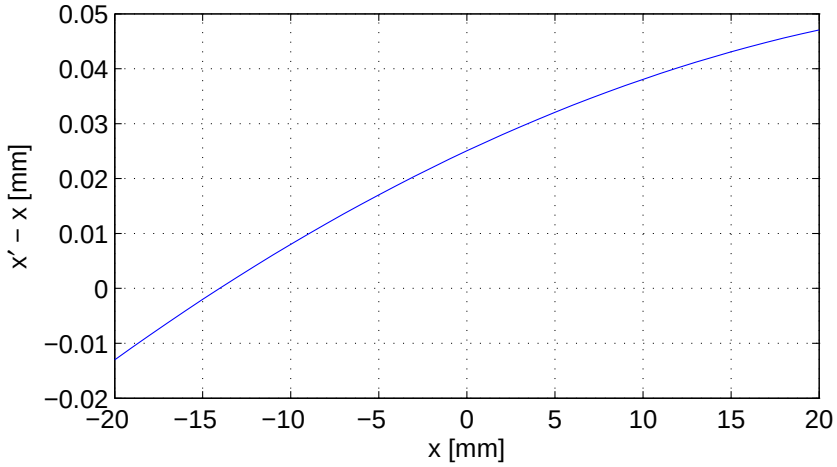

Figure 4.7: Difference in the beam displacement read-out as a function of beam position between a pick-up manufactured with 0.1 mm errors and a perfect monitor. See text for details.

and 4.8 as the offsets of the electrical centre with respect to the geometrical centre:

$$x = k \cdot \frac{\Delta U}{\Sigma U} + \delta. \tag{4.44}$$

4.3.6 Signal Digitisation

A digitisation of the analogue signal at an early stage offers its flexible processing without any future hardware modifications. However, a sufficiently high bandwidth, sampling rate and resolution are required and digitisation-related problems, such as digital noise, spectral leakage and aliasing, should be addressed in the first instance [195–200].

Digital Resolution and Noise

The quantization step size of a signal, or its granularity, depends on the number of bits b and the input voltage range $\pm U_{ADC}$ of an analogue-to-digital converter (ADC) [198,199]:

$$U_q = \frac{2 \cdot U_{ADC}}{2^b - 1} \tag{4.45}$$

The achievable granularity for different numbers of bits and maximum input voltage settings of an ADC is summarized in Table 4.1. As can be seen, the signal amplification should be set to match the voltage range, otherwise the resolution is reduced. Also the highest number of bits is preferred.

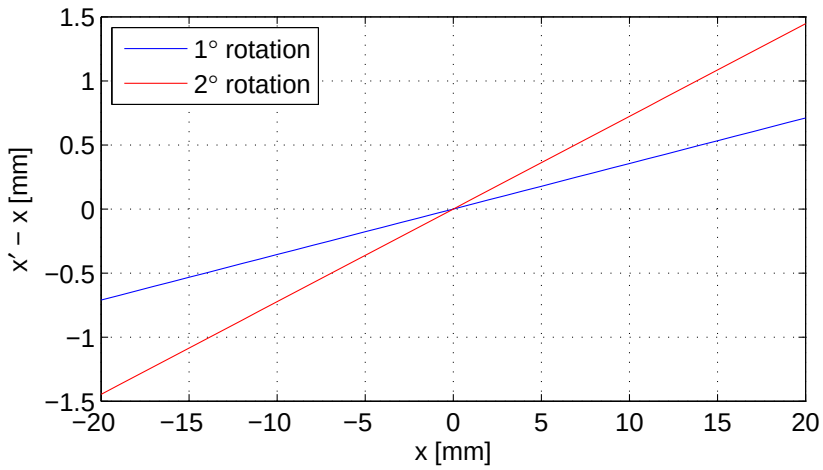

Figure 4.8: Difference in the beam displacement read-out as a function of beam position between a tilted pick-up and a perfectly aligned monitor. See text for details.

	U_{ADC}				
b	±50 mV	±100 mV	±200 mV	±500 mV	±1 V
10-bit	98 µV	0.20 mV	0.39 mV	0.98 mV	2.0 mV
12-bit	24 µV	49 µV	98 µV	0.24 mV	0.49 mV
14-bit	6.1 µV	12 µV	24 µV	61 µV	0.12 mV
16-bit	1.5 µV	3.1 µV	6.1 µV	15 µV	31 µV

Table 4.1: Signal granularity as a function of the number of bits and the ADC input voltage range.

The optimal amplifier gain G is chosen when the maximum signal amplitude U_{max} with the analogue noise is not clipped off by the ADC input range $\pm U_{ADC}$:

$$G = \frac{U_{ADC}}{U_{max}} \tag{4.46}$$

A minimum number of bits can be estimated from $U_{min} \cdot G > U_q$ as:

$$b > \log_2 \left(\frac{2 \cdot U_{ADC}}{U_{min} \cdot G} + 1 \right) \tag{4.47}$$

The above equation assumes that a fixed gain is used to cover a variety of signal amplitudes. With $U_{max} = 700$ µV and its amplification matched to the digitiser input range, a high-resolution system is required. If the beam displacement of 0.1 mm, corresponding to $U_{min} = 75$ nV, is to be detected, then $b > 14.2$ is expected. However, more bits are necessary to be able to properly sample a signal of such an amplitude. A state-of-the art ADC with a sampling frequency larger than $f_{RF} \approx 20$ MHz offers

16 bits at the most. In this case, the theoretical resolution is not better than 25 nV. Nevertheless, a noise contribution of the digitiser is to be expected and also the effective value of b of 16-bit ADCs is usually lower. For this reason, a worse overall resolution should be considered.

To illustrate the performance of a pick-up signal processing system, several parameters of commercially available components are assumed and modelled in MATLAB [201]. They include a low-noise amplifier with 46 dB gain (factor of 200) and a 12-bit ADC with 200 MS/s sampling rate, 20 MHz bandwidth and ±500 mV input range. Furthermore, analogue noise of 1 nV/$\sqrt{\text{Hz}}$ and digitiser input noise of 90 µV are considered. All the values, except the underestimated number of bits, correspond to the nominal parameters of the amplifier and digitiser under consideration and described in detail in Section 4.4.2.

Fig. 4.9 shows the resulting sum signals for both, uncooled and cooled beams. The black curves represent the theoretical pick-up signals without any noise, whereas green points correspond to the digitised noisy samples. Although the proposed gain is too low, the voltages are high enough to be sampled with sufficient resolution. Also the achieved signal-to-noise ratio enables the bunch structure to be observed.

The performance of the system is limited when also the difference signals are to be monitored, demonstrated in Fig. 4.10. Again, the black curves represent the noiseless pick-up signals, whereas the green points correspond to the values sampled by the ADC. Not only is the noise a dominant component seen by the pick-ups, but also is clearly digital in nature at $G = 200$. Consequently, the two charge distributions under consideration cannot be discriminated. However, with the gain increased to cover the full range of the digitiser at the minimum amplitudes, for uncooled ($G = 3200$) and cooled beams ($G = 600$) separately, the problem of digitisation is reduced. In this case, the noise becomes random and uncorrelated and the beam position can be resolved by either limiting the bandwidth, further averaging or both.

Although the useful signals in Fig. 4.10c and 4.10d seem to be lost in noise, it is still possible to recover the required information on the beam position. For closed orbit measurements, the average behaviour of the beam over thousands of turns, depending on its stability and lifetime, can be monitored. Figure 4.11 shows the spectra calculated for the sampled uncooled beam presented in Fig. 4.10c at various acquisition times. After 28 µs, which corresponds to only 50 turns of the 300 keV beam in the USR, a signal peak at the bunching frequency $f_{RF} = 1.78$ MHz can be distinguished from the noise level. However, a longer acquisition time is required to obtain a more accurate

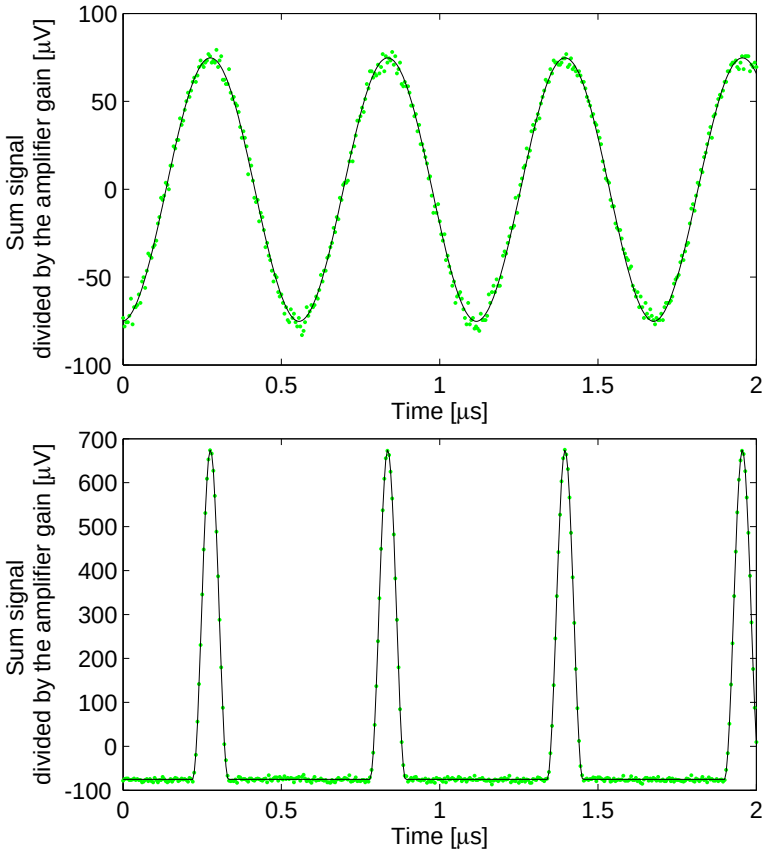

Figure 4.9: Pick-up sum signals divided by the amplifier gain $G = 200$ for the uncooled (top) and cooled beam (bottom) as modelled in MATLAB. See text for details.

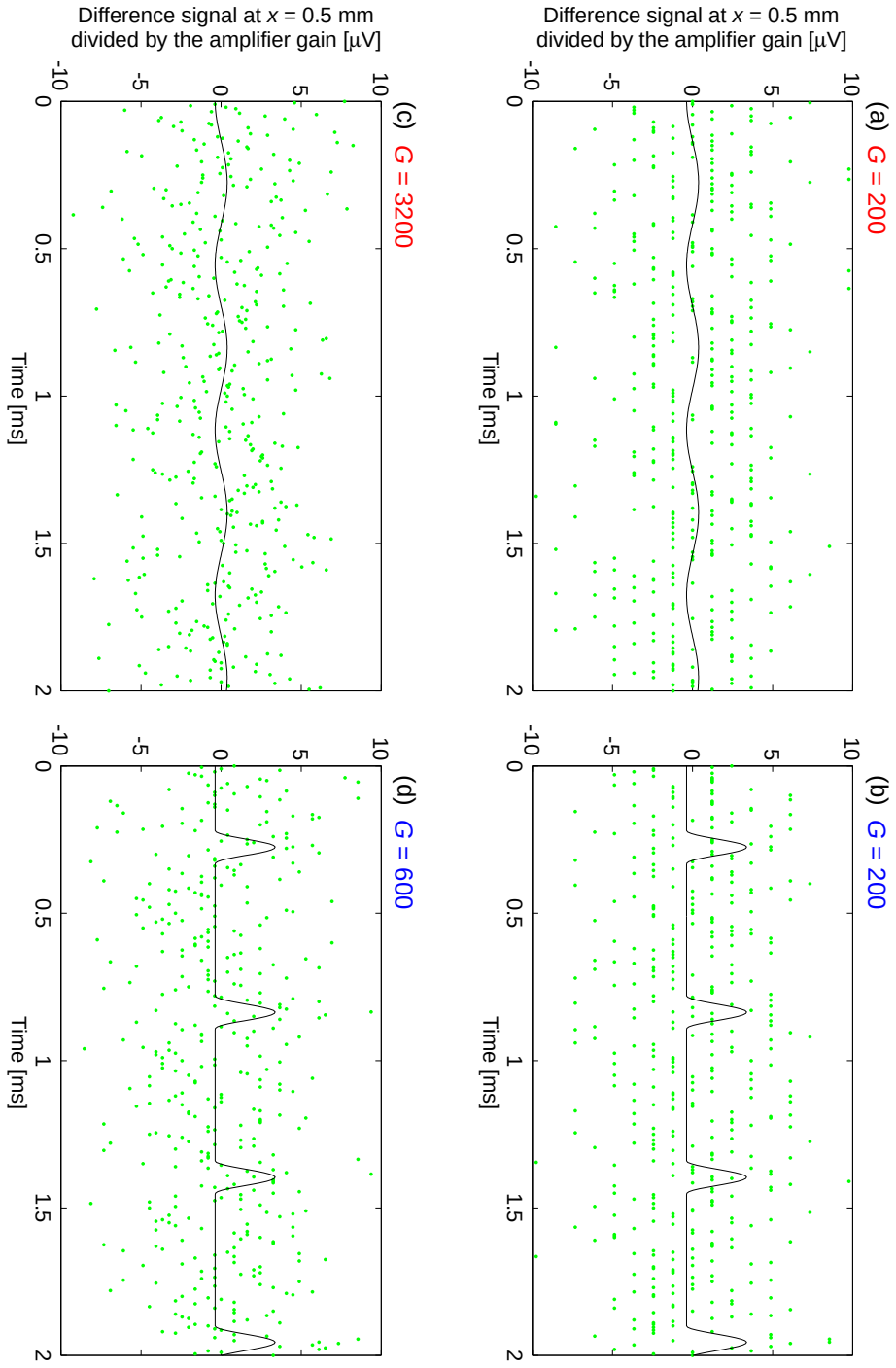

Figure 4.10: MATLAB simulation of pick-up difference signals at $x = 0.5$ mm divided by the amplifier gain: a) uncooled beam at $G = 200$, b) cooled beam at $G = 200$, c) uncooled beam at maximised $G = 3200$, and d) cooled beam at maximised $G = 600$. See text for details.

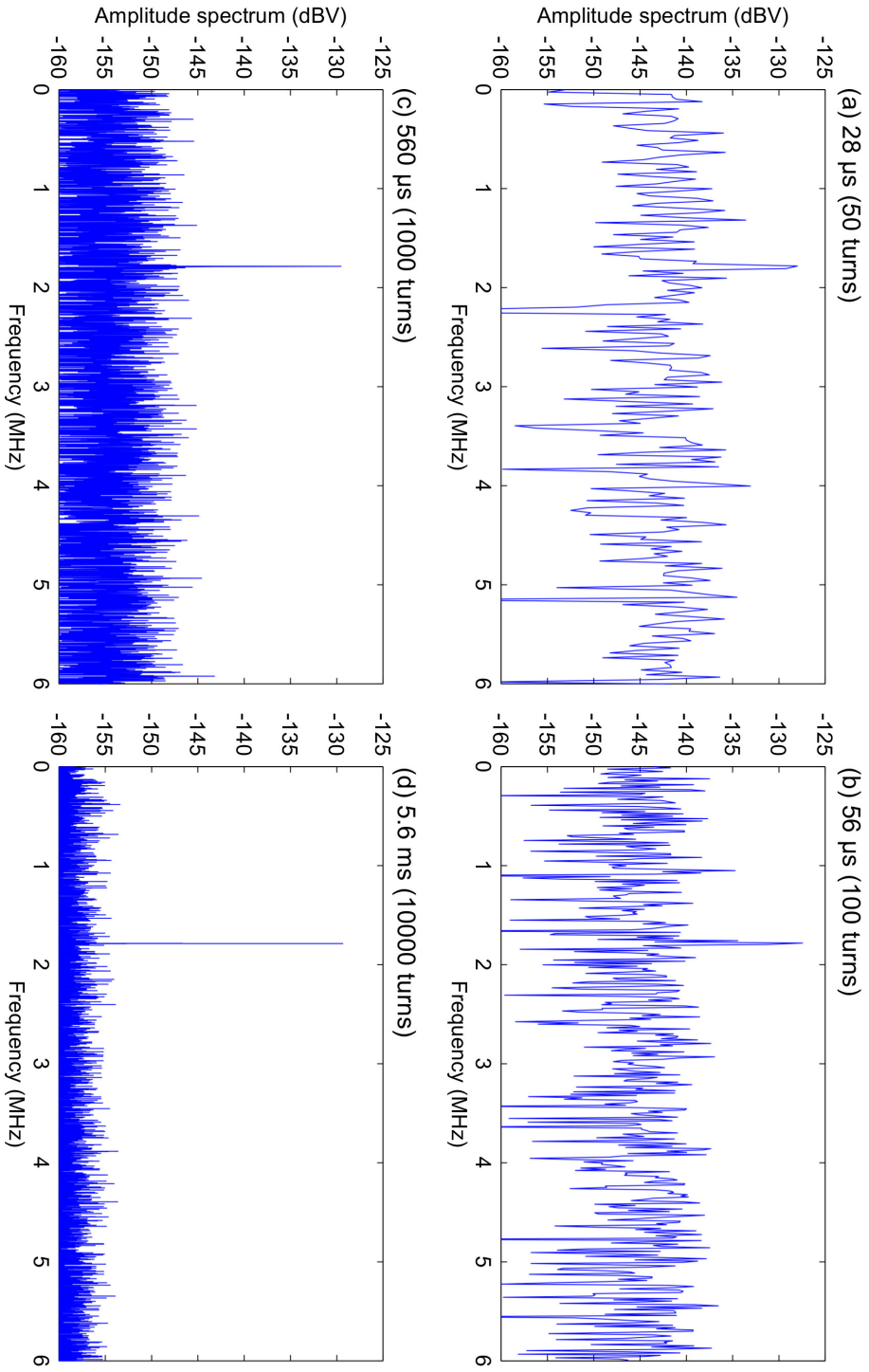

Figure 4.11: MATLAB simulation of spectra for the sampled uncooled beam shown in Fig. 4.10c at various acquisition times: a) 28 µs (50 turns), b) 56 µs (100 turns), c) 560 µs (1000 turns), and d) 5.6 ms (10000 turns).

beam position. The outcome depends on the averaging time and the following graphs in Fig. 4.11 show the results for 56 µs, 560 µs and 5.6 ms which correspond to 100, 1000 and 10000 turns, respectively. The resulting plots are based on the theoretical calculations discussed in the previous sections and do not include the $1/f$ noise. However, it can be filtered out, because only the AC part of the signal is of interest.

Finally, in order to determine the widest bandwidth that can be applied to achieve the expected position monitoring accuracy, the same reasoning applied to create Fig. 4.6 can be used. This time, however, the purely analogue system should incorporate the ADC noise and granularity as discussed above. The resulting minimum number of stored particles required for a given on-axis position uncertainty and bandwidth is plotted in Fig. 4.12. In this case, the performance for the optimum gain of 3200 is analysed. The wide-bandwidth part of the plot reflects the dominant contribution of the analogue noise and reflects the behaviour introduced in Fig. 4.6. However, the bandwidth reduction improves the SNR only up to a certain point where the quantization starts to dominate. For the given conservative assumptions, neither uncertainty of ±0.05 mm nor ±0.1 mm can be achieved.

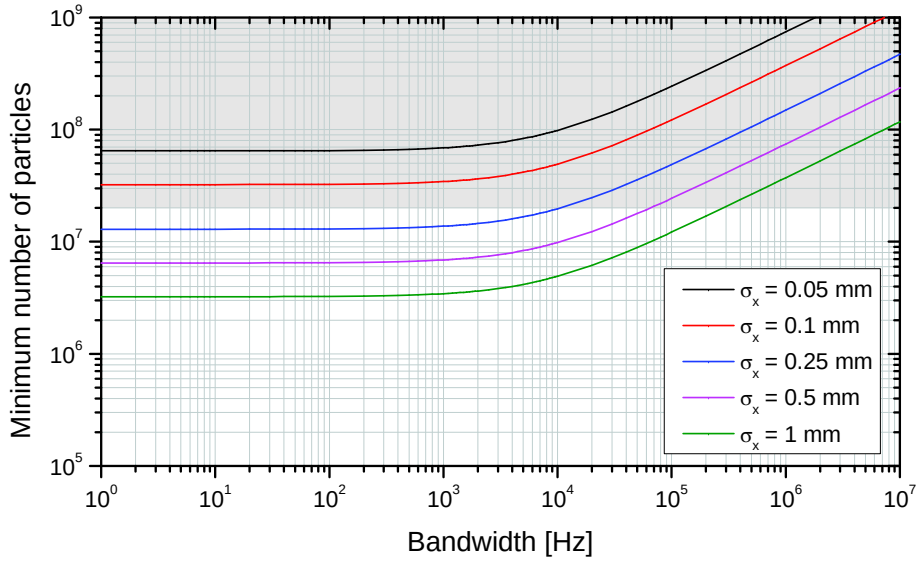

Figure 4.12: The total number of stored particles required for different position uncertainties as a function of bandwidth of a 12-bit digital signal processing system. See text for details.

Spectral Leakage

The frequency spectrum of a signal sampled by a digitiser can be obtained by the use of a discrete Fourier transform (DFT) [199]. The function transforms the measured time series into the discrete frequency domain components:

$$X_m = \sum_{n=0}^{N-1} \left\{ x_m \cdot \left[\cos\left(\frac{2 \cdot \pi \cdot n \cdot m}{N} \right) - i \cdot \sin\left(\frac{2 \cdot \pi \cdot n \cdot m}{N} \right) \right] \right\}, \tag{4.48}$$

where m is the index of the DFT output in the frequency domain, x_n is the sequence of the input samples, n is the time-domain index of x_n and N the number of samples of the input sequence and the number of frequency points in the DFT output [199]. X_m denotes the complex frequency-domain component at frequency:

$$f_m = m \cdot \frac{f_s}{N} = m \cdot \Delta f_s, \tag{4.49}$$

where f_s is the sampling frequency and Δf_s is the bin width of the frequency components. The frequency spectrum amplitudes, denoted by A_m, are expressed as:

$$A_m = \begin{cases} \dfrac{2 \cdot |X_m|}{N} & \text{for } m > 0, \\ \dfrac{|X_0|}{N} & \text{for } m = 0. \end{cases} \tag{4.50}$$

A Fourier transform is applicable to infinite periodic signals, thus a waveform sampled over a finite time is assumed to be a repeatable element of a periodic structure. This is not necessarily the case and the reconstructed signal may contain discontinuities at the margins of the rectangular window repetitions. As a consequence, the signal spectrum comprises artificial frequency components which were not present in the original waveform. This unwanted effect is called spectral leakage [200]. It is present whenever the window width does not correspond to the integer number of the measured signal periods.

In order to eliminate the spectral distortion, one needs to either apply a different window that smooths out the edges of the sampled waveform, or choose the phase and acquisition time of the digitiser accordingly [200]. The first approach does not require any a priori knowledge of the spectrum of the measured signal, but results in the decrease of the frequency resolution depending on the window type and width applied. In order to use the other technique, a well defined frequency and a common trigger have to be available. This is the case of the capacitive pick-up, because the bunches follow the predefined RF frequency. A requirement is, however, that the digitiser provides enough flexibility to choose any arbitrary acquisition time and to set an external trigger.

Aliasing

According to the Nyquist-Shannon theorem [194], a sampling rate f_s of at least twice the highest signal frequency f_{max} is required in order to exactly recover the original waveform:

$$f_s \geq 2 \cdot f_{max}. \tag{4.51}$$

If the condition 4.51 is not satisfied, the signal cannot be properly processed. As a consequence, its frequencies above $f_s/2$ appear folded into the low frequency component region. The distortion is known as aliasing and is irrevocable, thus either a sufficiently high sampling rate or low-pass filtering is required.

In the case of the USR, the frequency spectrum of the signal is known and both methods can be applied to avoid aliasing. The bandwidth of the simulated electron cooled bunches can be approximated as 0.35 of its rise time [194] and corresponds to about 10 MHz. It is therefore concluded that a sampling frequency > 20 MHz should be used. In addition, a low-pass filter can be applied to eliminate high-frequency noise which could be artificially reflected in the sampled signal.

4.4 Technical Design and Construction

4.4.1 Mechanical Design

A 3D model of the pick-up as well as 2D computer-aided design (CAD) drawings were created with Solid Edge [202]. A prototype of the monitor is shown in Fig. 4.13. It is a cylindrical device with diagonally cut electrodes and additional separating rings to reduce the parasitic coupling C_c. The electrodes and rings are made of non-magnetic stainless steel, whereas the outer shield is made of aluminium to reduce the overall weight of the monitor. The pick-up is installed in a vacuum vessel with appropriate SMA feedthroughs for signal transmission from vacuum.

The diagonally cut electrodes are 100 mm in length and 100 mm in diameter, whereas the dimension s, shown in Fig. 4.2, is 3.5 mm. The separating rings were introduced between them in order to reduce the influence of the coupling capacitance [203]. The rings can be grounded or removed from the setup. Their length is approximately 13 mm and the inner diameter matches that of the electrodes. The spacing between the rings and the electrodes is 2 mm.

The outer shield is to ensure shielding against electromagnetic noise. It is on a separate “clean” ground and is electrically isolated from the vacuum vessel in which

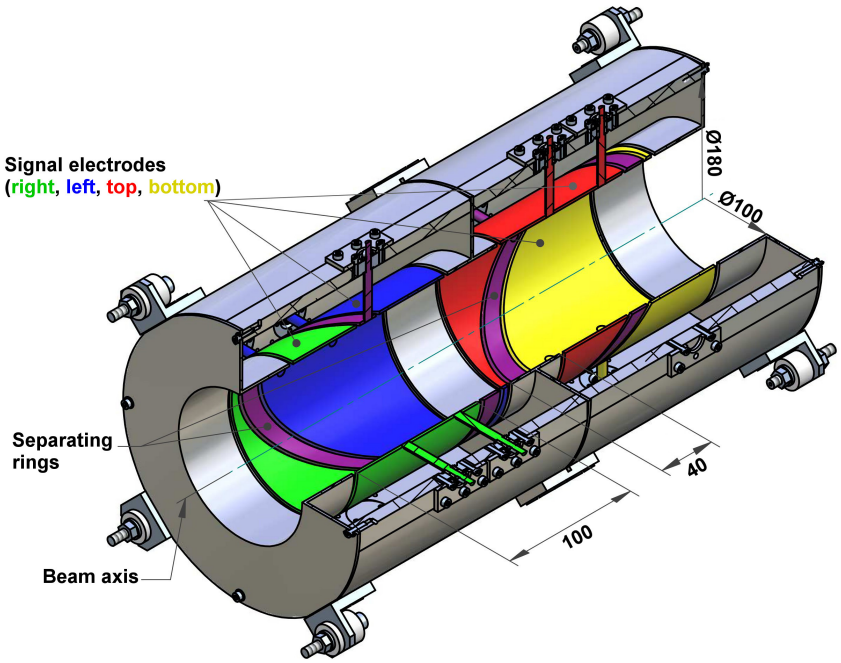

Figure 4.13: A cross-section view of the diagonally cut pick-up.

the monitor is installed. Its inner diameter is 170 mm and the total length is 376 mm.

In order to avoid distortion of the electric field in the vicinity of the monitor edges, the inner diameter of the pick-up, 100 mm, is the same as the one of the USR beam pipe. In addition, grounded rings are introduced at both ends and in the middle of the monitor. The outer ones minimize the effect of the transition between the pick-up and the vacuum chamber walls, whereas the inner reduces the coupling between x and y planes. As a rule of thumb, guard rings of length equal to the beam tube diameter eliminate unwanted distortions [204]. However, the length was limited to 40 mm in order to preserve space in the USR. With such a configuration, the theoretical discrepancies introduced by the boundary conditions are less than 2% for the scaling factor and less than 0.2 mm for the electrical centre displacement [204].

The pick-up vacuum vessel consists of a custom-made chamber and two reducer flanges DN250 to DN100. Its total length is approximately 450 mm. The inner diameter of the main chamber is 250 mm. There are four uniformly distributed DN16 flanges welded on the sides of the chamber for the SMA feedthroughs. In addition one more flange, also DN16, is introduced for the BNC feedthrough in order to provide a “clean” ground for the pick-up shield. Fig. 4.14 shows a cross-section view of the vessel together

with the pick-up in place.

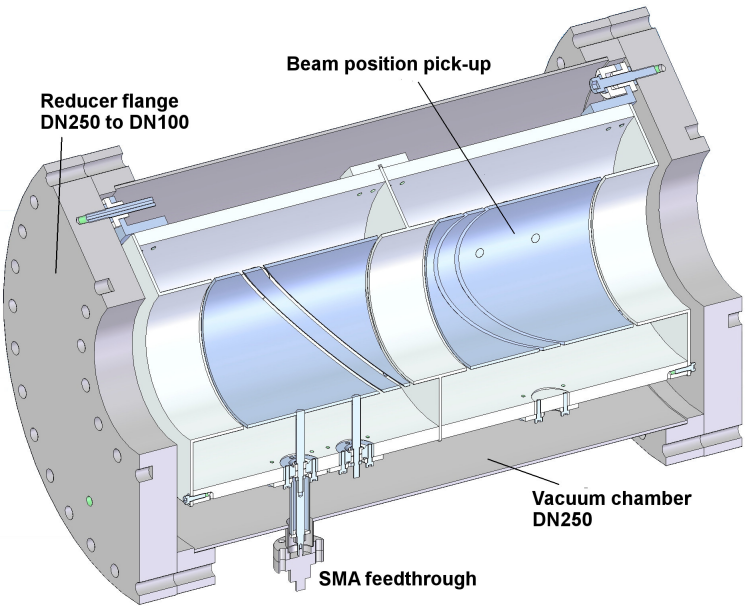

Figure 4.14: A cross-section view of the pick-up installed in the vacuum vessel.

4.4.2 Electronics and Signal Processing

A schematic drawing of the signal read-out system is shown in Fig. 4.15. The pick-up signal is coupled via a high input impedance amplifier and passed to a low-pass filter before digitisation. The analogue filtering is optional because the signal frequency range is much smaller than the sampling rate of the ADC. Nevertheless, it can be useful in the case of a high-frequency distortion of the signal resulting in artificial frequencies due to aliasing. The processing and beam position determination are then performed in a digital domain by a customized LabVIEW application.

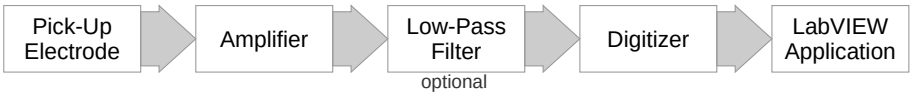

Figure 4.15: A diagram of the signal read-out chain for a single pick-up electrode.

Amplifiers

The signals generated on the electrodes are fed to the low-noise, high input impedance amplifiers installed directly on the vacuum feedthroughs.

For its best performance, a commercial amplifier SA-220F5 from NF Corporation was chosen. It offers 1 MΩ input impedance with 57 pF parallel capacitance, 0.5 nV/$\sqrt{\text{Hz}}$ input referred noise voltage density at 10 kHz – 1 MHz, and 200 fA/$\sqrt{\text{Hz}}$ noise current density at 100 kHz. The amplifier gain of 46 dB at 1 MHz corresponds to the amplification factor of 200. Its frequency range from 300 Hz to 100 MHz is more than enough for the USR signals. For the given parameters, the corresponding thermal and current noise densities contributing to equation 4.36 are 0.1 nV/$\sqrt{\text{Hz}}$ and 0.2 nV/$\sqrt{\text{Hz}}$, respectively at $f_{RF} = 1.78$ MHz. The total noise density is therefore 0.6 nV/$\sqrt{\text{Hz}}$ for the 300 keV beam. At $f_{RF} = 459$ kHz, the performance drops down due to a slightly higher value of $|Z|$, see equation 4.37. In this case, $e_{th} = 0.5$ nV/$\sqrt{\text{Hz}}$ and $i_{amp} \cdot |Z| = 0.8$ nV/$\sqrt{\text{Hz}}$, thus the total noise density is about 1 nV/$\sqrt{\text{Hz}}$ for the 20 keV beam.

The limited gain of the NF units can be compensated by adding an additional amplifier at the output. Such a solution would not sacrifice the SNR because it is determined by the first stage amplification and no large noise contribution of the second stage is to be expected. Due to a high price, however, only two NF amplifiers were procured for the pick-up tests.

An alternative solution was a custom-made amplifier prepared at the Manne Siegbahn Laboratory (MSL) in Stockholm [205]. Two units were provided for the experiments with the pick-up. The amplifier bandwidth is limited to 1.3 kHz – 10 MHz and the gain of 54 dB corresponds to the amplification factor of 500. It offers 5 MΩ input impedance with 30 pF parallel capacitance, and 0.9 nV/$\sqrt{\text{Hz}}$ input referred noise density. No voltage and current noise components were measured separately. The total noise density is therefore 0.9 nV/$\sqrt{\text{Hz}}$ for the 300 keV beam and 1 nV/$\sqrt{\text{Hz}}$ for the 20 keV beam.

Low-Pass Filters

Before digitisation, the amplified signals can be filtered to remove high-frequency components from their spectra. Although optional, such an approach eliminates unwanted noise in the high-frequency range and prevents aliasing distortions. In order to observe the full bandwidth of the bunches, a cut-off frequency of about 20 MHz is chosen.

Alternatively, a lower cut-off of approximately 2 MHz can be used to pass only the fundamental frequency of the signals. Either way, it has been demonstrated that a narrowband signal processing with $\Delta f < 1$ kHz is required and it needs to be implemented in the digital domain.

Two models of analogue filters from Mini-Circuits were chosen to meet the project needs and their parameters are summarised in Table 4.2. The passband is defined for the frequencies at which the losses are less than 1 dB, whereas the stopband frequencies are given for losses > 20 dB and > 40 dB. The so called voltage standing wave ratio (VSWR) is defined as:

$$\text{VSWR} = \frac{|V_{inc}| + |V_{ref}|}{|V_{inc}| - |V_{ref}|}. \tag{4.52}$$

where V_{inc} and V_{ref} are the amplitudes of the incident and reflected voltage component of a standing wave in a transmission line [206].

	Passband [MHz]	Cut-off [MHz]	Stopband [MHz]		VSWR	
Model	< 1 dB	3 dB	> 20 dB	> 40 dB	pass.	stop.
SLP-2.5	DC - 2.5	2.75	3.8–5.0	5.0–200	1.7:1	18:1
SLP-21.4	DC - 22	24.5	32–41	41–200	1.7:1	18:1

Table 4.2: Parameters of two commercially available low-pass filters selected for the pick-up system.

Digitiser

The signals are digitised by GaGe Razor CompuScope CS1642, a commercial digitiser equipped with 4 channels in a single-slot PCI with 128 MB of on-board acquisition memory. It offers 16-bit resolution with 125 MHz bandwidth and up to 200 MS/s sampling rate per channel. The input range is software-selectable between ±100 mV, ±200 mV, ±500 mV, ±1 V, ±2 V and ±5 V at 50 Ω. The RMS noise at ±100 mV and ±500 mV input ranges is 50 μV and 90 μV, respectively. The digitiser was provided with a software development kit for LabVIEW [207, 208].

LabVIEW Application

The amplified analogue signals are digitised after passing the low-pass filters and the processing is performed in the digital domain. A LabVIEW application was prepared to control the digitiser and to display, analyse and save the signals from the pick-up electrodes. The LabVIEW-based graphical user interface (GUI) is shown in Fig. 4.16.

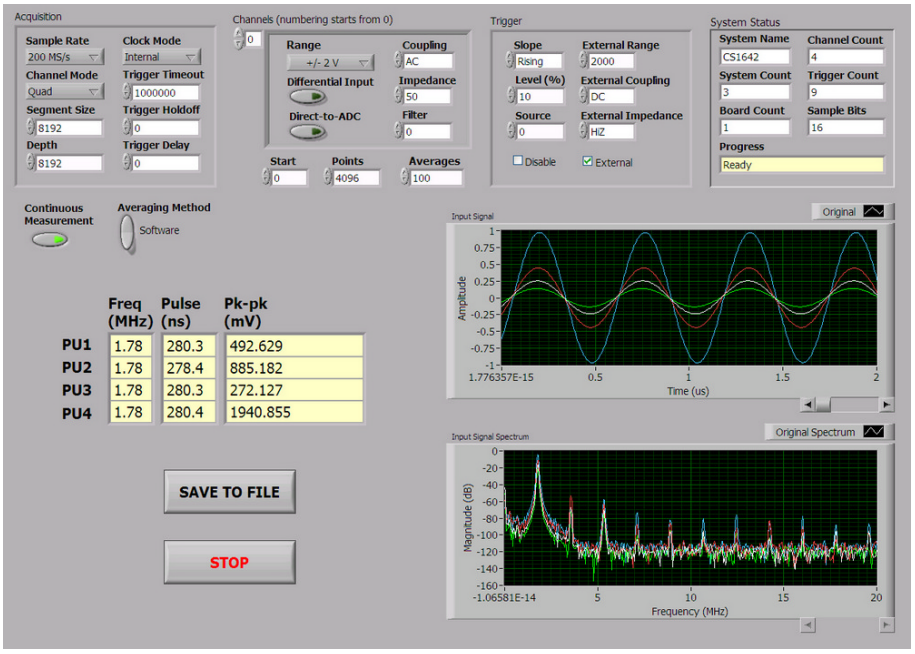

Figure 4.16: GUI of the pick-up prototype test stand application.

The application enables the control of the acquisition mode of the digitiser. The user can choose the sample rate of up to 200 MS/s and the number of channels to be monitored. The digitiser clock can be set in one of the three available modes: an internal one which uses the built-in internal sampling oscillator, an external one if such is connected to the relevant input, and a reference clock which uses a 10 MHz external clock signal to synchronise the internal sampling oscillator. Further settings enable the choice of the segment size and depth. The first one controls the total amount of memory allocated to the acquisition, whereas the latter is the number of samples to acquire after the trigger event. The maximum possible amount of pre-trigger data that can be acquired, therefore, is (Segment Size – Depth). The trigger time-out and hold-off are, respectively, the time in microseconds to wait before forcing a trigger event, and the time in samples during which trigger events will be ignored after the digitiser begins acquiring and awaiting a trigger event. The latter is useful for ensuring the accumulation of a specified amount of pre-trigger data that is equal to the Trigger Holdoff value. Finally, the trigger delay is the time in samples between logging of the trigger event and beginning of the count-down of the post-trigger depth counter. It can be useful for waveforms in which the signal feature of interest occurs long after the trigger event. In addition, it is possible to choose the acquisition to be either continuous

or single and whether the averaging method applied is software- or hardware-based, if supported [207, 208].

Further functionality of the LabVIEW application covers the control of the input channels and trigger settings. The channels acquire information from pick-up electrodes and are numbered from 0 to 3. They can be configured independently and it is possible to set their input voltage range, type of coupling and either 1 MΩ or 50 Ω impedance expressed in Ohms. For hardware that supports it, the application enables also the choice of the Differential Input and Direct-to-ADC modes [207,208]. The trigger control box offers options which include the slope type, either rising or falling, the level between ±100% and the source type as well as the external range, coupling and impedance. The source is an integer which sets the channel trigger source and is used if both the External and Disabled checkboxes are not selected. For the external trigger, its full scale range needs to be chosen in millivolts. External Coupling can be set to either DC or AC, whereas the Slope to either "rising" or "falling".

The application displays the status of the system as well. It includes the model name of the digitiser, number of available input channels, systems and boards in the active system as well as the number of trigger engines in the active system. The Sample Bits display shows the vertical resolution of the hardware.

In addition, two variables determine which captured data should be processed further. Start is the point from which to start, whereas Points is the number of points to transfer. Both variables define the window which is used for the signal processing and should be chosen accordingly to prevent spectral leakage.

The application displays the acquired signals in real time in both the time and frequency domain. The latter is obtained by applying a Fourier transform to the sampled signal. The bunching frequency, pulse length and peak-to-peak voltage are also calculated in real time and displayed for all four pick-up signals. The values can be saved to a file at any time.

The recorded waveforms can be averaged over a specified number of acquisitions. Because the averaging gives sufficiently accurate results for the prototype tests, no additional filtering is performed. Should the implemented method be insufficient for the real signals, the LabVIEW code can be easily extended to incorporate a narrowband filtering.

Because the GUI was prepared only for the prototype tests and calibration, no beam position is displayed by the system. However, all the variables necessary to calculate the difference and sum of the signals are available and their ratio can be related to the

beam position by the predefined scaling factors.

4.5 Experimental Tests with a Current-Carrying Wire

It is not straightforward to calibrate the response of a beam position monitor. It could be tested in an accelerator with a beam of similar parameters that the pick-up has been designed for, but it requires high flexibility and accuracy of the beam steering and positioning. Furthermore, a repetitive series of measurements for a large number of monitors would be impractical if all of them were to be verified and tested in the accelerator environment. For these reasons, an alternative technique needs to be found for a reliable commissioning of the position pick-up prototype.

The most common approach is the use of a current-carrying wire stretched inside the device under test [209]. Such a wire simulates the presence of a real particle beam. The technique can be used in a simple bench setup independently from the high-vacuum environment and limited beam time at an accelerator. The stretched-wire inside a monitor corresponds to a coaxial cable in which only the transverse electromagnetic (TEM) waves propagate, i.e. there is no component of the electric and magnetic fields in the direction of propagation of the wave [210]. This limits the use of the method to ultra-relativistic beams, because the longitudinal component of the electric field does not vanish at low beam velocities. However, as discussed in Section 4.3.2, the low-β corrections for the USR beams are negligible. The current-carrying wire technique should, therefore, be a reliable tool for experimental testing of the pick-up performance as well as benchmarking more complex simulations.

4.5.1 Experimental Setup

The pick-up assembly introduced in Fig. 4.14 was mounted vertically on a test stand as shown in Fig. 4.17. Both the flanges to which the pick-up was fixed in the vacuum vessel had been manufactured with outer reference holes to mark the alignment of the monitor inside. Two manual translation stages with 100 mm movement range were stacked in an xy configuration and then fixed on top of the setup in order to move a wire within the pick-up aperture.

An insulated 0.2 mm diameter wire was used as a signal carrier. It was stretched with an added weight which was freely dipped in a dense fluid to damp any potential swing motion of the wire caused by its movement to a new position. One end of the wire was connected to a signal generator and the other to an oscilloscope to observe

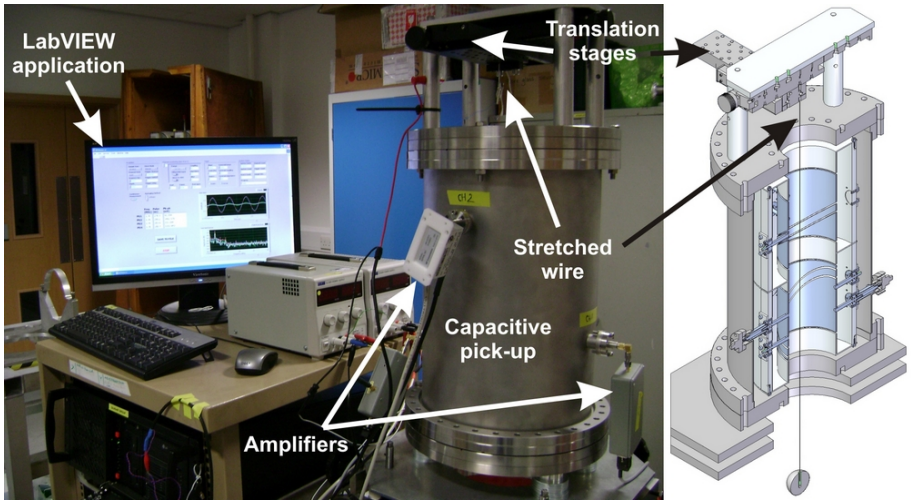

Figure 4.17: The current-carrying wire test stand with the prototype pick-up.

the signal delivered to the pick-up.

Sine-wave signals with frequencies of 459 kHz and 1.78 MHz were generated in the wire so that the response of the pick-up to the USR bunch frequencies could be tested.

It was important to properly align the wire and the beam position monitor. While the alignment of the wire was determined by gravity, the pick-up vessel was installed on three levelling screws enabling the adjustment of its position with respect to the wire. Also additional components, shown in see Fig. 4.18, were manufactured to define the main axes of the monitor and to match them with the axes of the translation stages. The x and y faces of the alignment tools were used to verify if the wire had been set perpendicular to the main axes and to position it coaxially with the pick-up.

4.5.2 Results with the Current-Carrying Wire

Sensitivity and Linearity

The pick-up was tested in two different configurations. At first, it was examined with the grounded separating rings included in the diagonal gaps between the electrodes. Later, the rings were removed and the measurements were repeated.

The sensitivity of the pick-up to beam displacement was recorded in terms of $\Delta U/\Sigma U$ along the main monitor axes. The response of the pick-up was linear in the tested range of ± 40 mm as shown in Fig. 4.19 for the x-axis example.

The presence of the separating rings and their electrical connections had a significant impact on the results. A higher position sensitivity was observed for the configuration

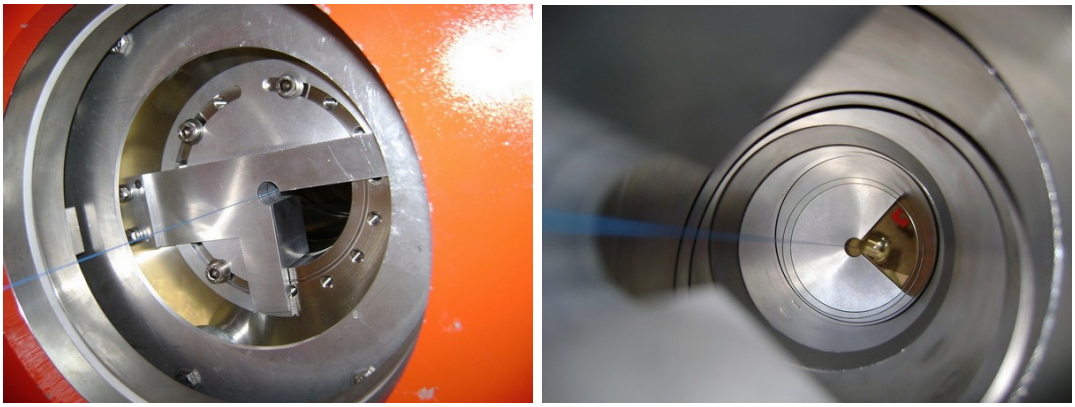

Figure 4.18: The pick-up with additional components temporarily attached to align the monitors and position the wire in its centre.

with the rings and it was almost 20% higher than for the setup without the rings. On the other hand, the relative voltage measured for no rings was higher by about 20% as compared to the pick-up with the rings added. This can be explained by an increased capacitance C introduced by the rings and the fact that the measured signal $U \propto 1/C$, see equation 4.6. There is, therefore, a trade-off between the decoupling of the pick-up electrodes and their detection sensitivity.

Table 4.3 summarises the obtained scaling factors k together with the determined offsets δ_x and δ_y of the electrical centre with respect to the geometrical centre. The values of k for a given monitor configuration were the same for x and y axes within less than 1%. They were also independent from the chosen frequencies. The uncertainties in k correspond to position uncertainties of the order of 0.1 mm. The electrical offsets were zero within an uncertainty of 0.1 mm for the setup with the separating rings, whereas they became non-negligible for the pick-up without the rings. This is consistent with the similar comparison reported in other studies [203] and may be caused by a higher coupling between the opposite electrodes when no separating ring is present. The diagonal cut configuration is not symmetric with respect to the beam arrival time and this may be reflected in the measurements. However, the determined beam position can be corrected for the reported values.

Signal, Noise and Position Resolution

The current-carrying wire technique did not provide information on the lowest detectable signals. The overall length of the unshielded wire, reflections, parasitic capac-

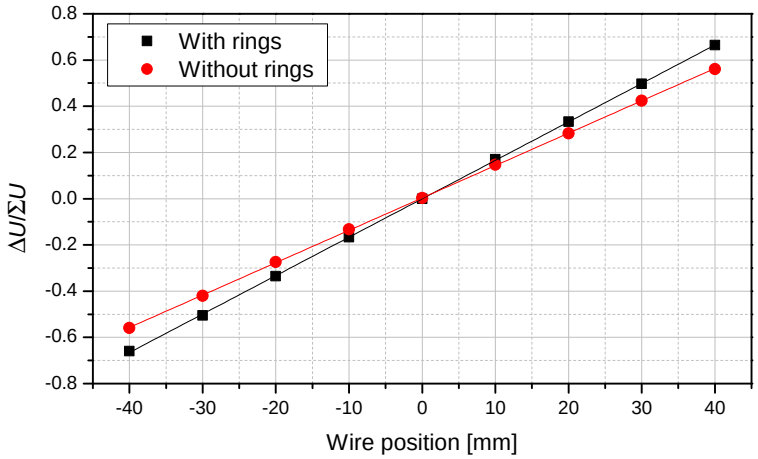

Figure 4.19: The pick-up response to the wire displacement in x axis with and without the separating rings. Uncertainties are smaller than the data points.

	With rings	Without rings
k_x [mm]	59.8 ± 0.1	71.5 ± 0.1
k_y [mm]	60.3 ± 0.3	70.8 ± 0.5
δ_x [mm]	–0.1 ± 0.1	–0.3 ± 0.2
δ_y [mm]	0.1 ± 0.1	–0.4 ± 0.2

Table 4.3: Scaling factors and offsets of the electrical centre in x and y for the pick-up with and without the separating rings.

itance and resistance had a considerable influence on the noise level. Because of the dominating character of the noise introduced by the wire setup, the technique could not be used to investigate the detection limits of the position monitor.

Despite the limitation, it is possible to provide more accurate estimates of the expected performance of the pick-up. The initial signal and noise calculations in Sections 4.3.1 and 4.3.3 were made without any prior knowledge of the final monitor design and can be verified. As indicated by equation 4.6, the pick-up signal depends on its capacitance to ground. In principle, it could have been measured with an LCR meter, but the method was neither very accurate nor reliable. A variation of 20% in the observed values was present, perhaps due to grounding problems, but it could not be improved. It is also not trivial to measure the capacitance of a single electrode without the coupling effects between different pick-up components. However, the upper limit of the capacitance to ground can be estimated to 80 pF for the setup with the separating ring in place. Therefore, the expected signals can be 20% higher than indicated in Section

4.3.1. All the relevant variables, such as gain or ADC input range, need to be scaled accordingly by the same factor. Also the measured value of scaling factor k is lower than assumed previously, which means that a higher difference signal can be assumed. Consequently, the expected sum and difference signals are approximately $\Sigma\hat{U} = 95$ µV and $\Delta\hat{U} = 1.6$ µV/mm. At the same time, the expected noise was confirmed to be about 1 nV/$\sqrt{\text{Hz}}$.

Although higher signals are expected, the overall performance of the system is improved only slightly, because the limiting factor is the digital resolution. The newly calculated amplitudes should be amplified by a lower gain not to be clipped off by the input range of the digitiser. Consequently, the digitised values are the same as indicated in Section 4.3.3. The number of bits $b = 12$ assumed previously corresponds to a beam position uncertainty of ±0.2 mm. With an effective $b = 14$, the uncertainty decreases to ±0.1 mm in the centre of the beam tube. This was confirmed experimentally with the stretched-wire. Additional position determination errors can occur depending on the accuracy of the pick-up installation in the beamline. These, however, can be measured and corrected for.

An improved performance can be achieved by pre-processing signals before feeding them into the digitiser. A customised analogue system can be included prior to the amplifiers to generate sum and difference signals. This way, different gains can be applied to exploit the full ADC range for various input amplitudes. Such a solution, however, offers less flexibility than a fully digitised system. Nevertheless, it can be implemented at a later stage to optimise the monitor performance for an existing machine.

4.6 Simulations of Particle Beams

In order to test the response of the pick-up to particle beams at various velocities, a 3D model of the monitor was created in CST Particle Studio [211]. The code is a part of CST Suite, a general-purpose electromagnetic simulator based on the Finite Integration Technique (FIT) and Perfect Boundary Approximation (PBA) algorithms [212–215]. The solving method requires discretisation of the entire calculation volume, thus the simulations are limited by the complexity of the structure. Particle Studio itself specializes in 3D computations of the charged particles dynamics. It offers several different solvers applicable to various problems and the wakefield simulator is the most appropriate for pick-up response modelling. Wakefield problems are calculated in the time domain and are driven by a bunch of charged particles. The electric field belonging

to the particle beam couples to the pick-up electrodes which leads to measurable signals at the predefined output ports [215].

A 3D model of one pair of the pick-up electrodes created in Particle Studio is shown in Fig. 4.20. Two position monitor geometries were simulated; one including the separating ring and one without it. The background and pick-up material was set to perfect electric conductor (PEC), whereas the volume in which the beam was travelling was chosen as vacuum. The beam was defined in the z direction with β either 1 or 0.025. The beam-induced pick-up voltages were measured at two discrete ports located at the end of the electrodes feedthroughs. The ports were defined as lumped elements with parallel 1 MΩ impedance and 57 pF capacitance corresponding to the input of the NF amplifier. Finally, a symmetry in the plane of the beam movement was applied to reduce the simulated volume, and so the number of mesh cells and simulation time, by a factor 2.

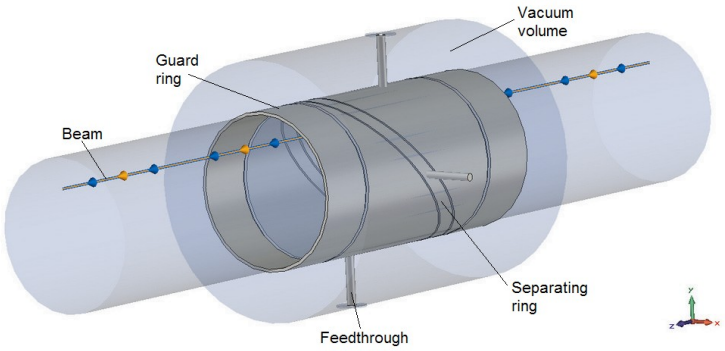

Figure 4.20: A 3D model of the pick-up monitor as simulated in CST Particle Studio.

The simulations require discretization of the calculation volume. Because only a Cartesian (hexahedral) mesh type is available in Particle Studio, the diagonal elements and round edges in the pick-up make the meshing non-trivial. On one hand, the finer model features had to be represented accurately enough to make the results independent from the meshing size and type. On the other, a larger number of small mesh cells results in long simulation times lasting hours or days per run, making the optimisation of the monitor response to different beam positions with Particle Studio impractical.

Particle Studio enables simulations of electromagnetic fields from beams travelling at velocities much smaller than the speed of light, but such problems become complex and sometimes cannot be solved. The main limitation comes from the fact that the computation time increases with decreasing β value. This is because the particle bunch

needs to be sent from outside the simulated structure, so that no corresponding fields are present in the modelled volume at time $t = 0$. At $\beta = 1$, the field lines are perpendicular to the beam and the pulse can be located just at the entrance to the pick-up structure. At $\beta \ll 1$, the computed volume needs to be significantly extended outside the defined model in z direction. Not only can it lead to an excessive number of mesh cells, but also make the algorithm fail to find a stable step size required to perform the calculations.

The influence of the mesh size on the simulation accuracy was tested. Initially, only the global mesh properties were defined, including the minimum mesh size of 0.5 mm and the maximum size of 5.5 mm, resulting in the final number of mesh cells of about $3 \cdot 10^5$. Later, the simulation accuracy was improved by changing the global maximum mesh step to 9.4 mm, but limiting it locally to 0.4 mm in the volume containing the beam and pick-up electrodes. The resulting total number of mesh cells was $8 \cdot 10^6$. It should be noted that the total number of cells is provided for $\beta = 1$ and no additional information on the hidden cells in the extended region at $\beta \ll 1$ is reported. The results obtained for different mesh settings at $\beta = 1$ and the pick-up without the separating ring are shown in Fig. 4.21. The scaling factors obtained are 70.1 mm $\pm$ 0.1 mm for the finer mesh size and 73.5 mm $\pm$ 0.7 mm for the coarser mesh. The values differ by about 4% which corresponds to a position error of less than 0.4%. In absolute values, it is about 0.16 mm for the beam positioned $x = 40$ mm away from the reference axis and only 0.02 mm at $x = 5$ mm.

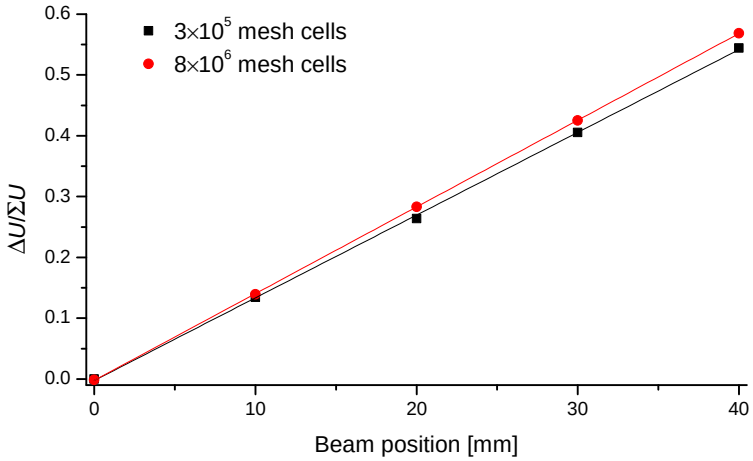

Figure 4.21: The pick-up response as calculated for different mesh settings at $\beta = 1$. See text for details. Uncertainties are smaller than the data points.

The results obtained for the finer mesh were compared with the measurements. As can be seen in Fig. 4.22, the response of the pick-up with and without the separating rings was accurately reproduced. The simulated values of scaling factors and centre offsets are summarised in Table 4.4. The agreement in k with the experimental data is better than the difference of 1% between the measurements in x and y themselves. The offsets are smaller in simulations by about a factor 3, which can be due to less accurate mechanical positioning of components in the pick-up assembly. However, the presence of the separating ring reduces the centre offset by a factor of 4 as it was observed also in experimental data. Although the geometry of the model was simplified compared to the real pick-up design, the agreement proves the current-carrying wire technique is a good approximation of bunches travelling at $\beta = 1$.

	With rings	Without rings
k [mm]	60.4 ± 0.05	70.1 ± 0.1
δ [mm]	0.03 ± 0.02	0.15 ± 0.04

Table 4.4: The scaling factor and offset of the electrical centre for the pick-up with and without the separating rings simulated with Particle Studio at $\beta = 1$.

The final step was to reduce β from 1 to 0.025 and test the response of the pick-up to the USR beams. Unfortunately, the finer mesh size could not be used, because the algorithm was abnormally terminated without any relevant information on the cause of the error. It could be due to a failure to find a stable calculation step size or a limit of the total number of mesh cells that can be simulated. Nevertheless, the simulations were successfully executed for the coarser mesh. Still, the time needed to compute the pick-up voltages for each beam position was about 1 day on a PC with 3.2 GHz CPU and 64 GB of RAM. In order to avoid small structures and gaps in the model which could have been improperly represented by the chosen mesh, only the pick-up without the separating ring was investigated. The results were compared with the simulations for $\beta = 1$ and are shown in Fig. 4.23. The observed difference in the calculated values of k is smaller than 0.03%. Although the result seems to confirm the conclusion made in Section 4.3.2 that low-β effects can be neglected at the USR, it is more reasonable to assume the mesh size was insufficient to properly model the response of the pick-up. The outcome of the final simulation should be taken with care, because it is very likely the mesh size was inappropriate to properly represent the behaviour of the system under investigation. Unfortunately, it was not possible to perform more accurate calculations.

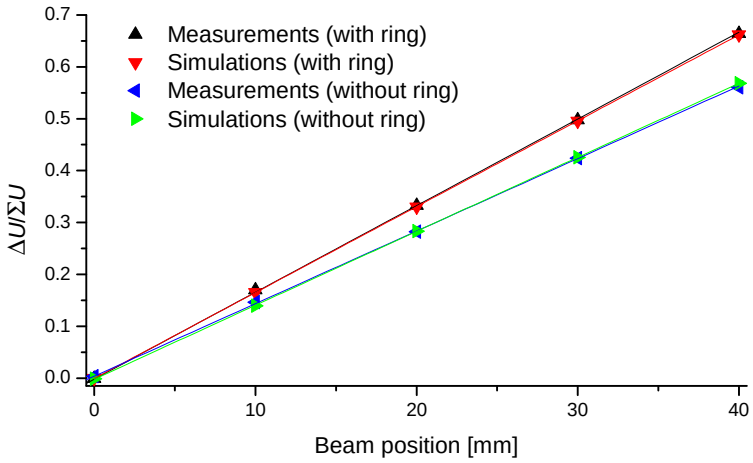

Figure 4.22: Comparison of the pick-up response with and without the separating rings, measured with the current-carrying wire and simulated with a ultra-relativistic bunch in Particle Studio.

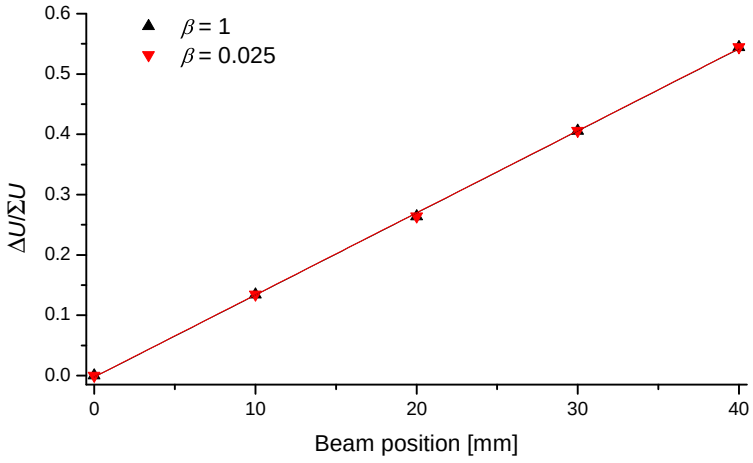

Figure 4.23: Comparison of the simulated pick-up response at $\beta = 1$ and 0.025 for a coarse mesh size.

4.7 Summary and Perspectives

A prototype of a capacitive pick-up for non-destructive beam position measurements in the USR was designed, built up and successfully tested. All the aspects of the monitor development were covered, including theoretical studies, computer simulations and optimisation towards the envisaged application, technical design and experimental verification.

The main motivation for the performed work was to provide a reliable monitor for closed-orbit measurements with low-energy, low-intensity antiproton beams. A capacitive pick-up is the device of choice for position measurements due to its non-destructive operation character. It couples to the electric field generated by a bunched beam of charged particles and the resulting signals can be compared to detect a displacement from the reference trajectory.

The theoretical basis of pick-up signal generation was introduced. A general formalism used to describe the response of the beam position monitors to ultra-relativistic beams was given. Its was extended to cover low-β effects and to find correction factors for the results with a current-carrying wire. The special case of a diagonally cut pick-up was presented and a difference-over-sum technique for beam position determination was chosen for its linearity.

The design of the pick-up was analysed in terms of the signal-to-noise ratio. The expected sum and difference signals are $\Sigma\hat{U} = 95$ μV and $\Delta\hat{U} = 1.6$ μV/mm, whereas the unavoidable noise is about 1 nV/$\sqrt{\text{Hz}}$. It was demonstrated that a narrowband signal processing is necessary and that it is possible to perform closed-orbit measurements.

The uncertainties due to overall noise, mechanical accuracy and signal digitisation were analysed in detail. The largest position determination error can be caused by a tilt of the monitor with respect to the beam axis, but can be corrected for if known. The performance of the pick-up is limited also by the resolution of state-of-the-art digitisers if the sum and difference signals are calculated after digitisation. With the effective number of bits $b = 14$, the position determination uncertainty is 0.2 mm. It is sufficient for the USR where beams as large as 20 mm in diameter are to be localised within the 100-mm aperture beam tube and means that the accuracy of 0.2% can be achieved.

It was demonstrated that the low-β values are generally not a problem at the USR as long as bunching frequencies are low and a narrow-band signal processing is used. The chosen harmonic number h=10 leads to a beam position determination error smaller than 0.02 mm, thus the correction can be omitted. Should the short, electron cooled

bunches be observed in the wide bandwidth, the low-β effect will have to be taken into account.

A prototype of the pick-up was built up and tested, and the necessary control, and acquisition software was developed. The monitor consists of two diagonally-cut cylindrical electrodes, installed in a custom-made vacuum vessel. In order to avoid distortion of the electric field in the vicinity of the pick-up edges, the inner diameter of 100 mm matches the aperture of the USR beam line. Additional guarding rings were introduced at both ends and in the middle of the monitor. Furthermore, separating rings were introduced in the diagonal gap between the electrodes. They minimise the parasitic coupling and improve the sensitivity of the pick-up. Ultra-low noise, high input impedance amplifiers were chosen to amplify the voltage signals before their digitisation and further processing. A customised LabVIEW application was prepared with the development kit for the purpose of the project to control the digitiser settings and display all recorded signals in real time.

The prototype was assembled and tested with a current-carrying wire. The arrangement is equivalent to measurements with an ultra-relativistic beam. The scaling factors and misalignment of the electrical centre with respect to the mechanical axis were determined in this setup. The linear response of the monitor to beam displacement was demonstrated.

Finally, the response of the pick-up to particle beams was modelled with a finite integration technique-based computer code. It was demonstrated that a small mesh size is critical for accurate simulations. The results obtained with an ultra-relativistic beam, i.e. $\beta = 1$, were in good agreement with the stretched-wire measurements which proves the bench tests can be successfully applied to calibrate the monitor for high-energy beams.

Future developments can focus on the improvement of the signal processing system, including analogue addition and subtraction prior to digitisation, gain optimisation and expansion of the LabVIEW code to offer wider functionality. In addition, a resonant amplification scheme can be implemented to increase the pick-up sensitivity [131]. Also the application of the monitor can be extended to beam current measurements [131].

Chapter 5

Faraday cup

In this chapter, a prototype of a sensitive Faraday cup for femtoampere beam current measurements is presented. The first section gives the rationale for the studies and optimisation of the monitor. The following part provides the analysis of the physical processes involved in destructive beam intensity measurements. Factors influencing the accuracy of the ultra-low current monitor are discussed in detail. Next, the design of the sensitive Faraday cup is introduced and reviewed in the light of the physical aspects presented previously. In order to verify the performance of the monitor, experiments with keV electrons and protons in the femtoampere region were performed and the results are presented in the following section. Finally, the outcome of the work and future perspectives are given.

5.1 Motivation

Physicists dealing with intense beams very rarely need to detect single particles, whereas those working on few-particles experiments and applications usually do not worry about high current beams. A gap exists between the two worlds where the applicability of different diagnostic techniques has not been fully explored.

Most beam intensity monitors used in particle accelerators have not been designed to measure femtoampere currents and need to be either pushed to their detection limits or replaced by other, more suitable devices known from few-particles experiments. Particle counters, such as scintillators or electron multipliers, can offer sufficiently high sensitivity, but get saturated or damaged if too high instantaneous currents are delivered [53, 54]. They also require absolute calibration and quality check to ensure a constant response with time. Similarly, polycrystalline chemical vapour deposition

(CVD) diamond detectors show promising perspectives for ultra-low current monitoring, but need to be calibrated and exhibit unstable leakage currents which vary with time, bias voltage, polarity and dose [151]. It is therefore desirable to provide a simple and reliable solution which could be used to monitor low DC-beam currents and sustain, or even measure, relatively high peak intensities.

Faraday cups seem to fulfil all the requirements, but their ultimate detection limits have not been investigated in detail. These monitors, introduced in Section 2.4.3, are the easiest to operate and no simpler yet reliable technique can be applied to absolute current measurements. At low energies, the design of a Faraday cup does not have to be complex and peak currents usually are not a problem, thus requiring no dedicated cooling. With a careful design, picoampere currents can be measured, but it is a challenge to obtain satisfactory results in the femtoampere region [85, 145]. The problem of an insufficient monitor sensitivity was encountered also during the tests with scintillators at INFN-LNS, as discussed in Chapter 3. The aim of this work was to investigate and optimise the design of a Faraday cup for femtoampere beam current measurements.

5.2 Design Considerations

5.2.1 Principle of Operation

The most straightforward way to measure the intensity of a charged particle beam is to transform it to the electric current in a conducting wire or cable connected to an ammeter outside the vacuum tube. In this sense, a Faraday cup is an interface designed to collect all primary and secondary charges and pass the resulting electrical signal to a current meter or amplifier. The whole system can be seen as an electric circuit with corresponding noise sources which needs to be optimised to work in an accelerator environment.

The destructive beam current monitoring method becomes complicated when dealing with high-intensity beams or, on the contrary, with a low number of particles. For high currents, the total power carried by the beam can damage the intercepting material. At the other extreme, very low intensities can get buried in noise generated by many sources present in an accelerator environment and no useful signals are observed.

A reliable Faraday cup is expected to collect the whole charge carried by the primary beam, introduce very low noise and work in a repetitive manner. It is therefore important to understand the interaction of the primary beam with the cup material,

creation of secondary particles, heat load, potential noise sources and other potential design issues. The following subsections describe the most important physical processes which should be considered in order to optimise the performance of the monitor.

The destructive character of the measurements with a Faraday cup make it unsuitable for antiproton beams. Stopped antiprotons will generate secondary particles of much higher energy than the primary beam and will carry the charge away from the monitor. Consequently, the observed signals will not reflect the real beam intensities and will be of limited use. The Faraday cup, as it is presented here, is intended to provide a sufficient sensitivity during the commissioning stage and regular diagnostics of proton and ion beams in a reliable, easy and absolute manner.

5.2.2 Range of Projectiles in Matter

Charged particles passing through matter lose their kinetic energy due to interaction with electrons and atoms of the medium. The measure of the average energy loss per unit path length, $-dE/dx$, is known as stopping power [91, 216]. The energy loss of a proton or an ion is mainly due to collisions with electrons of the target. The dominating character of the electronic stopping power, also referred to as collision stopping power, is shown in Fig. 5.1.

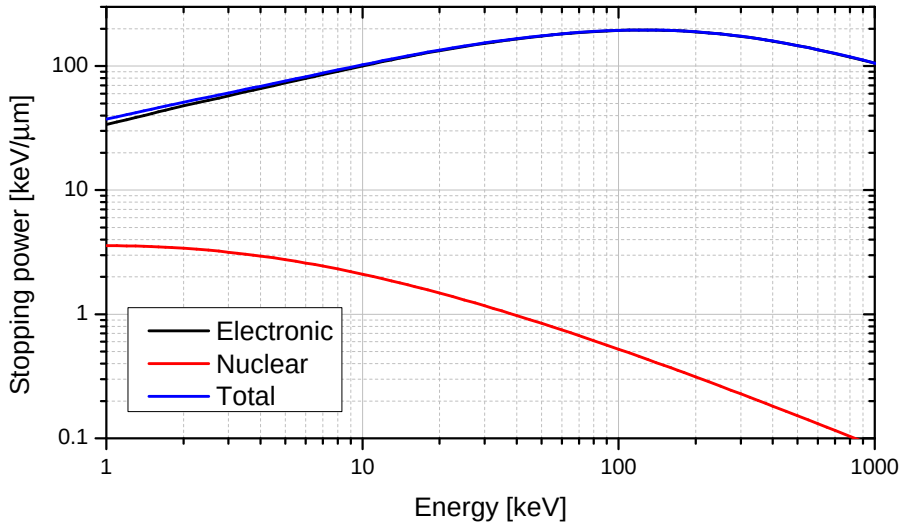

Figure 5.1: Stopping power of protons in copper [57].

The electronic stopping power of heavy charged particles can be described by [91]:

$$-\left(\frac{dE}{dx}\right)_{el} = K \cdot z^2 \cdot \frac{Z}{A} \cdot \frac{1}{\beta^2} \cdot L\left(\beta\right), \tag{5.1}$$

where $K = 0.307$ MeV $\cdot$ cm^2/g, z is the charge of the projectile, $\beta = v/c$ is the particle velocity in units of the speed of light, Z and A are the atomic number and relative atomic mass of the target atom, and L is the stopping number. The main features of the energy-loss process are described by the terms preceding the stopping number, whereas L takes into account finer details and is often expressed as:

$$L(\beta) = L_0(\beta) + z \cdot L_1(\beta) + z^2 \cdot L_2(\beta) + ... \tag{5.2}$$

The first term, based on a first-order Born approximation [91], is given by:

$$L_0(\beta) = \frac{1}{2} \cdot \ln\left(\frac{2 \cdot m_e \cdot c^2 \cdot \beta^2 \cdot \gamma^2 \cdot T_{max}}{I^2}\right) - \beta^2 - \frac{\delta(\beta \cdot \gamma)}{2}, \tag{5.3}$$

where m_e is the mass of an electron, T_{max} is the largest possible energy loss in a single collision with a free electron, I is the mean excitation energy of the medium, and $\delta/2$ is the density effect correction. Equation 5.1, incorporating only the $L_0(\beta)$ term is known as Bethe's formula and is appropriate for protons at energies above a few MeV. It gives accurate results of the mean rate of energy loss within a few percent.

Additional corrections have been introduced to extend the applicability of Bethe's formula to lower energies. The shell correction, denoted $-C/Z$ and added to the $L_0(\beta)$ term, takes into account the reduction of the energy loss due to the limited interaction with electrons in lower shells of the atoms. It becomes important when the velocity of the projectile is comparable to the velocities of the electrons bound in the target. The Barkas correction, $z \cdot L_1(\beta)$, is a higher order term in the series 5.2 that makes the stopping power dependent on the charge sign of the projectiles [217]. Low-energy particles of negative charge are subject to lower stopping power than their positive counterparts due to the respective repulsion and attraction of the target electrons [218–220]. The Bloch correction, $z^2 \cdot L_2(\beta)$, provides a bridge between the classical and quantum-mechanical range-energy calculations. It accounts for the scattering of electron wave packets for close collisions [221–223]. With all these corrections considered, Bethe's model is accurate to approximately 1% down to about 1 MeV for protons. However, no satisfactory theory exists for energies in the range from around 50 keV to 0.5–1 MeV and various phenomenological fitting procedures are applied to cover the experimental data [91, 217, 224, 225].

From the point of view of the Faraday cup design, a more practical quantity is the range of the keV protons in the beam stopper material. Equation 5.1, or effectively the plot shown in Fig. 5.1, can be integrated to find the continuous slowing-down

approximation (CSDA) range, that is the mean path length of the particle as it slows down to rest. However, a more useful quantity is the average value of the depth to which the projectile can penetrate the medium along its initial direction. It is known as projected range and is smaller than the CSDA range due to multiple scattering effects. Both quantities are plotted in Fig. 5.2 for keV protons in copper. The projected range of the USR beams is about 1.5 µm at 300 keV and approximately 120 nm at 20 keV which means that they can be stopped even in a sufficiently thick foil.

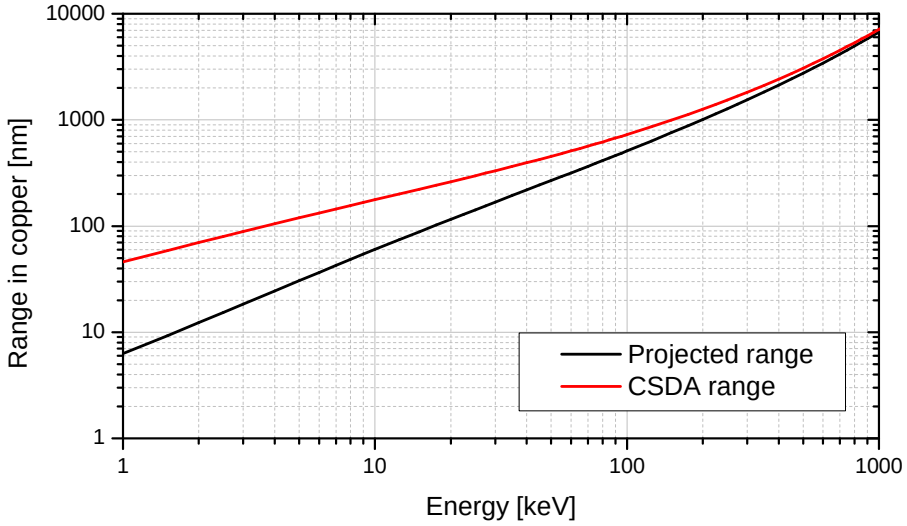

Figure 5.2: CSDA and projected range of protons in copper [57].

5.2.3 Backscattered Particles

The phenomenon in which light ions are reflected from the surface of the bombarded solid body is known as Rutherford backscattering. It is a classical elastic scattering of a charged particle in a Coulomb potential of a nucleus [226–228]. In general, the backscattering increases with the increasing atomic number of the target and decreases with the increasing energy of the projectile [229].

If the collision takes place at high energies, the projectile can approach the target nucleus at a distance smaller than the radius of the atomic shell. Consequently, the potential of the interaction of the colliding particles has a Coulomb character:

$$V(r) = \frac{1}{4 \cdot \pi \cdot \epsilon_0} \cdot \frac{Z_1 \cdot Z_2 \cdot e^2}{r}, \tag{5.4}$$

where Z_1 and Z_2 are the atomic numbers of the projectile and the target nuclei, whereas r is the distance from the target atom.

For low energies, the interactions of the nuclei are partially screened by the electrons of the atom and equation 5.4 has to be modified to correct for this effect:

$$V(r) = \frac{1}{4 \cdot \pi \cdot \epsilon_0} \cdot \frac{Z_1 \cdot Z_2 \cdot e^2}{r} \cdot \Phi\left(\frac{r}{a}\right), \tag{5.5}$$

where Φ is a screening function and a is the screening radius [226–228, 230]. The screening function is defined as the ratio of the actual atomic potential, at distance r, to the Coulomb potential. The screening radius has been proposed in different forms, yet they all give similar numerical results [227, 230, 231]. It is proportional to the Bohr radius of the first orbit in the hydrogen atom and inversely proportional to $Z^{1/3}$.

The proton beam energies at the USR fall into the range where the validity of different analytical descriptions of scattering is limited [232]. A single Rutherford backscattering model based on equation 5.4 gives accurate results for energies above a few hundred keV [233], whereas a multiple collision theory has to be applied at energies below 5–10 keV [234]. The energy gap can be bridged by a model of reflection by a single collision with assumption that the screening of the Coulomb interaction is not negligible [232]. A further complexity occurs when moving from a perpendicular to grazing incidence. Depending on the angle and energy of the projectiles, a single scattering model needs to be replaced by a small-angle multiple scattering type of reflection [232]. The most satisfying solution can be provided by Monte Carlo techniques which were used also to benchmark the models mentioned above [232, 233].

A simple Monte Carlo code TRIM [177] was used to calculate the reflection of keV protons from a flat solid surface and the resulting quantities were analysed in terms of their importance for the Faraday cup performance. Pencil beams at energies between 300 keV and 20 keV impinging on a copper block were simulated at normal incidence and at 75° as measured from the normal to the target surface, see Fig. 5.3. The number of primary protons varied between 10^5 and 10^7 from case to case in order to obtain a reasonably high number of backscattered particles.

The percentage of reflected protons as a function of energy for the two angles of incidence is shown in Fig. 5.4. The total number of backscattered particles increases with the increasing angle of incidence and decreases with the increasing energy. At 300 keV, it is less than 0.1% at 0° and about 4.7% at 75°, whereas the values are significantly higher at 20 keV and reach approximately 2.4% and 36% at 0° and 75°, respectively.

The energy distribution of the backscattered protons was analysed at 0° and 75° incidence at both the energies available at the USR. The results are shown in Fig. 5.5.

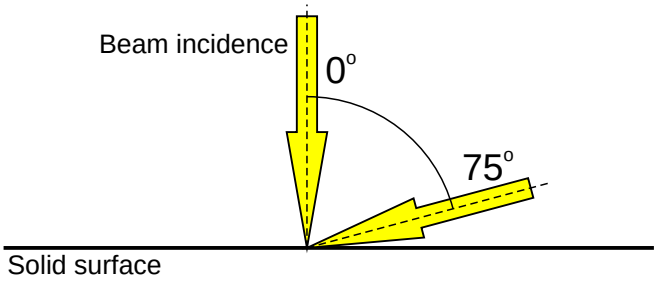

Figure 5.3: Two angles of incidence for beams modelled in TRIM.

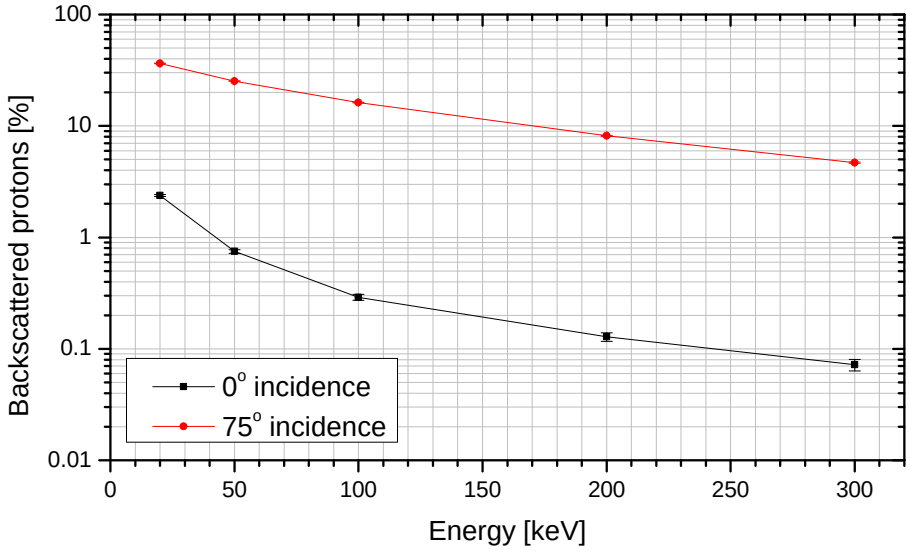

Figure 5.4: Percentage of the backscattered protons as a function of energy and angle of incidence of primary protons impinging on a copper block.

The bin size was set to 0.33 keV and 5 keV for 20 keV and 300 keV protons, respectively. The spectra extend up to the initial energy, but the majority of the particles are reflected with a reduced energy.

The scattering angle projected onto the plane of incidence was also studied. It is shown in Fig. 5.6 and the individual histograms correspond to the same beam settings as presented in the energy plots in Fig. 5.5. The bin size of 2° is used in all four cases. The maximum number of particles averaged over all energies is observed around the specular reflection angle.

To provide a clearer picture of the backscattered particles distribution, the reflected energy was plotted as a function of scattering angle, see Fig. 5.7. Reflected protons carrying the highest energy are observed at the specular angle and it can be seen at all energies and incidence angles shown in the figure. This can be explained by a single scattering from the surface which results in a small energy loss. At the same time, the most probable backscattered energy at oblique incidence is reduced to below 10 keV. The highest number of counts is observed around the specular reflection at 20 keV, whereas it is not the case at 300 keV.

The significant reduction of the reflection angle and energy for the latter can be explained by multiple collisions that 300 keV protons experience at oblique incidence. Their scattering in the backward direction is less probable and the particles are not bounced back from the target in the first collisions. Instead, most of particles follow the original paths experiencing small-angle deflections. Only in a fraction of all the cases, the net angle leads to the escape from the target. Protons at 300 keV incident at 75° penetrate a shallower layer of copper compared to 20 keV, but travel at larger distances before leaving the material, shown in Fig. 5.8. The number of protons that exit the material slowly increases to reach the maximum at about their range in copper and then drops down rapidly. The effect is due to multiple small-angle scattering and results in a different distribution of backscattered energy as a function of scattering angle. 20 keV protons scatter much easier and do not penetrate much of the copper target.

Several solutions can be applied to reduce the number of reflected protons. A simple plate is not sufficient to act as an effective beam collector and either additional side walls or a hollow block with a narrow entrance channel should be used. Backscatter depends on the atomic number of the target and a low-Z material is preferred. Also a biased grid can be introduced to reduce the number of reflected protons, but it would affect the number of incoming projectiles as well.

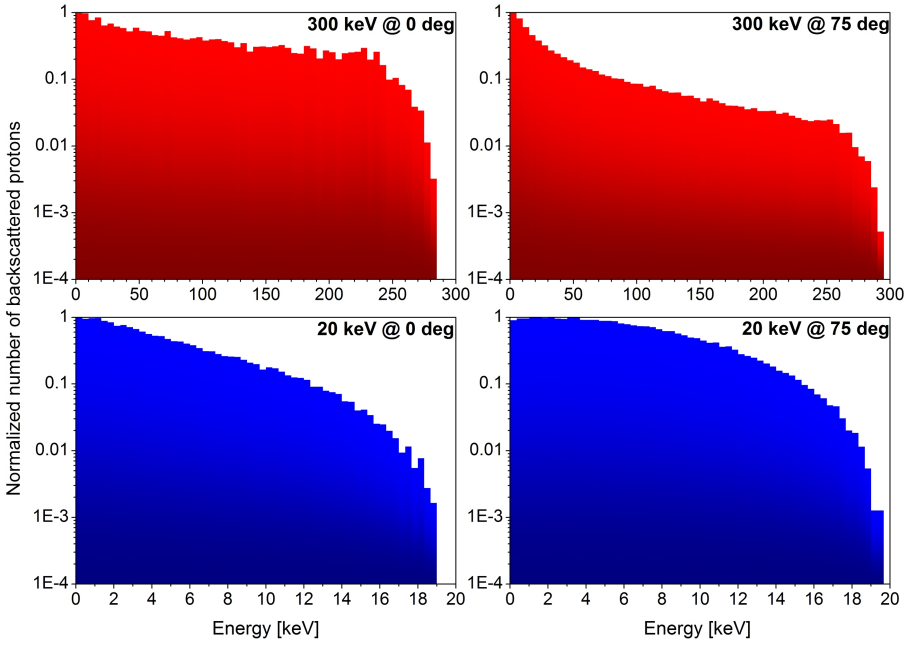

Figure 5.5: Backscattered energy spectra for 300 keV and 20 keV protons (top and bottom row) impinging on a copper surface at 0° and 75° (left and right column).

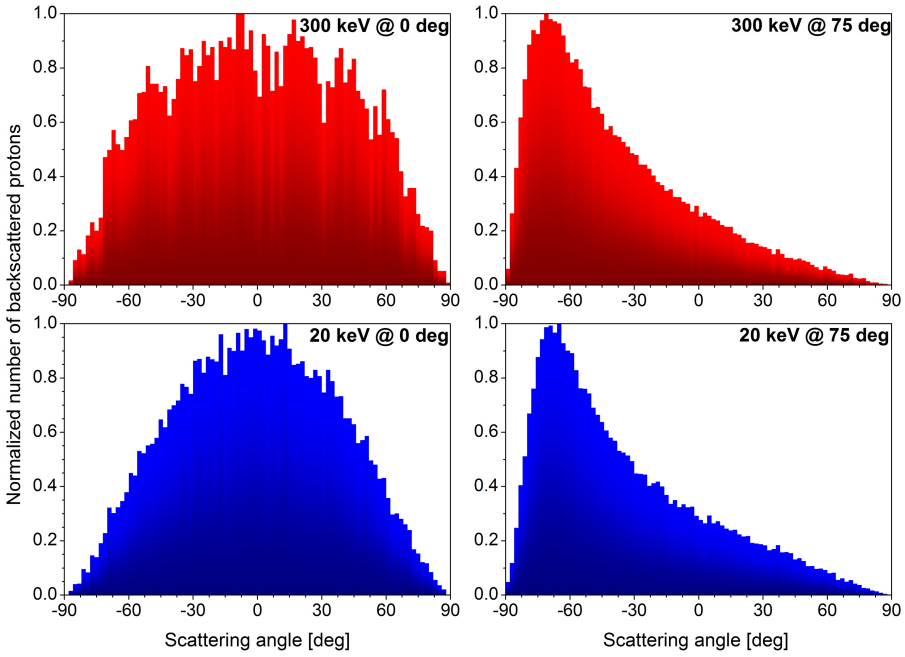

Figure 5.6: Scattering angles projected onto the plane of incidence for protons at 300 keV and 20 keV (top and bottom row) impinging on a copper surface at 0° and 75° (left and right column).

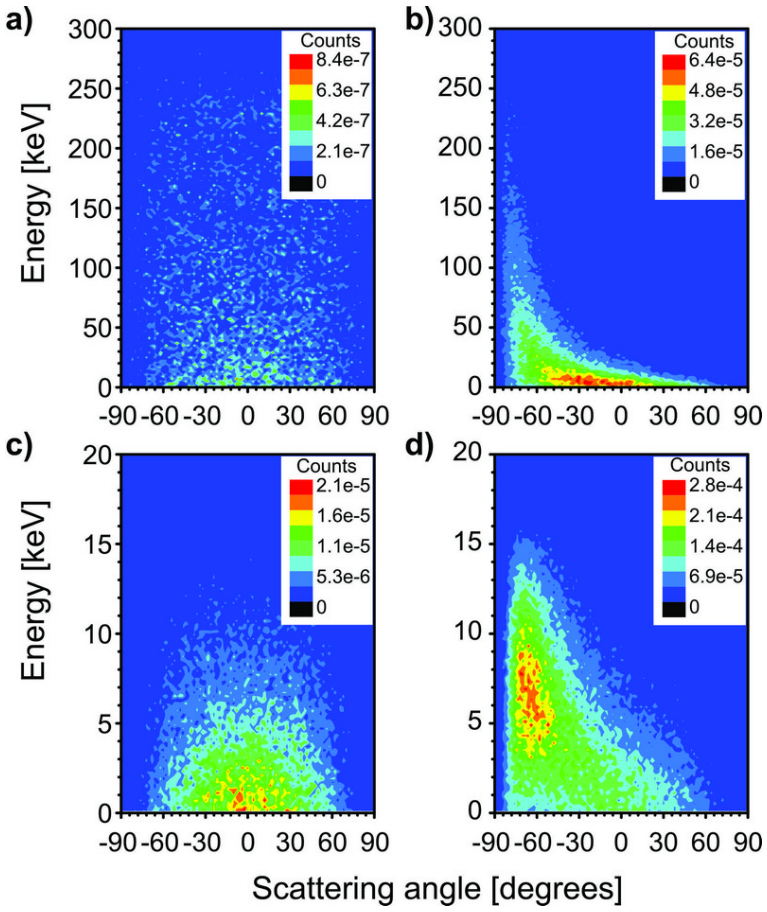

Figure 5.7: Backscattered energy distribution as a function of the scattering angle for 300 keV protons impinging on a copper surface at 0° and 75° (a and b, respectively) and 20 keV protons impinging at 0° and 75° (c and d, respectively).

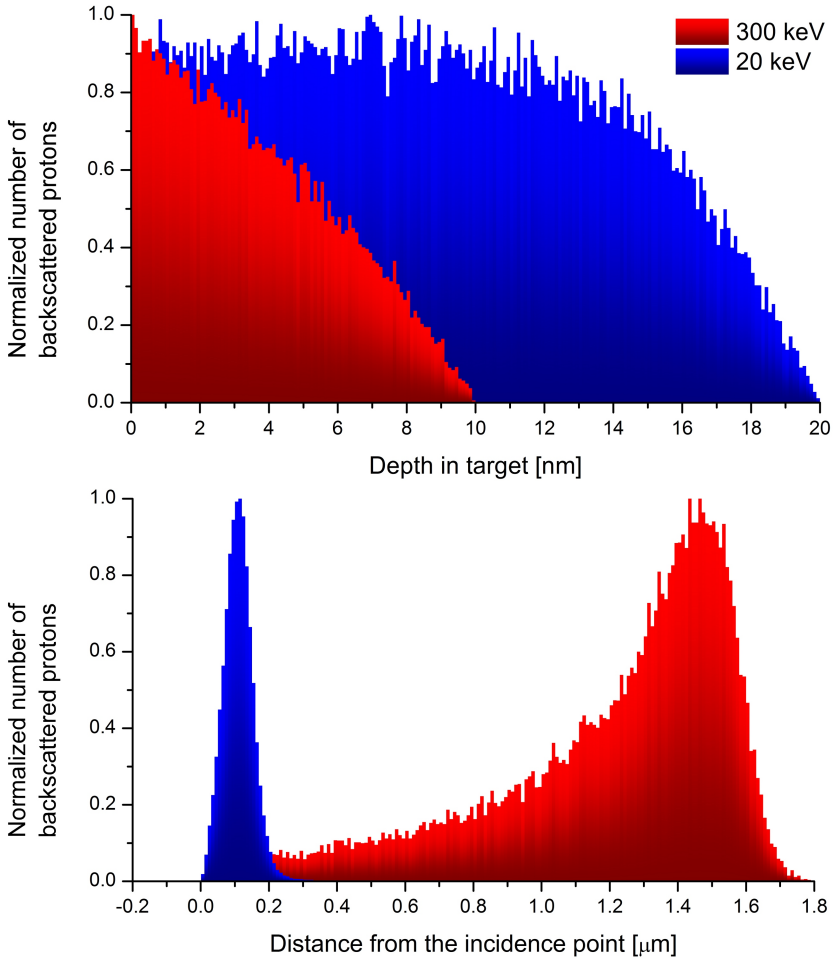

Figure 5.8: Depth at which the particles were declared backscattered (top) and the distance from the incidence point when they exit the copper target (bottom) at 20 keV (blue) and 300 keV (red) at 75° incidence.

5.2.4 Secondary Particles

The energy transfer from the projectiles interacting with the Faraday cup material can result in the ejection of other ions, neutrals, photons, and electrons. Given the fact that the detector accuracy depends on the collection efficiency of the total charge carried by the beam, secondary charged particle emission needs to be well understood and no charge should be allowed to escape the Faraday cup.

Secondary Electrons

Secondary electrons are the main charge carriers created by low-energy protons and their characteristics have been extensively studied by many groups [235, 236]. Electron emission is a surface phenomenon, since the mean free path of electrons with energies up to 100 eV does not exceed about 5 Å [237]. Consequently, only the energy deposited within the first few atomic layers of the medium contributes to the average number of emitted electrons.

The angular distribution of the emitted particles tends to obey a cosine shape independent of the incidence angle of the primary beam [236]. Also the peak energy at a few eV does not depend on the combination of the projectile and target used [236]. However, other important parameters, including the electron yield and the energy spectrum shape, are strongly influenced by many factors. These cover the energy and angle of incidence of the projectile or the electric field near the surface. To make the picture even more complicated, also the purity, oxidization and surface roughness of the target are significant experimental parameters [238]. For this reason, it is not easy to give a proper general description of secondary electron emission and the following considerations are only approximate.

The total electron yield γ_t is proportional to the electronic stopping power of the projectile in the target. It increases with increasing proton energy, then reaches a maximum in the 100 keV region and decreases thereafter. Figure 5.9 shows the behaviour of the total electron yield γ_t as a function of projectile energy for proton impact on different metal targets at normal incidence angle. The yield scales with the incidence angle θ, measured with respect to the surface normal, by a factor $1/\cos(\theta)$ for protons [236].

Figure 5.10 shows spectra of secondary electrons emitted by 500 keV protons from different clean metals. They all have peaks at about 2–3 eV with FWHM values of the same order of magnitude. These low-energy peaks contain about 85% of the emitted particles and are a result of a cascade process. The remaining tails of the distributions

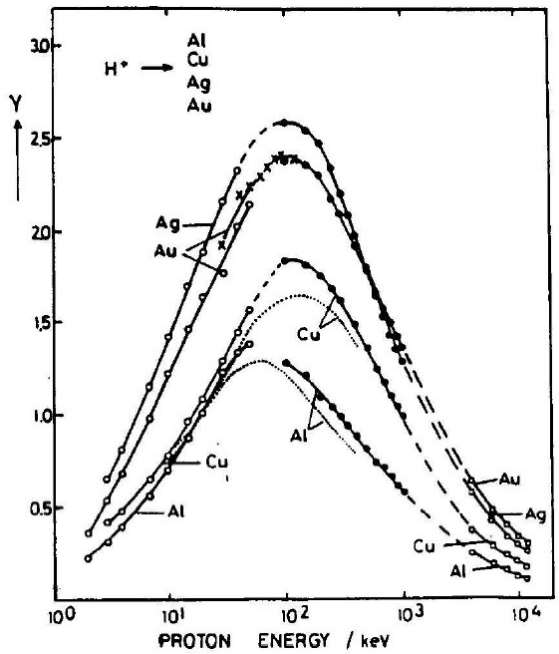

Figure 5.9: The total electron yield γ_t as a function of energy for proton impact on clean aluminium (Al), copper (Cu), silver (Ag) and gold (Ag). Picture taken from [236].

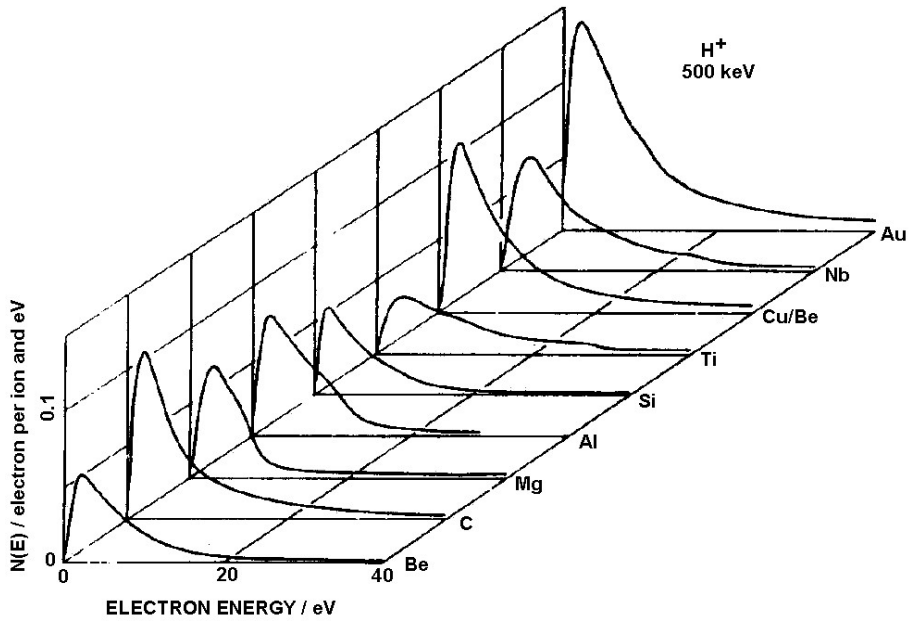

Figure 5.10: Low energy spectra induced by protons at 500 keV from different clean metals. Picture taken from [236].

follow decaying exponential-like curves and are due to a direct energy transfer from the projectiles to electrons of the target. However, the most energetic δ-electrons, able to knock-out further electrons, are expected to be emitted mostly in the forward direction.

The low-energy secondaries ejected backwards can be stopped by means of an electric field applied at the entrance of the Faraday cup. Also a narrow channel can minimise the probability of particles escape from the monitor.

Annihilation Products

In the case of antiprotons, the use of the Faraday cup will be strongly limited. The reason for this is that high-energy products of annihilation are able to escape the device very easily. As described in section 3.2.3, various combinations of charged pions will emerge at 100-MeV-scale energies. Due to momentum conservation, a nuclear recoil of a few tens of MeV, depending on the target material, will be observed as well. In addition, a fraction of annihilations will induce the production of an unstable nucleus; the nuclear breakup will result in fragments emitted in all directions and ionizing surrounding atoms. All in all, many annihilation products will have energies hundreds of times higher than the primary keV beam, thus their stopping in the detector without affecting the projectiles will be extremely difficult, if not impossible. Consequently, the annihilation products will leave the monitor and the charge measured will not reflect the absolute beam current.

Despite this limitation, the cup will be an important diagnostics tool during the USR commissioning with protons. In addition, it can be used to compare the response to both the proton and antiproton beams of similar intensities.

5.2.5 Heat Load

A particle beam stopped in a Faraday cup can cause a temperature rise. The beam stopper is electrically insulated from its environment, thus heat transfer by conduction is strongly limited. Also convection in a vacuum system is negligible and the only process of cooling down is thermal radiation. Considering energy of 300 keV and an instantaneous beam current of 1 μA, the peak beam power in the USR will be less than 300 mW. It was demonstrated that no additional cooling system needs to be used if the beam power does not exceed some Watts [54].

5.2.6 Signal Amplification

The beam collector should not be designed independently from the signal processing system. The charge carried by the beam is stopped in the cup and the resulting electrical signal is transferred outside the vacuum chamber, amplified and registered. All these steps can introduce significant noise and signal distortion if not optimised for ultra-low current measurements.

The Faraday cup system can be seen as an electric circuit. Because the beam stopper is isolated and floating, it can be treated as a high-resistance current source. The geometry of the detector, its cables and connections also introduce an input capacitance. Such a current source can be connected to an amplifier, but it is not easy to amplify the low-level signal without introducing additional noise and a considerable noise gain.

The two most common solutions for current measurements are a shunt impedance amplifier and a feedback ammeter [174, 239–241]. Both are shown schematically in Fig. 5.11.

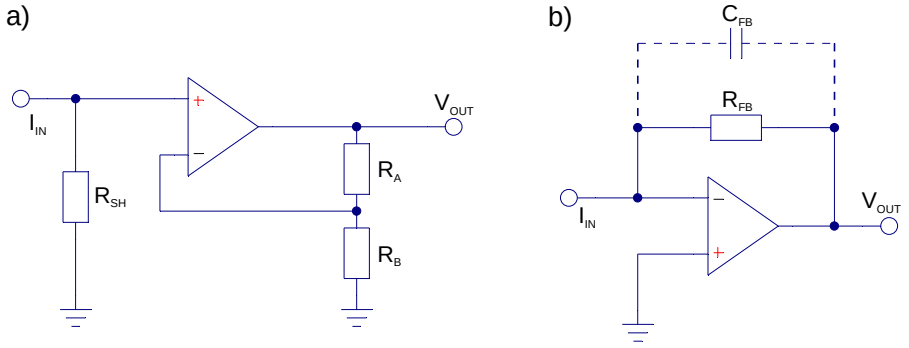

Figure 5.11: Diagrams of a shunt impedance amplifier (a) and a feedback ammeter (b).

In the case of the shunt ammeter, Fig. 5.11a, the input current I_{IN} flows through the shunt resistor R_{SH} and the output voltage can be calculated as:

$$V_{OUT} = I_{IN} \cdot R_{SH} \cdot \left(1 + \frac{R_A}{R_B}\right). \tag{5.6}$$

The voltage drop across the shunt is known as the voltage burden and is a series voltage error introduced by an ammeter. In order to minimize it, the input resistance R_{SH} should be small. However, the resistor thermal noise is proportional to $\sqrt{R}$ and a reduction of R_{SH} leads to low SNR.

In the case of a feedback ammeter, Fig. 5.11b, the input current is compensated through a feedback loop with resistance R_{FB}. The output voltage provides a feedback

current such that the net current at the inverting input of the amplifier is negligible, whereas the non-inverting input is grounded. The overall sensitivity is therefore determined by the feedback resistor R_{FB} and the voltage output is:

$$V_{OUT} = -I_{IN} \cdot R_{FB}. \tag{5.7}$$

Such an arrangement results in a much lower burden voltage because the "shunt" is in the feedback path and appears divided by the gain of the amplifier as the "input shunt". Consequently, the transimpedance gain, or simply the value of R_{FB}, can be much higher as compared to R_{SH} in the shunt impedance amplifier. Also the output voltage offset can be considerably smaller in the case of the feedback ammeter [241].

The performance of a feedback ammeter is affected by the stray capacitance C_{FB} present in parallel with the feedback resistance. In this case, the output voltage is described as [239]:

$$V_{OUT} = -I_{IN} \cdot R_{FB} \cdot \left(1 - exp\left(-\frac{t}{R_{FB} \cdot C_{FB}}\right)\right). \tag{5.8}$$

The existence of the stray capacitance limits the frequency response of the amplifier. The output voltage drops by –3dB at a frequency:

$$f = \frac{1}{2 \cdot \pi \cdot R_{FB} \cdot C_{FB}}, \tag{5.9}$$

which corresponds to the rise/fall time of the system:

$$\tau = R_{FB} \cdot C_{FB}. \tag{5.10}$$

In order to obtain a higher cut-off frequency and to keep the high gain, the single stage solution can be replaced by cascade amplifiers. An alternative approach is a resistive network with a single amplifier, as shown in Fig. 5.12a. However, the frequency is increased at the cost of a higher noise in that case. The immediate resistance R_1 determines the SNR and both the signal and noise are amplified by the same factor $(1 + R_2/R_3)$.

To overcome the problem of the trade-off between the frequency and the noise, an *RC* feedback network can be introduced as shown in Fig. 5.12b. In this case, the output voltage can be approximated by [239]:

$$V_{OUT} = -I_{IN} \cdot (R_1 + R_2) \cdot \frac{1 + 2 \cdot \pi \cdot R_2 \cdot C_2 \cdot i}{1 + 2 \cdot \pi \cdot R_1 \cdot C_1 \cdot i}. \tag{5.11}$$

If $R_1 \cdot C_1 = R_2 \cdot C_2$, the signal loss with the frequency can be compensated. Such a simple approach does not solve the problem perfectly due to other parasitic capacitances present in the circuit, but can improve the bandwidth about 30 times at $R_{FB} = 100$ MΩ [239].

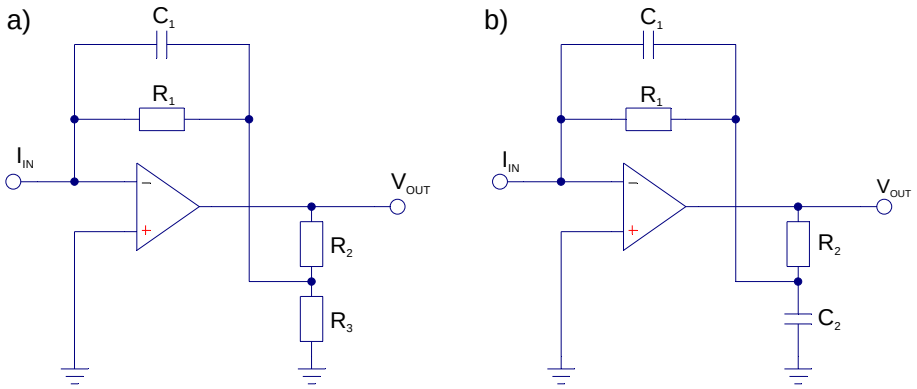

Figure 5.12: Feedback ammeters with an improved time response: the resistive network solution (a) and the *RC* compensation (b).

5.2.7 Noise

A number of noise sources can have a serious impact on the measurement of femtoampere currents and have been grouped by other authors [240, 241] in the following way:

- electromagnetic interference,
- electrostatic coupling,
- triboelectric effects,
- piezoelectric effects,
- ground loops,
- leakage currents,
- sputtering,
- backscattered and secondary particles,
- offset current,

- surface contamination,
- acoustic noise,
- thermal noise,
- shot noise.

An electromagnetic interference is an unwanted disturbance that affects an electrical circuit due to electromagnetic radiation emitted from an external source. Considering a limited bandwidth of a low-current monitoring system, the most significant sources of interference are the electrical power lines. To reduce their influence on the measurement system, a good shielding needs to be provided. Also an RF field generated by the RF buncher can be critical for the operation of the Faraday cup. Its influence can be minimised with the distance.

An electrostatic coupling between the suppressing electrode and the beam stopper can be another cause of noise. Assuming a parasitic capacitance C_p between the two, the voltage ripple of the high voltage (HV) power supply dV/dt and the capacitance change due to mechanical vibrations dC_p/dt can result in the current noise:

$$\frac{dQ}{dt} = C_p \cdot \frac{dV}{dt} + V \cdot \frac{dC_p}{dt}. \tag{5.12}$$

In order to minimise the effect, a low-ripple power supply should be used and a high rigidity of the system should be ensured.

Triboelectric effects are caused by the friction between a conductor and an insulator, as in a cable. Therefore, the bending and movement of cables should be avoided and the use of low noise cables is recommended.

Piezeoelectric effects are produced when a mechanical force is applied to crystalline materials that are used to insulate two different conductors. It is therefore important to remove mechanical stresses from the insulator and restrict the cable movement.

Noise and error signals can be caused also by ground loops. A loop is formed when a source and a measuring device are both grounded. A voltage difference between the two ground points can cause a small current to flow around the loop. It is recommended to ground all the equipment at a single point.

Leakage currents are generated by stray resistance paths and flow through the protective ground conductor to ground. They can be caused by the accumulation of electrical charges inside the insulator when exposed to an electrical field, and by a

limited value of insulation resistance. To solve the problem, it is necessary to protect the low signal by means of guarding. With triaxial cables, it is possible to keep the core and the inner shield, known as guard, at the same electrical potential. As a consequence, no voltage difference is present and no leakage currents flow between them, despite the imperfections of the insulation.

Atoms of a material exposed to a charged particle beam can be ejected from the surface and deposited elsewhere [242]. If a conductive material is deposited on an electrical insulation, it can result in leakage currents. To avoid deterioration of the isolating components, appropriate shielding should be provided.

As discussed previously, the charge can escape from a Faraday cup in a variety of ways, such as backscattered and secondary particles. In order to suppress the charge, external electric, magnetic or electromagnetic fields can be applied at the entrance of the cup. Also a long, narrow entrance channel can prevent the particles from escaping the monitor.

The offset current can change with temperature and a drift with time can be observed. It is therefore important to ensure the instrumentation has reached a thermal steady state and the temperatures are stable.

Contamination, such as humidity or dust, can degrade the insulation resistance properties of a dielectric. However, components to be used under vacuum are usually well cleaned and the problem is not critical.

Ambient noise can produce vibrations that can lead to other effects described above. The main sources of this error are the vacuum pumps and other vibrating equipment. The monitor should not be installed in their vicinity.

The thermal motion of electrons in a resistor results in Johnson-Nyquist noise, also known as thermal noise. The RMS value of the thermal voltage noise density in a resistor R at temperature T and bandwidth Δf is given by:

$$e_{th} = \sqrt{4 \cdot k_B \cdot T \cdot R \cdot \Delta f}, \tag{5.13}$$

whereas the RMS value of the thermal current noise density through the resistor R is:

$$i_{th} = \sqrt{\frac{4 \cdot k_B \cdot T \cdot \Delta f}{R}}. \tag{5.14}$$

The Johnson-Nyquist noise at a high-impedance resistor required by the low-current application can be reduced by limiting the bandwidth of the system and additional cooling.

The discrete nature of the current results in Schottky noise, also known as shot noise. The RMS value of the shot current noise density at the average DC current $\bar{I}$ is:

$$i_{sh} = \sqrt{2 \cdot e \cdot \bar{I} \cdot \Delta f}. \tag{5.15}$$

The only way to reduce the Schottky noise is to limit the bandwidth of the system.

Finally, noise amplification should be considered. The SNR performance of a feedback-ammeter based system depends on the input capacitance C_{IN} and resistance R_{IN} as well as the stray capacitance C_{FB} and feedback resistance R_{FB}. The input parameters are the products of the capacitance-to-ground and resistance of the source, the connections and the input of the amplifier itself. It can be shown [241, 243] that for a simple feedback ammeter circuit, the DC noise gain is proportional to the factor $(1+R_{FB}/R_{IN})$. The noise amplification increases for frequencies above the level defined by the resistances and capacitances of the measurement system:

$$f > \frac{1}{2 \cdot \pi \cdot (R_{IN}||R_{FB}) \cdot (C_{IN}||C_{FB})} = \frac{R_{IN} + R_{FB}}{2 \cdot \pi \cdot R_{IN} \cdot R_{FB} \cdot (C_{IN} + C_{FB})}. \tag{5.16}$$

The design of the system can be optimised in terms of the resistance and capacitance in order to maximise the SNR. The noise gain increases with increasing C_{IN} and decreases with increasing R_{IN}. A minimum recommended value of input resistance for femtoampere current measurements is of the order of 1 TΩ (10^{12} Ω) [174]. A floating beam stopper fulfils this requirement. The maximum recommended value of input capacitance depends on the particular circuit design. Nevertheless, it is usually possible to measure at higher source capacitance than specified by the manufacturer of an amplifier or a picoammeter by inserting a resistor in series with the ammeter input. However, it is not recommended because any series resistance increases the voltage burden by a factor of $I_{IN} \cdot R_{SERIES}$. Additionally, the series resistance results in the longer RC time constant of the measurement. A diode-based solution can serve as a useful alternative if a high input capacitance needs to be compensated [174].

5.3 Design and Construction

5.3.1 Conceptual Design and Performance Analysis

An initial, schematic design of the Faraday cup is presented in Fig. 5.13. The monitor consists of a cylindrical beam collector with a conical cut-out and a suppressing ring electrode. Both are electrically isolated from each other and shielded against external

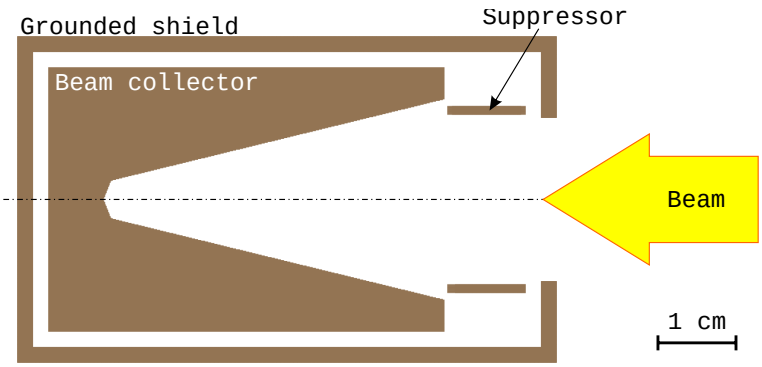

Figure 5.13: A cross section view of the initial design of the Faraday cup as modelled in SIMION .

influences by means of a grounded case. A cylindrical symmetry around the beam axis is assumed in the figure.

The shape of the beam collector was based on the design of a similar Faraday cup at Max-Planck-Institut für Kernphysik (MPI-K) [132]. The conical cut-out was chosen to maximise the collection efficiency of backscattered protons and secondary electrons and was modified to meet machining constraints. It is 51 mm in length and the opening angle of the conical cut-out is 28°. Since the reflected and secondary particles are not emitted from a surface normal to the primary beam, their escape solid angle is greatly reduced. Most of them would have to scatter from the beam stopper surface several times before reaching the exit. In addition, a larger area of the material is exposed to the incident beam. Therefore, the heat load per surface unit is lowered. Finally, the thickness of the beam collector is much larger than the µm penetration depth of 300 keV protons.

The suppressing electrode is used to prevent secondary electrons from leaving the monitor. Its inner diameter is 22 mm, whereas the length is 10 mm. A ring shape instead of a grid was chosen in order to avoid collision losses of the already few primary particles. In the given geometry, keV-scale protons can freely enter the cup, whereas the eV-range secondary electrons cannot surpass the potential barrier and are suppressed.

Backscattered Protons

Protons backscattered from the copper beam stopper were studied with Monte Carlo simulations. The TRIM package could not be used in this case because it can only cope with particles impinging on a flat surface. Instead, the beam stopper was modelled with

Geant4 release 9.5 [244–246]. A proton beam was simulated to hit the concave surface of the copper block. The QGSP_BERT_HP and QGSP_BIC_HP physics lists were used as suggested for low-energy applications yet no differences were observed [246]. The suppressing electrode and the outer shield were not included in the simulations as having very little influence on the primary proton beam. The electric field present at the entrance of the Faraday cup is only a few V/mm and can be neglected for 20 keV and higher energies.

A beam containing $5 \cdot 10^5$ protons with a diameter of 20 mm (6σ) and following a Gaussian distribution was simulated. At 300 keV, only 1 proton escaped the cup and it is a negligible amount even with the statistical fluctuations taken into account. At 20 keV, less than 0.2% particles were scattered back to the entrance and left the detector. Therefore, the current measurement by means of the proposed Faraday cup at the lowest energy of 20 keV is underestimated by approximately 0.2%. At 300 keV, backscattering is negligible and does not affect the observed beam intensity.

The number of escaping particles is much lower compared to the estimations made in Section 5.2.3 which can be explained by the shape of the beam collector. First, only a small fraction of the particles can be scattered back directly to the entrance. Second, the remaining backscattered particles have to be repeatedly reflected from the beam stopper surface towards the exit and also this process reduces the final number of escaping protons.

The spatial distributions of the primary 20 keV beam and the corresponding backscattered protons which exit the Faraday cup are shown in Fig. 5.14. In addition, the energy spectrum of particles able to leave the detector is shown in Fig. 5.15.

Secondary Electrons Suppression

This design concept was used as a starting point for the optimisation of the charged particles suppression. The electric field distribution as well as particles trajectories were simulated with SIMION [247]. The software does not incorporate any model for secondary electron emission, thus point sources were defined in arbitrary positions at the beam collector surface. There was no need to fully implement the angular distribution and the energy spectrum of secondary electrons, because only high-energy particles emitted in the backward direction could possibly exit the cup. It is shown in Fig. 5.16a where 300 eV electrons emitted towards the centre of the suppressing ring at –500 V leave the Faraday cup. It can be corrected by either increasing the suppressing voltage or the length of the suppressor.

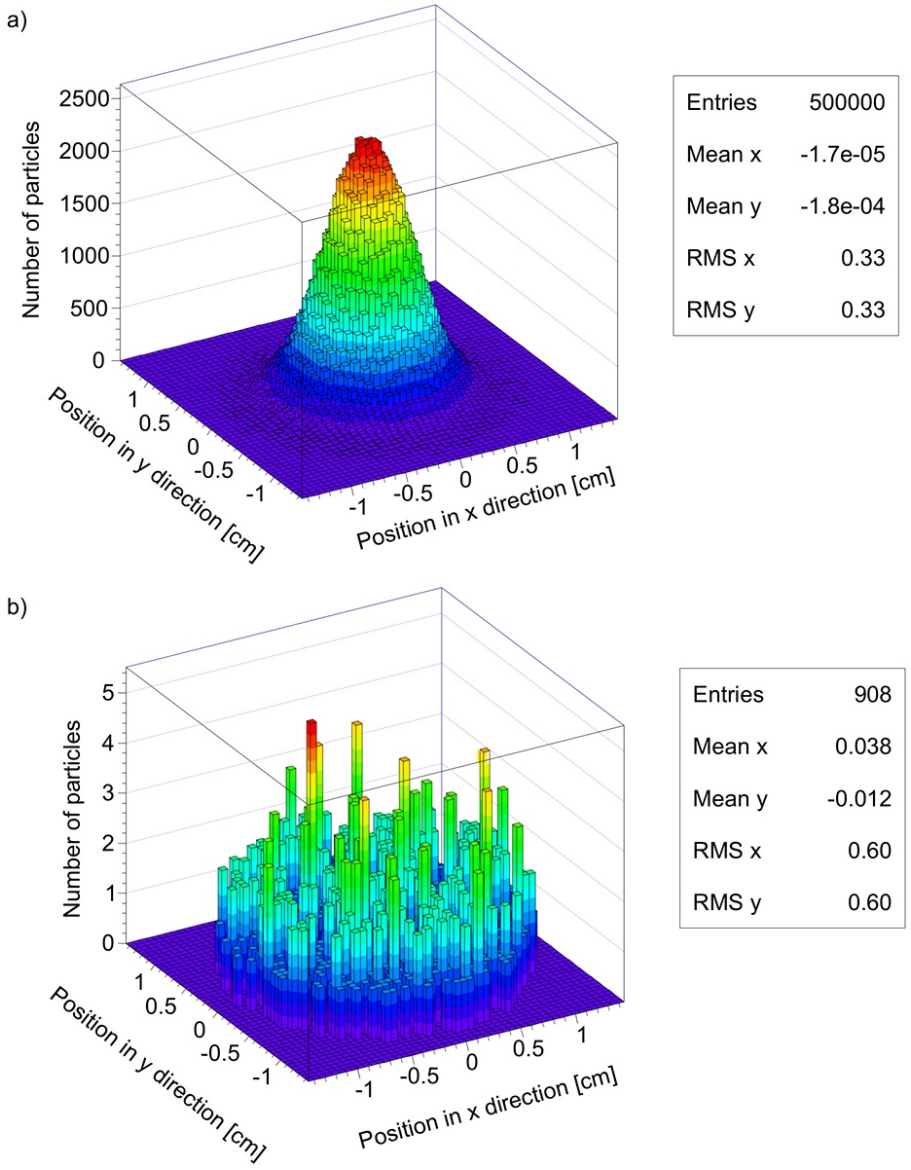

Figure 5.14: SIMION simulation of the primary 20 keV beam entering the cup (a) and the backscattered protons escaping the detector (b).

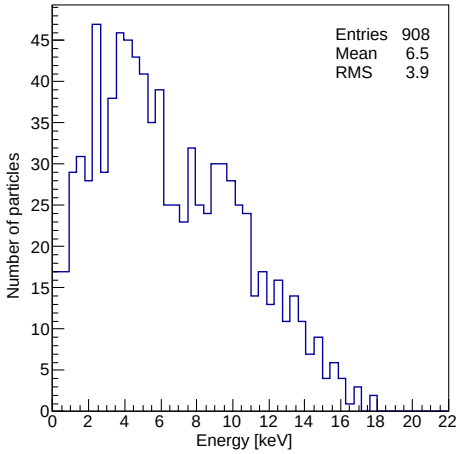

Figure 5.15: Energy distribution of backscattered protons that leave the Faraday cup.

In order to stop the electrons, shown in Fig. 5.16a, within the Faraday cup, the suppressor length was increased from 7 mm to 10 mm. It resulted in the drop of the potential at the central point of the monitor entrance by almost 20% and, consequently, all 300 eV secondary electrons were suppressed, see Fig. 5.16b. No further increase in the length of the ring was introduced because the probability of the electron emission at energies $\gg$ 100 eV in the small solid angle covering the critical exit point can be neglected [248]. Furthermore, the collection efficiency can be controlled also by the suppressing voltage as shown in Fig. 5.17. The voltage needed to stop all the secondaries can be adjusted experimentally during the operation of the device.

A more detailed CAD model of the Faraday cup was prepared and studied in terms of electric field distribution and electron collection efficiency. Figure 5.18 shows numerical calculations made with Particle Studio, a part of CST Studio Suite [211]. As discussed previously, the critical exit point of the cup is on the axis of the electrode where the electric field is reduced due to the finite length of the suppressor. The secondary electron emission model presented in Section 5.2.4 was implemented in the simulations and no electrons were observed to leave the Faraday cup. The escape of the secondaries is therefore neglected as having a very small impact on the accuracy of the beam current measurement compared with the other noise sources discussed in Section 5.2.7.

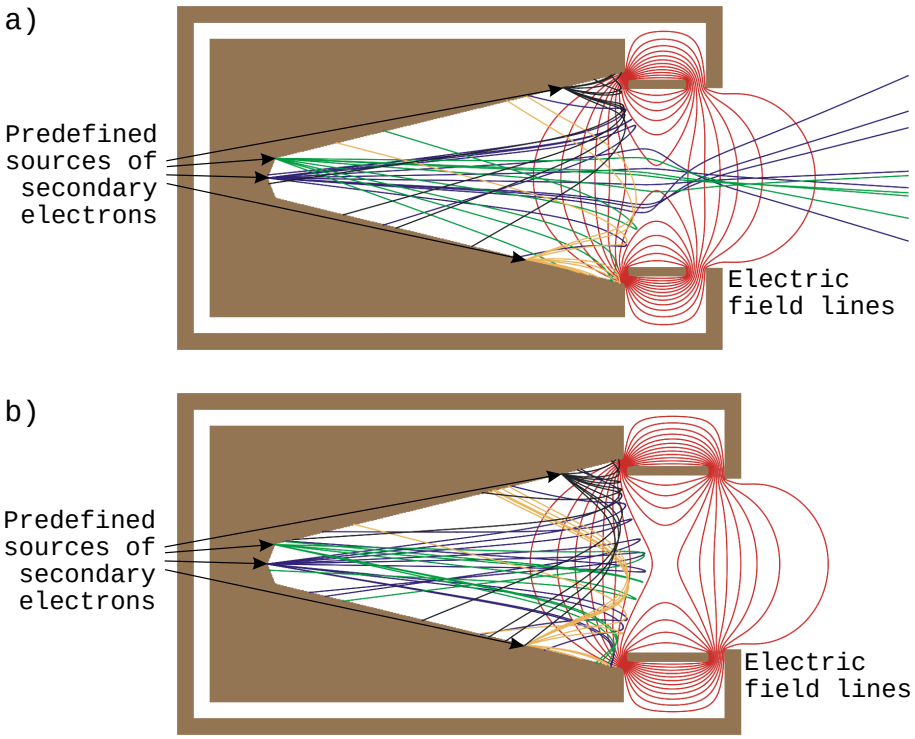

Figure 5.16: Simulation of the 300 keV secondary electrons escape from the Faraday cup with –500 V suppressing voltage.

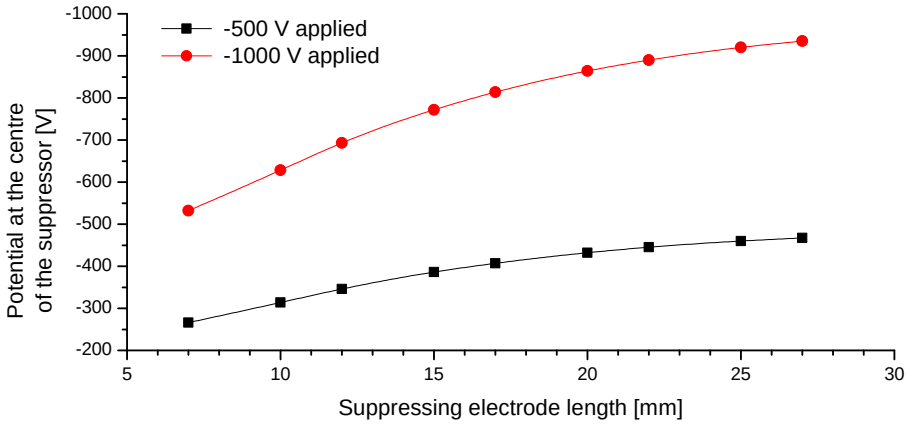

Figure 5.17: Potential at the centre of the suppressor as a function of the electrode length for –500 V and –1 kV applied.

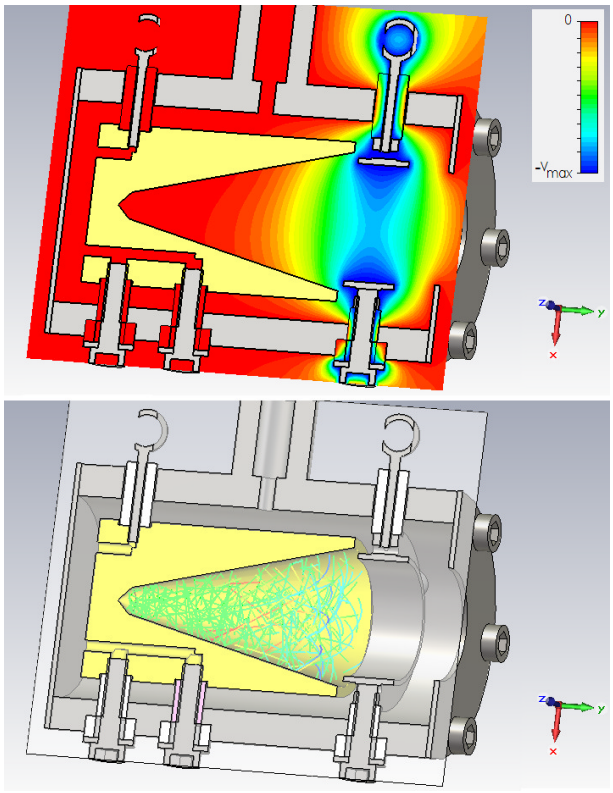

Figure 5.18: CST simulations of the field distribution (top) and the secondary electron emission (bottom) for a detailed Faraday cup model.

5.3.2 Mechanical Design

The final mechanical design of the Faraday cup is shown in Fig. 5.19. The suppressor and the shield are made of non-magnetic stainless steel, whereas the beam collector is made of oxygen-free high thermal conductivity (OFHC) copper. The entrance to the cup is 21 mm in diameter which was chosen to measure the USR beams of up to 2 cm diameter (6 σ value). The whole device is about 8 cm in length and 5 cm in diameter. The CAD model and the detailed technical drawings of the Faraday cup were prepared in Solid Edge [202].

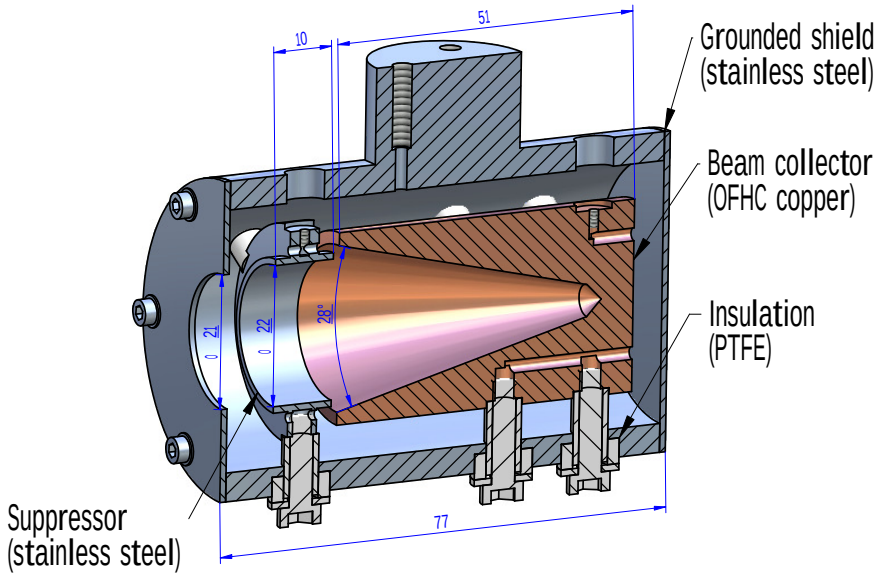

Figure 5.19: A cross-section view of the Faraday cup design.

The beam collector is fixed to the outer shield by means of six screws and is electrically insulated from the conductive steel case. Initially, insulating parts were made of machinable glass ceramic MACOR, but they were too fragile, thus not very robust. For this reason, the material was replaced by softer polytetrafluoroethylene (PTFE).

OFHC copper as a material for the beam collector was chosen because of its thermal properties. The high thermal conductivity of about 400 W/(m·K) makes the detector suitable for cryogenic applications. Although cryogenic design is not being considered for the USR any more, it was an important consideration at the early stage [249]. Compared to aluminium, however, copper has a higher atomic number Z, which results in more secondary electrons, see Fig. 5.9, and backscattered protons. Nevertheless, a negligible amount of particles can escape the cup and copper-based design meets the

diagnostic requirements.

The installation arrangement for the Faraday cup setup is presented in Fig. 5.20. The assembly consists of commercially available vacuum components. The detector is installed in a 4-way cross chamber DN100 and can be moved in and out by means of a pneumatic actuator with a 75 mm stroke. In the retracted position, the cup is fully hidden and the beam can freely pass through the chamber. A reducer flange DN100 to DN35 is used to minimise the size and cost of the other components of the setup. A 4-way cross DN35 with the feedhtrough flanges attached is provided to supply the voltage to the suppressor and for the signal read-out. These are described in more detail in Section 5.3.3.

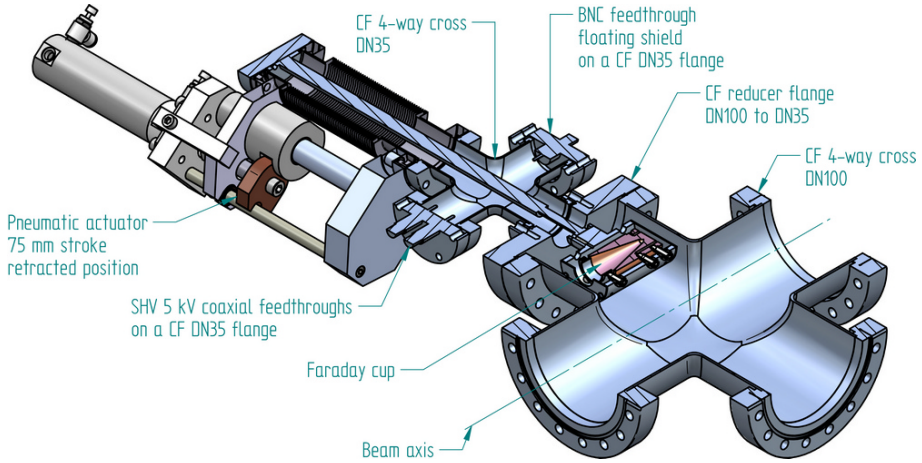

Figure 5.20: A cross-section view of the Faraday cup setup.

5.3.3 Electrical Design

Currents in the fA range are extremely difficult to measure already in the simplest setups due to theoretical and practical noise limitations [241]. The situation is far more complicated in a real accelerator where many noise sources, such as vacuum-to-air feedthroughs, long cables or vibrating vacuum pumps, cannot be eliminated. In addition, the USR extraction schemes will lead to a variable time structure and different peak intensities.

To overcome the difficulties with the measurements under different beam delivery schemes, a variable gain transimpedance amplifier DLPCA-200 from FEMTO [250] was purchased. It offers several gain and bandwidth settings of which three are summarized in Table 5.1. The gain of either 10^6 or 10^7 V/A is sufficiently high for sub-μA bunched

beam peak currents, whereas the rise/fall time is short enough to sample the inner bunch structure. For sub-pA quasi-DC beams, the highest sensitivity can be achieved with 10^{11} V/A and an internal low-pass filter with the upper cut-off frequency set to 10 Hz. For even higher sensitivity, an LCA-2-10T amplifier was also bought which can provide a gain of up to 10^{13} V/A and a narrow bandwidth as small as 0.1 Hz (–3 dB). The drawback, however, is a longer rise/fall time which for 0.1 Hz is 5 s. Also the maximum input current of ±1 pA at 10^{13} V/A limits the dynamic range of the detection system. Table 5.1 summarises the parameters of both FEMTO amplifiers.

	Fast extraction (DLPCA-200)		Slow extraction (DLPCA-200)	Slow extraction (LCA-2-10T)		
Gain setting	10^6 V/A	10^7 V/A	10^{11} V/A	10^{12} V/A	10^{13} V/A	
Maximum input current	±10 μA	±1 μA	±100 pA	±10 pA	±1 pA	
Upper cut-off frequency	500 kHz	400 kHz	1.1 kHz (10 Hz)	2 Hz	0.3 Hz	0.1 Hz
Rise/fall time (10% – 90%)	0.7 μs	0.9 μs	0.3 ms	0.2 s	1 s	5 s
Input noise per $\sqrt{\text{Hz}}$	1.8 pA	450 fA	4.3 fA	0.18 fA @ 0.2 Hz		

Table 5.1: Nominal parameters of DLPCA-200 and LCA-2-10T amplifiers as selected for different beam extraction schemes at the USR.

Only basic information on the circuitry of the FEMTO amplifiers is disclosed. The LCA-2-10T device uses 1 TΩ (10^{12} Ω) feedback resistor which is needed for the low-noise performance and high gain of the amplifier. The capacitance parallel to the resistor is as small as approximately 80 fF ($80 \cdot 10^{-15}$ F) in order to reach about 2 Hz bandwidth. The nominal bandwidth of DLPCA-200 is also guaranteed for any input capacitance up to 1 nF.

As discussed in Section 5.2.7, bending of cables and their length used in the low-current measurement setup should be minimised. However, the Faraday cup is a destructive monitor and needs to be retractable from the beam line. Its movement range is 75 mm and a sufficiently long cable is necessary. The cable will also bend due to the repositioning of the detector. Although the effect is undesirable for femtoampere current measurements, it cannot be avoided unless the Faraday cup is used as a fixed beam dump at the end of a beam line.

A triaxial cable provides double screening which reduces noise caused by ground

loops and other parasitic effects. Unfortunately, triaxal cables and corresponding feedthroughs are not available for the UHV of about 10^{-11} mbar under which the Faraday cup will be operated. For this reason, a custom-made Kapton-insulated, 50 Ω coaxial cable with an additional stainless steel screen was prepared. It includes an Accufast 875 connector, see Fig. 5.21, for a floating BNC vacuum feedthrough used in the setup shown in Fig. 5.20. The amplifier is connected directly to the air-side BNC connector of the feedthrough.

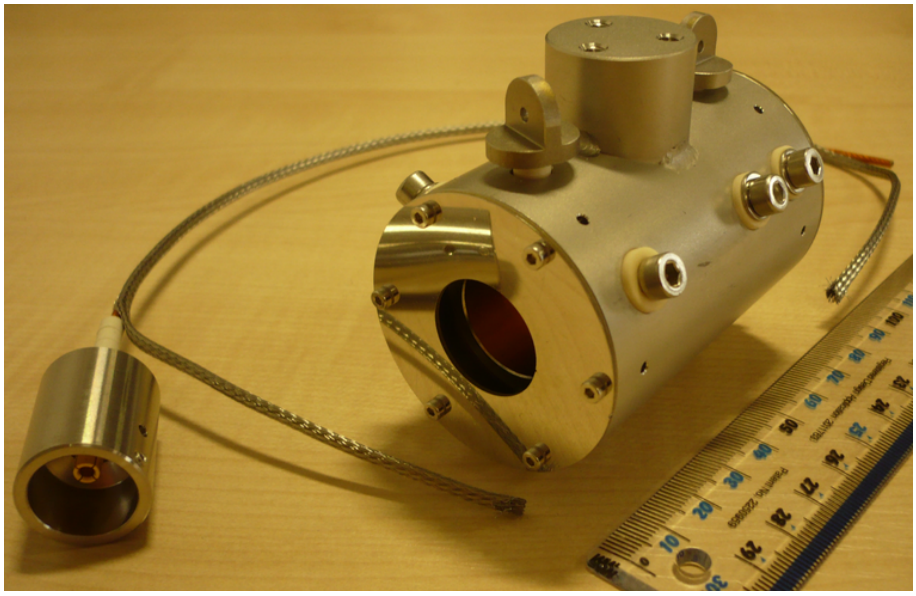

Figure 5.21: A photograph of the Faraday cup and the custom-made signal cable for UHV measurements.

It is important to properly shield and guard the signal. The shielding is ensured by the stainless steel braid grounded at its both ends to the vacuum chamber. The guarding is achieved by the inner shield grounded at the side of the amplifier and left floating at the Faraday cup side. This way, the voltage potential of the signal conductor is very close to the voltage potential of the inner shield which is set to zero.

For the suppressing electrode, an SHV feedthrough and a standard Kapton-insulated wire is used. The negative voltage required for the efficient suppression of secondary electrons is of the order of a few hundred volts. The HV power supply unit used for the suppressor electrode is DPS from ISEG [251] with a switchable polarity output variable up to 3 kV/4 mA and a peak-to-peak ripple less than 2 mV. A flange with two SHV feedthroughs is used in case one needs to connect two wires to the suppressor and

be able to check the voltage and connections without breaking the vacuum. A similar solution for the signal path was avoided in order to reduce additional ground loops and noise sources.

The electrical connections at the Faraday cup side were ensured by the large size connectors shown in Fig. 5.21, but the setup has been simplified. It is easier to connect the wires with small screws outside the detector shield, but several potential problems arise in such a configuration. The signal path and the Faraday cup itself are carefully shielded, whereas the large connectors are completely exposed. The connector providing the suppressing voltage introduces an electric field outside the beam monitor and the other connector attached to the beam collector can pick up additional noise. In the final design, the connectors are removed and the wires are attached directly to the components of the Faraday cup. For similar reasons, the stainless steel screws supporting the beam stopper and suppressor were replaced with ceramic screws.

5.4 Experiments with Electrons

5.4.1 Experimental Setup

Initial tests of the Faraday cup were performed with a small test stand equipped with an electron gun, a set of vacuum pumps, a vacuum window covered with phosphor and a vacuum gauge. The beam current monitor, as it was installed in the experiment, is shown in Fig. 5.22. The main 4-way cross vacuum vessel was fixed on a supporting frame and the electron gun, ELS5000 from PSP Vacuum Technology [252], was attached to the flange facing the Faraday cup entrance. The turbomolecular pump, TMU 200M from Pfeiffer [253], was mounted to the bottom flange and a flexible hose connected it with the piston pump, XtraDry 250-1 from Pfeiffer, placed on the floor. Downstream the beam current monitor, a T-shaped vacuum component was used to provide flanges for the vacuum window and the vacuum gauge. The latter was installed perpendicularly to the beam axis, thus it was not exposed to the main beam. The vacuum gauge, Pirani type from Pfeiffer, indicated that the vacuum of $7 \cdot 10^{-8}$ mbar was reached. The transimpedance amplifier, either DLPCA-200 or LCA-2-10T, was connected to the BNC feedthrough and the resulting output voltage was registered by a 60 MHz 8-bit oscilloscope, TDS 2004B from Tektronix [254].

With the Faraday cup retracted from the main vessel, the beam was stopped in the vacuum window placed in the back of the setup. The inner surface of the glass was covered with the phosphor powder, ESPI 311 P31 ZnS:Cu from ESPI Metals [255]. The

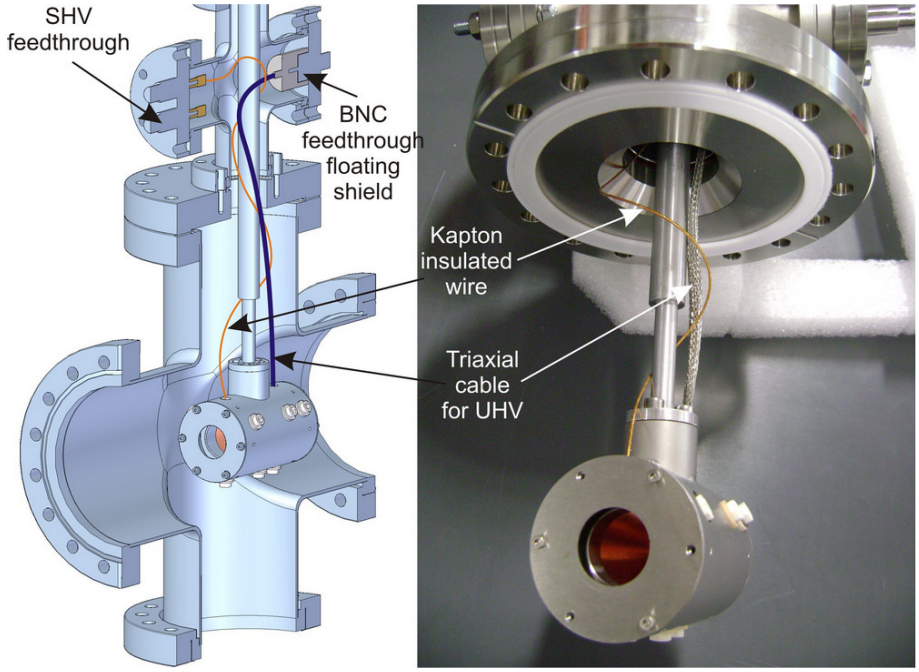

Figure 5.22: The Faraday cup installed as a part of the test stand.

electrons hitting it produced visible light which was used for beam imaging. However, the phosphor layer was not uniform and no camera was used to register the images, thus only approximate and qualitative observations were possible. It was sufficient to assess whether the beam was present, positioned on the axis and focused enough to be collected by the Faraday cup.

In order to control the intensity, energy, focusing and steering of the beam, the ELS5000 electronic unit with precision 10-turn potentiometers and a digital read-out was used. Electrons were thermionically emitted from the sharply bent tip of the heated filament and attracted to the anode. By changing the filament current and the extraction voltage, different beam currents and energies were achieved. The potentiometers enabled setting the filament current from 0 to 2.8 A, and the electron extraction voltage from 0 to 5 kV. The ELS5000 source had been designed to deliver electron beams with spot size < 50 μm diameter from approximately 1 keV to 5 keV and sample currents from 10 nA to 10 μA. However, it can produce beams also at kinetic energies as low as 50 eV with a lower maximum current and a larger minimum spot size [256]. The beam intensity depends on the initial flux of the emitted electrons and their transmission through the apertures of the electron gun components. It is therefore dependent on

the filament current, extraction voltage and beam focussing. However, no calibrated device was available to test the beam parameters independently.

The femtoampere current range was obtained by operating the electron gun under non-standard conditions without additional attenuators introduced in the beam path. First, an electron beam with a parameter setting corresponding to an intensity in the μA range [256] was directed onto the phosphorised glass and a beam image was obtained in the centre of the vacuum window. Afterwards, the Faraday cup was moved in and a voltage of –100 V was applied to the secondary electrons suppressor. With the DLPCA-200 amplifier and the 10^6 V/A gain setting, beam intensities of a few μA were observed. A more strict demonstration of the absolute character of the measurement was not possible at this stage, because the true current values of the generated beams were not known. Still, the performance of the Faraday cup was investigated. To achieve the lowest possible intensities, the filament current was decreased until no signal could be detected by the beam current monitor with the highest gain.

5.4.2 Results with Electrons

In all the experiments, the voltage output delivered by the transimpedance amplifier was registered by the oscilloscope and the beam current I was calculated as:

$$I = \frac{U}{G}, \tag{5.17}$$

where U is the measured voltage and G is the amplifier gain. The uncertainty of the current value was derived from:

$$\Delta I = \sqrt{\left(\frac{\partial I}{\partial U} \cdot \Delta U\right)^2 + \left(\frac{\partial I}{\partial G} \cdot \Delta G\right)^2}, \tag{5.18}$$

where ΔU and ΔG are the uncertainties of the voltage and gain, respectively.

Initially, the performance of the Faraday cup under vacuum without the beam was investigated. The DLPCA-200 current-to-voltage converter with 10^{11} V/A gain and 10 Hz bandwidth was used. It was fixed to the test stand frame and a 15 cm long BNC cable had to be employed to connect it to the BNC feedthrough. The baseline of the output voltage was set to zero by the offset potentiometer of the amplifier. Also the large unshielded connectors shown in Fig. 5.19 were still part of the assembly at this stage of the experiments. As can be seen in Fig. 5.23, significant noise was present in the system. The main noise contribution was at around 50 Hz and its harmonics

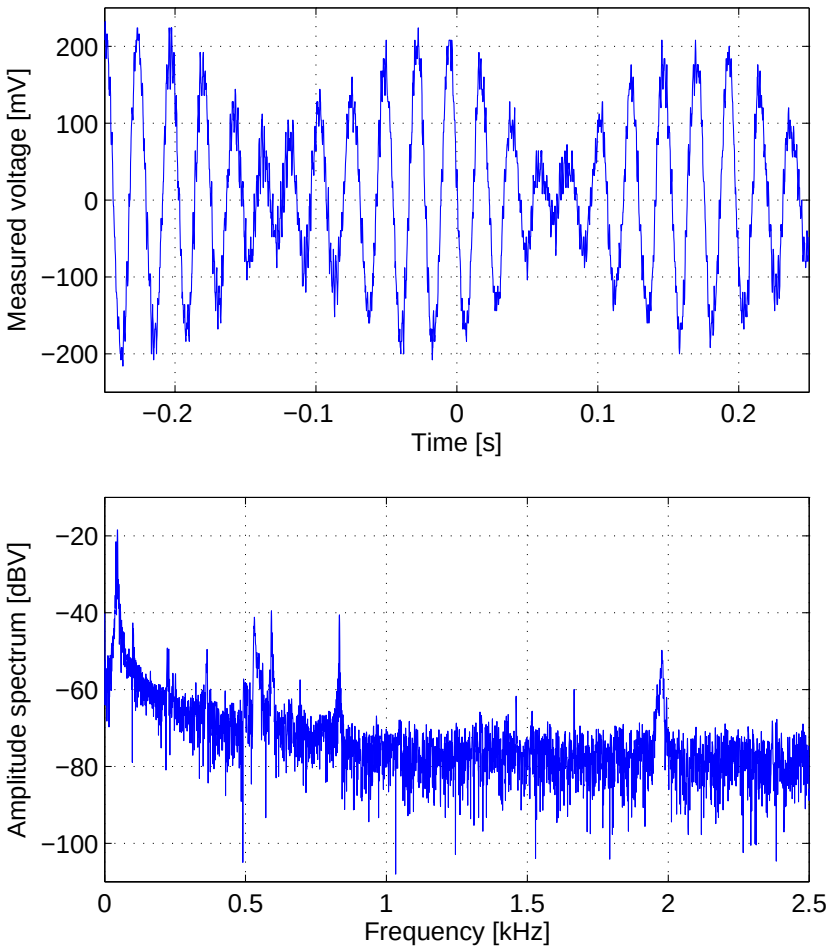

Figure 5.23: Initial Faraday cup response in the absence of the beam for 10^{12} V/A gain and 10 Hz bandwidth: time domain (top) and frequency domain (bottom).

which corresponds to the mains frequency. The resulting peak-to-peak noise was about 400 fA.

In order to improve the performance of the beam current monitor, several changes have been introduced in the setup. The unshielded connectors at the detector side have been removed and the wires have been placed inside the Faraday cup shield. Attention was paid also when installing the shielding and guarding of the signal wire. The DLPCA-200 unit has been replaced by LCA-2-10T which offers a lower bandwidth and input noise, see Table 5.1. The bandwidth of 0.1 Hz and the gain of 10^{12} V/A were chosen. Finally, the amplifier has been moved closer to the detector by connecting it directly to the BNC feedthrough. As a result, the noise was reduced by approximately

a factor of 10 which corresponds to the peak-to-peak value of about 40 fA.

To be able to detect the lowest DC currents, the baseline shift was measured. First, the background baseline without the beam was determined. Next, a DC component of the signal obtained with the beam was derived from the average over 16 seconds. The acquisition time was set on the scope as the power of 2 closest to the slow extraction time scale of the order of tens of seconds. The background offset was subtracted from the average and the result was saved as a function of time. Figure 5.24 shows the resulting plots for two different filament current settings.

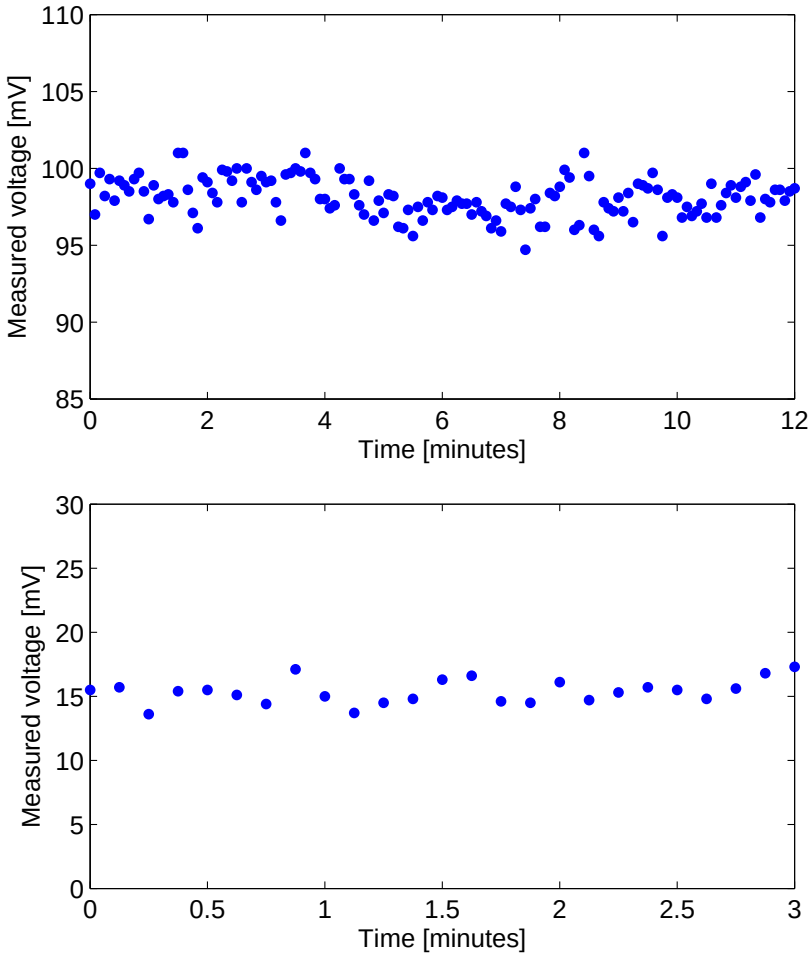

Figure 5.24: Electron beam current as measuremed at 1 kV extraction voltage and different filament currents: 2.13 A (top) and 2.10 A (bottom). The same transimpedance gain of 10^{12} V/A is used in both cases and each point is averaged over 16 s.

Assuming no significant losses and that the nominal gain of the amplifier is within

the specified accuracy of ±2%, a beam current of about 100 fA and as as low as approximately 15 fA was detected. The measurements presented in Fig. 5.24 were carried out a few minutes after the beam was switched on, hence no variation of temperature was expected. The results show high reproducibility with time and correspond to 97.7 ± 2.3 fA and 14.6 ± 0.9 fA.

The operation of the electron gun with the filament current below its nominal operation range met some difficulties. Electron emission is a thermal phenomenon and was not a linear function of filament current below 2.4 A. A small decrease in this current resulted in a significant decrease of emitted electrons. In addition, analogue control of the gun offered only limited precision in pre-setting the parameters. For these reasons, it was not possible to precisely set or reproduce the given beam intensity. For example, a change from 2.10 A to 2.13 A, as shown by the digital read-out, corresponded to a non-linear variation of the signal within one order of magnitude. However, the lack of repeatability was a property of the electron gun and not the Faraday cup. As can be seen in Fig. 5.24, the beam was measured in a reproducible manner at fixed filament current. Time scales for measurements at about 100 fA and 15 fA were chosen arbitrarily as only a general behaviour for times longer than a minute was investigated. Further studies can be carried out for daily, weekly, monthly or annual reproducibility.

5.5 Experiments with Protons

5.5.1 Experimental Setup

The response of the Faraday cup was investigated also with keV protons available at INFN-LNS. The 450 kV injector of the Tandem accelerator [167], described previously in Chapter 3, was employed as the particles source. Because the measurements with the Faraday cup were done two years after the experiments with the scintillating screens, the arrangement of the components in the beam line was slightly different. It is shown in Fig. 5.25.

Downstream the ion source and 90° to the analysing magnet, a pair of X and Y variable slits were used as collimators. The Faraday cup, labelled FC1 in Chapter 3, was moved downstream of the slits. It was followed by the two removable pepper-pot grids for intensity reduction, the same used previously during the measurements with the scintillators. The second Faraday cup (FC2) was moved closer to the attenuating grids. For the purpose of the experimental tests, it was replaced by the Faraday cup prototype for the USR. The final vacuum level reached in the beam line was 10^{-7} mbar.

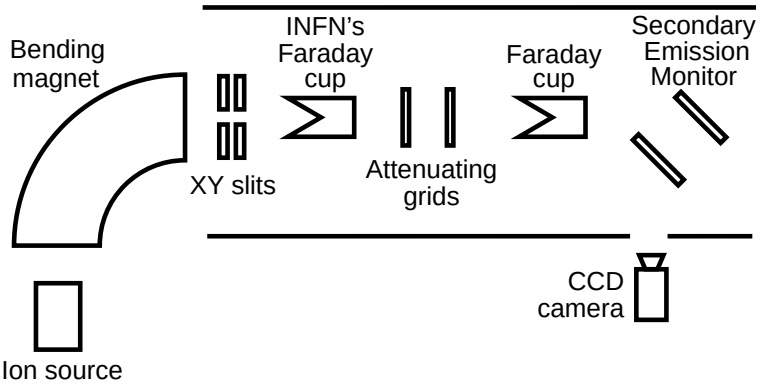

Figure 5.25: Experimental setup for the Faraday cup and secondary emission monitor tests at INFN-LNS.

In addition, a new profile monitor, called secondary emission monitor, was installed downstream of the Faraday cup and tested in parallel. It was placed in the vessel equipped with a vacuum window and a CCD camera, used previously for scintillating screens investigations. The design and performance of the detector are presented in Chapter 6.

The beam energy was set to 200 keV and its intensity was lowered to the pA level. Femtoampere currents were obtained by defocusing the beam and employing both the collimators and pepper-pot attenuators. Consequently, different intensities were observed at the beginning of the beam line and at the location of the USR prototypes a few metres away. It limited the application of the INFN-LNS Faraday cup as a reference monitor which was used for the initial beam setting but not for an absolute calibration. Furthermore, it was not suitable for the measurements of currents below a few pA.

Due to time constraints, only the LCA-2-10T amplifier with the lowest bandwidth of 0.1 Hz was tested. In parallel to the low-energy experiments, a high-energy beam was delivered to a neighbouring area and the time allocated for entering the radiation zone was reduced. Because each modification to the setup required following a lengthy procedure and two beam monitors were under investigation in parallel, it was not possible to test all configurations. Also the commercial amplifier was not controlled remotely due to limitation of infrastructure and it was practical to test only its lowest bandwidth setting. The amplified signals were transferred to the control room and registered by a 1 GHz 8-bit oscilloscope, WS104MXs-A WaveSurfer from LeCroy.

5.5.2 Results with Protons

The procedure of beam current measurements with protons was similar to the tests done with electrons. For a given combination of the beam steering parameters and the pepper-pot grids used, the resulting beam intensity was registered by the Faraday cup. The voltage output of the transimpedance amplifier was observed on a digital oscilloscope and analysed in both, the time and frequency domain. The Faraday cup with either 10^{12} V/A or 10^{13} V/A transimpedance gain was able to measure DC beams, but currents exceeding 10 pA or 1 pA, respectively, saturated the amplifier and could not be properly registered. Additional work was done to find the required minimum suppressing voltage and to assess the response of the system to bunches of a finite length.

Suppressing Voltage

The influence of secondary electrons emission on the proton beam current measurements was studied with different voltages applied to the suppressing electrode. Average beam currents were measured by the Faraday cup at various suppression voltage values and the results are shown in Fig. 5.26. The signal measured without suppression was 75% higher than for the fully suppressed secondaries. The ejection of electrons from the detector results in a higher positive charge in the beam collector and gives rise to the current flow in the system. The reading is therefore falsified by the amount of the charge carried away by the secondary electrons. Above around –100 V, the effect is minimised and the actual beam current is measured. All the following tests were done at a fixed suppression voltage of –300 V, well above the required value.

Time and Frequency Domain

The response of the Faraday cup to DC beams and bunches of a finite length was investigated. The beam delivered by the INFN-LNS injector was continuous and no RF buncher was available to modulate it. However, the primary Faraday cup installed on a pneumatic actuator was used as a beam chopper. It was moved in and out, and the resulting signals at various beam currents were registered to evaluate how the bandwidth and noise affect the performance of the Faraday cup. Two examples of the observed chopped beams are given in Fig. 5.27 and 5.28.

Fig. 5.27 shows a waveform registered at 10^{12} V/A gain and corresponds to the beam current of the order of 500 fA. The time between about -13 s and 10 s is when the beam

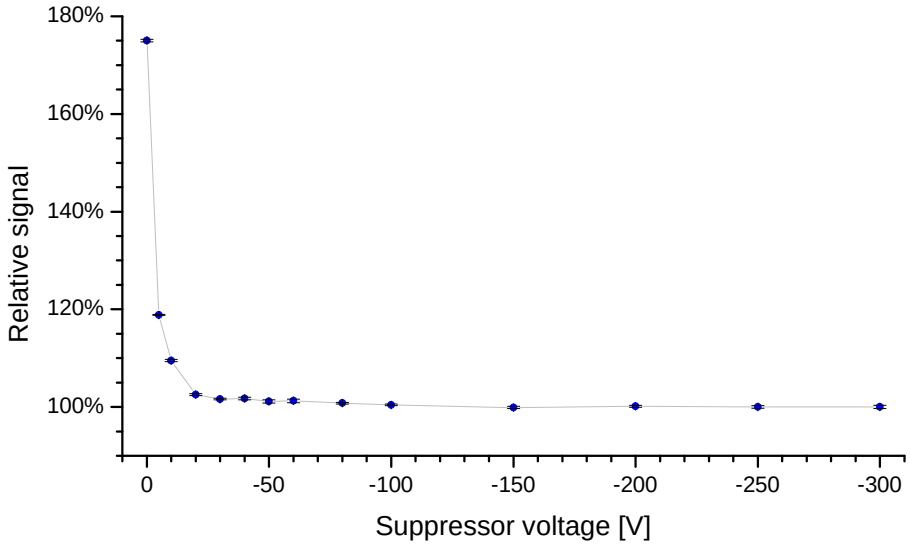

Figure 5.26: The suppression of secondary electrons as a function of the voltage applied to the suppressing electrode.

was delivered to the USR Faraday cup. The time outside this window corresponds to the beam stopped in the INFN-LNS monitor and not reaching the USR prototype. The time needed to move the beam stopper in or out was much shorter than a second and was small compared to the slow response of the FEMTO amplifier. The 10%–90% rise time of the signals corresponds to 5 s as specified by the manufacturer for 0.1 Hz bandwidth. The peak-to-peak noise of about 40 fA is present in the signal, but the rise and fall time of the pulse can be clearly noted.

The other example, given in Fig. 5.28, shows a waveform corresponding to the beam current of the order of 80 fA. The noise becomes a significant component of 50 fA peak-to-peak and the fluctuations make it more difficult to pinpoint the beginning and the end of the bunch. However, the form of the signal is still clear. The waveform was registered at 10^{13} V/A gain, but no difference in the signal-to-noise ratio was observed at 10^{12} V/A. It is because the amplification is done by the primary circuit related to 10^{12} V/A and an additional amplifier introduced at its output; consequently, both the signal and the noise are amplified and the SNR is not improved in the second stage.

In order to find possible noise sources affecting the performance of the monitor, the frequency spectra of the signals registered at various beam currents or without the beam (baseline) were calculated. As can be seen in Fig. 5.29, the noise related to the mains frequency of 50 Hz has been minimised, but other components are clearly

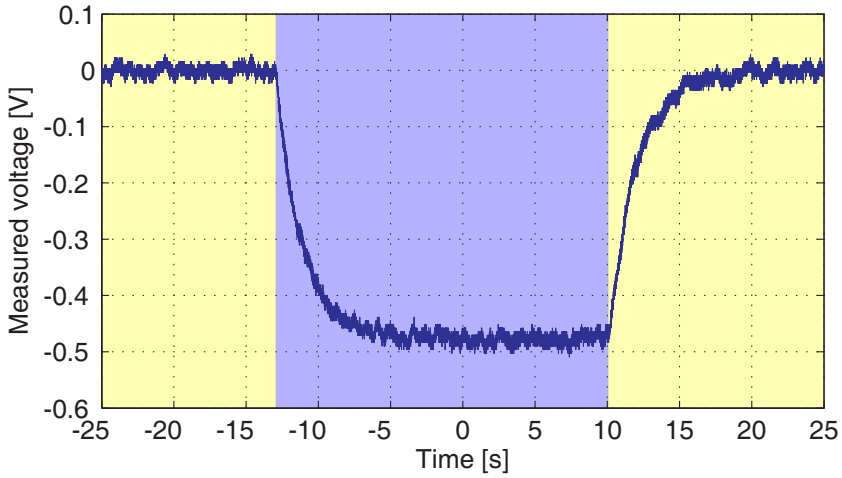

Figure 5.27: Response of the Faraday cup to a chopped beam registered for 10^{12} V/A gain.

visible in the spectra. The strongest influence on the monitor performance has a peak at around 13.5 Hz. Additionally, a frequency component around 165 Hz with two side bands is also registered by the Faraday cup. There is also a strong increase of noise below 4 Hz.

Although resolution of the Faraday cup is determined by the noise of the amplifier and its dependence on the analogue bandwidth, the frequencies present in the spectrum shown in Fig. 5.29 are also due to vibrational noise. Its sources cannot be easily identified, but Table 5.2 lists some of the most common causes of low-frequency noise in laboratory environment [257]. A few types of vacuum pumps were installed in the vicinity of the Faraday cup. It is likely that they were the main source of the noise picked up by the monitor, although other equipment was also used in or near the accelerator area.

Source	Frequency [Hz]
Air compressors	4 – 20
Pumps (incl. vacuum)	5 – 25
Building services	4 – 20
Foot traffic	0.5 – 6
Acoustics	100 – 1000
Transformers	50 – 400
Elevators	up to 40
Highway traffic	5 – 100

Table 5.2: Common vibration sources in a laboratory [257].

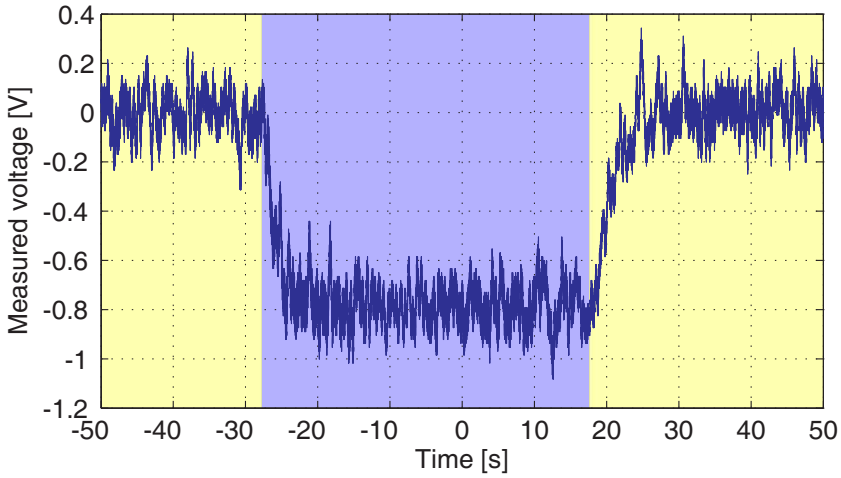

Figure 5.28: Response of the Faraday cup to a chopped beam registered for 10^{13} V/A gain.

Possible improvement of the Faraday cup system in the future should reduce the influence of the potential noise sources. Placing the monitor further away from the vacuum pumps seems to be crucial, but may not be possible due to limited space. Another aspect is the monitor design itself. The Faraday cup is attached to the actuator flange by means of a long rod which, perhaps, is likely to transfer the vibrations sensed by the detector. It may be worth verifying if the resonant frequency of the prototype is far from the noise frequency and if a more rigid design can be used. Furthermore, additional low-pass filtering with the upper cut-off frequency above a few Hz can be added to get rid of the noise components. Such a filter would have a negligible impact on the time response of the Faraday cup which is determined by the 0.1 Hz bandwidth of the FEMTO amplifier. However, the same result was obtained with the averaging method. Finally, the baseline noise, i.e. without the beam, can be subtracted as well.

Detection Limits

It is assumed that gross systematic errors influencing the Faraday cup response were ruled out and therefore that absolute measurements were performed. There were no predefined machine settings for the femtoampere currents and these could not be detected by the standard instrumentation installed in the beam line. However, it was possible to verify that the weak beams were delivered by observing them independently with a secondary emission monitor. The latter, although not calibrated in terms of absolute values, is clearly capable of detecting intensities well below 10^5 particles per

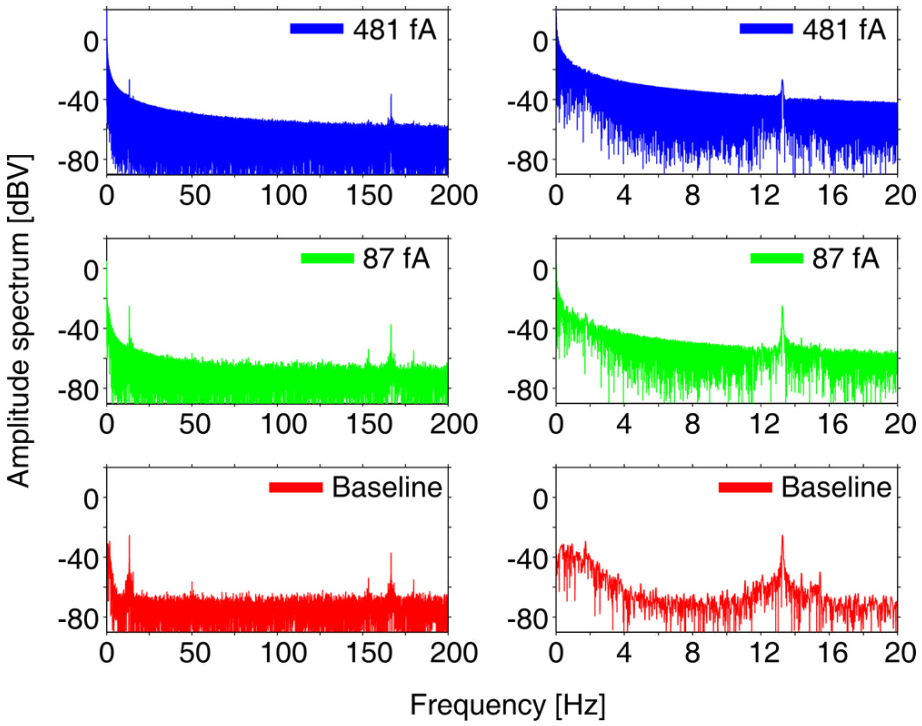

Figure 5.29: Frequency spectra to 200 Hz (left column) and 20 Hz (right column) of the signals registered at various beam currents at INFN-LNS. Both columns represent the same measurements, but the right one shows the low-frequency part in detail. Baseline is the measurement without the beam.

second, as it is shown in Chapter 6.

To investigate the detection limits of the Faraday cup prototype, the baseline shift measurements with additional averaging were performed. A similar procedure was used during the tests with electrons. First, the background baseline without the beam was determined. Afterwards, a DC component of the signal obtained with the beam was derived from the average over 20 seconds. The acquisition time was chosen to correspond to the slow extraction time scale of the order of tens of seconds. Various intensities were obtained by allowing only a fraction of protons to reach the monitor. Each time the current was set to an arbitrary level, the beam presence was verified by both, the USR Faraday cup and the secondary emission monitor. Fig. 5.30 shows different beam intensities as measured by the current monitor, from the level of about 500 fA to no beam at all. In order to study the reproducibility, the measurements were recorded over 10 minutes in each case and no drift of the results was observed. The results demonstrate that the DC beam currents as low as a few femtoamperes can by measured by the Faraday cup designed for the USR.

It should be noted that no independent method to measure absolute beam currents was used and it is assumed that the Faraday cup can be used as an absolute monitor without calibration. There were no monitors in the INFN-LNS beam line to measure such low intensities and the SEM did not provide absolute measurements. It could have been used to monitor relative change of beam current at least in terms of ratio as compared to Faraday cup measurements, but such information was not recorded as still not ensuring absolute verification of measured values.

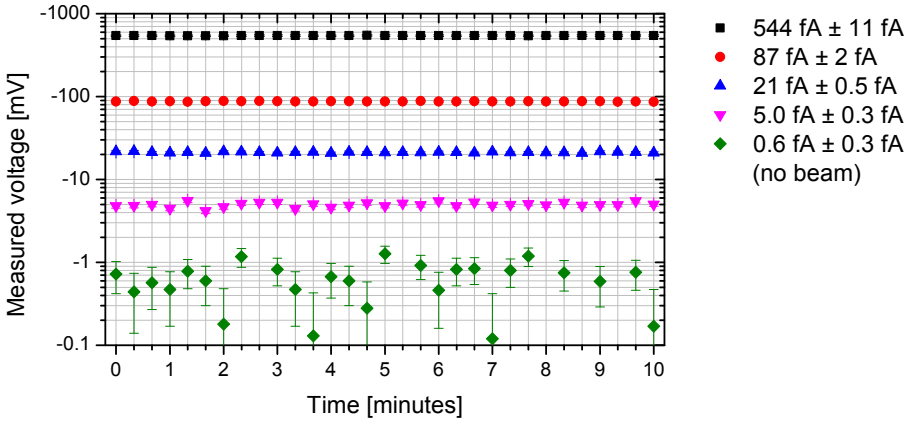

Figure 5.30: Beam current measurements at 10^{12} V/A transimpedance gain for various proton beam intensities at INFN-LNS. Each point is averaged over 20 s.

5.6 Summary and Perspectives

A prototype of a sensitive Faraday cup for femtoampere quasi-DC beam current measurements was designed and tested. All aspects of the project development were covered, including theoretical studies, computer simulations and optimisation, technical design and experimental verification.

The main motivation for the performed work was to provide a simple and reliable detector for absolute ultra-low current measurements suitable for high peak intensities at the same time. Other diagnostic techniques, such as electron multipliers, diamond detectors and current transformers, do not meet the requirements of the USR as they are either too fragile, too expensive, not sensitive enough or provide only relative information on the beam intensity. The purpose of this work was to identify the detection limits of the Faraday cup, known otherwise for its simplicity, robustness and reliability.

The underlying physical processes having an impact on the monitor performance and the absolute measurement accuracy were studied in detail. The interaction of the projectiles with the beam stopper was analysed in terms of their range in the medium, reflection from the surface and secondary particles generation. Although stopping of keV heavy charged particles requires only a thin layer of metal, the design of the Faraday cup had to solve the problem of the increased backscattering and emission of the charged secondaries. Both phenomena were studied theoretically and numerically, hence the optimised geometry of the beam collector with additional suppressing electrode was designed. Also possible noise sources were identified and special measures were taken to minimise their influence on the Faraday cup performance.

The mechanical and electrical design of the Faraday cup was prepared. The prototype can be integrated with a vacuum tube and is installed on an actuator, thus can be retracted from the beam line. It is a small and compact device designed to measure USR beams of up to 20 mm in diameter. However, it is possible to rescale the dimensions to make it applicable to different size beams. Two commercial amplifiers, DLPCA-200 and LCA-2-10T from FEMTO, were purchased for the system and offer a wide range of transimpedance gains and bandwidths. The in-vacuum electrical connections had to be designed, because no low-noise triaxial cables and connectors for the UHV exist on the market. The whole setup was assembled and installed first in a stand-alone test stand equipped with an electron gun. Later, it was also integrated with the low-energy beam line at INFN-LNS.

The initial experimental tests of the Faraday cup were performed with keV electrons

to verify the performance of the monitor in a vacuum environment. As a result of the study, it was possible to improve the sensitivity of the prototype and the peak-to-peak noise of the system was reduced from about 400 fA to 40 fA. Also the preliminary measurements gave a good idea of the capabilities of the system and average currents of 14.6 ± 0.9 fA were measured in a reproducible manner.

The main tests of the prototype were carried out with the group of Paolo Finocchiaro at INFN-LNS in Catania. It was possible to study the response of the monitor to 200 keV proton beams of various intensities in the femtoampere range. The influence of the suppressing voltage on the charge collection efficiency was analysed and the effect of a finite bunch length was evaluated. Finally, the detection limits of the Faraday cup were investigated. Due to the peak-to-peak noise of about 40 fA present in the system, the baseline detection after averaging over 20 seconds was performed. As a result, currents as low as 5.0 ± 0.3 fA were successfully measured. High stability of the system over the time of 10 minutes was also demonstrated.

The analysis of the results obtained during the tests shows that there is little room for improving the signal-to-noise ratio of the existing prototype. The resolution of the Faraday cup is determined by the noise of the amplifier in dependence of its analogue bandwidth. By limiting the band-pass of the system, the measurements uncertainty can be reduced but at the cost of its applicability to time varying beam pulses. The monitor is also sensitive to low-frequency noise present in accelerator environment and its sources, such as vacuum pumps, cannot be eliminated. In order to minimise their effect, the Faraday cup can be installed on a shorter, more rigid support. Ideally, it should be installed as close as possible to the feedthroughs to minimise the length of the signal cable and no actuation would be allowed. Perhaps also the chamber with the detector should be isolated from the noisy environment by means of an anti-vibration support. Additional low-pass filtering can be applied with a cut-off frequency above the bandwidth of interest, but this can also be obtained by averaging introduced in this work. Should a higher sensitivity with a shorter response time be required, other beam intensity monitors will have to be considered. These are summarised in Chapter 7.

For low-energy antiproton beams, which require non-destructive diagnostic techniques, other solutions have to be foreseen. The in-ring intensities are higher than femto- or picoamperes due to multiple revolutions of particles about the machine circumference, yet they are still too low for standard monitors, such as current transformers. It is possible to use signals measured by capacitive pick-ups, but these can provide

only relative values. However, the absolute number of protons after the first turn can be determined by a sensitive Faraday cup, used to calibrate the pick-up signals and then use them for non-destructive measurements of any beams stored in the USR. It is another important application of the destructive monitor described in this chapter.

Chapter 6

Secondary Emission Monitor

In this chapter, a prototype of a foil-based secondary emission monitor for beam profile measurements is presented. The first section gives the rationale for the studies and optimisation of the monitor. The following part introduces the detector operation principle and its subcomponents. Next, several design alternatives are considered. In order to verify the performance of the monitor, experiments with keV electrons and protons were performed and the results are presented in the following section. Finally, the outcome of the work is summarised and future perspectives are given.

6.1 Motivation

As shown in Chapter 3, scintillating screens can be very useful for low energy beam diagnostics, but they suffer from limited dynamic range and are not an ideal tool for antiproton beam monitoring. More complex monitors equipped with a microchannel plate (MCP) offer a variable amplification and their applicability to antiproton diagnostics has already been demonstrated [110, 112]. However, special care needs to be taken in order not to damage the MCP plates and the detector placed directly in the beam is fully destructive. For this reason, other configurations have been proposed to limit the perturbation of the beam and to spare the MCP from a direct beam hit [95, 115–118].

One of the solutions to measure the beam profile with microchannel plates is based on the detection of secondary electrons emitted from a foil intercepting the primary beam. In such a system, the MCP is placed at some distance from the beam and only secondaries can reach its surface. They need to be guided in a region of a strong electric field which in turn can affect the primary beam as well. This is not a problem in high-energy or heavy-ion applications, but becomes very important for keV proton

or antiproton beams. Also, the annihilation of antiprotons results in emission of other high energy particles which may affect the response of the monitor. It was the main goal of this work to investigate into the limitations of a foil-based secondary electron emission monitor and test its usability for keV beam imaging.

6.2 Principle of Operation

6.2.1 Secondary Emission Monitor Working Principle

A foil-based SEM consists of a grounded mesh and a foil on negative potential, an MCP with a phosphor screen and a CCD camera recording the image. Its schematic diagram is shown in Fig. 6.1.

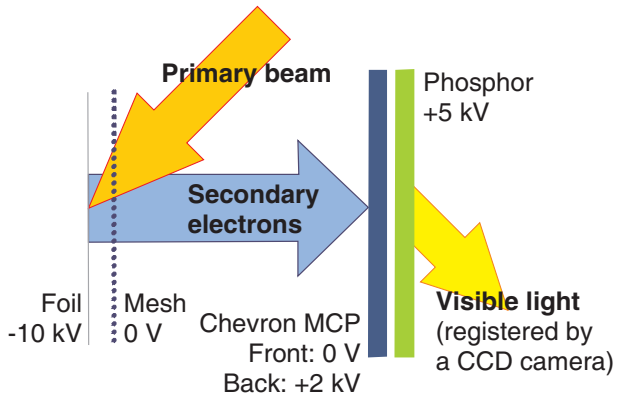

Figure 6.1: Operation principle of a foil-based secondary emission monitor.

The primary beam passes through the mesh at 45° and ejects eV-range secondary electrons from the foil surface. These secondaries are accelerated towards the mesh by the negative voltage applied to the foil. By the time they reach the mesh, they are already highly directional and fly towards the detection system. There, they are multiplied by the microchannel plate and converted to visible light by the phosphor screen producing a beam image which can be recorded by a CCD camera.

6.2.2 Secondary Electron Emission and Guidance

The phenomenon of secondary electrons emission is discussed in detail in Section 5.2.4. The secondaries are emitted from the first few atomic layers of a solid body, thus the thickness of a foil, or even a plate, does not play an important role in their production. The energy of these electrons is concentrated around a few eV with a FWHM value

of the same order of magnitude. These low energy peaks contain about 85% of the emitted particles. The angular distribution of emitted electrons tends to obey a cosine shape independent of the incidence angle of the primary beam [236]. However, their yield depends not only on the target material used, see Fig. 5.10, but also on its purity and oxidisation.

Emitted electrons need to be guided from the emission points to the detection system in a way that preserves information on their origin. By applying a negative voltage to the foil, low energy secondaries are repelled from the surface towards the mesh. With a voltage difference of some kV and a distance of a few mm, the electrons can gain about 1 keV/mm. When they cross the mesh and exit the region of acceleration, they travel towards the detection system almost perpendicularly to the foil surface carrying spatial information on the primary beam profile.

The foil and mesh assembly should be optimised in terms of the minimal primary beam disturbance as well as the highest secondary electron emission and focusing. The ideal mesh would introduce no leakage field outside the region of high gradient and be transparent to primary and secondary particles; the foil would produce a maximum number of secondary electrons and perturb the primary beam to a minimum degree. In the ideal case, no antiprotons would be stopped in the assembly to minimise the number of annihilation products that can reach the detection system.

6.2.3 Secondary Electron Detection

The secondary electron detection system comprises an image intensifier MCP coupled to a phosphor screen, viewed with a CCD camera.

The principle of MCP operation was introduced in Section 2.2.4. Two MCPs stacked together constitute the so-called "chevron type" MCP and offer a gain of the order of 10^7. If the plates are impedance matched, a single 2 kV supply can be used to bias the MCP assembly, because the voltage will be uniformly distributed. Otherwise, either a voltage divider or two independent 1 kV supplies should be provided.

Multiplied electrons leaving the MCP are directed onto a scintillating screen where they are converted to photons. Usually, a thin layer of inorganic phosphor powder deposited onto a glass plate is used. Such a configuration enables visible light created in the 10 – 15 μm phosphor layer to pass through the glass and be recorded by a CCD camera. The phosphor is aluminised, thus up to about 5 kV can be applied to its surface to accelerate incoming electrons and increase the energy transferred to the phosphor. The Al layer is typically only 250 – 500 Å thick.

6.3 Design Considerations

6.3.1 Considerations for Primary keV Beams

A low-energy beam can be affected by the monitor in various ways: particles can be scattered, change their trajectories in the presence of an electric field or lose a considerable fraction of their energy and eventually be stopped in the mesh and foil assembly. These effects can cause beam loss, but also introduce strong distortions to the image of the real beam profile.

Range in Matter and Scattering

At low energies, the range of antiprotons and protons in matter differs. Particles of negative charge are subject to lower stopping power than their positive counterparts due to polarization of target electrons. As a result, the penetration depth for antiprotons is slightly larger than for protons at the corresponding energy. The phenomenon is known as Barkas effect and has been extensively studied for low energy particles in the last years [218–220]. The difference in proton and antiproton stopping powers is shown in Fig. 6.2.

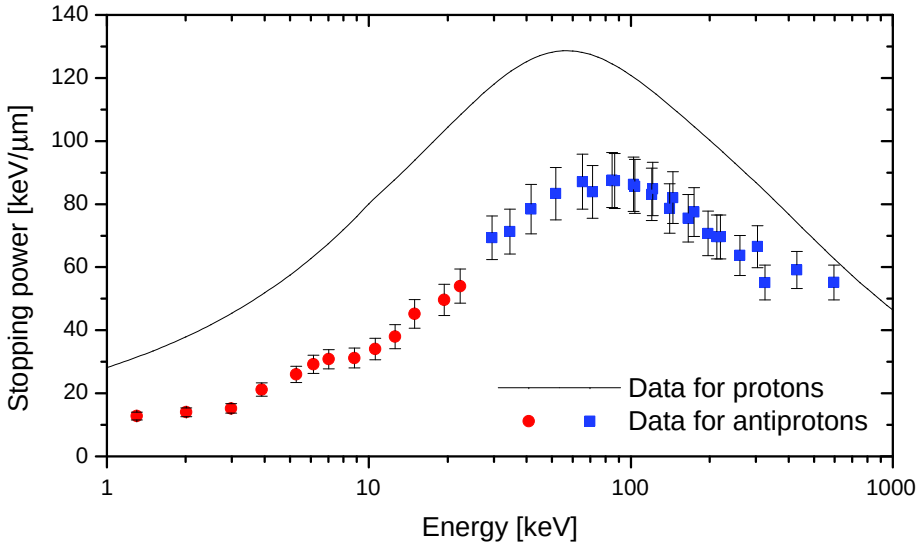

Figure 6.2: Stopping power of protons [57] and antiprotons [219] in aluminium.

The stopping power S can be used to calculate the continuous slowing-down approximation (CSDA) range, that is the mean path length of the particle as it slows

down to rest:

$$R_{CSDA}(E) = \int_0^E \frac{dE'}{S(E')}, \tag{6.1}$$

where E is the particle energy. For example, the CSDA range for protons in aluminium is 3 µm at 300 keV and 0.3 µm at 20 keV [57], whereas for antiprotons it is about 4.5 µm at 300 keV and approximately 0.8 µm at 20 keV. Due to multiple scattering effects, however, the penetration depth of particles is lower and for protons drops to 2.8 µm at 300 keV and 0.2 µm at 20 keV [57]. Furthermore, even thinner layers are expected to disturb the beam and lead to its loss. This is qualitatively shown in Fig. 6.3.

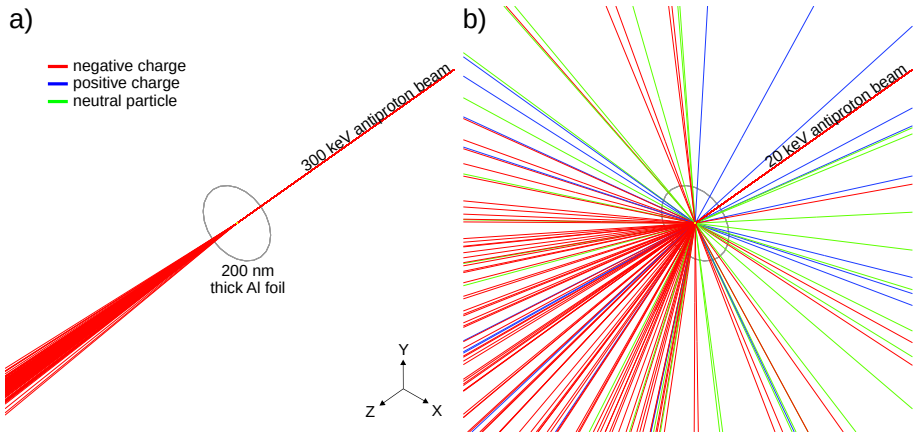

Figure 6.3: Qualitative simulations of 300 keV (a) and 20 keV (b) antiprotons interaction with a 200 nm thick aluminium foil. See text for details.

The influence of a thin aluminium foil on low energy antiprotons was simulated with Geant4 [244, 245]. A pencil-like beam of antiprotons impinges on an aluminium disk, 50 mm in diameter and 200 nm thick, at normal incidence; the resulting trajectories of primary and secondary particles are shown in Fig. 6.3. No secondary eV electron emission is modelled in Geant4, but scattering and annihilation can be observed. Because 300 keV antiprotons are not stopped in the target material, their behaviour is similar to protons at the corresponding energy. However, annihilation introduces a significant change in the picture for 20 keV antiprotons. Not only does the low energy beam blow up, but also annihilation products emerge from the foil in random directions. It can be concluded that even a 200 nm foil makes the SEM a destructive beam monitor. It can be used in beam transfer lines and for first turn diagnostics, but needs to be optimised for minimal image distortion due to electric fields and annihilation products noise.

Perturbation in an Electric Field

A simple model of the SEM assembly was studied with SIMION [247]. The foil and mesh were approximated by two parallel circular disks of 50 mm diameter and separated by 5 mm. In addition, the foil was clamped with a thin ring at its edges and the whole object was on a negative potential of up to –10 kV. The grounded mesh surface was made transparent to the beam. Approximately 50 mm away from the foil, a simplified MCP and phosphor assembly was located with 0 volts and 2 kV applied to the front and the back of the microchannel plate, respectively, and 5 kV applied to the scintillating screen. Finally, electric fields generated by the monitor in its surroundings were computed.

The resulting field map was used for particle tracking, performed also in SIMION, to study the influence of the monitor on the primary beams. A point source of particles was located at a distance of about 20 cm from the centre of the foil. Particles of either positive or negative charge and various energies were emitted in a small angle of 1° around the beam axis and their trajectories were recorded. The results are shown in Fig. 6.4.

For 300 keV particles and the highest voltages applied to the monitor, see Fig. 6.4a, the beams are only slightly perturbed. Their centres hit the foil 0.6 mm away from the reference trajectory and the shift direction depends on the charge of the particles. Positive protons are attracted by the foil, whereas negative antiprotons are repelled, thus the latter follow a slightly longer path. The influence of the monitor on 20 keV beams is much stronger and results in a shift of the proton beam centre by almost 8 mm, whereas 20 keV antiprotons do not hit the foil at all, see Fig. 6.4b. With the foil voltage decreased from –10 kV to –5 kV, see Fig. 6.4c, the distortion of initial trajectories is reduced, but still reaches about 4 mm and 5 mm for protons and antiprotons, respectively.

In order to minimise the influence of the electric fields of the SEM on the primary beams, additional shielding was included in the model. As shown in Fig. 6.5, the foil is surrounded by grounded walls with an exit window in the back to let the high energy beams go through unaffected. In the low energy mode, the back is covered by either a mesh or a foil. Also the electric fields around the MCP and phosphor assembly are screened by additional grounded walls. Furthermore, they protect the back of the assembly from the direct beam hit.

In the case of –10 kV applied to foil, a 20 keV proton beam centre is deflected by 0.8 mm, but antiprotons are still too strongly repelled and a significant fraction of the

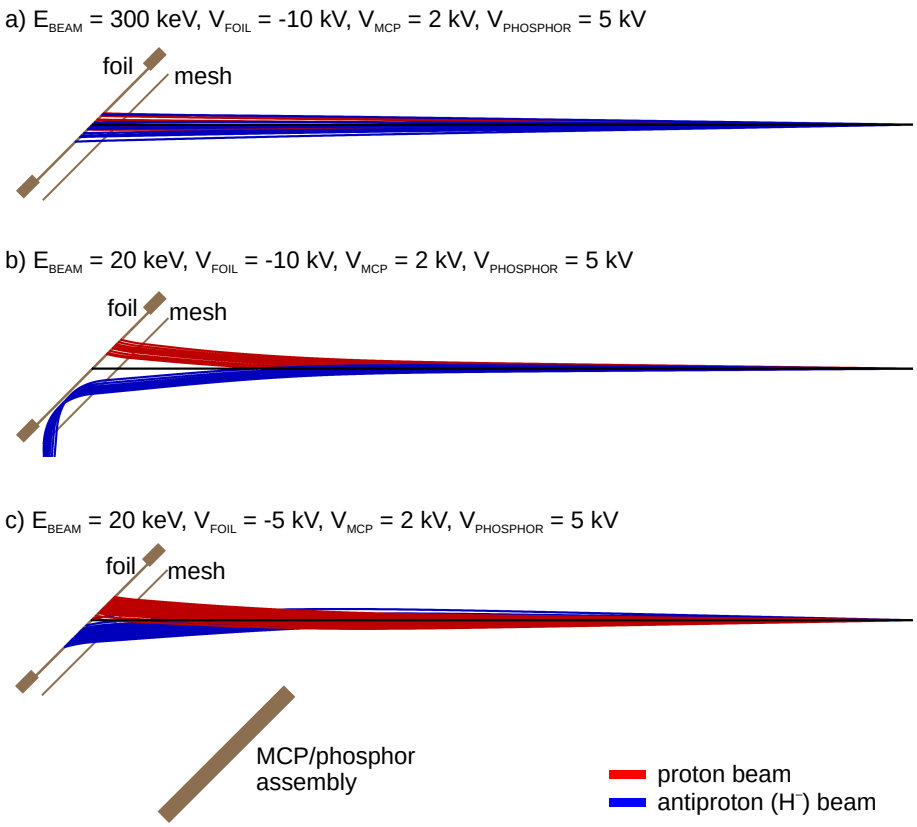

Figure 6.4: SEM influence on the primary beams for various beam energies and foil voltages as modelled in Simion: a) 300 keV and –10 kV, b) 20 keV and –10 kV, and c) 20 keV and –5 kV. The MCP at 2 kV and phosphor at 5 kV were present in all simulations but are shown only in the last figure.

beam is bent away from the monitor, see Fig. 6.5a. With the voltage reduced to -5 kV, both beams reach the foil and their displacement is 0.5 mm and 0.9 mm for protons and antiprotons, respectively, see Fig. 6.5b.

6.3.2 Considerations for Secondary Particles

The principle of SEM operation is based on imaging secondary electrons emitted from a surface bombarded with primary particles. A proper guidance of secondary electrons is, therefore, an important part of the detector optimisation.

In the case of antiprotons, a further challenge arises due to annihilation products, such as pions and recoil ions. These particles emerge in random direction and cannot be easily guided, thus contribute to the overall noise of the system.

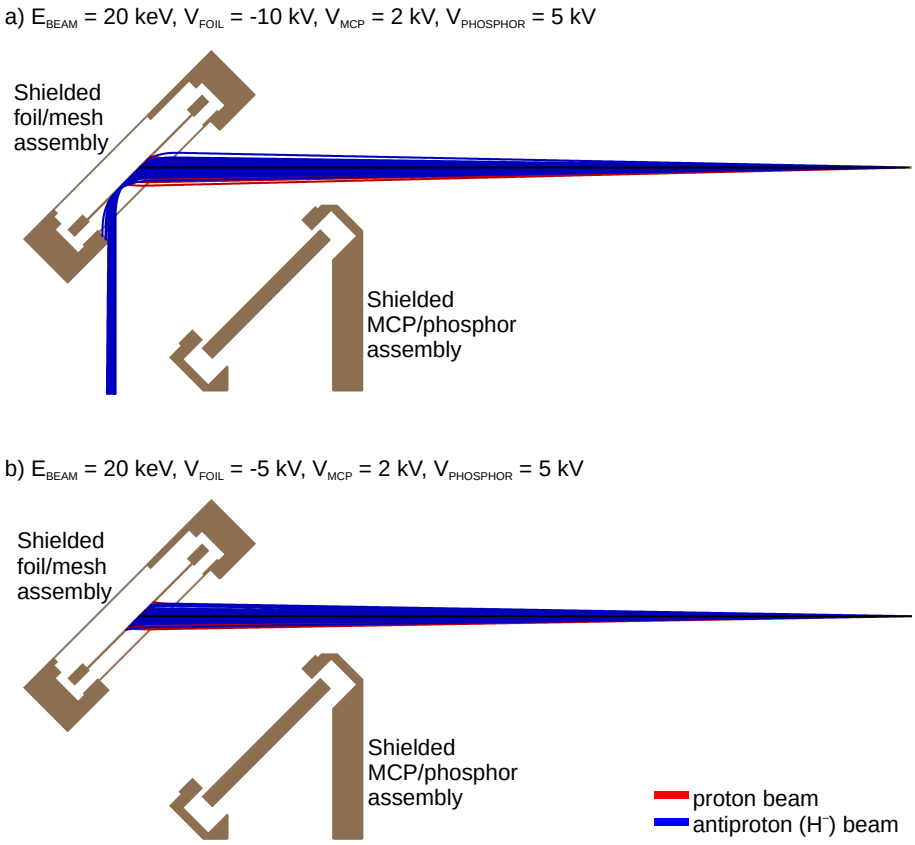

Figure 6.5: Shielded SEM influence on the 20 keV primary beams for various foil voltages as modelled in Simion: a) –10 kV, and b) –5 kV.

Secondary Electrons

In order to verify the capability of the monitor to image a primary beam profile, transport of secondary electrons from the foil to the detection system was studied. A Monte Carlo routine was written for SIMION, see Appendix A, to generate electrons at the foil surface and thus emulate secondary emission. A point source of electrons was defined and the particles were tracked through the electric field until stopped in the MCP. Their angular distribution was defined as a cosine distribution with the peak emission direction normal to the foil surface [236]. The energy distribution followed the spectrum for clean aluminium presented in [258]. Both distributions are shown in Fig. 6.6, whereas the SIMION model used in the study is presented in Fig. 6.7. Initially, the mesh was approximated by a plane of zero voltage fully transparent to particles ("ideal mesh"), but also a more realistic model was implemented.

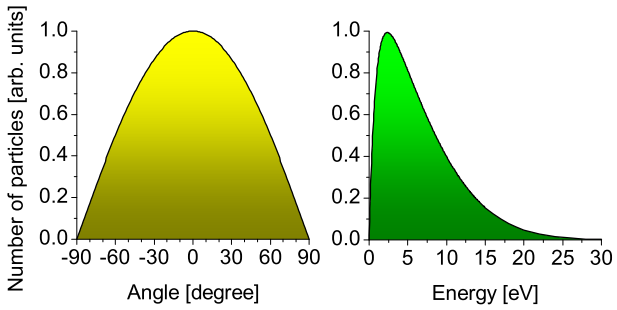

Figure 6.6: Angular (left) and energy distribution (right) of simulated secondary electrons.

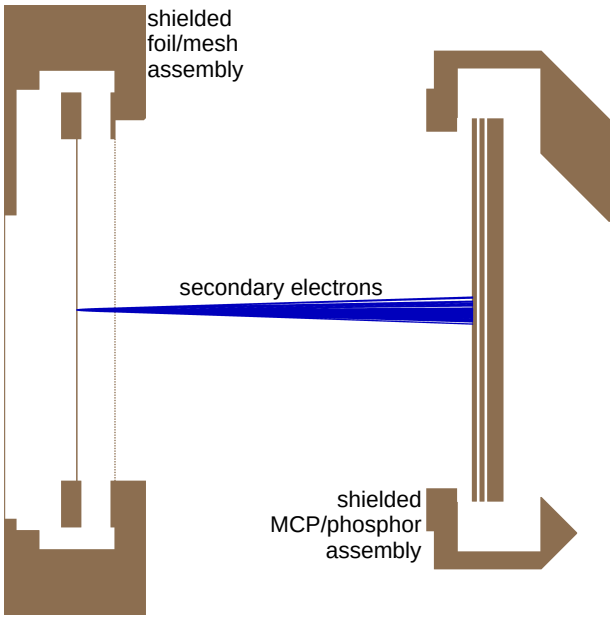

Figure 6.7: Shielded SEM model for secondary electrons guidance as modelled in Simion.

The spatial resolution is determined mainly by the secondary electrons guidance system at the distance between the foil and the detector. Further amplification is done in the narrow MCP channels of μm diameter and converted to visible light straight after multiplied electrons leave the MCP. Additional loss of resolution can be caused by the limited pixel size of a CCD camera placed at some distance from the phosphor screen. Nevertheless, the primary source of image blurring is the guidance of secondary particles from the foil.

To study the response of the system to a point source of electrons, the so called point spread function [259], various voltage values were applied to the foil and the position of particles hitting the MCP were recorded as shown in Fig. 6.8. The higher the accelerating gradient between the foil and the mesh, the better focusing of secondary electrons on the imaging system was obtained. Fig. 6.9 illustrates the dependence of the image FWHM as a function of applied voltage. At –1 kV, the imaged beam is strongly blurred and its FWHM reaches about 6.5 mm. Spatial resolution is considerably improved at –5 kV and reaches 3 mm. At –10 kV, further improvement is observed, but the FWHM is not lower than 2 mm. Although not ideal, it is still acceptable for beams of diameter up to a few centimetres delivered at the USR. Nevertheless, this theoretical prediction, hence also the Monte Carlo model, required experimental verification.

The capability of the system to register two spatially separated beams was also investigated. For a chosen foil voltage of –5 kV, two point sources of electrons were defined at the foil surface at various distances between each other, from 2 mm to 5 mm. The resulting images at the MCP surface are shown in Fig. 6.10. At –5 kV applied to the foil, only images of pencil beams separated by at least 3 mm can be distinguished as two separate objects. Spatial resolution improves to 2 mm if –10 kV is used. The results are consistent with the point source analysis.

Further studies incorporated a more realistic model of the mesh. It was approximated by 20 μm thick wires equally spaced every 350 μm which corresponds to about 95% transmission. Electrons were affected by the non-uniform field near the wires as well as the fringe fields outside the acceleration region and some particles were stopped in the mesh. The response of the system to a point electron source was examined at –5 kV. Fig. 6.11 shows the point spread functions for a particle source placed at the foil surface opposite to one of the wires as well as at a height of the centre between the wires. In addition, a Gaussian shape for an ideal mesh is also shown. It can be noted that the resulting image strongly depends on the location of the source. Trajectories of electrons are affected by the mesh and some regions of the MCP register fewer

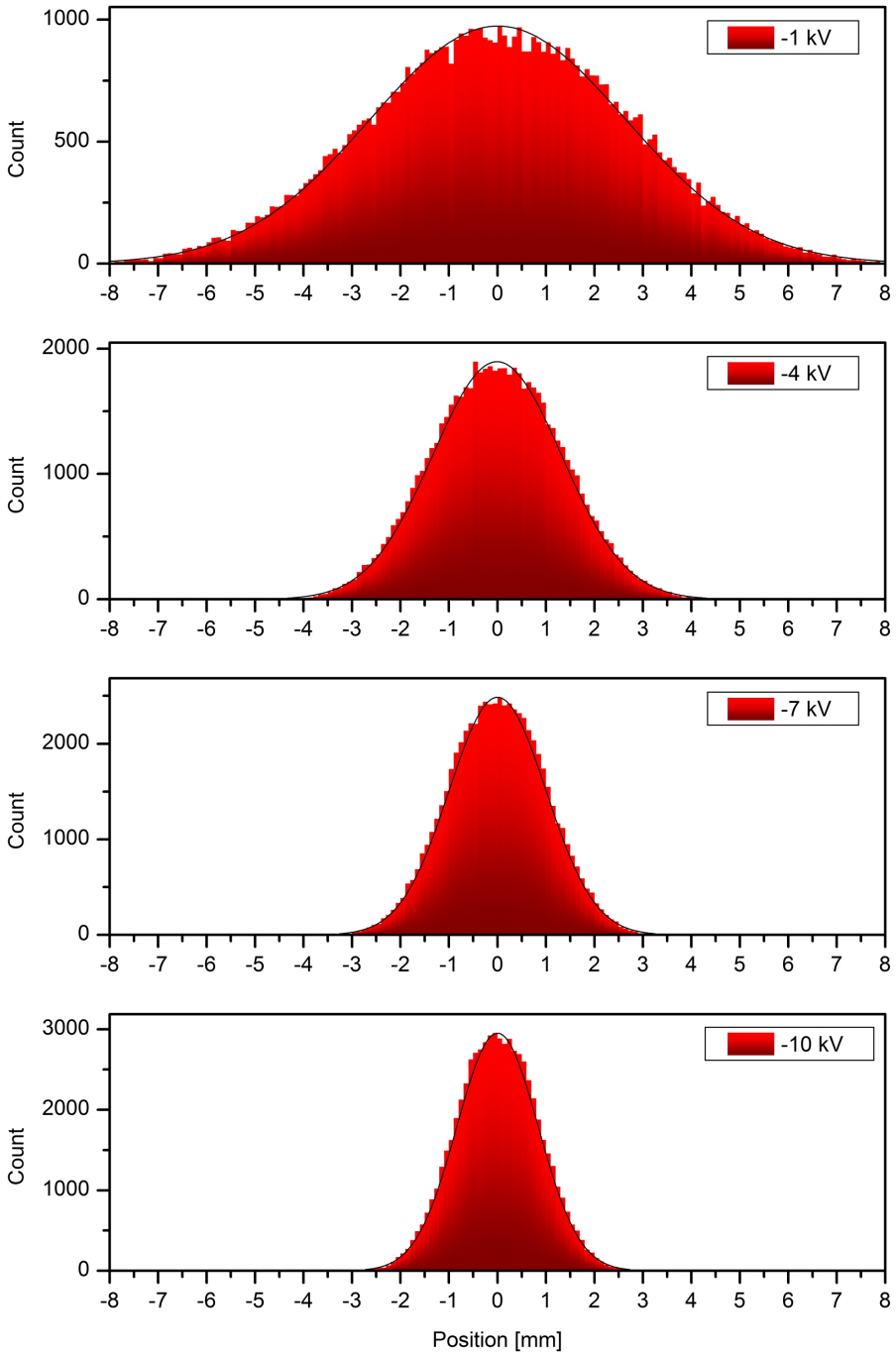

Figure 6.8: Focusing of secondary electrons, emitted from a point source, on the MCP surface at various voltages applied to the foil.

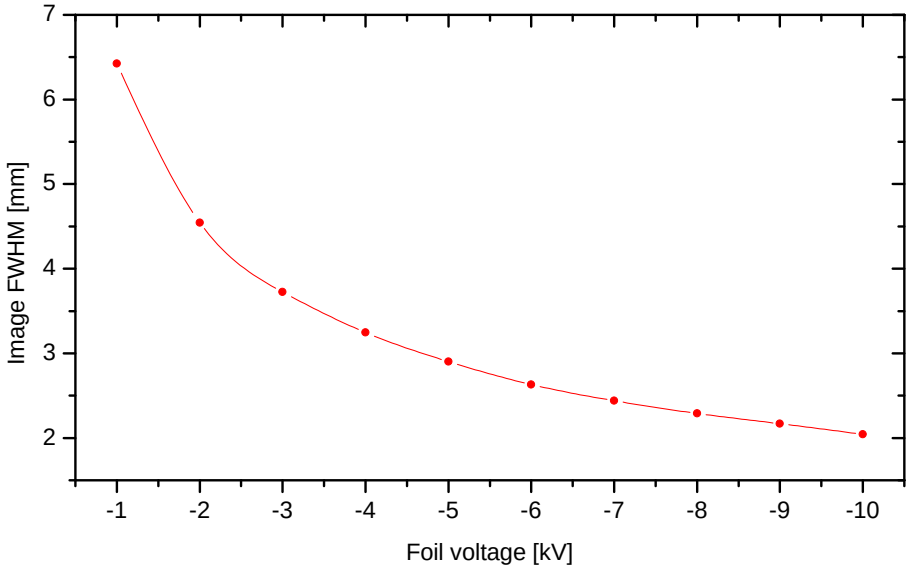

Figure 6.9: Simulated FWHM of the images recorded at the MCP surface as a function of voltage applied to the foil. Uncertainties are smaller than the data points.

particles than in the ideal mesh setup; the images no longer resemble a normal distribution. However, if only five point sources of electrons spaced every 175 µm, i.e. half the spacing between the wires, are introduced, the response of the system gets closer to the Gaussian distribution, as shown in Fig. 6.12. For a continuous distribution of electron sources at the foil surface, the image at the MCP can be well approximated by a bell-shaped curve.

Finally, a uniform, continuous source of secondary electrons was defined for the region within 5 mm from the foil centre, i.e. a uniform beam of 10 mm diameter was modelled. The result obtained at –5 kV accelerating voltage is presented in Fig. 6.13. A flat top can be noted together with blurred edges due to limited electron focusing. The edges can be characterised by their 10% – 90% width which is 3.4 mm in this case. The result is consistent with the point source analysis.

An attempt to improve resolution by applying a positive voltage of 500 V to the front of the MCP was made, but did not bring significant change. At –5 kV, the resolution improves by about 2% as compared to the setup with the grounded front face, but at –10 kV, it is improved only by less than 0.01%.

In order to estimate the average number of electrons reaching the MCP surface, an assumption of the electron yield of roughly 1 particle per proton [236] is made. For an area of 20 mm diameter, this corresponds to approximately $3 \cdot 10^{-3}$ $e^-/mm^2/proton$.

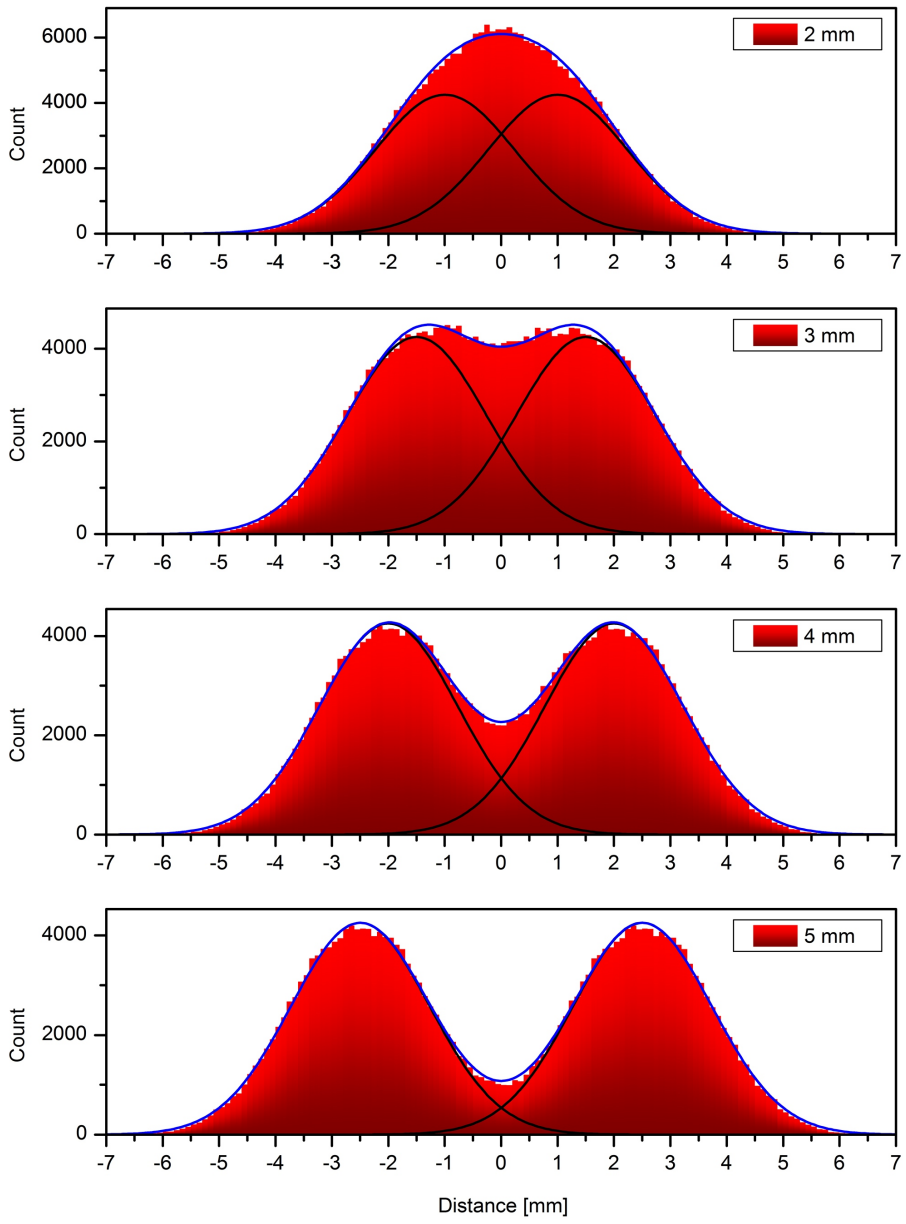

Figure 6.10: Beam image profiles at –5 kV for two point sources of secondary electrons separated by 2 mm, 3 mm, 4 mm, and 5 mm. Images of single source distributions are shown as black lines.

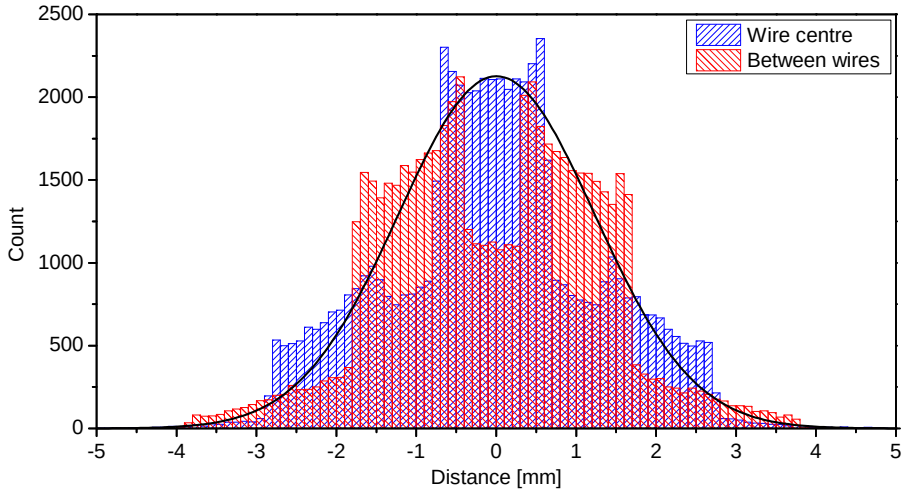

Figure 6.11: Profiles of secondary electron point-sources emitted from a foil at –5 kV for a realistic mesh (blue and red) and an ideal mesh (black), see text for details. All distributions are centred around zero.

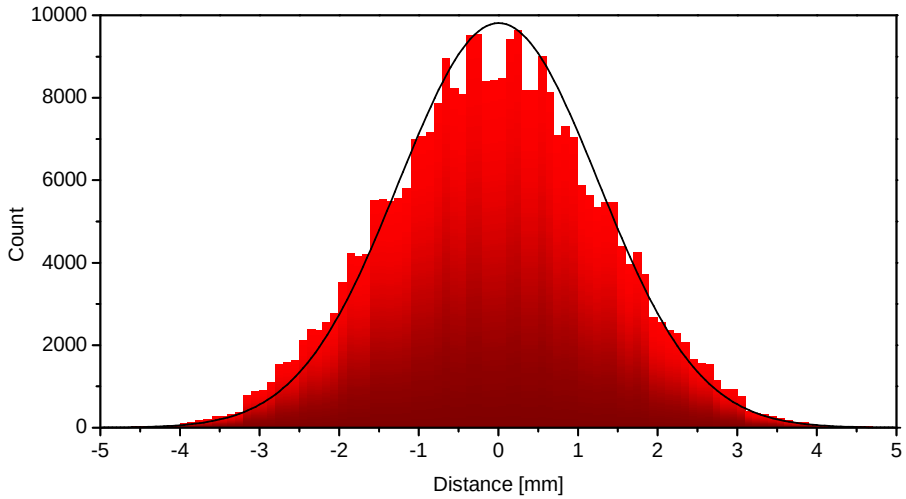

Figure 6.12: Cumulative profile at the MCP surface of five point sources positioned every 175 µm at the foil surface at –5 kV for a realistic mesh (red histogram) and an idealised mesh (black line).

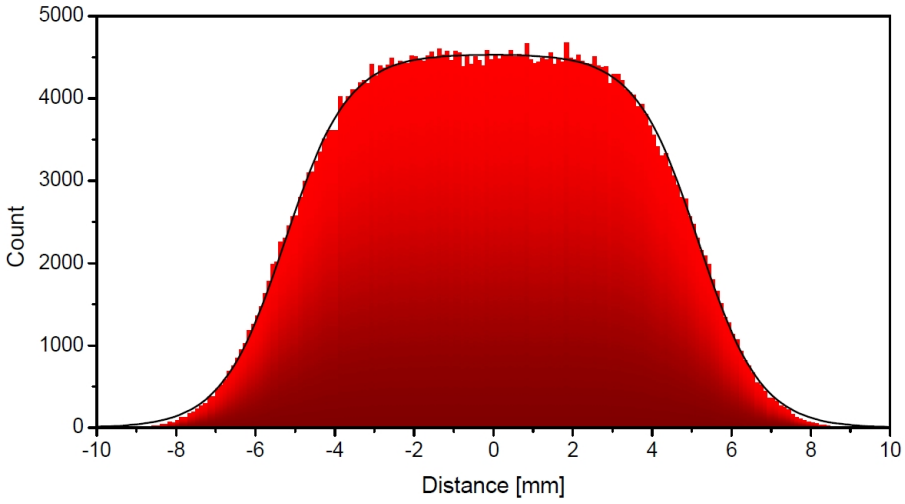

Figure 6.13: Cumulative profile at the MCP surface of a uniform, continuous distribution of secondary electrons with a width 10 mm at the foil surface at –5 kV.

The results presented above are valid for the secondary emission model described in Appendix A. However, secondary emission depends on a number of factors that cannot be simulated with high precision, such as material oxidisation, purity or surface roughness. For this reason, measurements can show a different performance of the monitor and an experimental validation was needed.

The setup can be improved by introducing additional magnetic or electric fields close to the imaging system. These, however, should not influence the low energy primary beam trajectory. Also, aluminium can be replaced by gold or other material exhibiting a higher emission of very low energy electrons, see Fig. 5.10, that can be guided more easily. Such modifications can be considered at a later stage, but the simplest setup should be experimentally tested in the first instance.

Annihilation Products

It is not possible to precisely model the behaviour of the SEM bombarded with low energy antiprotons because of a variety of events which occur due to and after annihilation [58, 112]. A combined charge signal from all of effects would be extremely complicated and rather impossible to simulate in any precise way. Existing Monte Carlo codes can provide only a simplified picture of the processes inside the SEM without taking into account many substantial aspects, such as creation of eV-scale secondaries. Most importantly, computer codes are limited by the experimental data which are not

yet complete for low energy antiprotons. However, it is clear that the annihilation of antiprotons will increase the number of particles reaching the MCP and therefore will affect the observed image. A more quantitative assumption can be based on a simplified Monte Carlo model, but with the above limitations kept in mind.

Because of available resources and help offered [260], Fluka [261–263] was used to estimate the number of particles generated in a collision of 300 keV antiprotons with a 100 µm aluminium foil. A 20 mm diameter beam with a uniform distribution contained $2 \cdot 10^7$ antiprotons and was fully stopped in the foil placed at 45°. No additional materials or electric fields were introduced. The resulting fluence of particles created in the process is shown in Fig. 6.14.

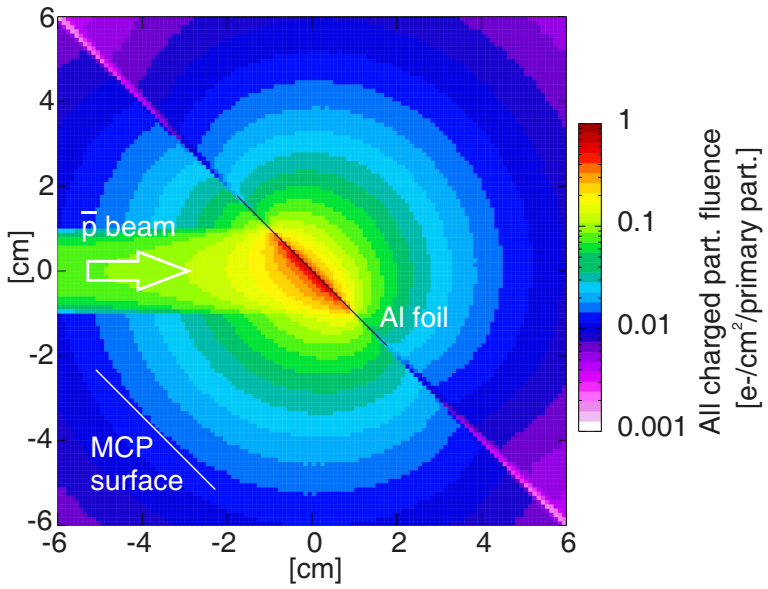

Figure 6.14: Fluka simulated fluence of charged particles created in the annihilation of 300 keV antiprotons.

According to the simulations, approximately $6 \cdot 10^{-5}$ charges/mm^2/$\bar{\text{p}}$ will reach the MCP surface. However, eV-scale secondary particles were not considered. The annihilation products and their energy spectra simulated with Fluka are shown in Fig. 6.15. The results give only an idea of what particles can be expected due to annihilation, but require experimental verification.

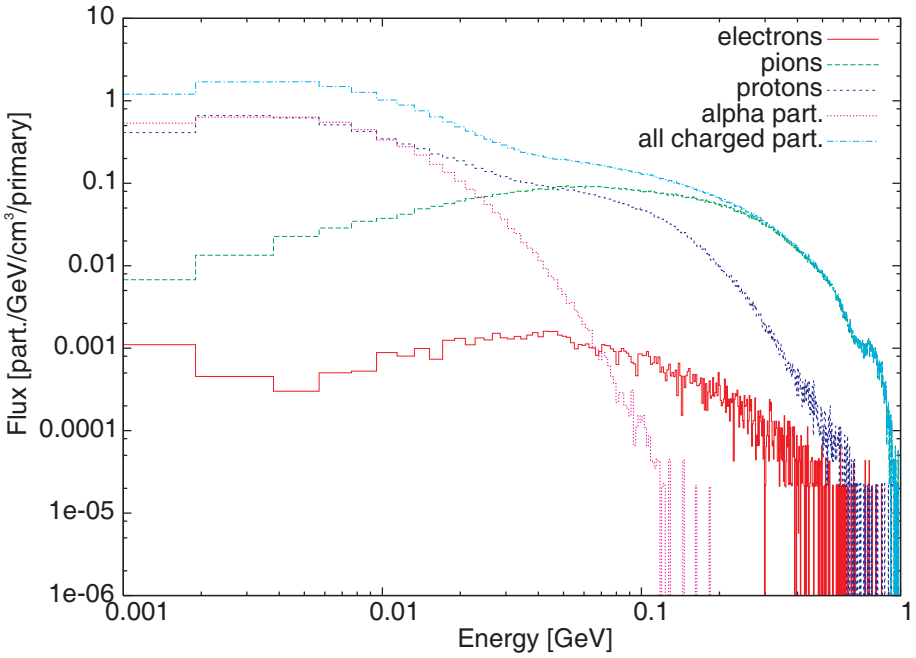

Figure 6.15: Energy spectra of charged particles following the annihilation of 300 keV antiprotons in aluminium as simulated with Fluka.

6.3.3 Technical Considerations

Apart from the interaction of the primary and secondary particles with the monitor, several important design issues should also be addressed in this study. These include foil heat load, thickness choice and deformation due to electrostatic forces.

Foil Heating

The beam stopped in the foil exchanges its kinetic energy with electrons of the medium causing heating of the target. As discussed in Section 5.2.5, the only possible process of cooling down of electrically and thermally isolated components in vacuum environment is thermal radiation. In equilibrium, the absorbed heat is equal to the emitted heat and the approximate temperature can be expressed by the balance condition of black body radiation [264]:

$$Q_{absorbed} = Q_{emitted} = A \cdot \sigma \cdot \beta \cdot (T^4 - T_0^4), \tag{6.2}$$

where A is the heated area of the foil, σ is Stefan-Boltzmann constant, β is the emissivity coefficient, and T_0 is the ambient radiation temperature. The emissivity coefficient of 0.04 for aluminium foil [265] and ambient room temperature of 293 K were assumed.

The absorbed heat can be calculated as the energy of a single particle times the number of extracted particles per second. From equation 6.2, the foil temperature rise can be estimated to less than 0.2 degree for a 1 mm diameter beam incident at the foil surface at 45° and is negligible for larger beams.

Foil Thickness

The influence of annihilation could be minimised by the use of an ultra-thin foil with a thickness smaller than the range of projectiles in matter. As discussed in Section 6.3.1, a sub-μm thick film is required in order to reduce the number of particles stopped in the monitor. The foil needs to be at least 50 mm in diameter to ensure an area large enough for imaging 20 mm diameter beams and mechanical support at the edges.

A solution developed at CERN was used for the SLIM beam monitor [119]. The thin foil produced for the SLIM detector consists of a support of 100–200 nm thick aluminium oxide (Al_2O_3), coated on each side with 10–50 nm thick layer of aluminium, and has a diameter of 65–70 mm. The pure aluminium evaporation process leads to discharging to electrical ground any electrostatic build-up within the oxide [119].

The use of a 30 μg/cm^2 (about 150 nm) thick carbon foil coated by a ∼10 μg/cm^2 lithium fluoride (LiF) layer was reported [266]. The latter was added to improve the secondary electron emission of pure carbon, yet no quantitative results were provided.

At Grand Accélérateur National d'Ions Lourds (GANIL), 0.5–0.9 μm mylar foils with ∼100 nm Al evaporated on one face for electrical conductivity were used [267]. The number of secondary electrons is enhanced by a factor of about 5 by a ∼50 nm thin CsI coating on the Al.

Foil Deflection due to Electrostatic Forces

The foil and mesh assembly can be simplified and seen as two parallel plates at a distance d and a constant voltage. The pressure between them due to an electrostatic potential difference U can therefore be written as:

$$p = \frac{\epsilon_0}{2} \cdot \frac{U^2}{d^2}. \tag{6.3}$$

According to [268], the deflection of a solid circular plate of radius a, clamped at $r = a$, due to a uniform pressure p can be calculated as:

$$w(r) = \frac{p \cdot \left(a^2 - r^2\right)^2}{64 \cdot D}, \tag{6.4}$$

where D is the bending stiffness of a plate and is defined as:

$$D = \frac{E \cdot h^3}{12 \cdot (1 - \nu^2)}, \tag{6.5}$$

with the modulus of elasticity E, also known as Young's modulus, Poisson's ratio ν and plate thickness h [268]. Young's modulus is a measure of the stiffness of an elastic material, whereas Poisson's ratio is the ratio of transverse contraction strain to longitudinal extension strain in the direction of the applied force. Table 6.1 lists values of both parameters for selected materials [265]. It is not possible to provide a single value of Young's modulus for carbon, because it depends on a particular structure and composition under investigation [269]. It is even more complicated for graphene for which the modulus of elasticity depends also on the definition of the material thickness [270–274]. Currently, graphene films of 50 mm diameter are not available, but it is not unlikely that ongoing studies will lead to an extremely stiff solution with $E > 1$ TPa and thickness of a single or only few atomic layers [275].

Material	Modulus of elasticity [GPa]	Poisson's ratio
Aluminium	69	0.33
Aluminium oxide	300 – 400	0.21
Beryllium	290	0.03
Carbon	<100 – >500	∼0.3
Copper	117	0.36
Gold	74	0.42
Nickel	214	0.31
Silver	72	0.37
Stainless steel	180–200	0.30

Table 6.1: Moduli of elasticity and Poisson's ratios for selected materials. See text for details.

It should be noted that equation 6.4 is only a first-order approximation of a real deformation, because the pressure, as a function of distance, changes with the bending of the plate. Furthermore, this linear approximation is valid only for small deflections, typically less than one-half of the plate thickness. For larger deformations, stretching and bending of the plate are coupled and in-plane stress resultants are not constant but location-dependent. In such a case, the analysis should be carried out numerically [268]. However, the linear approximation can give an idea of the significance of the foil deflection.

Carbon and Al_2O_3 films offer the highest stiffness and can be considered the most suitable materials. Assuming $E = 1$ TPa, $\nu = 0.3$, foil radius $a = 25$ mm and distance

to mesh $d = 5$ mm, equation 6.4 leads to at least 10 mm deformation for a 3 μm thick foil and voltage of –5 kV. In reality, it may mean that the foil breaks.

A way around the problem is to place the foil symmetrically between two grids so that the electrostatic forces are present in both directions and cancel out. However, such a solution would be sensitive to inhomogeneities and any asymmetry would expose the foil to considerable forces. Also, the grids would still be bent towards the foil, thus their thickness cannot be too small. From this point of view, it is therefore preferred to use a thick foil or even a plate.

6.4 Prototype Design and Construction

6.4.1 Mechanical Design

The final design of the prototype detector is shown in Fig. 6.16. The foil and mesh assembly as well as the MCP and phosphor assembly are shielded as discussed previously. The latter arrangement is shown in the exploded view to present its subcomponents.

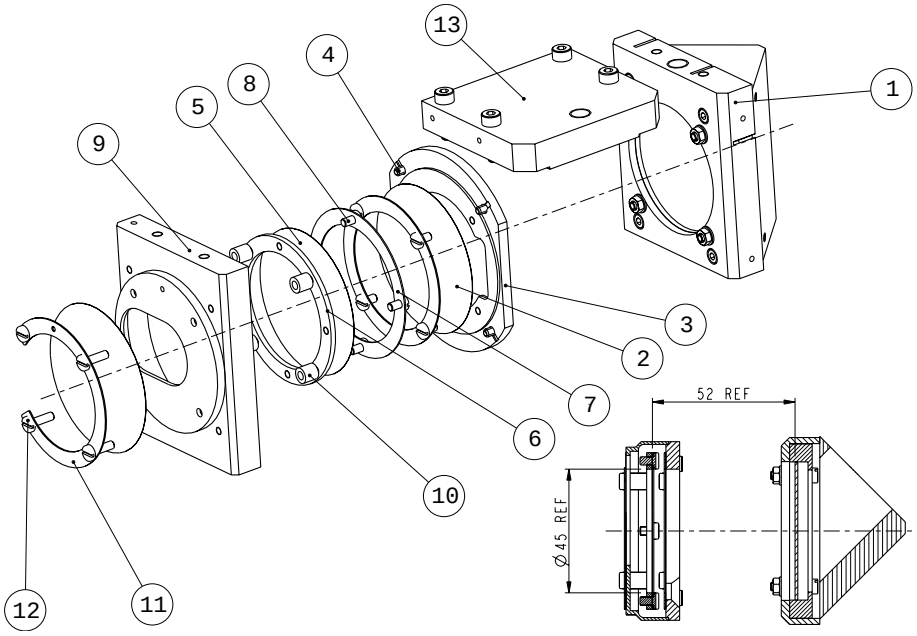

Figure 6.16: Secondary emission monitor design.

The MCP and phosphor assembly is a commercially available product described in detail in Section 6.4.2. It is mounted inside a custom made shield (1). The mesh (2) is fixed to a mesh holder (3) by means of a stainless steel ring and four PEEK screws (4).

The foil (5) is clamped between two rings (6 and 7), also by means of PEEK screws (8), and fixed to the main foil and mesh holder (9). Additional MACOR spacers (10) are used to electrically separate the foil from the grounded shield. The mesh holder is then used to close the assembly and screen the foil from the front side. At the back, an additional foil or mesh can be fixed for the same purpose by means of a stainless still clamp (11) and PEEK screws (12). The foil and mesh assembly is rigidly fixed to the MCP and phosphor assembly by means of the support plate (13). The latter is also used to fix the detector to an actuator.

The distance of 52 mm between the foil and the MCP is a compromise between the spatial resolution and the maximum beam diameter that can be observed. Secondary electrons accelerated towards the detection assembly are divergent, thus the resolution drops down with distance from the source. On the other hand, the MCP placed too close to the foil covers the area of the beam which hits the back of the microchannel plate. As a consequence, only a fraction of the primary particles reach the foil, whereas the rest is either dumped or interacts directly with the MCP and phosphor assembly. In the given configuration, the USR beams as large as 20 mm in diameter can be monitored.

The monitor is mounted inside a 4-way cross vacuum vessel as shown in Fig. 6.17. A custom-made vacuum window flange goes inside the main chamber which enables placing a CCD camera as close to the phosphor screen as possible. A pneumatic actuator is used to place the monitor in the beam path and has a movement range of 100 mm. A custom-made top flange is equipped with SHV feedthroughs to supply voltages required by the detector.

The overall design of the monitor was made flexible to enable the use of two configurations, the foil-based SEM described above and a stand-alone MCP placed directly in the beam path. Both settings are compared in Fig. 6.18.

6.4.2 Detector Components

A UHV clean aluminium foil of 25 µm thickness was installed in the monitor, but also a 200 µm thick aluminium plate was prepared. A solution of sub-µm was not used in the prototype due to its fragility, price and electrostatic forces that can deform a thin film. It was decided to make the first tests with a standard UHV clean foil available in the lab instead of a thick plate to investigate the difficulties with its installation and behaviour in the real setup.

A nickel mesh was available for tests and was installed as a part of the assembly. It

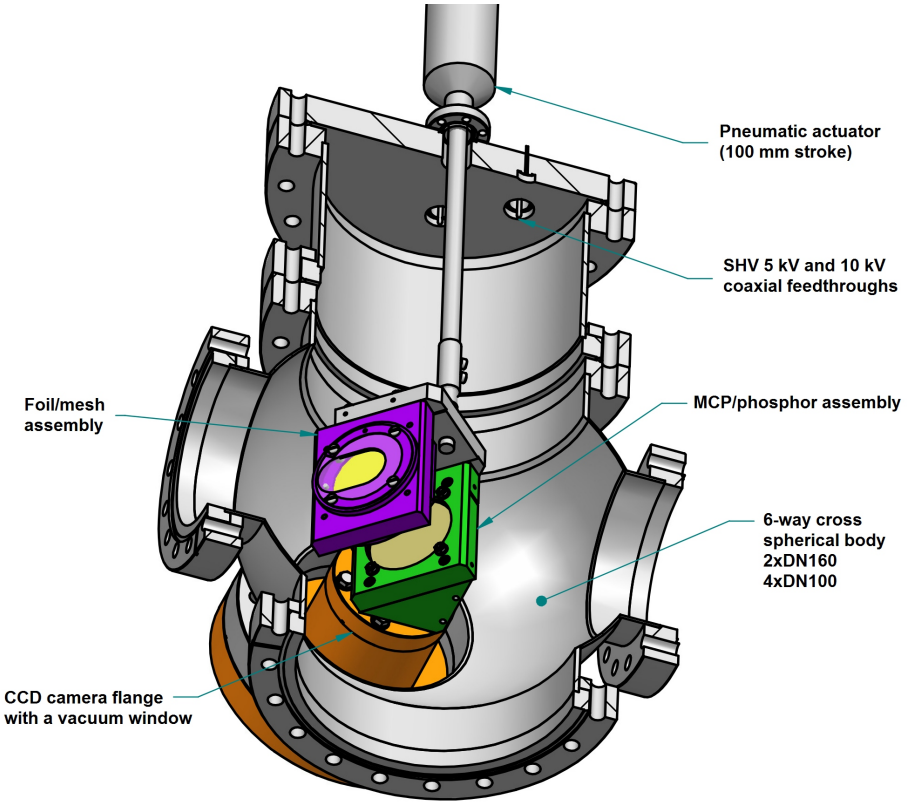

Figure 6.17: A cross-section view of the secondary emission monitor setup.

has 80 lines per inch which is approximately 3 wires per millimetre. Each wire is 25 μm thick and the hole size is 293 μm in diameter. The parameters of the mesh correspond to a transmission of 85%.

The MCP and phosphor assembly, model BOS-40, was procured from Beam Imaging Solutions [276]. It consists of a chevron type microchannel plate and a P-43 phosphor screen housed in a ceramic base. The beam energy range specified for the model is 1 eV to over 50 keV. Should it be used for beam currents greater than 3.2 nA/mm^2, a 90% attenuation needs to be used. The assembly is UHV compatibile and the maximum bakeout temperature is 300°C. Vacuum of at least 10^{-6} mbar or better is required to operate the MCP. An exploded view of the assembly is shown in Fig. 6.19.

The chevron type microchannel plate is a stack of two MCPs, each of 50 mm diameter and effective imaging area of 44 mm diameter. Their channels are 10 μm in diameter with 12 μm pitch and 8° bias angle. The thickness of a single plate is 0.46 mm which corresponds to a 46:1 aspect ratio. The maximum gain that can be achieved

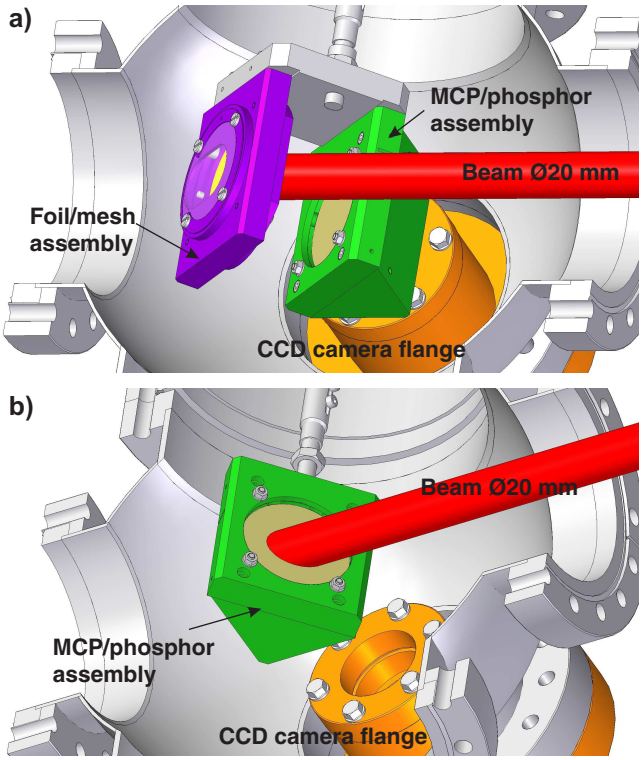

Figure 6.18: Two possible configurations of the monitor: (a) a foil-based SEM, and (b) an MCP placed directly in the beam path.

is approximately $2 \cdot 10^4$ for a single plate at 1000 V, and more than 10^7 for the chevron configuration at 2000 V.

The phosphor screen is an aluminised P-43 ($Gd_2O_2S{:}Tb^{3+}$) on a glass (Pyrex) plate. Its typical peak wavelength is 545 nm, and the fluorescent colour is green, whereas the decay time is of the order of 1 ms. The thickness of the phosphor layer is 10 – 15 µm and of the aluminium layer is 250 – 500 Å. The glass plate is 1.5 mm thick and its outer diameter is 50 mm, with a diameter of the imaging area of 44.9 mm.

6.4.3 Electrical Design

A 3-channel HV power supply 19" THQ from ISEG is used to supply voltages to the MCP, phosphor and foil. Two DPS series modules with a switchable polarity and 5 kV SHV output connectors can supply up to 3 kV/4 mA and 5 kV/2mA to the MCP and the phosphor, respectively. Peak-to-peak ripple and noise for DPS modules are typically less than 2 mV and 7 mV maximum. A single CPS module with a fixed polarity and 16 kV LEMO output connector can supply up to –10 kV/1 mA to the foil.

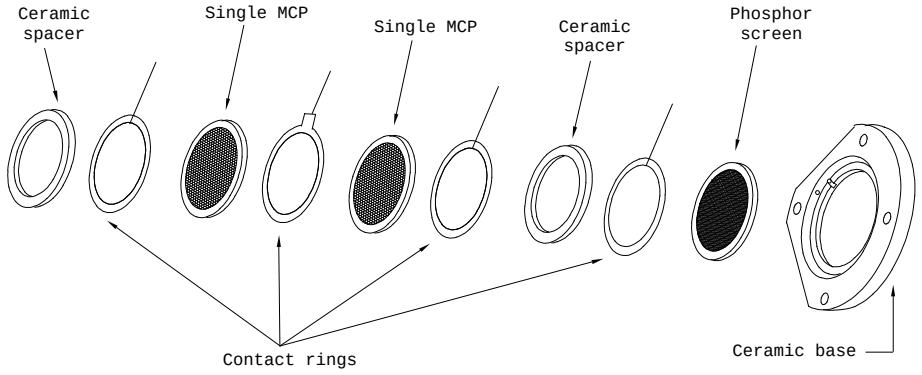

Figure 6.19: Exploded view of the BOS-40 chevron type MCP and phosphor assembly.

Peak-to-peak ripple and noise for the CPS modules is typically less than 200 mV and 500 mV maximum.

In order to apply proper voltages with a single HV power supply and to vary them for both MCPs at the same time, a custom-made voltage divider is used. It incorporates two micro-ammeters in series with the power supply to monitor current flow across the MCPs, two digital voltmeters to read the voltage divided between the MCPs and two current limiting resistors to help prevent damage to the MCPs in the event of a HV breakdown within the internal detector assembly. The schematic circuit of the voltage divider is shown in Fig. 6.20.

For the interface between air and vacuum, four 5 kV SHV feedthroughs and one 10 kV SHV feedthrough were welded to the actuator flange. The first three feedthroughs supply voltage to the front, middle and rear of the MCP assembly, the fourth 5 kV SHV is used for the phosphor screen, whereas the 10 kV SHV is for the foil.

The MCP and phosphor assembly is built as a sandwich with metal rings placed between the components, see Fig. 6.19. Kapton-insulated wires, rated up to 5 kV, were spot welded to the rings separating the MCP plates.

For the foil, a more stiff Kapton-insulated wire, rated up to 10 kV, is used.

6.5 Experiments with Electrons

6.5.1 Experimental Setup

Prior to tests in a beam line, the monitor was assembled and tested in terms of its vacuum and electrical performance as well as response to a low-energy electron beam. The setup shown in Fig. 6.17 was used with an electron gun, ELS5000 from PSP Vacuum

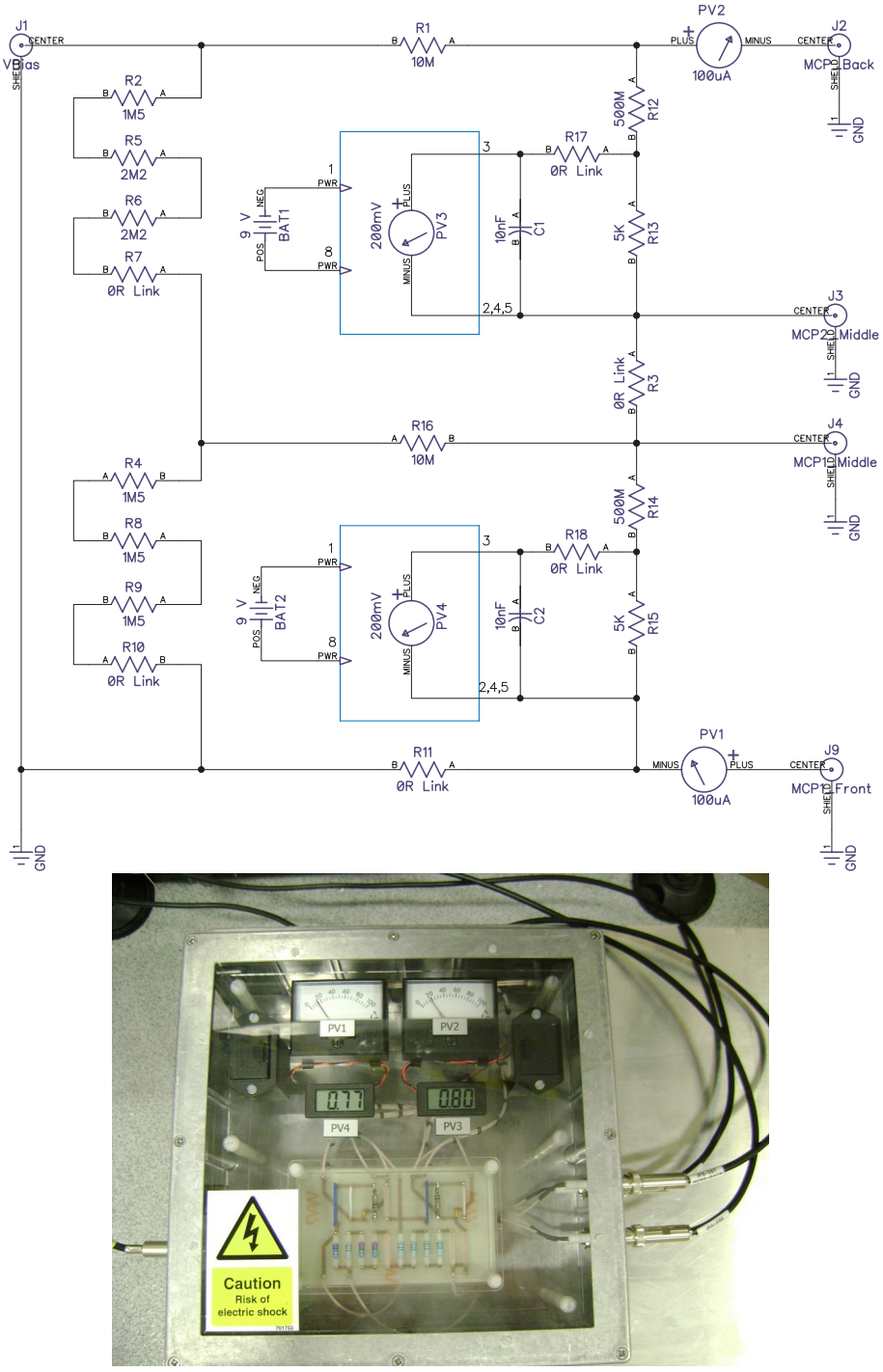

Figure 6.20: Voltage divider for the chevron type MCP: a schematic diagram (top) and the practical implementation (bottom). See text for details.

Technologies, attached to deliver the beam in the monitor direction. Additionally, the same vacuum gauge and pumps were used as described in Section 5.4. The detector was tested in both configurations shown in Fig. 6.18.

Two flanges were used to install viewports for monitor observation. The custom-made vacuum window reductor was installed as shown in Fig. 6.17, but a large size DN100 viewport was also mounted downstream of the detector. The latter made it easier to observe images in the stand-alone MCP configuration.

The main purpose of the tests was to establish whether no major mechanical, electrical or vacuum problems could be found prior to shipping the equipment for experiments with protons. For this reason, only qualitative data related to electron beam imaging are reported.

6.5.2 Experimental Results

Fig. 6.21 shows an image obtained through the downstream viewport with the MCP placed directly in the beam path. In this configuration, the monitor was perpendicular to the beam. In the middle of the detector, green light produced by the electron beam hitting the MCP and phosphor assembly is visible. Although the shape of the beam image is neither circular nor uniform, the effect is not caused by the monitor, but by the way the electrons are focused and guided in the gun. This was confirmed by changing the beam parameters, i.e. scanning the beam vertically and horizontally as well as focusing and defocusing. An example of the latter test result is shown in Fig. 6.22.

Next, the monitor was assembled in foil-based configuration. In this case, the image can be recorded only by a camera placed at 90° to the beam. The voltages applied to the foil did not exceed approximately –2.5 kV, because higher values affected the trajectory of a 5 keV electron beam too strongly to register it. The effect was verified in simulations as shown in Fig. 6.23

The beam image observed in the foil-based SEM differs from that seen for the MCP placed directly in the beam path. This is because of a better spatial resolution of the latter solution. For each particle hitting the microchannel plate surface, an avalanche of secondary electrons is generated in an MCP channel which are then directed onto a phosphor screen and converted to visible light. The image resolution is, therefore, limited by the channel diameter of 10 μm, a slight divergence of the beam at a distance < 1 mm between the MCP output and the phosphor screen, and scattering effects in the latter. In the case of a foil-based SEM, the main contribution to image blurring comes from the large distance between the foil and the MCP surface, because electrons

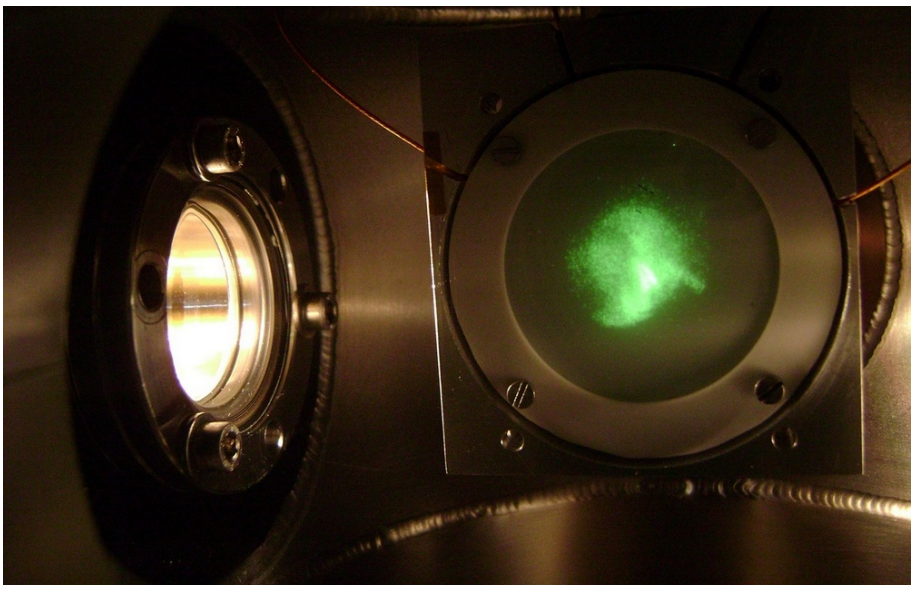

Figure 6.21: SEM chamber: an image of 5 keV electrons striking on the MCP placed directly in the beam path is visible in the central part of the detector (green light).

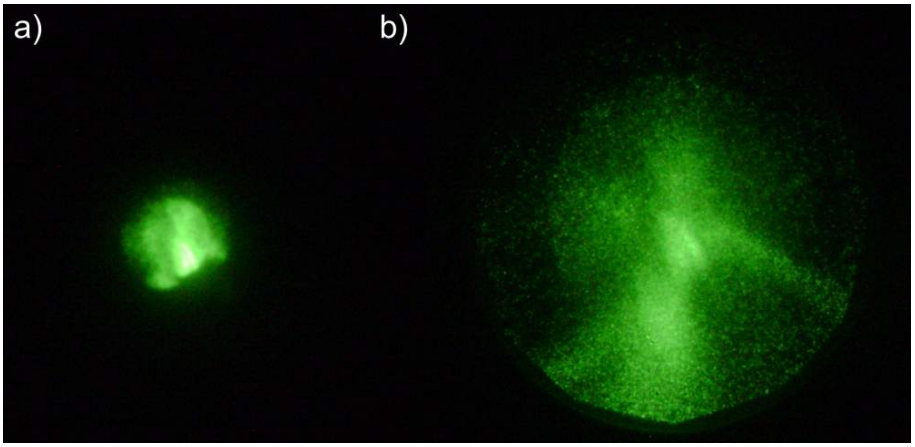

Figure 6.22: Example of electron beam images obtained with an MCP placed directly in the beam path for various focussing settings of the electron gun: a) partially defocused beam, and b) fully defocused beam.

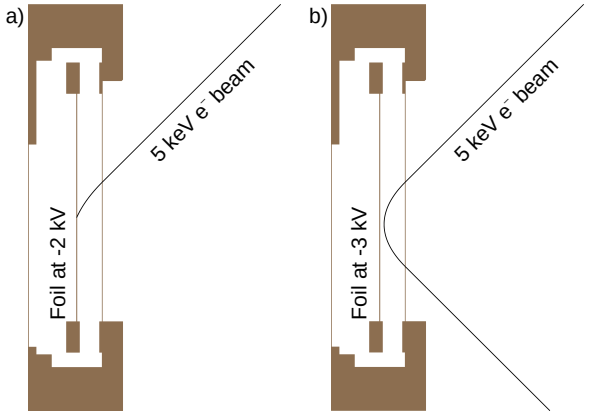

Figure 6.23: Interaction of a 5 keV electron beam with the SEM: a) at –2 kV, and b) at –3 kV applied to the foil.

cannot be guided with sub-mm precision.

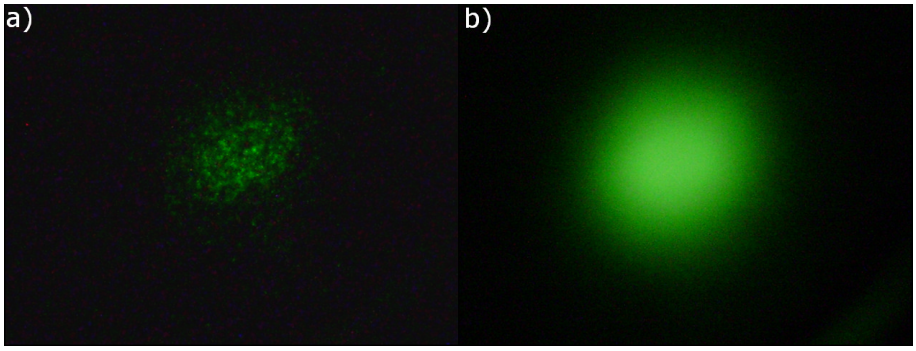

Figure 6.24: Example of electron beam images obtained with the foil-based SEM: a) sub-fA current and maximum MCP/phosphor amplification, and b) μA current and a few hundred volts amplification.

An example of images obtained with 5 keV electrons interacting with a foil-based monitor is shown in Fig. 6.24. The first image (a) shows the situation when the electron beam intensity is reduced below the value measured by the Faraday cup in Section 5.4, whereas the MCP and phosphor voltages are set to maximum of 2 kV and 5 kV, respectively. The small spots visible in the picture correspond to single electrons emitted from the foil and reaching the MCP surface where they are multiplied and converted to visible light. Some flickering of the image was observed due to the statistical nature of the process and also due to dark current noise in the MCP and phosphor assembly operated at maximum amplification. The second image (b) shows the results for an

electron beam current of the order of 1 μA and half the voltages applied to the MCP and phosphor assembly. The image is smooth and exhibits the blurring demonstrated in Fig. 6.8.

6.6 Experiments with Protons

6.6.1 Experimental Setup

Studies of the SEM performance were done with 200 keV protons at INFN-LNS with the group of Paolo Finocchiaro. The monitor was installed in a low energy beam line downstream the USR Faraday cup as described in detail in Section 5.5 and shown in Fig. 5.25. The vacuum vessel of the SEM had been designed to be compatible with the Istituto Nazionale di Fisica Nucleare - Laboratori Nazionali del Sud (INFN-LNS) beam line, thus the arrangement shown in Fig. 6.17 was easily reproduced for the tests. Only the foil-based configuration was tested and no images for the MCP placed directly in the beam path were obtained.

Additionally, a collimator was prepared to investigate the resolution of the secondary emission monitor. A set of holes, 2 mm and 3 mm in diameter, were drilled in a 5 mm thick aluminium plate as shown in Fig. 6.25. The collimator was attached to the back of the MCP and phosphor assembly in order not to block the path of secondary electrons. As a consequence, the distance between the exit of the collimator and the centre of the foil reached 76 mm. SIMION [247] simulations showed that the significant distance does not affect the separation of the holes images, see Fig. 6.26.

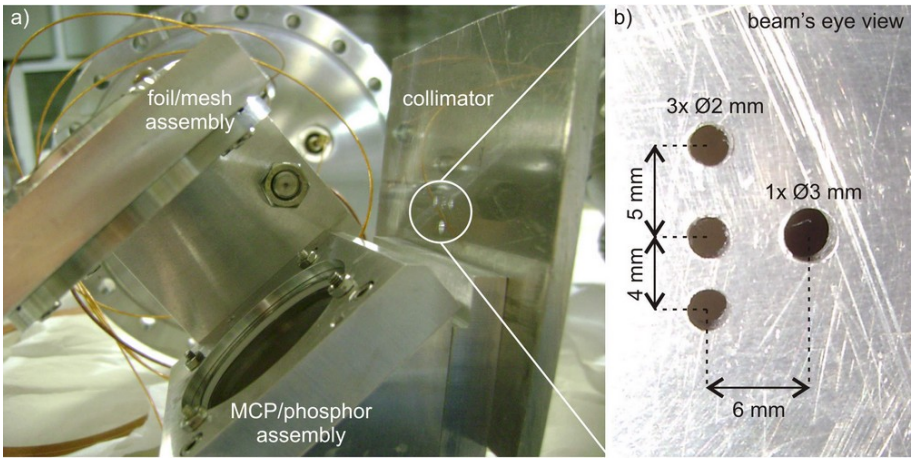

Figure 6.25: SEM with collimator as installed at INFN-LNS.

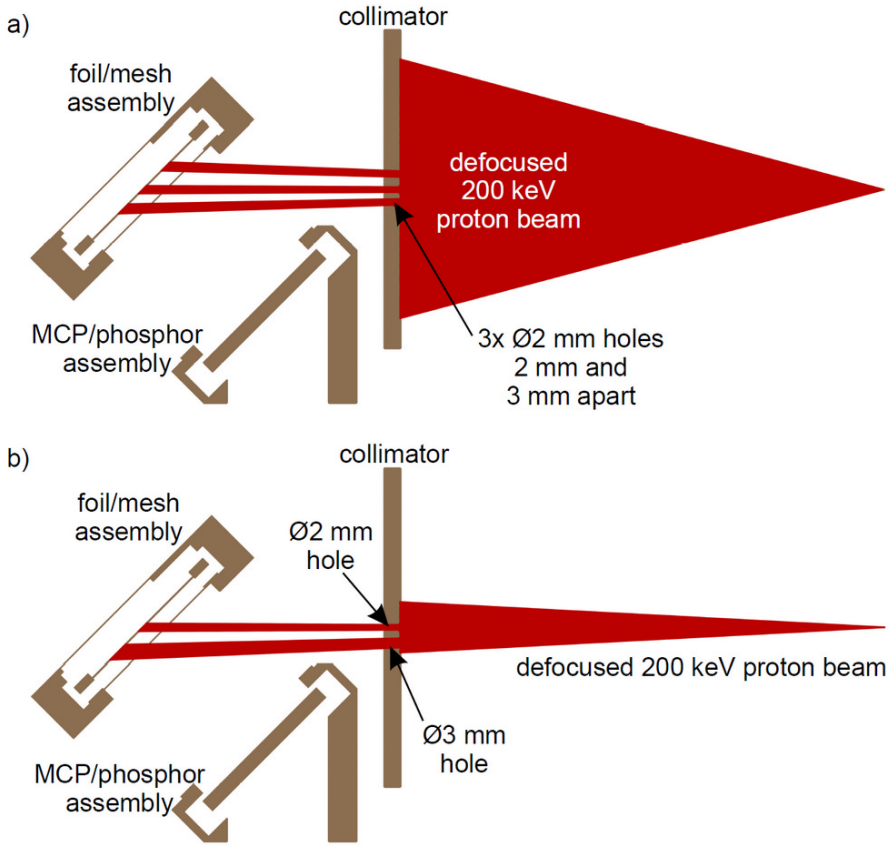

Figure 6.26: Simulation of the primary beam transport trough a 5 mm thick collimator plate with various holes: a) three holes 2 mm in diameter at a distance of 4 mm and 5 mm, and b) a 2 mm hole and a 3 mm hole 6 mm apart.

Beam images were recorded with a high performance 14-bit CHROMA CX3 still camera produced by DTA, featuring a 1534×1024 pixel KAF1600 CCD, manufactured by Kodak. The device was installed in the in-vacuum viewport at 90° to the beam axis, thus the back of the phosphor screen was observed at 45°. The camera was connected to a frame grabber computer board which enabled live display capture. The images were binned at 3×3 with an effective number of 512×341 pixels. Systematic noise, due to intrinsic non-uniformity of the CCD response and its readout, was reduced by taking an image under the same conditions, but with the shutter closed and subtracting it from a real image. This dark image subtraction was done automatically by the camera software.

6.6.2 Experimental Results

The first beam images were recorded without the collimator. The beam current measured by the Faraday cup FC1 was about 50 pA, but only a fraction of particles reached the monitor due to the use of two pepper-pot grids upstream the SEM. The current at the detector location was estimated to be less than 20 fA.

Each beam image was analysed according to the same procedure. A dark image had been automatically subtracted before any off-line analysis was started and ImageJ [173] was used for further processing. A built-in ImageJ filter was applied to the image to remove bad pixels visible even without the beam. Afterwards, the intensity values of the 2D picture were projected onto the X-axis and a Gaussian distribution was fitted. The result was used for the beam width and centre position determination. An image of the MCP and phosphor assembly was taken with reference markers at the back of the screen, which allowed translating the number of pixels to millimetres. This provided a calibration factor of 27.0 ± 0.3 pixels/mm. In addition, black-and-white images were colour-coded to present the 2D data in a clearer way.

The influence of the MCP gain on the image was investigated at fixed voltages applied to the foil and phosphor screen. The foil was at –10 kV, the phosphor at 5 kV, and the chevron MCP voltage varied between 1.6 kV and 2 kV. The result is shown in Fig. 6.27. Due to a low number of particles, no images were observed below 1.6 kV MCP voltage. However, a clear image is seen even below 2 kV, which means that the detection limit of the monitor was not reached.

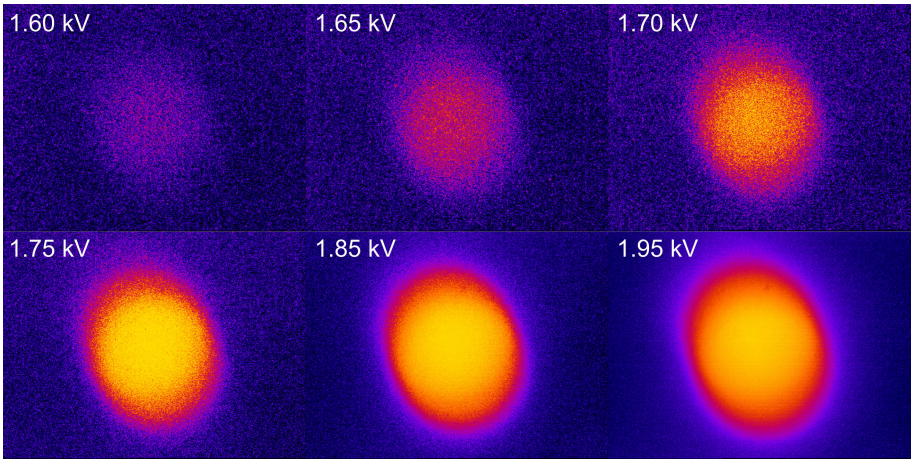

Figure 6.27: Influence of the MCP gain on the image quality. See text for details.

Also the influence of secondary electrons guidance on the beam image was studied.

In this case, the MCP voltage was set to 2 kV, the phosphor to 5 kV and the foil voltage varied from 0 to –10 kV. Fig. 6.28 shows a selection of colour-coded 2D images.

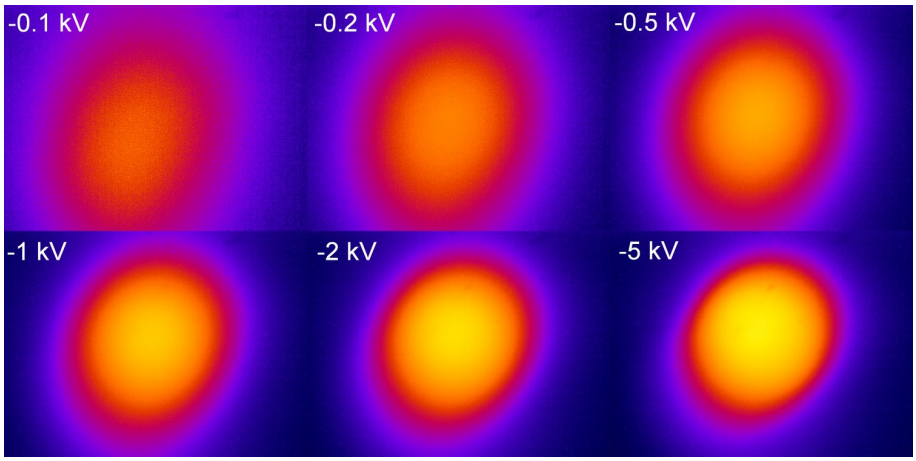

Figure 6.28: Influence of the foil voltage on the image quality. See text for details.

The acquired 2D images were projected onto one axis and cumulative intensity distributions were obtained. Next, fitted Gaussian profiles were used to calculate the peak centre position and FWHM value at different foil voltages as shown in 6.29.

The observed beam size, shown in Fig. 6.29a, decreases with increasing voltage applied to the foil. The FWHM value reaches about 10 mm at the maximum voltage, but the width differs only slightly for lower voltages. This is consistent with behaviour modelled in Simion and shown in Fig. 6.9. In addition, a variation of the centre position is observed in Fig. 6.29b. A large uncertainty of the centre determination for a weakly focused beam was assumed, thus its displacement was calculated relative to the position at –1 kV. A significant variation in the projected beam position for low voltages can be explained by a large size of the beam image and a blurred, noisy peak which becomes clearer only above a few hundred volts. Above –500 V the discrepancy is smaller than 0.1 mm. In the range between –1 kV and about –7.5 kV, a steady yet small shift of the beam image centre is observed. It reaches about 0.3 mm and can be explained by the influence of the electric field on the primary beam. A different behaviour is seen above –7.5 kV where both the image width and centre position become disturbed. The beam shift reaches almost 0.7 mm. A possible explanation is a deformation of the thin aluminium foil due to the high voltage applied.

It is possible that the high potential difference between the foil and the mesh caused a noticeable deformation of the aluminium, leading to a change in the primary beam

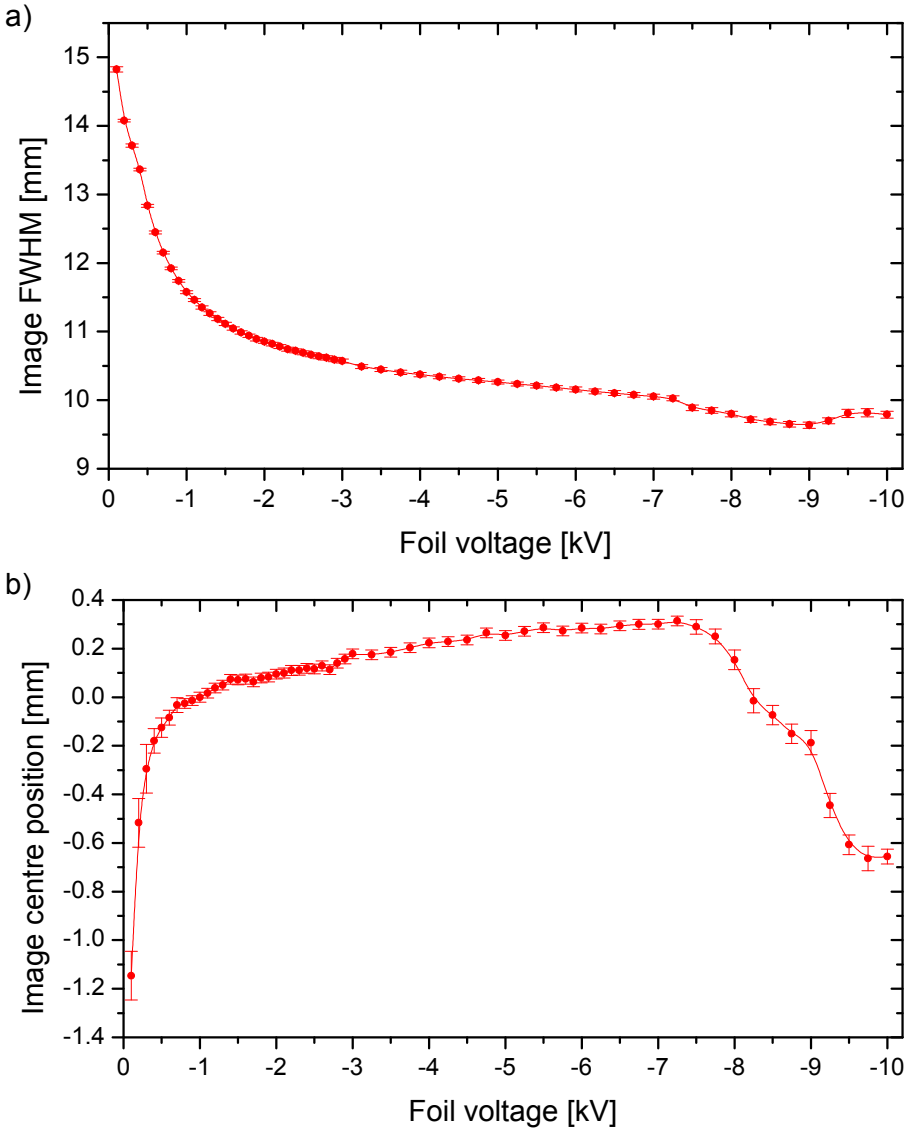

Figure 6.29: Beam image FWHM (a) and centre displacement relative to the beam position at –1 kV (b) as a function of the voltage applied to the foil.

hit position. The aluminium foil and nickel mesh used in the tests were both 25 μm and 50 mm in diameter. By using equation 6.4, deformation of the foil can be estimated in a simplified case with two parallel plates separated by 5 mm clamped at the edges in the presence of a uniform, constant pressure. At –10 kV, it results in the centre's deflection of 1 mm and 0.3 mm for aluminium and nickel, respectively. With an additional grounded aluminium foil placed in the back of the monitor at the distance of 9.5 mm from the main foil, the electrostatic force is present also in the opposite direction and the deflection is reduced from 1 mm to 0.8 mm.

The results obtained with equation 6.4 should be taken with care. First, the formula is applicable only to small deformations, less than one-half the foil thickness, i.e. $<$ 12 μm; above that threshold, non-linear effects need to be taken into account. Second, the electrostatic pressure is not constant, but increases with the increasing deflection due to the change in distance between the plates. Third, the back of the monitor is not symmetric, thus the force pulling the foil back is not uniform. Finally, the clamped foil was neither stretched nor ideally flat. The deformation is too complex to be treated analytically, but also a numerical solution would be of a limited accuracy due to unknown factors, such as wrinkles in the foil and its initial tension. Nevertheless, a very simple assumption of a symmetric deformation reaching 1 mm in the centre can be made to analyse its influence on the monitor response.

A simplified deflection is shown in Fig. 6.30. The lack of symmetry in the real design is ignored, but the directions of electrostatic forces acting on the foil are marked by arrows. The force pulling the foil to the back of the monitor is not uniform due to the shape of the shield and the aluminium should be bent asymmetrically. Nevertheless, it can be demonstrated that for a deformation of 1 mm in the centre, the beam hits a different point of the foil shifted by almost 1 mm as compared to a setup with a flat foil. A possible explanation of the different behaviour of the image centre shift above –7.5 kV as shown in Fig. 6.29 can be that the aluminium film exhibits a non-linear behaviour for large electrostatic pressures and changed its shape significantly only above a certain threshold. Independently from the actual cause of the observed effects, it is concluded that the use of a thin plate instead of a foil is preferred in future applications.

Finally, the collimator was attached to the monitor and images were taken for a new configuration. These are shown in Fig. 6.31 for various beam steering settings. The beam size upstream the collimator was not registered, but it was expected to cover the area of the collimator and produce four distinguishable spots in the image. The positions of the collimator apertures are indicated by dashed circles. By changing

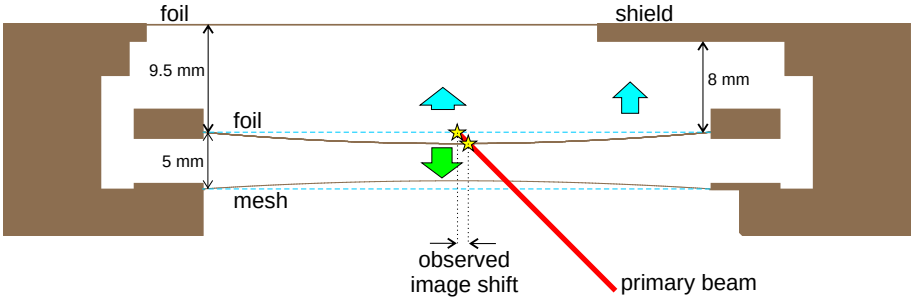

Figure 6.30: Simplified deflection of the aluminium foil and nickel mesh and its influence on the beam hit position. Arrows indicate electrostatic forces acting on the foil.

the beam optics, it was possible to defocus and scan the beam through a variety of positions at the collimator surface which resulted in the various beam images shown in the Fig. 6.31a) to f). However, under no circumstances was the lower hole visible in the images. The projection of a 3-mm diameter aperture on the right hand side is clearly distinguishable from the other objects. The same applies to the upper 2-mm diameter hole. Some ghost structures are visible around the middle 2-mm diameter hole. These can be caused by reflected particles at oblique incidence within the apertures but also by scattered secondary electrons due to aluminium surface aberrations. The nature of the image distortion is not fully understood and is subject to further analysis which can be based on measurements with a thin foil replaced with a flat plate.

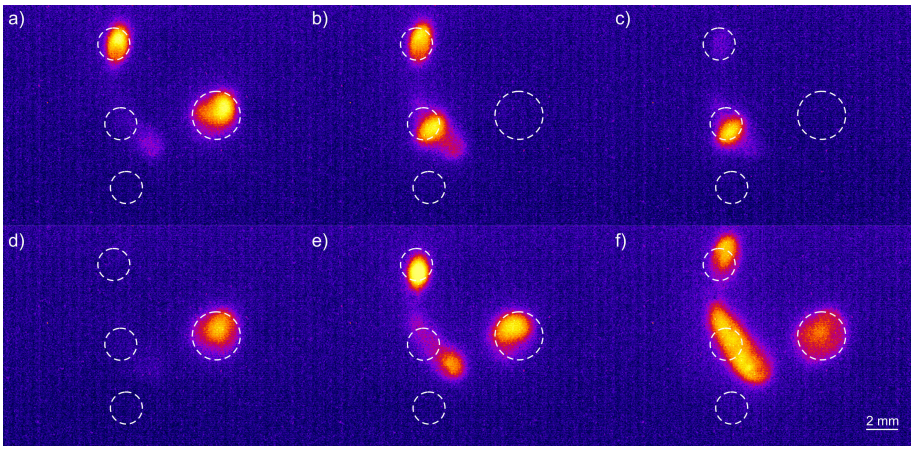

Figure 6.31: Images of the collimator holes shown in Fig. 6.25 for various proton beam position and focus settings.

Although the image does not perfectly resemble the shape of the collimator holes, an important conclusion can be made. The beam spots obtained during the experiment

are of the same size as the apertures in the collimator, without additional blurring of 2–3 mm expected from theoretical calculations. This means that a spatial resolution better than 2 mm can be obtained and the secondary emission model used in the simulations overestimates the energy and angular spread of guided electrons.

6.7 Experiments with Antiprotons

In parallel to the experiments with protons at INFN-LNS, tests with low energy antiprotons were anticipated. For this reason, it has been planned to integrate the monitor with the beam line of the Antihydrogen Experiment: Gravity, Interferometry, Spectroscopy (AEGIS) at CERN [37]. Simulations and the design of the setup were prepared, the SEM was shipped and integrated in the beam line, but the unfortunate failure of the injection septum of the PS made it impossible to deliver antiprotons in the foreseen beam time. Nevertheless, the progress of the work is reported.

6.7.1 Antihydrogen Experiment AEGIS

The primary scientific goal of the AEGIS experiment is a direct measurement of the Earth's gravitational acceleration on antihydrogen [17,37]. A schematic drawing of the setup is shown in Fig. 6.32.

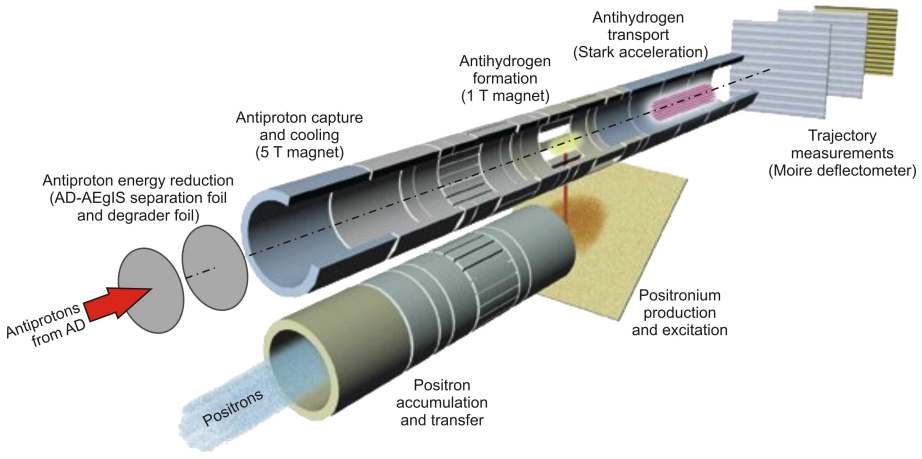

Figure 6.32: Schematic drawing of the AEGIS experiment. Image taken from [277].

Approximately 10^7 antiprotons will be delivered to the experiment by the AD every about 100 seconds. A set of foils placed along the antiprotons path will result in the

reduction of their kinetic energy from 5.3 MeV to hundreds of keV. Next, antiparticles will be captured in a catching trap mounted in a horizontal cryostat inside the bore of a 5 Tesla magnetic field and cooled down to sub-eV energies in a cryogenic environment at about 4 K. The antiproton cloud will be radially compressed and then transferred into a second trap for antihydrogen formation mounted in a colder region with a magnetic field of 1 Tesla. Here, antiprotons will be cooled down to 100 mK. By stacking several AD shots and by careful handling of antiprotons, an average of about 10^5 cold antiprotons ready for recombination is expected [17].

In parallel, approximately 10^8 positrons accumulated in about 200–300 seconds will be transferred from the accumulator in a dedicated trap mounted inside the same magnetic field as the antiproton catching trap. Here, the bunch will be compressed and accelerated towards a nanoporous target material where ground state positronium (Ps) atoms with a velocity of the order of a few 10^4 m/s will be produced. The positronium cloud emerging from the target will be excited by two laser pulses into a selected Rydberg state and about $5 \cdot 10^6$ excited positronium atoms can be obtained. Cold (100 mK) antihydrogen atoms will be produced in a charge exchange reaction during the time in which the Rydberg Ps atoms traverse the antiproton cloud:

$$\mathrm{Ps}^* + \bar{\mathrm{p}} \rightarrow \bar{\mathrm{H}}^* + \mathrm{e}^-. \tag{6.6}$$

The expected number of Rydberg antihydrogen atoms is in the range between 100–1000 per cycle [17].

The resulting antiatoms will be accelerated by means of inhomogeneous electric fields towards a deflectometer for gravity measurements. While neutral atoms are not sensitive, to first order, to constant electric fields, they do experience a force when their electric dipole moment is exposed to an electric-field gradient. If the excited atoms are moving in a region where the amplitude of the electric field is changing, their internal energy changes and thus, to conserve the total energy, they are accelerated or decelerated. Since the dipole moment scales approximately with the square of the principal quantum number, Rydberg atoms are especially amenable to being manipulated in this way. The technique is related to the splitting of spectral lines due to the presence of external electric fields (the Stark effect) and is therefore called Stark acceleration [278, 279].

The gravitational acceleration will be obtained by detecting the vertical deflection of the antihydrogen beam flying horizontally with a velocity of a few 100 m/s for a path length of about 1 metre. The small deflection of a few tens of μm will be measured

using two material gratings coupled to a position sensitive detector working as Moire deflectometer in the classical regime [17, 278, 279].

6.7.2 Secondary Emission Monitor Setup at AEGIS

In November 2011, when the first beam run was scheduled for AEGIS, only a fraction of the apparatus was installed for primary experiments with antiprotons. It had been planned to include the 5 Tesla magnet and the trap, but neither the 1 Tesla section nor the Moire deflectometer had been foreseen at this stage. The purpose of the experiments was to test available detectors and trapping of antiprotons. The end of the beam line was used to install the SEM vessel shown in Fig. 6.17. The motivation was to extend its application to the SEM and other instrumentation tests with low-energy antiprotons.

It was necessary to find a way to integrate the prototype USR detector setup with the AEGIS experiment. In order to avoid any contamination in the experiment region operating at a cryogenic temperature and a vacuum level a few orders of magnitude lower than in the SEM vessel, it had to be separated by means of a thin vacuum window. Also a collimator was foreseen to investigate the resolution of the monitor. Furthermore, an additional detector, called Mimotera [119, 127, 280], was to be tested in parallel. It is a monolithic active pixel sensor of crystalline silicon used for real-time beam imaging. The purpose of the experiment with Mimotera was to investigate its response to low energy antiprotons annihilating directly in its active area. It was decided to expose Mimotera only to halo particles.

A Geant4 model of the AEGIS setup was used to simulate the properties of the beam reaching the monitors placed downstream the 5 Tesla magnet region [246]. It is schematically shown in Fig. 6.33. The 5.3 MeV antiproton beam passes a 8 μm thick AD separation window made of magnesium, a 100 μm thick silicon beam counter, and a 175 μm thick aluminium energy degrader. In addition, a 2 μm thick aluminium window is added upstream of the SEM vessel. Not included in the simulations are a gate valve and vacuum components for attaching the SEM setup to the magnet vessel. The monitor is placed about 40 cm from the separation window, depending on whether it is assembled in the foil-based SEM configuration or the stand-alone MCP setup. Mimotera is placed off-axis, so that both monitors can register incoming particles. Between the window and the detectors, there is a place for a collimator which had to be designed for the purpose of the planned experiments.

An important aspect of the beam available for SEM studies should be pointed out. Most antiprotons delivered at the AEGIS experiment carry energy below 10 keV which

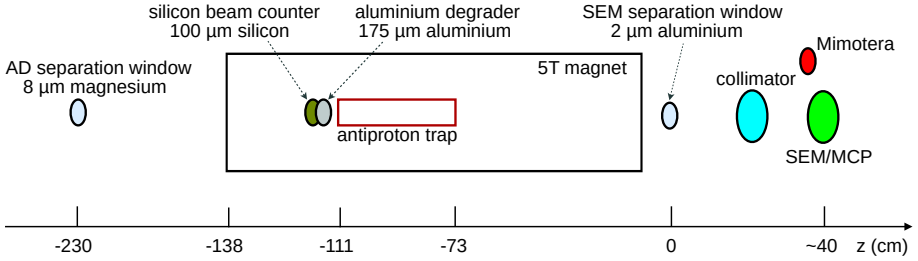

Figure 6.33: Schematic diagram of the AEGIS beam line components included in the Geant4 simulations for the SEM collimator studies.

is too low for tests with the foil-based SEM configuration. Particles with an energy smaller than some tens of keV will be bent away from the foil at a high negative potential, thus they will annihilate in the monitor surroundings producing a large amount of noise. In this case, only a stand-alone MCP is suitable for beam observation. However, it could be possible to test the foil-based SEM with a degraded beam from the AD passing through the apparatus and foils without trapping. In any case, the beam reaching the monitor is strongly defocused and requires additional collimation.

Collimator Simulations

Several collimator configurations proposed for the tests at AEGIS are shown in Fig. 6.34. One of the first ideas, a 5 mm thick aluminium plate with a set of holes of various dimensions as depicted in Fig. 6.34a, was included in the simulations and positioned 28.7 cm downstream of the SEM separation window. The design was shown to be ineffective, because the blurred image of the holes created only by antiprotons was further affected by annihilation products generated mostly in the collimator. Although a central hot spot in the particle distribution was observed, separate holes could not be distinguished.

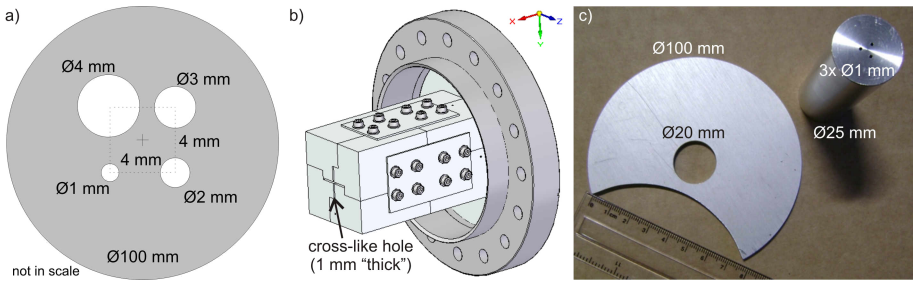

Figure 6.34: Various collimators under consideration. See text for details.

In order to find a more suitable configuration for resolution tests, a similar aluminium plate 0.5 cm thick with a 1 mm wide cross-like cut-out in the middle was modelled. The results are shown in Fig. 6.35. Although the cross-like structure is visible in the fluence of particles recorded in the plane of the monitor, see Fig. 6.35a, it is still strongly blurred and is several times wider than the actual hole. The image is formed mainly by low energy antiprotons, see Fig. 6.35b, and secondary particles contribute to an approximately uniform noise, Fig. 6.35c. The only secondaries that are more focused in the centre are electrons with energies below 1.5 MeV. Fig. 6.35d shows a relative number of particles reaching the monitor, whereas Fig. 6.35e–i show their energy spectra. Because the degraders had been chosen to maximise the number of low energy antiprotons for trapping efficiency, the peak in their energy spectrum is observed at below 10 keV with a quickly decaying tail up to 300–400 keV only. The total number of antiprotons reaching the plane of the SEM position is only about 11% of the simulated 125000 primaries. A similar number of protons and pions is registered. Their peak energy is around 5 MeV, whereas the maximum energy goes beyond 100 MeV. Both protons and pions are uniformly distributed, thus contribute to the noise in the detector. However, it can get saturated if too many particles hit the surface of the MCP. Other secondary particles include MeV-scale electrons and MeV-scale alphas, and their number is 50% and 20% of antiprotons reaching the monitor plane, respectively.

A few modified versions of the collimator with a cross-like cut-out were also studied. The width of the narrow hole was set to be 0.5 mm and then 2 mm. The results for $1.25 \cdot 10^5$ simulated antiprotons are compared with the initial width of 1 mm in Fig. 6.36a–c. The image of the 2 mm wide cut-out is the widest, yet too large to be properly seen by a monitor with an effective diameter of 20 mm or even 40 mm. In the case of the 0.5 mm hole, the number of antiprotons reaching the detector plane is 20% lower than the number of protons. This leads to a decreased SNR and poorer image quality. No option is better than the initial configuration with a 1 mm hole, hence the aluminium plate thickness was increased from 0.5 cm to 10 cm. For such a configuration, 10^5 antiprotons were simulated and the result is shown in Fig. 6.36d. The number of antiprotons reaching the detector plane is reduced to about 9%, whereas the number of protons is only 80% of this amount. However, the number of MeV-scale secondary electrons is doubled as compared to the results with the 0.5 cm thick collimator. The image becomes clearer as a result of two factors: the beam is better collimated by a long and narrow channel, and the collimator ends closer to the monitor. However, such

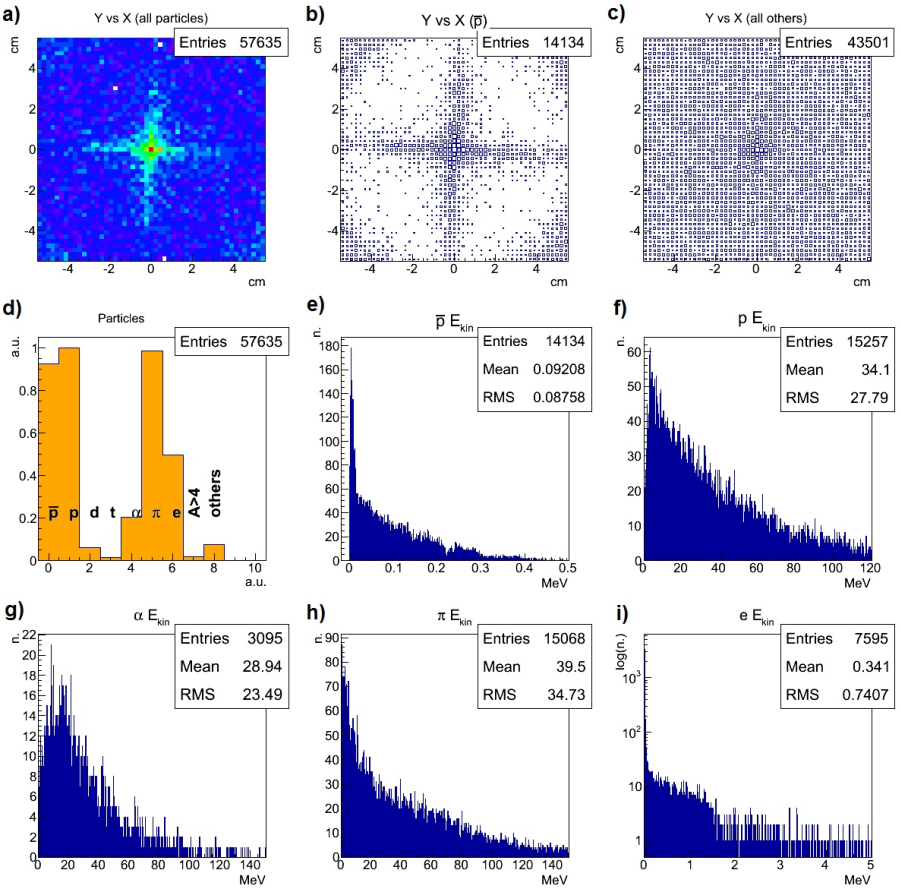

Figure 6.35: Simulation of the AEGIS beam passing through a 0.5 mm thick aluminium plate with a cross-like hole of 1 mm width. The information on the particles fluence (a-d) and energy spectra (e-i) was recorded in the plane of the SEM position. See text for details.

a geometry is difficult to manufacture.

Because machining a cross-like shape in a long aluminium block is problematic, a solution consisting of several likewise pieces put together was proposed. It is shown in Fig. 6.34b and demonstrates that precisely manufactured pieces can form a shape that resembles the idea of a collimator with a cross-like cut-out. They are assembled in a way that no straight trajectory can go through without interacting with one of the blocks except in the central part of the collimator.

The cross-like collimator is quite a complex solution and also results in a wider hot spot in the central part of the image. For this reason, a possibility to prepare several holes in a long metal block was tested. Three holes of 1 mm diameter uniformly dis-

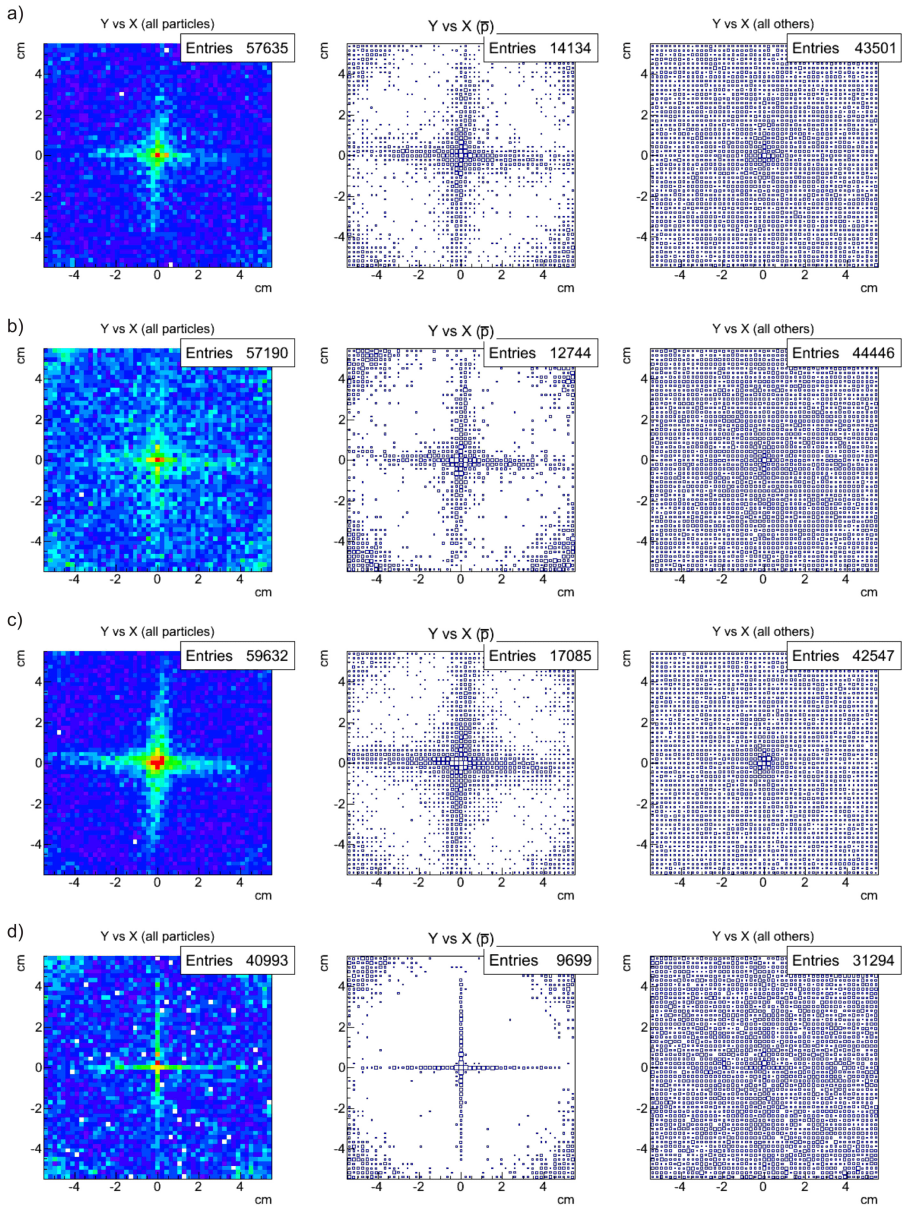

Figure 6.36: Simulation of the AEGIS beam passing through a 0.5 mm thick collimator with a 1 mm wide cross-like hole (a), a 0.5 mm wide cross-like hole (b), a 2 mm wide cross-like hole (c), and a 10 mm thick collimator with a 1 mm wide cross-like hole (d). The first column shows the total fluence, the second column presents only antiprotons, whereas the last one all other particles.

tributed on a 5 mm diameter circle were successfully drilled in an 8 cm long aluminium cylinder, although they were not ideally parallel. The result is shown in Fig. 6.34c. The idea was to fix the cylinder to a larger aluminium plate, called a primary collimator. The latter was to be installed as far as possible from the detector. This way, a solid angle in which generated secondary particles can reach the monitor is minimised, thus the background noise is reduced. An off-axis cut-out in the primary collimator was included not to stop all halo antiprotons and let some of them reach Mimotera. The long cylinder was to collimate the most useful part of the beam for the measurements with SEM/MCP. However, simulations showed that for 1 mm diameter holes, none of 10^5 primary antiprotons was able to reach the 20 mm diameter effective area of the monitor.

Finally, a long collimator with a set of holes of a diameter larger than 1 mm was studied. It was decided to fix it to the SEM assembly, thus its shape was restricted by the inner diameter of the flange and the closest possible distance to the monitor which still enables secondary electrons to pass from the foil to the MCP. The setup is shown in Fig. 6.37. The primary collimator is a 5-mm thick aluminium plate with a cut-out enabling measurements with Mimotera. The main collimator is fixed to the SEM which is assembled either in the foil-based configuration (shown in the figure) or in the stand-alone MCP setup. The maximum distance between the collimator and the foil is 54 mm for the shorter edge of the collimator, whereas the shortest distance is 20 mm for the longer edge. For the stand-alone MCP, the surface of the collimator is parallel to the MCP surface and can be placed at any arbitrary distance.

In the Geant4 simulations, the collimator was simplified by a 67 mm long block which corresponds to the length of its shorter edge and reflects the worst case scenario. The particle fluence was recorded at the distance of 1 mm and 54 mm downstream the collimator. Various sets of holes with diameter from 2 mm to 5 mm were simulated and the results for 3 mm and 4 mm are shown in Fig. 6.38. As expected, the image of the holes is clearly visible just behind the collimator, but becomes blurred further away. Much less than 1% of the primary antiprotons reaches the plane of the monitor. The observed ratio of antiprotons to other particles is 1.5 and 2 for the 3 mm and 4 mm hole, respectively. However, the simulations do not take into account the interaction of particles with the MCP. Due to annihilation, two effects are expected: amplification of the signal and further blurring of the image. The processes are too complex to be studied with the available Monte Carlo codes and experimental verification is needed.

In the presented Geant4 model, antiprotons were extracted to the SEM vessel after

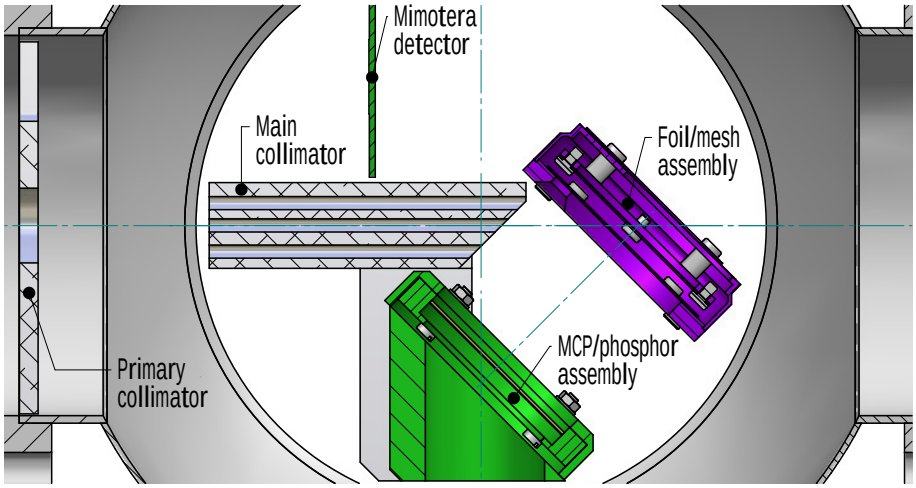

Figure 6.37: A cross-section view of the setup with the primary collimator and the main collimator for the simultaneous measurements with Mimotera and SEM.

trapping. The resulting energy distribution was therefore optimised for the AEGIS experiment and not for spatial resolution tests of the SEM. In such a case, the peak $\bar{p}$ energy was below 10 keV, i.e. in the region not suitable for the foil-based monitor due to the presence of the high repelling voltage. Only a fraction of antiparticles carried energy of hundreds of keV, yet it was contaminated by other high energy particles. This is a condition completely different from what is expected at the USR. Nevertheless, the stand-alone MCP can still be tested with one of the collimators under consideration. A simple solution with half the MCP surface covered from the beam can also be used, but there was no possibility to perform any experimental tests in the 2011 run.

In order to optimise the extracted beam parameters for foil-based SEM tests, no antiproton trapping should be applied. This can be done in the future and the prepared test stand setup can be explored further.

6.8 Summary

A sensitive beam profile monitor with variable signal amplification was developed. It makes use of secondary electrons emission from a foil traversed by a particle beam. Emitted electrons are guided by electric field toward a microchannel plate and phosphor assembly, then multiplied and converted to visible light to form an image of the primary beam recorded by a CCD camera. Since the secondary particles are accelerated by means of a high voltage applied to the system, also the primary beam traverses a region

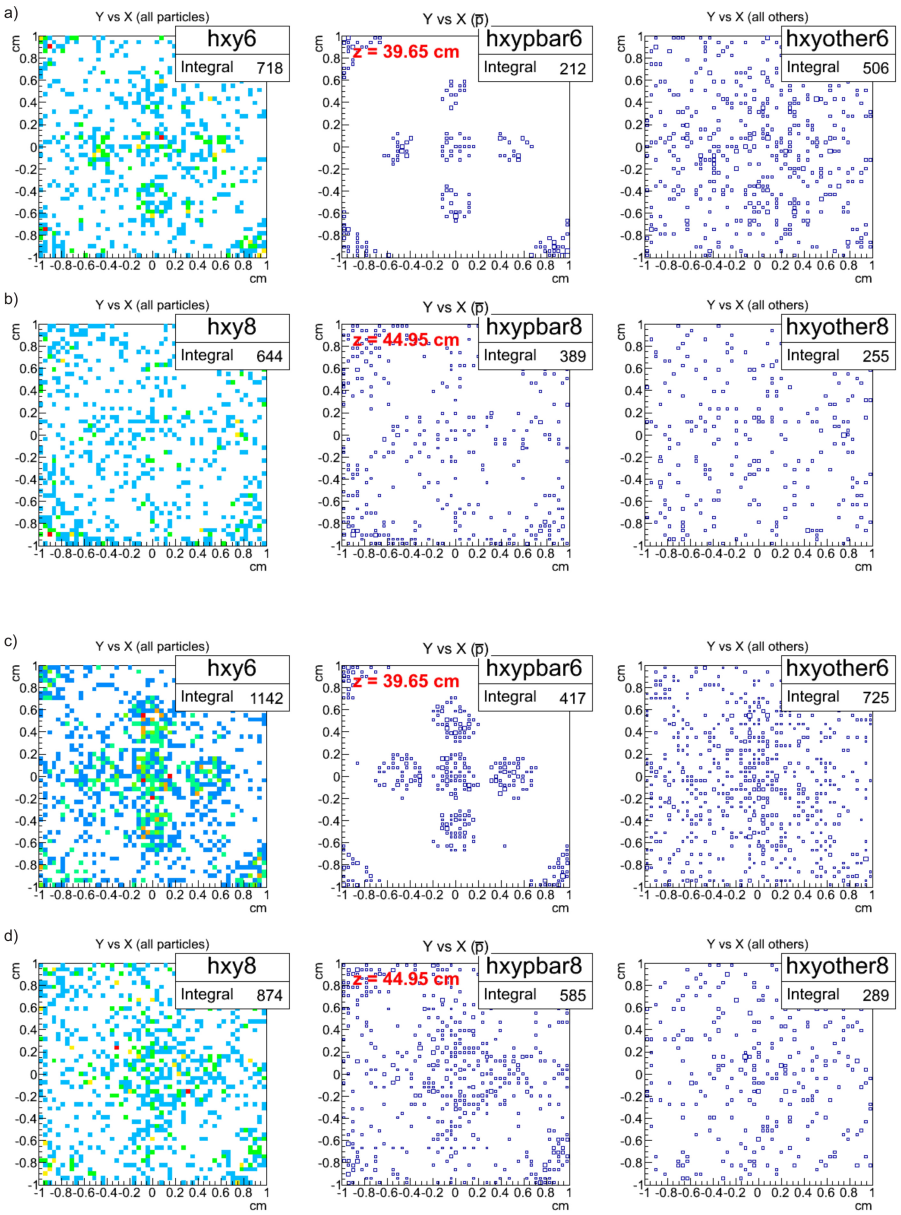

Figure 6.38: Simulation of the AEGIS beam passing through the collimator shown in Fig. 6.37 expressed in particle fluence: a) image of 3 mm holes at a distance of 1 mm from the collimator, b) image of 3 mm holes at 54 mm, c) image of 4 mm holes at 1 mm, and d) image of 4 mm holes at 54 mm.

of the high electric field. It is not a problem in high energy or heavy ion applications, but easily affects the trajectories of keV protons.

Various aspects of the foil-based SEM influence on the primary beam of low energy protons and antiprotons were discussed. The range in matter and scattering of keV particles makes the monitor destructive even with a state-of-the-art technology and commercially available foils. However, the detector is still expected to be very important for the first turn beam diagnostics and measurements in transfer lines. Additional shielding makes it applicable to beam energies available at the USR. With a reduced resolution, due to a limited foil voltage that can be applied, even 20 keV beams can be imaged.

Generation and guidance of secondary electrons was also investigated. A Monte Carlo model was developed to study the image quality obtained with the monitor at various voltages. It was theoretically demonstrated that a resolution of at least 2 mm can be obtained, but the experimental results showed that a better performance can be achieved. It is concluded that the Monte Carlo routine overestimates the energy and angular spread of guided electrons.

Production of other particles due to annihilation of antiprotons in the foil was studied as well. Fluka was used to estimate the numbers of expected high energy secondaries, including MeV-scale protons, electrons and pions. However, a combined charge signal from all of the effects following interaction of antiprotons with the SEM is impossible to simulate in any precise way, thus the results should be treated with care.

A prototype of the SEM was designed and constructed. It was prepared in a way which enables its use in two different configurations: a foil-based secondary emission monitor and a stand-alone MCP placed directly in the beam path. Although not designed for this purpose, the principle of operation of the detector was proved with 5 keV electrons.

The main experimental tests of the monitor were performed at INFN-LNS in Catania. The response of the foil-based SEM was studied in terms of the voltage applied to the MCP and the foil. It was demonstrated that the detector is capable of monitoring beams of sub-femtoampere currents. Some unexpected distortion of the image, such as beam centre shift, was attributed to the foil deflection in a high potential gradient. For this reason, a thin plate instead of a foil is preferred in future applications. Finally, spatial resolution was tested with a custom collimator. Also in this case the observed image was different than expected. Some holes could not be properly repro-

duced and their image changed depending on the beam trajectory and focus. The most probable explanation is that the beam was scattered from the collimator placed at a significant distance from the monitor. Nevertheless, images of other holes were clearly visible showing a better performance of the foil-based SEM than it appeared from the calculations.

Additional feasibility studies were performed to investigate how the monitor can be used at the AEGIS experiment beam line. It was a challenging task not only because antiprotons are delivered through a set of degraders without any additional beam focusing or steering, but also because the resulting beam carries very low energy and is contaminated by high energy secondary particles. Geant4 was used to model the whole setup and various collimators were examined for their usability for the SEM tests. It was demonstrated that the resulting AEGIS beam after trapping is not optimal for the foil-based SEM studies, yet the beam line and the setup can be developed further for a range of experiments with various detector arrangements.

The use of the stand-alone MCP can be experimentally tested, but the amount of secondary particles is much higher than the primary antiprotons. However, secondaries are uniformly distributed and should contribute to a quasi-uniform noise. It would be interesting to test the response of the detector to a collimated beam and compare it with the results for a fully blocked beam. Such a configuration gives a chance to subtract the background noise if only the monitor is not saturated.

Chapter 7

Conclusions

7.1 Summary

The primary objective of the project was to develop and test a set of beam instrumentation for profile, position and intensity monitoring at the future Ultra-low-energy Storage Ring (USR) at FLAIR. In order to achieve this goal, state of the art diagnostic tools for low-energy, low-intensity beams were reviewed and described in Chapter 2. In the following parts of the thesis, details of the optimised monitors were introduced. The detectors include beam profile monitors based on scintillating screens and secondary electron emission, a capacitive pick-up and a sensitive Faraday cup. Although the devices were primarily developed and tested for the USR, they can find application at other low-energy, low-intensity accelerators, storage rings and beam lines.

In Chapter 3, the application of scintillators to keV protons and antiprotons was discussed. Experimental tests were performed at INFN-LNS with several screen materials irradiated with proton beams. It was demonstrated that CsI:Tl and the SFOP are sensitive enough for beam profile monitoring in the ultra-low energy, ultra-low intensity regime. With 200 keV beams, it was possible to measure currents even in the sub-fA range corresponding to about $5 \cdot 10^3$ particles per second. For 50 keV beams, the sensitivity of both screens dropped down and was about 4 times lower for CsI:Tl. Additionally, a resolution of at least 0.3 mm was demonstrated. An absolute light yield calibration technique was applied to estimate the beam current of impinging protons. A design of the monitor based on the scintillators under investigation was developed and will be used at the USR. However, a bulk scintillating screen introduced in the beam path is not suitable for the accurate imaging of low-energy antiproton beams.

In Chapter 4, a non-destructive beam position monitor was discussed. All aspects

of the monitor development were covered, including theoretical studies, computer simulations and optimisation towards the envisaged application, technical design and experimental verification with a current-carrying wire setup. It was demonstrated that the diagonally cut electrodes guarantee linear response of the system to beam displacements. The expected sum and difference signals are $\Sigma\hat{U} = 95$ µV and $\Delta\hat{U} = 1.6$ µV/mm, whereas the unavoidable noise is about 1 nV/$\sqrt{\text{Hz}}$. It was shown that non-linear effects caused by low beam velocities are not a problem in the USR and that it is possible to perform closed-orbit measurements with a narrowband signal processing.

In Chapter 5, a sensitive Faraday cup for beam current measurements was presented. The full project development process was introduced, including theoretical studies, computer simulations and optimisation, technical design and experimental verification. A prototype of the monitor was tested with 200 keV protons at INFN-LNS. The Faraday cup, equipped with a commercial amplifier with a gain of 10^{12} V/A and a bandwidth of 0.1 Hz, yielded the peak-to-peak noise of about 40 fA and further averaging over 20 seconds was applied. It was demonstrated that currents as low as 5 fA ± 0.3 fA can be measured in a reproducible manner. Although the monitor cannot be used for absolute intensity measurements with antiproton beams, it is still an important tool for the initial commissioning phase.

In Chapter 6, an MCP-based secondary emission monitor was introduced. All aspects of the monitor development were discussed, including theoretical studies, computer simulations and optimisation, technical design and experimental verification. The construction of the monitor was made flexible to enable the use of two configurations, the foil-based SEM and an SEM placed directly in the beam path. The SEM setup was tested with 200 keV protons at INFN-LNS. It was demonstrated that beam currents of a few femotamperes can be observed, yet no detection limits were reached. It was shown that there are no advantages in using a thin foil for proton or ion imaging and a plate can be employed instead. A spatial resolution of at least 2 mm was demonstrated with a customised collimator, but the recorded images indicate that further tests may reveal better performance. The images of 2 mm holes yielded higher spatial resolution than predicted in theoretical estimates. In addition, the setup was adapted for future experimental tests with antiprotons at the AEGIS beam line at CERN.

The here-presented monitors will be important for the successful operation of the USR. Four capacitive pick-ups will be used for non-destructive measurements of the beam position in the ring, whereas SEMs and Faraday cups will be used for first-turn

beam diagnostics. The design of the CsI:Tl screen support is made fully compatible with the SEM geometry, thus both profile monitors are interchangeable and can be studied further with the USR beams.

7.2 Future Developments

The subject of low-energy, low-intensity instrumentation has not been exhausted and future work can be undertaken. This includes further investigation into limitations of the here-presented solutions, testing of their applicability to other tasks and systems as well as implementation of different diagnostic techniques.

Position resolution as well as application of the capacitive pick-up can be extended. A customised analogue system can be included before the digitiser to obtain and equalise the amplitudes of sum and difference signals and fully exploit the ADC range. In addition, a resonant amplification circuit can be implemented [131]. Finally, application of the pick-up can be stretched beyond its primary function as a beam position monitor. By calibrating the PU signals against an absolute monitor, such as a Faraday cup, non-destructive intensity measurements of stored beams are possible.

Little room exists for improving resolution and time response of the Faraday cup, i.e. to go below femtoampere currents and time scales of the order of seconds, but other beam intensity monitors can be considered, depending on needs. For non-destructive measurements of beams circulating in a storage ring, an AC beam transformer with customised electronics can be used. Such a solution has been developed and implemented at CRYRING and offers current noise of approximately 1 nA RMS at 20 Hz bandwidth [138]; it can be transferred to the USR if such need emerges. Additionally, relative measurements by means of capacitive pick-ups or analysis of Schottky signals can extend the range of beam currents measured down to the picoampere range [55,138]. Although still under development, also a cryogenic current comparator (CCC) technology can considered as it has been proven to provide resolution of tens to hundreds $\mathrm{pA}/\sqrt{\mathrm{Hz}}$ [141]. For attoampere currents and below, particle counters and antiproton annihilation detectors can be investigated, but they require calibration against an absolute intensity monitor.

The foil-based secondary emission monitor can be improved and investigated further. The foil needs to be either properly stretched or replaced by a thick plate. Also, its material can be chosen to maximise the number of secondary electrons. Furthermore, its spatial resolution limits have not been reached yet and can be studied by

means of either collimators with small diameter holes or edge spread function analysis [281] for half the field of view covered. Finally, the use of the monitor for antiproton beams requires additional experimental tests. In addition, other solutions, such as a supersonic gas jet screen [99] or a SEM grid [122], are either under construction for the USR or can be transferred from other facilities. Alternatively, wire scanners or semiconductor detectors can be investigated in more detail.

Appendix A

Secondary Electron Emission Model

A Lua code [282] was written for SIMION [247] to model secondary electron emission from an aluminium target bombarded with protons of a few hundred keV energy. The angular distribution of electrons followed a cosine-like shape with the peak emission direction normal to the foil surface as reported in [236]. The energy distribution was reproduced from the data for clean aluminium presented in [258]. A polynomial was fitted to the energy spectrum plotted on a semi-logoarithmic scale and used to generate particles of the given energy distribution. The maximum energy of simulated electrons was limited to 30 eV and their number set to 65000.

```
local rand = simion.rand
local exp = math.exp

local a = -9.4e-02
local b =  1.1e+00
local c =  1.3e-01
local d = -7.8e+00
local f =  1.5e+01
local g = -1.2e-02
local h =  8.5e-01
local i =  7.6e-02
local cc = 7.2e-02

function secondaries_rand()
        while true do
                U1 = 30 * rand()
                U2 = 30 * rand()
```

```
                Edstr_cc = a / cc * exp(-1 * b * U1)
                        + c / cc * exp(-1 * (U1-d)^2 / f^2)
                        + g / cc * exp(-1 * (U1-h)^2 / i^2)
                if U2 < Edstr_cc then
                        return U1
                end
        end
end

function acosine_rand()
        return 180 / math.pi * math.acos(2*rand()-1) - 90
end

particles {
  coordinates = 0,
  standard_beam {
    n = 65000,
    tob = 0,
    mass = 0.000548579903,
    charge = -1,
    ke = distribution(secondaries_rand),
    az = 0,
    el = distribution(acosine_rand),
    cwf = 1,
    color = 3,
    position = vector(10, 40, 0)
  }
}
```

Bibliography

[1] P. A. M. Dirac. Quantised singularities in the electromagnetic field. *Proceedings of the Royal Society of London. Series A*, 133(821):60–72, January 1931.

[2] O. Chamberlain, E. Segrè, et al. Observation of antiprotons. *Physical Review*, 100(3):947–950, November 1955.

[3] L. Yarris. Fifty years of antiprotons. *CERN Courier*, 45(9), November 2005.

[4] G. Arnison, A. Astbury, et al. Experimental observation of lepton pairs of invariant mass around 95 GeV/c2 at the CERN SPS collider. *Physics Letters B*, 126(5):398–410, July 1983.

[5] D. Denegri. When CERN saw the end of the alphabet. *CERN Courier*, 43(4), May 2003.

[6] G. Baur, G. Boero, et al. Production of antihydrogen. *Physics Letters B*, 368(3):251–258, February 1996.

[7] M. Amoretti, C. Amsler, et al. Production and detection of cold antihydrogen atoms. *Nature*, 419(6906):456–459, September 2002.

[8] G. Gabrielse, N. S. Bowden, et al. Background-free observation of cold antihydrogen with field-ionization analysis of its states. *Physical Review Letters*, 89(21):213401, October 2002.

[9] G. B. Andresen, M. D. Ashkezari, et al. Trapped antihydrogen. *Nature*, 468(7324):673–676, November 2010.

[10] H. H. Gutbrod, editor. *FAIR - Baseline Technical Report.* September 2006.

[11] E. Widmann, editor. *Technical Proposal for the Design, Construction, Commissioning and Operation of FLAIR.* December 2005.

[12] Gerald Gabrielse. Slow antihydrogen. *Physics Today*, 63(3):68–69, 2010.

[13] News from experiments at CERNs antiproton decelerator - 104th meeting of the SPSC. http://indico.cern.ch/conferenceDisplay.py?confId=171728, January 2012.

[14] Masaki Hori, Anna Sótér, et al. Two-photon laser spectroscopy of antiprotonic helium and the antiproton-to-electron mass ratio. *Nature*, 475(7357):484–488, July 2011.

[15] Tom Kirchner and Helge Knudsen. Current status of antiproton impact ionization of atoms and molecules: theoretical and experimental perspectives. *Journal of Physics B: Atomic, Molecular and Optical Physics*, 44(12):122001, June 2011.

[16] C. Amole, M. D. Ashkezari, et al. Resonant quantum transitions in trapped antihydrogen atoms. *Nature*, 483(7390):439–443, March 2012.

[17] G. Yu Drobychev, P. Nédélec, et al. Proposal for the AEGIS experiment at the CERN antiproton decelerator (Antimatter experiment: Gravity, interferometry, spectroscopy), 2007.

[18] G. Chardin, P. Grandemange, et al. Proposal to measure the gravitational behaviour of antihydrogen at rest, 2011.

[19] Niels Bassler, Jan Alsner, et al. Antiproton radiotherapy. *Radiotherapy and Oncology*, 86(1):14–19, January 2008.

[20] K. F. Long. Towards relativistic propulsion: Antimatter and the interstellar ramjet. In *Deep Space Propulsion*, pages 219–233. Springer New York, 2012.

[21] D. M. Kaplan. Prospects for antiproton experiments at fermilab. *arXiv:1106.3358*, June 2011.

[22] I. S. Hughes. *Elementary Particles*. Cambridge University Press, November 1991.

[23] Bertalan Juhász. *Effect of foreign molecules on the lifetime of antiprotonic helium atoms*. PhD thesis, University of Debrecen, Debrecen, 2004.

[24] H. Koziol and S. Maury. Parameter list for the antiproton accumulator complex (AAC). Technical Report CERN-PS-95-15 AR BD, CERN, Geneva, 1995.

[25] H. Koziol and D. Möhl. The CERN antiproton collider programme: accelerators and accumulation rings. *Physics Reports*, 403-404:91–106, December 2004.

[26] S. Gilardoni and D. Manglunki, editors. *Fifty years of the CERN Proton Synchrotron: Volume 1*. CERN, Geneva, 2011.

[27] Design study of an antiproton collector for the antiproton accumulator (ACOL). Technical Report CERN-83-10, CERN, Geneva, 1983.

[28] B. de Raad. The CERN SPS proton-antiproton collider. *IEEE Transactions on Nuclear Science*, 32(5):1650–1652, October 1985.

[29] M. Chanel and D. Möhl. The CERN low-energy antiproton and ion rings LEAR and LEIR. In *Fifty years of the CERN Proton Synchrotron: Volume 2*. 1st revision manuscript, 2010.

[30] S. A. Baird, D. Berlin, et al. Design study of the antiproton decelerator: AD. Technical Report CERN-PS-96-043-AR, CERN, Geneva, 1996.

[31] S. Baird, D. Berlin, et al. The antiproton decelerator: AD. *Nuclear Instruments and Methods in Physics Research Section A: Accelerators, Spectrometers, Detectors and Associated Equipment*, 391(1):210–215, May 1997.

[32] L. Bojtár. Antiproton decelerator status report. In *Proceedings of COOL09*, Lanzhou, China, 2009.

[33] ALPHA experiment. http://alpha-new.web.cern.ch.

[34] ATRAP antihydrogen studies. http://gabrielse.physics.harvard.edu.

[35] T. Eriksson. ELENA project at CERN. In *Proceedings of COOL11*, Alushta, Ukraine, 2011.

[36] W. Oelert. ELENA: an upgrade to the anti-proton decelerator at CERN. *International Journal of Modern Physics A*, 26(03n04):390, 2011.

[37] AEgIS - antihydrogen experiment: Gravity, interferometry, spectroscopy. http://aegis.web.cern.ch/aegis/home.html.

[38] ASACUSA - atomic spectroscopy and collisions using slow antiprotons. http://asacusa.web.cern.ch/ASACUSA/.

[39] Y. Bylinsky, A. M. Lombardi, et al. RFQD - a decelerating radio frequency quadrupole for the CERN antiproton facility. Monterey, California, August 2000. eConf C000821 (2000) TUD05.

[40] CERN-Bulletin. ELENA prepares a bright future for antimatter research. *BULNA-2011-185. 30/2011*, 2011.

[41] G. Tranquille, P. Belochitskii, et al. ELENA: from the first ideas to the project. In *Proceedings of IPAC'12*, New Orleans, Louisiana, May 2012.

[42] ELENA project. https://espace.cern.ch/elena-project/SitePages/Home.aspx.

[43] T. Eriksson, W. Bartmann, et al. The ELENA project: Progress in the design. In *Proceedings of IPAC'12*, New Orleans, Louisiana, May 2012.

[44] E. Widmann, editor. *FLAIR: A Facility for Low-energy Antiproton and Ion Research, Letter of Intent for the Future Accelerator Facility for Beams of Ions and Antiprotons at Darmstadt.* 2004.

[45] E. Widmann. FLAIR, a next-generation facility for low-energy antiprotons. In *Proceedings of 8th International Conference on Nuclear Physics at Storage Rings STORI'11*, Frascati, Italy, October 2011.

[46] FAIR: facility for antiproton and ion research. http://www.fair-center.de.

[47] M. Steck, C. Dimopoulou, et al. The concept of antiproton accumulation in the RESR storage ring of the FAIR project. In *Proceedings of IPAC'10*, Kyoto, Japan, 2010.

[48] LSR low-energy storage ring. Technical report, Manne Siegbahn Laboratory, Physics Department, Stockholm University, Stockholm, May 2011.

[49] K. Abrahamsson, G. Andler, et al. CRYRING — a synchrotron, cooler and storage ring. *Nuclear Instruments and Methods in Physics Research Section B: Beam Interactions with Materials and Atoms*, 79(1–4):269–272, June 1993.

[50] Håkan Danared, Anders Källberg, et al. CRYRING at the LSR at FLAIR. *Hyperfine Interactions*, 194(1):129–135, 2009.

[51] Carsten Welsch, A. Papash, et al. Ultra-low energy storage ring at FLAIR. *Hyperfine Interactions*, pages 1–11, November 2011.

[52] G. Kube. Specific diagnostics needs for different machines. In *CERN Accelerator School: Beam Diagnostics*. Dourdan, France, 2009.

[53] P. Forck. Lecture notes on beam instrumentation and diagnostics. In *Joint University Accelerator School*. 2011.

[54] Peter Strehl. *Beam Instrumentation and Diagnostics*. Springer, April 2006.

[55] H. Koziol. Beam diagnostics for accelerators. In *CERN Accelerator School: Introduction to Accelerator Physics*. Loutraki, Greece, 2000.

[56] J. Bosser. Beam instrumentation, November 1994. CERN-PE-ED 001-92.

[57] M. J. Berger, J. S. Coursey, et al. ESTAR, PSTAR, and ASTAR: computer programs for calculating stopping-power and range tables for electrons, protons, and helium ions. http://physics.nist.gov/Star, 2005.

[58] M. Inokuti. Interactions of antiprotons with atoms and molecules. *International Journal of Radiation Applications and Instrumentation. Part D. Nuclear Tracks and Radiation Measurements*, 16(2-3):115–123, 1989.

[59] Søren Pape Møller. ELISA, and electrostatic storage ring for atomic physics. *Nuclear Instruments and Methods in Physics Research Section A: Accelerators, Spectrometers, Detectors and Associated Equipment*, 394(3):281–286, July 1997.

[60] S.P. Møller and U.V. Pedersen. Operational experience with the electrostatic storage ring, ELISA. In *Particle Accelerator Conference, PAC 1999*, volume 4, pages 2295 –2297 vol.4, 1999.

[61] S. P. Møller, P. Bowe, et al. Intensity limitations of the electrostatic storage ring ELISA. 2000.

[62] K. Støchkel. Detectors and what we use them for at ELISA, November 2009.

[63] T Tanabe, K Chida, et al. An electrostatic storage ring for atomic and molecular science. *Nuclear Instruments and Methods in Physics Research Section A: Accelerators, Spectrometers, Detectors and Associated Equipment*, 482(3):595–605, April 2002.

[64] T. Tanabé, K. Chida, et al. An electrostatic storage ring for molecular science. 2000.

[65] S. Jinno, T. Takao, et al. TMU electrostatic ion storage ring designed for operation at liquid nitrogen temperature. *Nuclear Instruments and Methods in Physics Research Section A: Accelerators, Spectrometers, Detectors and Associated Equipment*, 532(1–2):477–482, October 2004.

[66] T. Azuma, S. Jinno, et al. An LN2-Cooled electrostatic ring. In *Proceedings of COOL05*, Galena IL, USA, 2005.

[67] S. Jinno, T. Takao, et al. Storage and mass-selective control of ions in an electrostatic ion storage ring. *Nuclear Instruments and Methods in Physics Research Section A: Accelerators, Spectrometers, Detectors and Associated Equipment*, 572(2):568–579, March 2007.

[68] R. D. Thomas, H. T. Schmidt, et al. The double electrostatic ion ring experiment: A unique cryogenic electrostatic storage ring for merged ion-beams studies. *Review of Scientific Instruments*, 82(6):065112–065112–18, June 2011.

[69] S. Das and A. Kallberg. Diagnostics for DESIREE. In *DITANET Workshop: Low Current Low Energy Beam Diagnostics*, Hirschberg-Großsachsen, Germany, November 2009.

[70] K.E. Stiebing, V. Alexandrov, et al. FLSR – the frankfurt low energy storage ring. *Nuclear Instruments and Methods in Physics Research Section A: Accelerators, Spectrometers, Detectors and Associated Equipment*, 614(1):10–16, February 2010.

[71] K. Stiebing. Zum status des frankfurter niederenergie-speicherrings FLSR. In *Non Neutral Plasma Physics Group Seminar, Goethe University Frankfurt*, Frankfurt, Germany, January 2011.

[72] C Krantz, F Berg, et al. The cryogenic storage ring and its application to molecular ion recombination physics. *Journal of Physics: Conference Series*, 300:012010, July 2011.

[73] Manfred Grieser, Robin Bastert, et al. The diagnostic system at the cryogenic storage ring CSR. Proceedings on European JACoW Server, 2010. IPAC'10/ACFA.

[74] V. Chohan, M. Angoletta, et al. Beam measurement systems for the CERN antiproton decelerator (AD). In *19th Particle Accelerator Conference (PAC 2001)*, pages 2302–2304, 2001.

[75] M. E. Angoletta, Belochitskii, et al. ELENA - an updated cost and feasibility study. Technical Report CERN-BE-2010-029, CERN, Geneva, November 2010.

[76] M. Hori. Beam instrumentation for low energy transfer lines. In *ELENA Transfer Lines Workshop*, Geneva, January 2012.

[77] F. Wenander. Survey of available and innovative beam diagnostics alternatives for HIE-REX, February 2008.

[78] G. J. Focker. CERN ISOLDE and REX instrumentation. In *DITANET Workshop: Low Current Low Energy Beam Diagnostics*, Hirschberg-Großsachsen, Germany, November 2009.

[79] F. Wenander. Operational experience from the ISOLDE/REX transfer lines. In *ELENA Transfer Lines Workshop*, Geneva, January 2012.

[80] M. Witthaus, H. Reeg, et al. Beam diagnostics for the HITRAP decelerator. In *DITANET Workshop: Low Current Low Energy Beam Diagnostics*, Hirschberg-Großsachsen, Germany, November 2009.

[81] J. Pfister, U. Ratzinger, et al. HITRAP low energy diagnostics and emittance measurement. In *DITANET Workshop: Low Current Low Energy Beam Diagnostics*, Hirschberg-Großsachsen, Germany, November 2009.

[82] D Rifuggiato, L Calabretta, et al. Radioactive ion beam facilities at INFN LNS. *Journal of Physics: Conference Series*, 267:012007, January 2011.

[83] P. Finocchiaro, L. Cosentino, et al. Low-energy/low-intensity beam diagnostics detectors: experience at INFN-LNS catania. In *DITANET Workshop: Low Current Low Energy Beam Diagnostics*, Hirschberg-Großsachsen, Germany, November 2009.

[84] S. Gales. GANIL-SPIRAL1-SPIRAL2: highlights and perspectives. *AIP Conference Proceedings*, 1238(1):26–35, June 2010.

[85] Christophe Jamet. Secondary beams overview and low current measurements of SPIRAL1 and SPIRAL2 facility. In *DITANET Workshop: Low Current Low Energy Beam Diagnostics*, Hirschberg-Großsachsen, Germany, November 2009.

[86] Jean Luc Vignet, Eloïse Guéroult, et al. Beam profile monitors for SPIRAL2 RIB and experimental rooms. In *DITANET Workshop: Low Current Low Energy Beam Diagnostics*, Hirschberg-Großsachsen, Germany, November 2009.

[87] T. Eriksson. Beam quality monitoring in the CERN antiproton decelerator (AD). In *4th Workshop on Accelerator Operation WAO 2003*, Tsukuba, Japan, March 2003.

[88] S. S. Kapoor and V. Ramamurthy. *Nuclear Radiation Detectors.* New Age International, 1993.

[89] Fabio Sauli. Gas detectors: recent developments and future perspectives. 1998.

[90] G. F. Knoll. *Radiation Detection and Measurement.* John Wiley and Sons, August 2010.

[91] K. Nakamura and Particle Physics Group. Review of particle physics. *Journal of Physics G: Nuclear and Particle Physics*, 37(7A):075021, July 2010.

[92] Brian Martin. *Nuclear and Particle Physics: An Introduction.* John Wiley & Sons, August 2011.

[93] M. Hori. Parallel plate chambers for monitoring the profiles of high-intensity pulsed antiproton beams. *Nuclear Instruments and Methods in Physics Research Section A: Accelerators, Spectrometers, Detectors and Associated Equipment*, 522(3):420–431, April 2004.

[94] S Duarte Pinto, R Jones, et al. GEM-based beam profile monitors for the antiproton decelerator. *Journal of Instrumentation*, 7(03):C03001–C03001, March 2012.

[95] G. Cuttone, C. De Martinis, et al. Low intensity beam diagnostics with microchannel plate detectors. In *Particle Accelerator Conference, 1997. Proceedings of the 1997*, volume 2, pages 2038 –2040 vol.2, May 1997.

[96] Gerard Tranquille. Recent highlights from the CERN-AD. *Nuclear Instruments and Methods in Physics Research Section A: Accelerators, Spectrometers, Detectors and Associated Equipment*, 532(1–2):111–117, October 2004.

[97] G. Tranquille. Influence of the BIPM gas injectors on AD performance, 2002. PS/BD/Note 2002-15.

[98] M. Putignano, K. Kühnel, et al. A fast, low perturbation ionization beam profile monitor based on a gas-jet curtain for the ultra low energy storage ring. *Hyperfine Interactions*, 194(1):189–193, 2009.

[99] M. Putignano. *Supersonic gas-jet based beam profile monitor*. PhD thesis, University of Liverpool, Liverpool, UK.

[100] Anders Källberg. Diagnostics at CRYRING. In *DITANET Workshop: Low Current Low Energy Beam Diagnostics*, Hirschberg-Großsachsen, Germany, November 2009.

[101] T. Sieber, H. Fadil, et al. A beam diagnostics system for the heidelberg cryogenic storage ring CSR. In *EPAC2006 - European Particle Accelerator Conference*, Edinburgh, UK, 2006.

[102] Luigi Cosentino and Paolo Finocchiaro. Ion beam imaging at very low energy and intensity. *Nuclear Instruments and Methods in Physics Research Section B: Beam Interactions with Materials and Atoms*, 211(3):443–446, November 2003.

[103] J. Bosser, G. Ferioli, et al. Profile measurement in LEAR transfer line. Technical Report SPS/ABM/Note/87-06, January 1987. LEAR Note 87-04.

[104] A.M. Lombardi, W. Pirkl, et al. First operating experience with the CERN decelerating RFQ for antiprotons. In *Particle Accelerator Conference, PAC 2001*, volume 1, pages 585 –587 vol.1, 2001.

[105] M. Hori. (Max Planck Institute of Quantum Optics, Germany), private communication (2008-2012).

[106] V. Agoritsas, L. Colomer, et al. Beam profile monitor for very low energy antiprotons using position sensitive photomultiplier. *Nuclear Physics B - Proceedings Supplements*, 16(0):503, August 1990.

[107] Joseph Ladislas Wiza. Microchannel plate detectors. *Nuclear Instruments and Methods*, 162(1–3):587–601, June 1979.

[108] Hamamatsu. Image intensifiers, 2009.

[109] A. Povilus. (University of California, USA), private communication (2008).

[110] G. B. Andresen, W. Bertsche, et al. Antiproton, positron, and electron imaging with a microchannel plate/phosphor detector. *Review of Scientific Instruments*, 80(12):123701–123701–5, December 2009.

[111] J. S. Hangst. Status report on experiment AD5-ALPHA, January 2009. 90th Meeting of the SPSC.

[112] H. Imao, H. A. Torii, et al. Observation of Ultra-Slow antiprotons using microchannel plate. *AIP Conference Proceedings*, 1037(1):311–317, August 2008.

[113] M. Hori and K. Hanke. Spatial and temporal beam profile monitor with nanosecond resolution for CERN's linac4 and superconducting proton linac. *Nuclear Instruments and Methods in Physics Research Section A: Accelerators, Spectrometers, Detectors and Associated Equipment*, 588(3):359–374, April 2008.

[114] Masaki Hori and Anna Soter. Operational experience with beam monitors for MeV and keV antiproton beams at CERN's AD. In *DITANET Workshop: Low Current Low Energy Beam Diagnostics*, Hirschberg-Großsachsen, Germany, November 2009.

[115] K. Kruglov, L. Weissman, et al. A beam diagnostic system for low-intensity radioactive beams. *Nuclear Instruments and Methods in Physics Research Section A: Accelerators, Spectrometers, Detectors and Associated Equipment*, 441(3):595–604, March 2000.

[116] P. N. Ostroumov, P. Billquist, et al. Design and test of a beam profile monitoring device for low intensity radioactive beams. *Review of Scientific Instruments*, 73(1):56–62, January 2002.

[117] T. Sieber, K. Blaum, et al. Beam diagnostics for the prototype of the cryogenic storage ring CSR. In *Proceedings of EPAC2008*, Genoa, Italy, 2008.

[118] S. Das, A. Källberg, et al. Spatial resolution test of a BPMS for DESIREE beam line diagnostics. In *Proceedings of DIPAC11*, Hamburg, Germany, 2011.

[119] L. Badano. *Développement d'un moniteur de faisceau innovant pour la mesure en temps réel des faisceau utilisés en hadronthérapie.* PhD thesis, Université Louis Pasteur, Strasbourg, September 2005.

[120] Michael Plum. Interceptive beam Diagnostics—Signal creation and materials interactions. *AIP Conference Proceedings*, 732(1):23–46, November 2004.

[121] P. Forck, P. Kowina, et al. Beam position monitors. In *CERN Accelerator School: Beam Diagnostics*. Dourdan, France, 2009.

[122] Masaki Hori. Photocathode microwire monitor for nondestructive and highly sensitive spatial profile measurements of ultraviolet, x-ray, and charged particle beams. *Review of Scientific Instruments*, 76(11):113303–113303–6, November 2005.

[123] Leonardo Rossi. *Pixel Detectors: From Fundamentals to Applications.* Springer Science & Business, March 2006.

[124] A. Rovelli. Review of beam diagnostics for radioactive beams. In *Particle Accelerator Conference, PAC 1999*, volume 1, pages 482 –486 vol.1, New York, 1999.

[125] P. Pusa. (University of Liverpool, UK), private communication (2012).

[126] CERN RD50 collaboration: Radiation hard semiconductor devices for very high luminosity colliders. http://rd50.web.cern.ch/rd50/.

[127] R. Boll. *A Monolithic Active Pixel Sensor as Direct Monitor for Therapeutic Antiproton and Ion Beams.* PhD thesis, University of Heidelberg, Heidelberg, December 2010.

[128] Rhodri Jones and Hermann Schmickler. Introduction to beam instrumentation and diagnostics. In *CERN Accelerator School: Intermediate Accelerator Physics.* Zeuthen, Germany, 2006.

[129] M. Le Gras, L. Søby, et al. The closed-orbit measurement system for the CERN antiproton decelerator. In *Proceedings of DIPAC99*, Chester, UK, May 1999.

[130] L. Søby and J. Harasimowicz. ELENA orbit, project overview. ELENA Beam Instrumentation Review Meeting, CERN, 12 Apr. 2012.

[131] F. Laux. *Entwicklung von Kapazitiven Positions-, Strom- und Schottkysignal-Messsystemen für den Kryogenen Speicherring CSR*. PhD thesis, Ruprecht-Karls-Universität, Heidelberg, July 2011.

[132] Manfred Grieser. (Max Planck Institute for Nuclear Physics, Germany), private communication (2008-2012).

[133] Robert C. Webber. Tutorial on beam current monitoring, June 2000. FERMILAB-Conf-00-119.

[134] C. González and F. Pedersen. An ultra low noise AC beam transformer for deceleration and diagnostics of low intensity beams. In *18th Biennial Particle Accelerator Conference PAC 1999*, New York, 1999.

[135] M. E. Angoletta. The AD schottky system and future evolutions. In *CARE-N3-HHH Workshop: Schottky, Tune and Chromaticity Diagnostic (with Real Time Feedback)*, Chamonix Mont Blanc, France, December 2007.

[136] Bergoz instrumentation. http://www.bergoz.com.

[137] A. Paal and A. Simonsson. Bunched beam current measurements with 1 nArms resolution at CRYRING using a BERGOZ integrating current transformer (ICT), 2006.

[138] A. Paal, A. Simonsson, et al. Bunched beam current measurements with 100 pA rms resolution at CRYRING. In *EPAC2006 - European Particle Accelerator Conference*, Edinburgh, UK, 2006.

[139] Andreas Peters, Wolfgang Vodel, et al. A cryogenic current comparator for the absolute measurement of nA beams. *AIP Conference Proceedings*, 451(1):163–180, December 1998.

[140] M. Schwickert, T. Hoffmann, et al. Diagnostic devices for beam intensity measurement at FAIR. In *Second International Particle Accelerator Conference IPAC 2011*, volume IPAC'11, San Sebastian, Spain, September 2011.

[141] Wolfgang Vodel. The SQUID based cryogenic current comparator - a useful tool for beam diagnostics. In *DITANET Workshop: Low Current Low Energy Beam Diagnostics*, Hirschberg-Großsachsen, Germany, November 2009.

[142] Manfred Grieser, S. Artikova, et al. Beam current measurements at the TSR heidelberg. In *Second International Particle Accelerator Conference IPAC 2011*, volume IPAC'11, San Sebastian, Spain, September 2011.

[143] D. Belohrad. Beam charge measurements. In *Proceedings of DIPAC11*, Hamburg, Germany, 2011.

[144] Christopher A. Gresham, Phillip J. Rodacy, et al. Micro faraday-element array detector for ion mobility spectroscopy, October 2004. U.S. patent no. 6809313.

[145] J. Harasimowicz, L. Cosentino, et al. Scintillating screens sensitivity and resolution studies for low energy, low intensity beam diagnostics. *Review of Scientific Instruments*, 81(10):103302, 2010.

[146] P. Heeg and O. Keller. A scintillator-photodiode-beam intensity monitor. In *4th European Particle Accelerator Conference*, London, UK, 1994.

[147] R W Wijnaendts van Resandt, H C den Harink, et al. A position dependent particle counter using microchannel plates. *Journal of Physics E: Scientific Instruments*, 9(6):503–509, June 1976.

[148] Stefan Rosén, Henning T. Schmidt, et al. Operating a triple stack microchannel plate-phosphor assembly for single particle counting in the 12–300 k temperature range. *Review of Scientific Instruments*, 78(11):113301–113301–5, November 2007.

[149] Joachim Fricke, Alfred Müller, et al. Single particle counting of heavy ions with a channeltron detector. *Nuclear Instruments and Methods*, 175(2–3):379–384, September 1980.

[150] Jens Ulrik Andersen, Preben Hvelplund, et al. The combination of an electrospray ion source and an electrostatic storage ring for lifetime and spectroscopy experiments on biomolecules. *Review of Scientific Instruments*, 73(3):1284–1287, March 2002.

[151] E. Griesmayer, H. Pernegger, et al. High-resolution energy and intensity measurements with CVD diamond at REX-ISOLDE. *CERN-BE-Note-2009-028*, 2009.

[152] M.C Fujiwara and M Marchesotti. A novel current mode operating beam counter based on not preamplified HPDs. *Nuclear Instruments and Methods in Physics*

Research Section A: Accelerators, Spectrometers, Detectors and Associated Equipment, 484(1–3):162–173, May 2002.

[153] M. Amoretti, C. Amsler, et al. The ATHENA antihydrogen apparatus. *Nuclear Instruments and Methods in Physics Research Section A: Accelerators, Spectrometers, Detectors and Associated Equipment*, 518(3):679–711, February 2004.

[154] M. Hori, K. Yamashita, et al. Analog cherenkov detectors used in laser spectroscopy experiments on antiprotonic helium. *Nuclear Instruments and Methods in Physics Research Section A: Accelerators, Spectrometers, Detectors and Associated Equipment*, 496(1):102–122, January 2003.

[155] M. C. Fujiwara, M. Amoretti, et al. Three dimensional annihilation imaging of antiprotons in a penning trap. *AIP Conference Proceedings*, 692(1):131–139, December 2003.

[156] W. R. Leo. *Techniques for nuclear and particle physics experiments: a how-to approach*. Springer, 1994.

[157] S. Tavernier. *Experimental Techniques in Nuclear and Particle Physics*. Springer, February 2010.

[158] S. Derenzo, M. Boswell, et al. Scintillation properties. http://scintillator.lbl.gov/, 2011.

[159] J. B. Birks. *The theory and practice of scintillation counting*. Pergamon Press; [distributed in the Western Hemisphere by Macmillan, New York], 1964.

[160] R.L. Craun and D.L. Smith. Analysis of response data for several organic scintillators. *Nuclear Instruments and Methods*, 80(2):239–244, April 1970.

[161] M. Vogel, D.F.A. Winters, et al. Scintillation light produced by low-energy beams of highly-charged ions. *Nuclear Instruments and Methods in Physics Research Section B: Beam Interactions with Materials and Atoms*, 263(2):518–522, October 2007.

[162] J. Camas, G. Ferioli, et al. High sensitivity beam intensity and profile monitors for the SPS extracted beams. 1993.

[163] C. Bal, E. Bravin, et al. Scintillating screens study for LEIR/LHC heavy ion beams. In *7th European Workshop on Beam Diagnostics and Instrumentation for Particle Accelerators*, Lyons, France, June 2005.

[164] W. Markiel, H. Daniel, et al. Emission of helium ions after antiproton annihilation in nuclei. *Nuclear Physics A*, 485(3-4):445–460, August 1988.

[165] R. S. Hayano. Physics using trapped antiprotons. In *Hadron Physics: Proceedings of the International School of Physics CLVIII*. IOS Press, 2005.

[166] R. S. Hayano. Trapped antiprotons. In *Symposium on the Physics at FAIR*, Darmstadt, Germany, November 2007.

[167] G Ciavola, M Castro, et al. Operational experience with the 450 kV injector for the superconducting cyclotron. *Nuclear Instruments and Methods in Physics Research Section A: Accelerators, Spectrometers, Detectors and Associated Equipment*, 382(1-2):192–196, November 1996.

[168] Hilger crystals. http://www.hilger-crystals.co.uk/.

[169] Collimated holes, inc. http://www.collimatedholes.com/.

[170] CRYTUR, spol. s r.o. http://www.crytur.cz/pages/6/contacts.

[171] DTA srl. http://www.dta.it/.

[172] Eastman kodak company. http://www.kodak.com.

[173] W. S. Rasband. ImageJ: image processing and analysis in java, u. s. national institutes of health, bethesda, maryland. http://imagej.nih.gov/ij/, 1997.

[174] *Low Level Measurements Handbook. Precision DC Current, Voltage, and Resistance Measurements.* Keithley Instruments, Inc., 6th edition, 2004.

[175] A. Pappalardo, L. Cosentino, et al. An imaging technique for detection and absolute calibration of scintillation light. *Review of Scientific Instruments*, 81:033308, 2010.

[176] A. Pappalardo, L. Cosentino, et al. Erratum: "An imaging technique for detection and absolute calibration of scintillation light" [Rev. sci. instrum. 81, 033308 (2010)]. *Review of Scientific Instruments*, 82(4):049903–049903–1, April 2011.

[177] J. Ziegler. Stopping and range of ions in matter (SRIM) & transport of ions in matter (TRIM). http://www.srim.org/, 2010.

[178] A. Whetstone, B. Allison, et al. Photoproton scintillation spectrometer. *Review of Scientific Instruments*, 29(5):415–419, May 1958.

[179] R. A Peck, H. P Eubank, et al. Response of CsI(Tl) to p, d, and alpha particles. *Review of Scientific Instruments*, 30(8):703–706, August 1959.

[180] Y.K. Gupta, D.C. Biswas, et al. Characteristics of CsI(Tl) crystal coupled with PIN photodiode for gamma-rays and charged particle. In *Proceedings of the International Symposium on Nuclear Physics*, Mumbai, India, 2009.

[181] R. Gwin and R. B. Murray. Scintillation process in CsI(Tl). i. comparison with activator saturation model. *Physical Review*, 131(2):501–508, July 1963.

[182] C. Bueno. New luminescent glasses and fiber optic scintillators for use in x-ray imaging. In *Proceedings of the 182nd Meeting of the Electrochemical Society*, Toronto, Canada, 1992.

[183] E. E. Ovechkina, V. Gaysinskiy, et al. Multiple doping of CsI:Tl crystals and its effect on afterglow. *Radiation measurements*, 42(4-5):541–544, May 2007. PMID: 18449339 PMCID: 2170897.

[184] Giuseppe Vismara. The comparison of signal processing systems for beam position monitors. In *Proceedings of DIPAC99*, Chester, UK, May 1999.

[185] G. Vismara. Signal processing for beam position monitors. In *Proceedings of BIW2000*, Cambridge, MA, USA, May 2000.

[186] I. N. Bronshtein, K. A. Semendyayev, et al. *Handbook of Mathematics*. Springer, October 2007.

[187] J. H. Cupérus. Monitoring of particle beams at high frequencies. *Nuclear Instruments and Methods*, 145(2):219–231, September 1977.

[188] R. E. Shafer. Beam position monitor sensitivity for low-beta beams. *AIP Conference Proceedings*, 319(1):303–308, October 1994.

[189] R. E. Shafer. Beam position monitoring. *AIP Conference Proceedings*, 212(1):26–58, October 1990.

[190] F. Bowman. *Introduction to Bessel functions*. Courier Dover Publications, 1958.

[191] C. P. Welsch and J. Ullrich. FLAIR – a facility for low-energy antiproton and ion research. *Hyperfine Interactions*, 172(1-3):71–80, June 2007.

[192] M. Grieser, R. Bastert, et al. Acceleration, deceleration and bunching of stored and cooled ion beams at the TSR, heidelberg. In *Proceedings of HIAT09*, Venezia, Italy, June 2009.

[193] R. E. Shafer. Bunch shapes, fourier transforms, and spectral power densities. Technical report, 2002.

[194] N. Kularatna and Institution of Electrical Engineers. *Digital and analogue instrumentation: testing and measurement*. IET, 2003.

[195] J. Belleman. From analog to digital. In *CERN Accelerator School: Beam Diagnostics*. Dourdan, France, 2009.

[196] I. Biļinskis. *Digital Alias-Free Signal Processing*. John Wiley and Sons, June 2007.

[197] E. Bogatin. *Signal integrity: simplified*. Prentice Hall Professional, 2004.

[198] S. L. Bressler. Data acquisition. 2008.

[199] K. Craig. Digitization: Sampling and quantization, 2011.

[200] J. L. Huertas. *Test and design-for-testability in mixed-signal integrated circuits*. Springer, 2004.

[201] MathWorks MATLAB. http://www.mathworks.co.uk/products/matlab.

[202] Solid Edge. http://www.plm.automation.siemens.com/en_gb/products/velocity/solidedge/, 2009.

[203] P. Kowina. BPM simulations for the FAIR SIS100 synchrotron using microwave studio. In *4th CARE-N3-HHH-ABI Workshop*, Lueneburg, Germany, November 2006.

[204] J. H. Cupérus. Edge effect in beam monitors. *Nuclear Instruments and Methods*, 145(2):233–243, September 1977.

[205] Andras Paál. (Manne Siegbahn Laboratory, Sweden), private communication (2011).

[206] Ed da Silva and Eduardo da Silva. *High Frequency and Microwave Engineering*. Elsevier, March 2001.

[207] GaGe. CompuScope software development kit (SDK) for LabVIEW for windows: User's guide, 2011.

[208] GaGe. CompuScope software development kit (SDK) for LabVIEW for windows: CsTool VI guide, 2011.

[209] A. Chao. *Handbook of accelerator physics and engineering*. World Scientific, 1999.

[210] V. V. Sarwate. *Electromagnetic fields and waves*. bohem press, 1993.

[211] CST STUDIO SUITE - EM simulation software. http://www.cst.com/, 2009.

[212] T. Weiland. A discretization model for the solution of maxwell's equations for six-component fields. *Archiv Elektronik und Uebertragungstechnik*, 31:116–120, March 1977.

[213] B. Krietenstein, R. Schuhmann, et al. The perfect boundary approximation technique facing the big challenge of high precision field computation. Chicago, IL, USA, August 1998.

[214] U. Becker. Recent developments in 3D electromagnetic and charged particle simulation. In *Vacuum Electronics Conference, 2007. IVEC '07. IEEE International*, pages 1–4. IEEE, May 2007.

[215] CST studio suite 2010 help, 2010.

[216] P. Sigmund. *Particle Penetration and Radiation Effects: General Aspects and Stopping of Swift Point Charges*. Springer, 2006.

[217] International Commission on Radiation Units and Measurements. *ICRU Report 49: Stopping Powers and Ranges for Protons and Alpha Particles*. International Commission on Radiation Units and Measurements, 1993.

[218] S.P. Møller, E. Uggerhøj, et al. Measurement of the barkas effect around the stopping-power maximum for light and heavy targets. *Nuclear Instruments and*

Methods in Physics Research Section B: Beam Interactions with Materials and Atoms, 122(1):162–166, January 1997.

[219] S. P. Møller, A. Csete, et al. Antiproton stopping at low energies: Confirmation of velocity-proportional stopping power. *Physical Review Letters*, 88(19):193201, April 2002.

[220] S.P. Møller, A. Csete, et al. Antiproton and proton energy loss straggling at keV energies. *The European Physical Journal D*, 46(1):4, 2008.

[221] Steven P. Ahlen. Calculation of the relativistic bloch correction to stopping power. *Physical Review A*, 25(4):1856–1867, April 1982.

[222] V. A. Khodyrev. On the origin of the bloch correction in stopping. *Journal of Physics B: Atomic, Molecular and Optical Physics*, 33(22):5045–5056, November 2000.

[223] Brian J. McParland. *Nuclear Medicine Radiation Dosimetry: Advanced Theoretical Principles*. Springer, May 2010.

[224] H. Paul. Stopping power for light ions: Graphs, data, comments and programs. http://www.exphys.uni-linz.ac.at/Stopping/, 2011.

[225] J. F Ziegler. Stopping of energetic light ions in elemental matter. *Journal of Applied Physics*, 85(3):1249–1272, February 1999.

[226] M. A. Nastasi, J. W. Mayer, et al. *Ion-solid interactions: fundamentals and applications*. Cambridge University Press, 1996.

[227] V. Kozlovski and V. Abrosimova. *Radiation Defect Engineering*. World Scientific, 2005.

[228] H. Friedrich. *Theoretical Atomic Physics*. Birkhäuser, 2006.

[229] R. O. Dendy. *Plasma Physics: an Introductory Course*. Cambridge University Press, February 1995.

[230] P. Misaelides. *Application of particle and laser beams in materials technology*. Springer, July 1995.

[231] R. Smith. *Atomic and Ion Collisions in Solids and at Surfaces: Theory, Simulation and Applications*. Cambridge University Press, September 2005.

[232] J.V. Vukanić, R.K. Janev, et al. Total backscattering of keV light ions from solids at oblique and grazing incidence. *Nuclear Instruments and Methods in Physics Research Section B: Beam Interactions with Materials and Atoms*, 18(1–6):131–141, 1986.

[233] W. Eckstein and J. P. Biersack. The reflection of light swift particles from heavy solid targets. *Zeitschrift für Physik A Atoms and Nuclei*, 310(1-2):1–8, March 1983.

[234] U. Littmark and A. Gras-Marti. Energy spectra of light ions backscattered from random solids. *Applied Physics*, 16(3):247–253, July 1978.

[235] M. Rösler, W. Brauer, et al. *Particle Induced Electron Emission I.* Springer-Verlag, 1991.

[236] D. Hasselkamp, H. Rothard, et al. *Particle induced electron emission II.* Springer-Verlag, 1992.

[237] C. J. Powell and A. Jablonski. NIST electron inelastic-mean-free-path database. http://www.nist.gov/srd/nist71.cfm, 2011.

[238] I. Bojko, N. Hilleret, et al. Influence of air exposures and thermal treatments on the secondary electron yield of copper. *Journal of Vacuum Science & Technology A: Vacuum, Surfaces, and Films*, 18(3):972–979, 2000.

[239] C. J. Chen. *Introduction to Scanning Tunneling Microscopy.* Oxford University Press, USA, May 1993.

[240] L. E. Frenzel. Accurately measure nanoampere and picoampere currents. *Electronic Design*, Supplement, February 2007.

[241] A. Amato. Low level DC-current measurements and their applications in beam diagnostic at INFN-LNS, 2009.

[242] R. Behrisch and W. Eckstein. *Sputtering by Particle Bombardment.* Springer, 2007.

[243] Application bulletin: Noise analysis of FET transimpedance amplifiers, February 1994.

[244] S. Agostinelli, J. Allison, et al. Geant4 - a simulation toolkit. *Nuclear Instruments and Methods in Physics Research Section A: Accelerators, Spectrometers, Detectors and Associated Equipment*, 506(3):250–303, July 2003.

[245] Geant4: A toolkit for the simulation of the passage of particles through matter. http://geant4.cern.ch/, 2011.

[246] Germano Bonomi. (University of Brescia, Italy), private communication (2011).

[247] Inc. Scientific Instrument Services. SIMION: ion and electron optics simulator. http://simion.com/, 2009.

[248] K. Kiyohara, Y. Koba, et al. Study of the angular and energy distribution of secondary electrons emitted by high energy heavy ion impact. *Progress in Nuclear Science and Technology*, 1:222–225, 2011.

[249] C. P. Welsch, M. Grieser, et al. Layout of the USR at FLAIR. In *Proceedings of EPAC06*, Edinburgh, UK, 2006.

[250] FEMTO messtechnik GmbH. http://www.femto.de/.

[251] iseg spezialelektronik GmbH. http://www.iseg-hv.com/.

[252] PSP vacuum technology ltd. http://www.pspvacuum.com.

[253] Pfeiffer vacuum GmbH. http://www.pfeiffer-vacuum.com/.

[254] Tektronix inc. http://www.tek.com/.

[255] ESPI metals. http://www.espimetals.com.

[256] Ltd. PSP Vacuum Technology. ELS5000 electron source and control unit instruction manual, 2003.

[257] Thorlabs. Sources of vibration. http://www.thorlabs.com/tutorials/Tables2.cfm, 2011.

[258] D. Hasselkamp and A. Scharmann. The ion-induced low energy electron spectrum from aluminium. *Surface Science*, 119(2–3):L388–L392, July 1982.

[259] B. Dörband, H. Müller, et al. *Handbook of Optical Systems, Metrology of Optical Components and Systems.* John Wiley & Sons, June 2012.

[260] Juan Luis Fernandez-Hernando. Cockcroft Institute and STFC/DL/ASTeC, UK, private communication (2011).

[261] A. Ferrari, P. R. Sala, et al. FLUKA: a multi-particle transport code. *CERN-2005-010, INFN/TC_05/11, SLAC-R-773*, 2005.

[262] G. Battistoni, F. Cerutti, et al. The FLUKA code: description and benchmarking. *AIP Conference Proceedings*, 896(1):31–49, March 2007.

[263] The official FLUKA site. http://www.fluka.org/, 2011.

[264] L. M. Jiji. *Heat Conduction*. Springer, July 2009.

[265] Engineering ToolBox. http://www.engineeringtoolbox.com/, 2012.

[266] A. Musumarra, P. Figuera, et al. Measuring total reaction cross-sections at energies near the coulomb barrier by the active target method. *Nuclear Instruments and Methods in Physics Research Section A: Accelerators, Spectrometers, Detectors and Associated Equipment*, 612(2):399–406, January 2010.

[267] O.H. Odland, W. Mittig, et al. A fast position sensitive microchannel plate detector for ray-tracing of charged particles. *Nuclear Instruments and Methods in Physics Research Section A: Accelerators, Spectrometers, Detectors and Associated Equipment*, 378(1–2):149–154, August 1996.

[268] V. Birman. *Plate Structures*. Springer, July 2011.

[269] B. Schultrich, H.-J. Scheibe, et al. Elastic modulus as a measure of diamond likeness and hardness of amorphous carbon films. *Diamond and Related Materials*, 5(9):914–918, July 1996.

[270] Y. Huang, J. Wu, et al. Thickness of graphene and single-wall carbon nanotubes. *Physical Review B*, 74(24):245413, December 2006.

[271] Why is the reported elastic modulus of carbon nanotube so scattered? "Yakobsons paradox" and perspective from huang et. al. http://www.imechanica.org/node/791, February 2007.

[272] J.-W. Jiang, J.-S. Wang, et al. Young's modulus of graphene: A molecular dynamics study. *Physical Review B*, 80(11):113405, 2009.

[273] A. Sakhaee-Pour. Elastic properties of single-layered graphene sheet. *Solid State Communications*, 149(1–2):91–95, January 2009.

[274] F Scarpa, S Adhikari, et al. The bending of single layer graphene sheets: the lattice versus continuum approach. *Nanotechnology*, 21(12):125702, March 2010.

[275] A. K Geim. Graphene: Status and prospects. *Science*, 324(5934):1530–1534, June 2009.

[276] Beam Imaging Solutions Inc. http://www.beamimaging.com/.

[277] A. Kellerbauer. The AEgIS experiment: Measuring the free fall of antihydrogen, May 2012.

[278] G. Testera, A. S. Belov, et al. Formation of a cold antihydrogen beam in AEGIS for gravity measurements. *AIP Conference Proceedings*, 1037(1):5–15, August 2008.

[279] M. Doser, Y. Allkofer, et al. Measuring the fall of antihydrogen: the AEgIS experiment at CERN. *Physics Procedia*, 17(0):49–56, 2011.

[280] M. Caccia, L. Conte, et al. Monolithic active pixel dosimeter, September 2009. U.S. patent no. 7582875.

[281] William R. Hendee and E. Russell Ritenour. *Medical Imaging Physics*. John Wiley & Sons, May 2002.

[282] The Programming Language Lua. http://www.lua.org/.

List of Figures

List of Tables

LIST OF TABLES